Title
Ultrafast Nonlinear Spectroscopy of Semiconducting Carbon Nanotubes

Author
Graham, Matthew Werden

Publication Date
2010

Peer reviewed|Thesis/dissertation

Ultrafast Nonlinear Spectroscopy of Semiconducting Carbon Nanotubes

by

Matthew Werden Graham

A dissertation submitted in partial satisfaction
of the requirements for the degree of

Doctor of Philosophy

in

Chemistry

in the

GRADUATE DIVISION

of the

UNIVERSITY OF CALIFORNIA, BERKELEY

Committee in charge:

Professor Graham R. Fleming, Chair
Professor Paul A. Alivisatos
Professor Steven G. Louie

Fall 2010

Ultrafast Nonlinear Spectroscopy of Semiconducting Carbon Nanotubes

by

Matthew Werden Graham

Abstract

Ultrafast Nonlinear Spectroscopy of Semiconducting Carbon Nanotubes

by

Matthew Werden Graham

Doctor of Philosophy in Chemistry

University of California, Berkeley

Professor Graham R. Fleming, Chair

Single-walled carbon nanotubes (SWNTs) are often considered the prototypical nanomaterial with their characteristic large aspect ratios, high tensile strength and size tunable physical properties. While their remarkable electrical and mechanical properties have been well studied, the optical properties of semiconducting SWNTs are continuously emerging with recently reported developments such as greatly enhanced fluorescence yields and highly efficient nanotube photodiodes. The scope of optoelectronic applications for SWNTs depends critically on a detailed understanding of their highly congested absorption features consisting of strongly bound excitonic (E_{11}, E_{22}, etc.), vibronic and dark state transitions. Until recently, carbon nanotubes consisted of highly inhomogeneous distributions of tubes types that made advanced spectroscopic studies impractical. Enabled by samples highly enriched in specific tube types, we investigate carbon nanotubes photophysics in real-time by applying a wide range of techniques including transient absorption, photon echo and 2D Fourier transform spectroscopy. Through detailed analysis and simulation of these femtosecond nonlinear results, fundamental properties concerning excitonic structure, exciton-phonon interactions, and the dynamics of coherent excitons for these quasi one-dimensional nanomaterials are revealed.

Population relaxation dynamics in SWNTs are probed from the visible to mid-infrared regions using transient absorption or grating spectroscopy. Measurements in mid-IR region reveal a broad excited state absorption feature consistent with previously unobserved intra-excitonic transitions and bound vibrational states. Simulation of visible and near-IR transient absorption results suggest efficient exciton-exciton annihilation occurring by both one-dimensional diffusion or delocalized overlap of coherent excitons depending upon the timescale, state transitions, or temperature investigated (4.4 to 292 K). Throughout all the measurements reported, strong contributions from exciton-exciton scattering processes are evident.

The timescales for pure optical dephasing (and the corresponding homogeneous lineshape) were obtained through photon echo measurements. Surprisingly long room temperature dephasing times of 285 fs are reported, suggesting unusually weak exciton-phonon coupling and an inhomogeneously broadened absorption lineshape. At lower temperatures

the dephasing induced by SWNT optical phonons is mitigated, and we show how acoustic phonon processes and environmental disorder determines the absorption line-shape properties.

Professor Graham R. Fleming
Dissertation Committee Chair

Contents

List of Figures

List of Tables

Acknowledgements

Dr. Ying-Zhong Ma (primary collaborator, Oak Ridge)
Professor Graham R. Fleming (Ph.D. advisor)

Theoretical support:

Professor Leonas Valkunas (Vilnius)
Dr. Darius Abramavicius (U.C. Irvine)
Jevgenij Chmeliov (Vilnius)

Nanotube synthetic collaboration:

Professor Mark Hersam (Northwestern)
Dr. Alexander A. Green (Northwestern)
Professor Hisanori Shinohara (Nagoya)
SouthWest Nanotechnolgies

Collaboration for mid-IR work:

Professor Jigang Wang (Iowa State)
Dr. Robert Kaindl (Lawrence Berkeley Labs)
Dr. Matt Prantil (Lawrence Livermore Labs)

Two-dimensional electronic spectroscopy collaboration:

Tessa R. Calhoun

The Graham Fleming Group

Curriculum Vitæ

Matthew Werden Graham

Education

2005	University of Toronto Hon.B.Sc., Chemical Physics
2010	University of California, Berkeley Ph.D.

Selected Fellowships and Awards

- NSERC Postdoctoral Fellowship, 2010–
- NSERC Postgraduate Doctoral Scholarship, 2008-2010
- NSREC Postgraduate Masters Scholarship (*declined*)
- Society for Chemistry in Industry Merit Award, 2005
- Canadian Society for Chemistry Silver Medal, 2004

* NSERC is Natural Sciences and Engineering Research Council of Canada

Selected Conference Presentations

- Ultrafast Phenomena XVII, Snowmass, CO, 2010
- Ultrafast Phenomena in Semiconductors and Nanostructures XIV (SPIE), 2010
- Workshop on Nanotube Optics and Spectroscopy (WONTON), Japan 2009
- 91^{1st} Canadian National Chemistry Conference and Exhibition, 2009
- Ultrafast Phenomena XVI, Stresa, Italy, 2008
- 87^{th} Canadian National Chemistry Conference and Exhibition, 2005

Selected publication references can be found in the headers of the dissertation chapters.

Chapter 1

Introduction

1.1 Background and Motivation

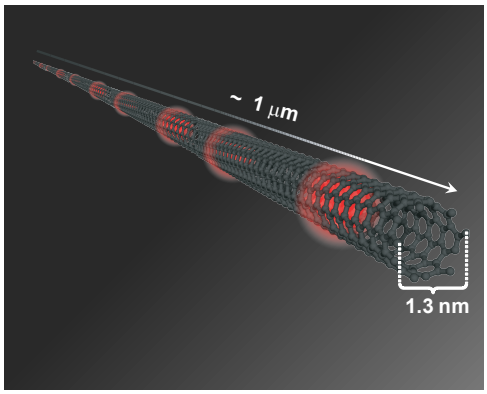

Figure 1.1. Schematic of a single-walled carbon nanotube with multiple optical excitations, highlighting the large length to width aspect ratio.

In 1991, Iijima *et al.* reported discovery of a cylindrical formation of carbon atoms whose physical structure spanned the molecular and crystalline divide.[1] Quickly rising to forefront of nanomaterials research, carbon nanotubes continue to drive an expanding array of novel applications in diverse fields ranging from mechanical engineering to medical biology.

Nanotechnology exploits the novel material properties which arise when bulk condensed matter systems are shrunk down to small dimensions. With an unprecedented aspect ratio (see figure 1.1) that can exceed 10^7, single-walled carbon nanotubes (SWNTs) behave as a one-dimensional (1D) material, possessing molecular-like confinement effects along the circumferential direction, and bulk-crystalline transport properties along the axial

coordinate.[2] When these properties are combined, ubiquitous carbon atoms are transformed into a material which is more conductive than copper, stronger than steel and optically darker than our blackest absorbers.[3, 4, 5, 6]

Application oriented interest in nanotubes predates their discovery; for decades carbon fibers have been used to enhance material strength and rigidity. Later, it was mechanically confirmed that when pulled along it axis, carbon nanotubes have a tensile strength $\sim$300 times greater than that of the strongest steel.[3] Soon after, the electrical properties of carbon nanotubes were harnessed. Electrically, metallic SWNTs can behave like one-dimensional conduits for electrons with near zero effective resistance.[6] These properties makes SWNTs ideally suited for fabricating nanocircuitry, and they are generally considered as one of most promising candidates to replace the silicon transistor as it approaches its fundamental size limitations.[5]

Comparatively less explored, are the photoninc applications of SWNTs. Optically, semiconducting single-walled carbon nanotubes (s-SWNTs) absorb and emit light at a frequency tunable with the nanotube diameter.[7, 2] Synthetic nanotubes contain both metallic and semiconducting tubes across a broad distribution of diameters, as such, they are one of the most efficient know solar absorbers spanning the UV to the near-IR regions.[5, 2] The potential of this efficiency has yet to be harnessed for solar voltaic applications owing in part fundamental unanswered questions concerning photophysics of ensembles of semiconducting SWNTs. In this dissertation, we explore such unanswered questions as "what processes make-up a nanotube linear absorption spectrum", "what electronic and vibrational states are relevant to describe optical relaxation", and "how do multiple optical excitations interact with each other in a 1D confined system". In addressing these questions, time is used as our metric, whereby ultrafast spectroscopic processes are used to resolve dynamic processes on the femtosecond (10^{-15} s) timescale in which they transpire.

1.2 Organization of Dissertation

Attracted by its elegantly simple molecular structure, and potential for optoelectronic applications carbon nanotubes remain an area of intense scientific investigation at the fundamental level. Beyond extensively reported transient absorption studies[8], application of nonlinear, time-resolved optical spectroscopy to carbon nanotubes is an unexplored area. After introducing the fundamental properties of carbon nanotubes and nonlinear spectroscopy (chapters 2 to 3), conventional pump probe measurement are extended into the mid-IR region in order to probe the electronic and vibrational structure (chapters 4 and 5). In chapter 6, multi-exciton generation processes in nanotubes are modeled to reveal how exciton-exciton annihilation processes depend strongly on the initial populated state, temperature and the applied beam fluence. A generalized stochastic approach to model the dynamics of multi-exciton states is also developed.

The coherent dynamics of SWNT excitons are difficult to access by conventional time-resolved techniques. In chapter 7, photon echo spectroscopy is introduced as a direct way

to determine the optical dephasing time associated with the loss of coherence from exciton-phonon scattering. Such exciton-phonon coupling also determines the homogeneous lineshape, which is measured for select SWNTs in chapter 8, by application of photo echo peakshift spectroscopy. Photon echo spectroscopy is also found to be a remarkably sensitive probe of exciton-exciton scattering processes which arise from the multiple exciton generation discussed in chapter 6. The unusually strong dependence of optical dephasing on photon fluence is theoretically modeled in chapter 9 by a non-perturbative technique accounting for up to 10th order interactions. The end result derives how exciton-exciton annihilation induces optical dephasing in SWNTs.

In chapter 10, the temperature dependence of the E_{11} exciton-exciton annihilation rate is investigated to illustrate the importance of both diffusive and delocalized mechanisms for exciton annihilation. A strong correlation between intensity induced optical dephasing, and exciton-exciton population annihilation is also reported. In chapter 11, long pure optical dephasing times for SWNTs of 285 fs (294 K) are measured through a combination of transient absorption and photon echo spectroscopy, consistent with unusually weak room temperature exciton-phonon coupling. Cooling to 4.4 K results in only moderately longer pure dephasing times that scale predominately with the acoustic phonon population. The role of 1D exciton delocalization in exciton-phonon coupling processes is also discussed. Lastly in chapter 12, application of two-dimensional electronic spectroscopy to SWNTs is demonstrated to yield valuable, dynamic information about the E_{22} homogeneous linewidth, phonon side-bands and $E_{22} \leftrightarrow E_{11}$ electronic coupling processes, revealing a rich, unexplored approach to obtain a holistic picture of SWNT exciton dynamics.

1.3 References

[1] S. Iijima. Helical microtubules of graphitic carbon. *Nature*, 354:56–56, 1991.

[2] S. Reich, C. Thomsen, and J. Maultzsch. *Carbon Nanotubes: Basic Concepts and Physical Properties*. Wiley-VCH Verlag GmbH & Co. kGaA, Weinheim, 2004.

[3] S. Saito, G. Dresselhaus, and M.S. Dresselhaus. *Physical Properties of Carbon Nanotubes*. Imperial College Press, London, 1998.

[4] L.X. Zheng, M.J. O'Connell, S.K. Doorn, X.Z. Liao, Y.H. Zhao, E.A. Akhadov, M.A. Hoffbauer, B.J. Roop, Q.X. Jia, R.C. Dye, D.E. Peterson, S.M. Huang, J. Liu, and Y.T. Zhu. Ultralong single-wall carbon nanotubes. *Nat. Mater.*, 3:673–676, 2004.

[5] P. Avouris, J. Chen, M. Freitag, V. Perebeinos, and J.C. Tsang. Carbon nanotube optoelectronics. *Phys. Stat. Sol. B*, 243(13):3197–3203, 2006.

[6] P. Avouris. Molecular electronics with carbon nanotubes. *Acc. Chem. Res.*, 35:1026–1034, 2002.

[7] M.J. O'Connell, S.M. Bachilo, C.B. Huffman, V.C. Moore, M.S. Strano, E.H. Haroz, K.L. Rialon, P.J. Boul, W.H. Noon, C. Kittrell, J. Ma, R.H. Hauge, R.B. Weisman, and R.E. Smalley. Band gap fluorescence from individual single-walled carbon nanotubes. *Science*, 297:593–596, 2002.

[8] Y.-Z. Ma, T. Hertel, Z.V. Vardeny, G.R. Fleming, and L. Valkunas. Ultrafast spectroscopy of carbon nanotubes. Solume 111, pages 321–352., Eds. A. Jorio, M.S. Dresselhaus, G. Dresselhaus, Springer-Verlag Berlin, Heidelberg, 2008.

Chapter 2

Carbon Nanotubes

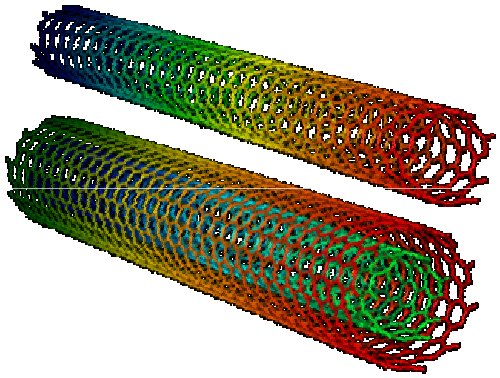

Figure 2.1. Structure of a (7,5)-type chiral single-walled carbon nanotube (SWNT), and its double-walled (DWNT) counterpart with an outer (17,6)-type shell.

2.1 Physical and Electronic Structure of Carbon Nanotubes

The novel electrical, mechanical and optical properties of carbon nanotubes are a direct consequence of their unusual structure. Structurally, a carbon nanotube can be described as a monolayer of graphite (graphene) rolled up into a cylinder along a lattice vector. The length of the cylindrical tube can be arbitrarily long, and is generally capped at the ends by two hemispherical sections of appropriately sized fullerene-like structures. The resulting

structure is termed a single-walled carbon nanotube (SWNT).[1] Alternatively, a SWNT can be enveloped in concentric cylindrical casings of graphene to form double or even multiple-walled carbon nanotubes (D/MWNTs, see figure 2.1).

The physical properties of carbon nanotubes are largely determined by their associated chiral vector ($\mathbf{C}_h$). $\mathbf{C}_h$ is defined by the integral indices (n, m) which span the the honeycomb Bravais lattice vectors $(\mathbf{a}_1, \mathbf{a}_2)$ for a graphene sheet,

$$\mathbf{C}_h = n\mathbf{a}_1 + m\mathbf{a}_2 \equiv (n, m) \tag{2.1}$$

and its magnitude provides the circumference of the corresponding nanotube.[1] To geometrically construct the carbon nanotube, the tip and stem of $\mathbf{C}_h$ are connected, effectively rolling up the graphene sheet as shown in figures 2.2a and b. Accordingly, the chiral vector is also a direct measure of nanotube diameter (d_t), i.e.

$$d_t = \frac{|\mathbf{C}_h|}{\pi} = \frac{a}{\pi}\sqrt{n^2 + m^2 + nm} \tag{2.2}$$

where a is the magnitude of the (nonorthogonal) graphene Bravais lattice vectors, i.e. $|\mathbf{a}_1| = |\mathbf{a}_2| = \sqrt{3}a_{CC} = 1.42 \times \sqrt{3} = 0.246$ nm.[2, 3, 4] It is also useful to define a chiral angle(θ) of $\mathbf{C}_h$ with respect to the $\mathbf{a}_1$ lattice vector[5],

$$cos\theta = \frac{\mathbf{C}_h \cdot \mathbf{a}_1}{|\mathbf{C}_h||\mathbf{a}_1|} = \frac{2n + m}{2\sqrt{n^2 + m^2 + nm}} \tag{2.3}$$

which has range of $0 \leq \theta \leq 30^o$.

The vector $\mathbf{C}_h$ defines not only the carbon nanotube circumferential direction, but also the translational vector ($\mathbf{T}$) along the nanotube that is required to form the complete unit cell. $\mathbf{T}$ runs perpendicular to $\mathbf{C}_h$ (see figure 2.2a), and can be similarly expressed in terms of the honeycomb lattice vectors as,

$$\mathbf{T} = t_1\mathbf{a}_1 + t_2\mathbf{a}_2 \tag{2.4}$$

$$t_1 \equiv \frac{2m + n}{d_R}, t_2 \equiv -\frac{2n + m}{d_R} \tag{2.5}$$

where d_R is the greatest common divisor of $(2n + m)$ and $(2m + n)$.[1] For instance, this dissertation primarily examines the spectroscopy associated with nanotubes having a $\mathbf{C}_h$= (6,5), and a mean tube length of 600 nm. Using the (6,5) chirality in equation 2.5, we obtain a $\mathbf{T}$=$(16, -17)$, corresponding to a unit cell length of $|\mathbf{T}| = |\mathbf{a}_1|\sqrt{n^2 + m^2 + nm}/d_R \cong 4.06$ nm. With this cell length, a ∼600 nm long tube would be composed of approximately 148 unit cells. Using the lattice geometry shown in figure 2.2a, we can further calculate the number of carbon atoms per unit cell (N) as,

$$N = \frac{|\mathbf{C}_h \times \mathbf{T}|}{|\mathbf{a}_1 \times \mathbf{a}_2|} = \frac{2(m^2 + n^2 + nm)}{d_R} \tag{2.6}$$

which for a (6,5) SWNT is 364 atoms per unit cell.[1] Using a ∼600 nm long (6,5) SWNT nanotube investigated here, we can expect 364 $\frac{atoms}{cell} \times$ 148 $\frac{cells}{nanotube} \cong 5.4 \times 10^4$ carbon atoms

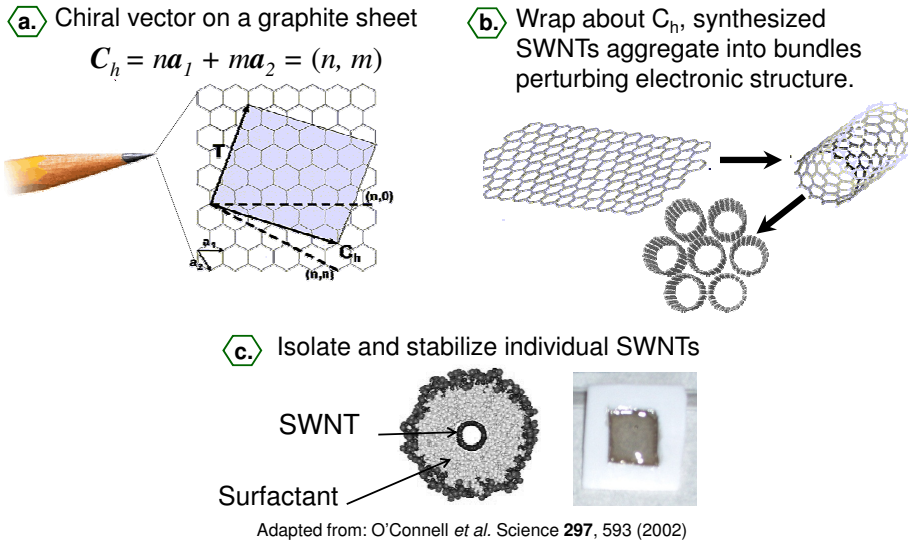

Figure 2.2. Single-walled carbon nanotubes; from structural construction (a) to individually separated tubes stabilized in polymer composites(c).

per (6,5) nanotube. The sheer number of carbon atom per tube clearly distinguishes SWNTs from any comparable molecular based system, and highlights the essential role for solid state physics principles such as band structure and **k**-space to adequately describe optical processes in carbon nanotubes.

2.1.1 Graphene; the tight binding model

The complex network of bonding in a carbon nanotube derives from the much studied σ and π bonds associated with graphitic carbon. In the planar direction, the σ bonds are sp^2 hybridized and form the main hexagonal network.[1] The π bonding network of p_z orbitals are oriented parallel to the graphene surface, and further give rise to van der Waals interactions that are ultimately responsible for phenomena such as bundling in carbon nanotubes and the characteristic inter-planer separation between graphene sheets.[6] When a sheet of graphene is constrained to the cylindrical formation of SWNT, strong π bond interactions are expected because of steric interactions. In contrast, the planar σ bonds are too far away from the Fermi level, and play only a minor role in the electrical and optical properties of SWNTs.[5] As a consequence, the electronic properties of graphene can be sufficiently modeled by applying the tight-binding approximation to obtain the band structure associated with the π bonding

network. Full details for this calculation are reported elsewhere (see [7, 5] for example). Briefly, the Schrodinger equation ($H\psi(\mathbf{k}) = E(\mathbf{k})\psi(\mathbf{k})$), is solved for the eigenvalues $E(\mathbf{k})$. The eigenfunctions are expressed as linear combination of Bloch functions, $\varphi(\mathbf{k})$. In the tight binding approximation it is assumed that the Bloch functions can be written as linear combinations of the atomic orbitals(LCAO) to provide the wave functions associated with the perpendicular $2p_z$ orbitals for graphene.[8] Since the graphene unit cell only has 2 atoms per cell, in the solution to the above Schrodinger equation it is sufficient to diagonalize a 2×2 matrix for interactions between the nearest neighbors only. The resulting eigenvalues, $E(\mathbf{k}) = E(k_x, k_y)$ provide the corresponding energy dispersion relations for the valence and conduction bands for graphene[5, 6]. The general form of the first Brillouin zone is shown in figure 2.3a. The regions of primary interest are at the so-called K high-symmetry points where the conduction and valence band intersect to make graphene a zero-band gap material. This region is magnified in figure 2.3a, revealing a cone-like intersection region that will ultimately dominate the electrical and optical properties graphene and carbon nanotubes alike.

2.1.2 The zone-folding approximation

To move from a two-dimensional graphene structure to a quasi-1D carbon nanotube one can naively imagine simply reducing the two-dimensional (k_x, k_y) Brillouin zone, into a 1D zone. In this case, the nanotube Brillouin zone is obtained by drawing 1D cutting lines through the regions of highest interaction, which in this case are about the K high-symmetry points of graphene, labeled in figure 2.3a. Along the z-axial direction, free particle behavior is assumed for an infinite length tube, which corresponds to a free particle reciprocal lattice vector $k_z = 2\pi/|\mathbf{a}_1|$. The circumferential direction however, is quantized according to the boundary condition that the wavefunction $\psi(\mathbf{r} + \mathbf{C}_h) = \psi(\mathbf{r})$, which implies the circumferential reciprocal lattice vector $(\mathbf{k}_{x,y})$ is also quantized as;

$$\mathbf{k}_{x,y} = \frac{2\pi}{|\mathbf{C}_h|} \cdot I = \frac{2}{d_t} \cdot I \tag{2.7}$$

where I is an integer value.[1, 9] As a consequence, the corresponding nanotube Brillouin zone, consists of 1D cutting lines (figure 2.3a) of length $2\pi/|\mathbf{a}_1|$ spaced at intervals of $2/d_t$ parallel to the tube axis. This approach known as the zone-folding approximation, allows one to read off the nanotube band structure for any given tube chirality by simply drawing the corresponding cuttings about the K-point region of the tight-binding band structure for graphene.[5, 9] This approximation neglects important complications which arise from the new cylindrical geometry as well as the strong influence of tube wall curvature, but nonetheless provides an excellent predictive model for the basic physical properties of carbon nanotubes (e.g., rough band gaps, semiconducting or metallic, etc.).

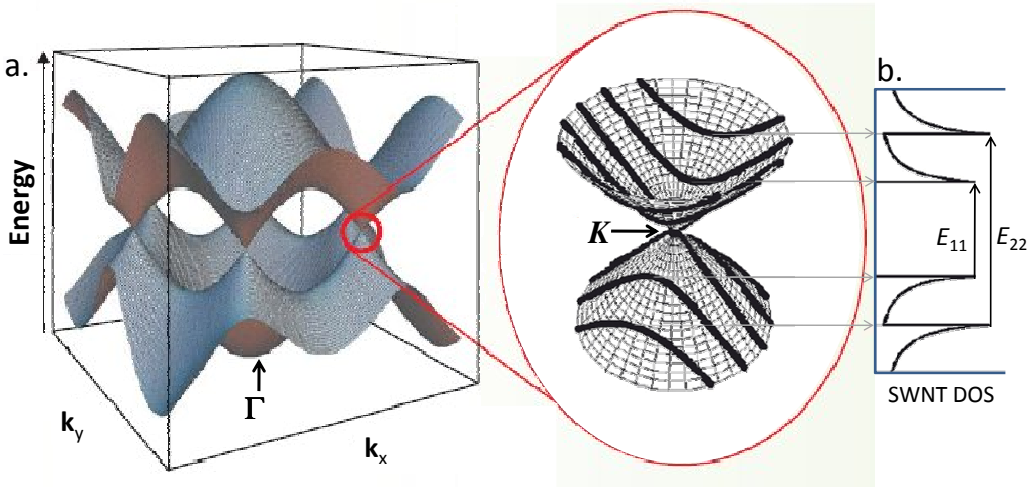

Figure 2.3. a. Graphene Brillouin zone; electronic and optical properties of SWNTs depends on band structure near the magnified cone-like intersections connecting the corresponding conduction and valence bands. b. SWNT electronic properties can be modeled in zone folding approximation on graphene shown by the cutting lines and for corresponding one-dimension density of states. For semiconducting tubes, these resulting van Hove singularities cause gaps to appear in the band structure.

2.1.3 Semiconducting and metallic nanotubes

Carbon nanotubes are either semiconducting or metallic, depending on the nanotube chirality. When the carbon nanotubes Brillouin zone cutting lines cross though the the K symmetry point the nanotube will be metallic, with a zero band-gap much like graphene.[1, 4]

To account for the semiconducting case, we need to first define the coordinates in reciprocal space that take us from the Γ high symmetry point (see figure 2.3a) to any of the six nearest K high symmetry points of the graphene. Translating our original Bravais lattice vectors $\mathbf{a}_1$ and $\mathbf{a}_2$ into reciprocal space using Cartesian coordinates one obtains $\mathbf{k}_1 = (k_x, k_y) = 4a\pi/\sqrt{3}(0, 1)$ and $\mathbf{k}_2 = 4a\pi/\sqrt{3}(\frac{\sqrt{3}}{2}, -\frac{1}{2})$.[5] Using this geometry, it can be seen that the vector $\mathbf{K} = \frac{1}{3}(\mathbf{k}_1 - \mathbf{k}_2)$ translates from Γ to the K high symmetry points. As a result, a nanotube will be metallic if $\mathbf{K}$ is a reciprocal lattice vector of a particular tube with chiral vector $\mathbf{C}_h$ [10], or alternatively,

$$\mathbf{K} \cdot \mathbf{C}_h = 2\pi I = \frac{1}{3}(\mathbf{k}_1 - \mathbf{k}_2) \cdot (n\mathbf{a}_1 + m\mathbf{a}_2) = \frac{2\pi}{3}(n - m). \tag{2.8}$$

The above expression shows that in order for a cutting line to cross the K point and acquire metallic behavior, the nanotube chiraility will be $(n - m) = 3I$.[5] Additional criteria for metallicity can also be obtained by searching for the conditions on k_z where the nanotube conduction and valence band meet. This condition can be evaluated by finding where the

translational vector crosses a K-high symmetry point, i.e.

$$\mathbf{K} \cdot \mathbf{T} = 2\pi k_z \tag{2.9}$$

which crosses K when $\mathbf{K} \cdot \mathbf{T} = 0$ or when the continuous wavevector $k_z = 0$. Equation 2.9 can be evaluated through substitution with equation 3.5 to show that this criteria is satisfied for the so called armchair tubes $(n, n = m)$ and select zig-zag $(n, m = 0)$ tubes where n is multiple of three, making them metallic within the zone folding approximation.[6, 5] Using the rules obtained from equations 2.8 and 2.9, metallic tubes collectively represent approximately $\frac{1}{3}$ of all tube types possible.[1] However their prevalence can be selectively controlled by synthetic and purification approaches. In this dissertation, only optical properties of semiconducting carbon nanotubes are considered, and all the samples have been enriched (up to 97%) in tube chiralities with a characteristic semiconducting band structure.[11]

2.2 Carbon Nanotube Synthesis

Numerous synthetic techniques exist for carbon nanotubes, but they all rely on three basic requirements originally discovered by Iijima *et al.*; they are a source of carbon, high activation temperatures and surface catalysis to nucleate growth.[12] Today, the primary synthetic routes can by grouped in three categories of plasma arc discharge, laser ablation, and chemical vapor deposition (CVD). These synthetic approaches differ primarily in their method of providing the activation energy required to make nanotube formation thermodynamically favorable.[13, 14]

The arc-discharge route was the first reported method of nanotube synthesis, and relies on DC arc discharge between two graphite electrodes.[12] The resulting carbon nanotubes accumulate at the device cathode. In absence of catalysts to mediate the reaction, only multi-walled carbon nanotubes are formed. By adding metallic catalysts at the anode and controlling the ambient gas, SWNTs can be preferentially formed. However, the arc-discharge method has a distinct draw-back of producing highly bundled SWNT with extensively tangled morphologies.[1]

To obtain samples highly concentrated is specific nanotube tube types, chemical vapor deposition (CVD) is the generally preferred method. CVD uses hydrocarbon gases and transition metal catalysts (e.g. Fe, Ni, Co) to provide a surface nucleation site for growth. The two most widely used CVD approaches are the HiPCO (High-Pressure carbon monoxide) and CoMoCAT (Cobalt Molybdenum CATatalyst) methods. HiPCO technique uses Fe catalysts, and was the synthetic route used for many early spectroscopic measurements done in this field (e.g. [15, 16]). For the work presented in chapters 4-12, the CoMoCAT method was preferred synthetic route due to its enhanced selectivity for specific nanotube chiralities such as the (6,5), (7,5) and (6,4) types (see figure 2.5). In particular, CoMoCAT technique can produces SWNTs with as little as 3% metallic tube content, compared to the $\sim$30% common with other techniques. In CoMoCAT synthesis, a constant stream of carbon monoxide gas flows past bimetallic strips of cobalt-molybdenum catalyst particles supported

on SiO_3. Compared to the arc discharge approach, CoMoCAT operates at comparitively low temperature ranging from 500-1000^o C.[14] After synthesis, a post processing method is used to remove residual catalyst particles, silica and amorphous carbon depositions. The end product is a black semi-crystalline fibrous powder that is highly enriched in semiconducting tubes.

2.3 Optical Properties

2.3.1 Electronic density of states

In contrast to bulk semiconductors, carbon nanotubes are a true *quasi*-1D nanomaterial, and the ensuing confinement effects greatly modify the electronic structure. To examine the behavior of the density of states ($n(E)$) under 1D confinement, we consider a particular nanotube subband and allow for free particle motion along the z-axis, and quantized energy eigenstates along the circumferential direction. The corresponding density of states in 1D can be evaluated from the textbook expression for the i^{th} transition,

$$n_i(E) = \frac{2}{V}\int dk_z \delta(k_z - k_i)\left|\frac{\partial E(\mathbf{k})}{\partial k_z}\right|^{-1} \tag{2.10}$$

where V is the Brillouin zone volume.[8, 17] To evaluate the above partial derivative, we note that close to the Fermi level the cone-like graphene dispersion (see figure 2.3a) can be used to extract the SWNT band structure, which can further be approximated by a set of straight lines about the Fermi vector ($\mathbf{k}_f$), i.e.

$$E(\mathbf{k}) \propto \pm\left|\mathbf{k} - \mathbf{k}_f\right| = \sqrt{\Delta k_i^2 + \Delta k_z^2} \tag{2.11}$$

where the $\mathbf{k}$-dependence has been decomposed into their circumferential (k_i) and z components(k_z) about about the Fermi level.[5] This energy dispersion relation can then be used to evaluate the derivative in equation 2.10,

$$\left|\frac{\partial\sqrt{\Delta k_i^2 + \Delta k_z^2}}{\partial k_z}\right|^{-1} = \frac{|E(\mathbf{k})|}{\sqrt{E^2 - E_i^2}} \tag{2.12}$$

where E_i is the energy associated with the quantized k_i wavevectors for the circumferential nanotube direction. The corresponding nanotube density of states is then obtained by substitution in equation 2.10 and integration over k_z,

$$n_i(E) \propto \int dk_z \delta(k_z - k_i)\frac{|E|}{\sqrt{E^2 - E_i^2}} \tag{2.13}$$

$$\Rightarrow n_i(E) \propto \begin{cases} \frac{|E|}{\sqrt{E^2 - E_i^2}} & \text{if } E > E_i \\ 0 & \text{if } E < E_i \end{cases}$$

revealing that the density of states diverges as $E \to E_i$ for each subband denoted by the quantum number i.[18, 19] In figure 2.3b, the density of states is plotted for $i = 1, 2$. The resulting divergence produces a van Hove singularity as $E \to E_i$, and the existence of finite band gap for semiconducting tubes. Using Fermi's Golden Rule, the diverging density of states, $n_i(E)$ can be directly related to the electronic transition probability.[8] The net end result is a series of spectrally sharp optical transitions (denoted E_{11}, E_{22}, etc.) that dominate the opticla absorption spectrum.[15, 20]

2.3.2 Linear absorption

The linear absorption spectrum of a typical sample of synthetic carbon nanotubes is shown in figure 2.4. In contrast to the sharp van Hove singularities predicted in the previous section, two broad peaks are observed corresponding to the first and second subband transitions in semiconducting carbon nanotubes. In their natural state, SWNTs have a tendency to bundle with neighboring tubes because of mutual van der Waals attraction.[1] These bundles of carbon nanotubes produce a broad absorption spectrum, and contain contributions from many different nanotube chiralities. The quantization condition along the circumferential tube direction from equation 2.7 shows that $k_{x,y} \propto 1/d_t$, and when substituted into the linear dispersion relation from equation 2.11, it is readily seen that energy gap for semiconducting tubes scales as,

$$E_g \propto \frac{1}{d_t}. \tag{2.14}$$

As a consequence, the observed spectral broadening in an ensemble measurement of many tube types, results predominately from the inverse energy gap dependence with tube diameter.[15] Such a broad linear absorption spectrum makes spectroscopy inherently difficult since each individual tube type has intrinsically different physical properties. To resolve this problem, and probe the optical properties of individually separated nanotubes, post-processing of synthetic carbon nanotubes is required.

2.3.3 Nanotube purification and sample characteristics

In comparison to extensively studied nanoscale systems like quantum dots and wells, the electronic and spectroscopic properties of semiconducting carbon nanotubes remains nebulous. A chief limiting factor for unambiguous results has been the need for highly individualized SWNTs samples, that are highly pure in a specific carbon nanotube chirality. The ability to isolate a single tube type from a bulk sample of carbon nanotubes is presently an unsolved synthetic problem. Fortunately, by applying post-processing techniques such as the one outlined below, the distribution of tube types can be sufficiently narrowed, so that a desired tube of $\mathbf{C}_h = (n, m)$ can now be optically probed using on-resonant excitation.[21]

Synthetic carbon nanotubes are naturally sparingly soluble in water.[1] To dissolve and

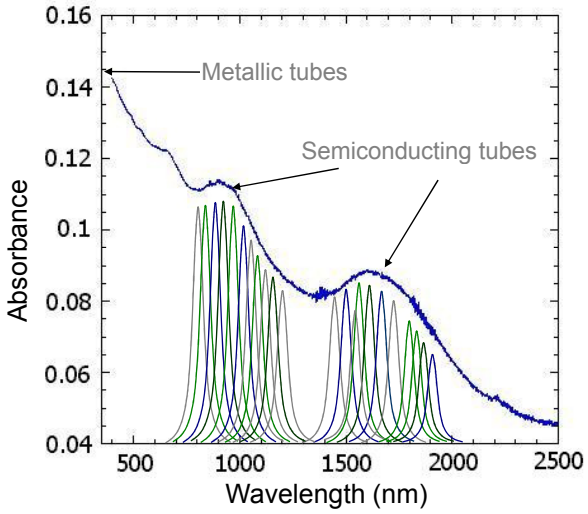

Figure 2.4. Bulk synthetic nanotubes give broad and ambiguous linear absorptions features owing largely to nanotube bundling. Within the spectrum are comparatively sharp resonances corresponding to the chirality dependent ($\mathbf{C}_h$) absorption.

to separate SWNT bundles, subsequent post-processing steps are required. While such bundles of carbon nanotubes retain their large tensile strength, the electronic properties are thought to be strongly perturbed as demonstrated for instance by the markedly lower photoluminescence yields of bundled carbon nanotubes.[22] In order to study the optical properties of SWNTs, it is necessary to separate the bundles into individualized tubes. This process is accomplished by sonicating the SWNTs, resulting in mechanical tube separation at the atomic level. Further aggregation among nanotubes can be prevented by introduction of stabilizing surfactant that forms micelles on the tube surface (see figure 2.3c).[23] As final step, ultracentrifugation is employed to remove remaining nanotube bundles and residual amorphous carbon. Upon comparing absorption spectra of bundled nanotubes (figure 2.4) to aqueous suspensions of individualized SWNTs (figure 2.5), comparatively sharp absorption resonances are apparent revealing the previously hidden van Hove singularity transitions (E_{11}, E_{22},etc.) of different tube types. This process of nanotube individualization was first reported by O'Connell *et al.* in 2001, and provides nanotubes free from inter-tube coupling, that enabled the very first optical investigations on individual carbon nanotubes.[24, 23]

Individually separated SWNTs prepared by the CoMoCAT synthesis, give a highly structured linear absorption and fluorescence spectra, and the peaks of various tube types still overlap strongly as shown in figure 2.5. In 2006, Arnold *et al.* developed a density gradient approach that further narrowed the distribution of tube types for CoMoCAT synthesized SWNTs.[21] The resulting electronic properties yield distinct absorption peaks (see figure 2.6), which readily permit on-resonant excitation of one tube types to exclusion of all others. For instance, the dotted lines indicates typical laser pulse spectrum used in our spectroscopic

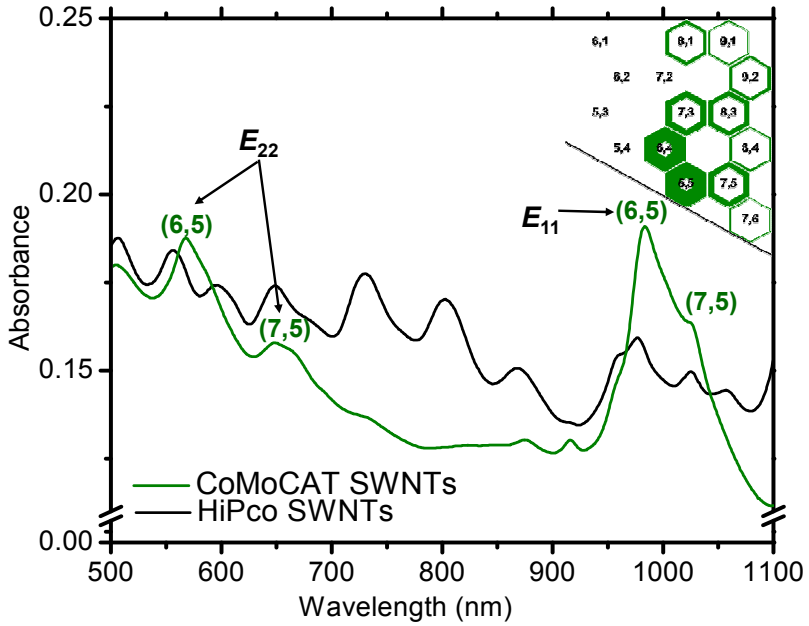

Figure 2.5. Linear absorption spectrum of aqueous samples of SWNTs in surfactants. Synthesis by the CoMoCAT CVD method preferentially produces semiconducting tubes with a much narrower chirality distribution than form HiPCO CVD synthesis. The relative abundances of the different tube types obtained from the CoMoCAT synthesis [(top right), *courtesy of SouthWest Nanotechnologies*]

studies, and it highlights the exclusive resonant excitation of the E_{11} optical transitions for the (6,5) tube type.

The precise method for carrying out this density gradient enrichment is outlined in subsequent chapters. Briefly this technique exploits that nanotubes selectively coated in surfactants and bile salts will have a different inherent buoyancy in solution depending upon their nanotube chirality. Exploiting this principle, Arnold *et al.* demonstrated that after ultracentrifugation, the solution of nanotubes separates into spatially separated layers that are in enriched in specific tube types (shown in figure 2.6, right). Once extracted, these aqueous layers yield remarkably strong absorption, photoluminescence and nonlinear optical response for nanotubes of the (6,5) chirality.[21, 25] The recent availability of such high-purity samples has drastically changed the scope of spectroscopic characterization tools that can be applied with a sufficiently good signal-to-noise response.

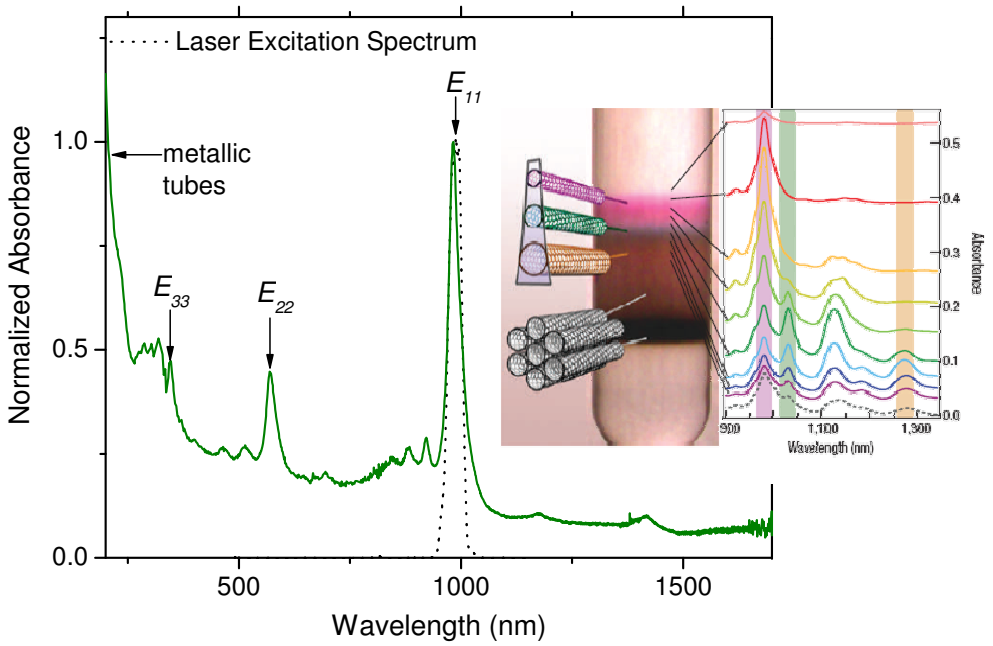

Figure 2.6. Carbon nanotubes can be purified and enriched in the (6,5) chirality, to yield sharp transitions that can be resonantly excited with a laser pulse to exclusion of other tube types (shown). The enrichment process is done by density gradient separation (side inset, *reproduced with permission from Arnold et al.*)[21].

2.4 Semiconducting Single-Walled Carbon Nanotubes: an Excitonic Picture

The ability to obtain individually separated SWNTs as demonstrated by O'Connell *et al.*, gave rise to a period of intense study of nanotube photoluminescence.[23, 15, 26] Through comparison of the obtained two-dimensional SWNT fluorescence spectrum against established Raman scattering measurements, spectroscopic assignment of absorption peaks to specific tube chirality was finally made possible.[15] At the time of this work by Bachilo *et al.* in 2002, the zone-folding approximation on graphene was assumed sufficient and the band transitions were stilled modeled using 1D electron-hole van Hove singularity picture (see figure 2.3).[5] For this model to be sufficient, each subband transition ($n_i(E)$) must have equal energetic spacing because of the linear dispersion relation in equation 2.11 (about the K high symmetry points). However, after spectral assignment of the peaks by Bachilo *et*

al., it became clear that for semiconducting tubes $E_{22}/E_{11} \neq 2$, but rather $\sim$1.7.[27, 15] This so called "ratio problem" could not be explained by a one-electron model, and it was postulated that the discrepancy could be explained by many-body effects such as exciton formation originally suggested by the *ab initio* calculations of Ando *et al.* and Spataru *et al.*[28, 29]

2.4.1 Experimental determination of the exciton binding energy

Stable excitons are prevalent in wide variety of semiconducting systems from GaAs quantum wells to quantum dots. A stable exciton forms when electron-hole Coulombic attraction gives rise to an energetically favorable lower state. The corresponding energy separation with respect to the continuum state is known as the exciton binding energy (E_B). Typically binding energy for three-dimensional semiconductors like GaAs are small with E_B <10 meV.[30] Such weakly bound excitons are not considered stable at room temperature since the system thermal energy exceeds the binding energy ($E_B \geq k_B T \cong 25$ meV at 294 K).[31]

Numerous experimental reports provided anecdotal evidence that stable excitons might exist in semiconducting SWNTs; these included the ratio problem reported in Bachilo *et al.*,[15] the weak absorption lineshape dependence with temperature by Htoon *et al.*,[26] and intensity-dependent decay dynamics reported by Ma *et al.*[32] However, these reports only offered indirect support for exciton formation, and so despite strong theoretical predictions, the simpler 1D van Hove singularity model was generally preferred.

In 2005, two independent works by Wang *et al.* and Ma *et al.* reported a direct measurement of the exciton binding energy for semiconducting SWNTs that was in excess of 0.4 eV for the lowest E_{11} transition.[34, 33] Each respective work employed very different methodologies; Wang *et al.* employed two-photon luminescence and Ma *et al.* used spectrally resolved transient absorption. Shortly after, a more comprehensive study of binding energies of various tube types was reported by Maultzsch et al.[35] In figure 2.7, the transient absorption work by Ma *et al.* is briefly summarized. Using spectrally resolved transient absorption, the spectrum 50 fs after initial excitation reveals a salient transient peak that can be assigned to the impulsively populated electron-hole continuum (shown in green). Also observed was a secondary feature (shown in orange), that persists for 100s of ps and is assigned to the corresponding bound exciton state. The resulting energetic difference between transient peak gave a direct measurement for the (8,3) SWNT binding energy of 0.41 eV.[33] Such large binding energies are substantial fraction of the overall energy gap, and showed conclusively that the bright optical transitions observed correspond to stable exciton states.[34, 19, 36]

2.4.2 Properties of confined excitons

Electrons and holes are the preferred carriers within the solid-state elementary excitation model.[37] In many systems such as semiconducting SWNTs however, the mutual Coulombic attraction between electron-hole pairs is sufficiently strong that they are best described by

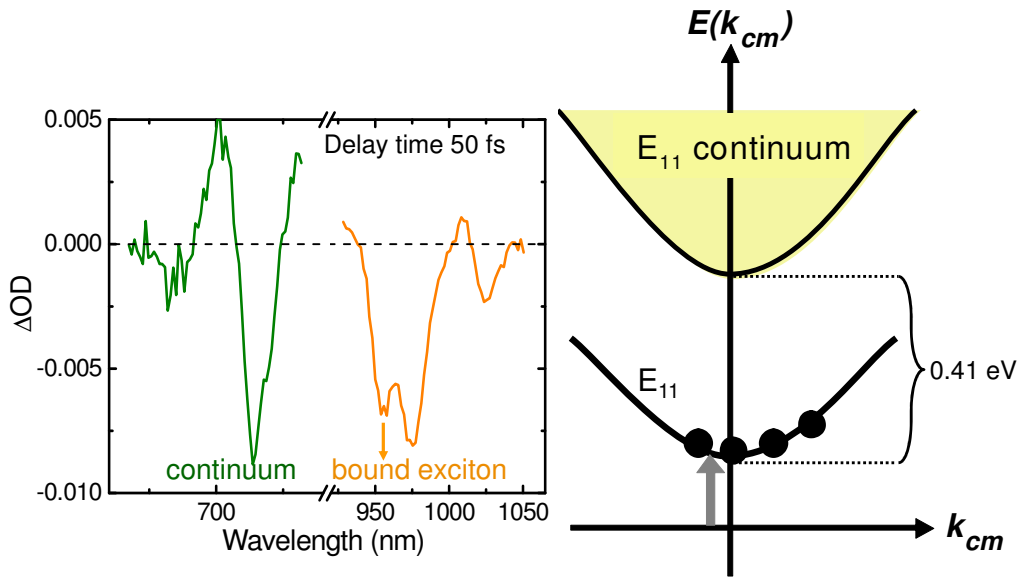

Figure 2.7. Transient absorption spectrum after a 50 fs pump-probe delay time showing the respective peaks for the E_{11} transition and a continuum state transition for the (8,3) type SWNT. This energetic peak separation defines the associated exciton binding energy as 0.41 eV. (*the first panel is reproduced with permission from Ma et al.* [33])

a composite quasi-particle, the exciton. Under such a strong Coulombic interaction the respective group velocities of the electron(v_e) and hole(v_h) necessarily become correlated in their respective bands such that,

$$v_e = v_h = \frac{1}{\hbar}\frac{\partial E(\mathbf{K}_{cm})}{\partial \mathbf{K}_{cm}}. \tag{2.15}$$

where $\mathbf{K}_{cm}$ is the center of mass wavevector for the exciton and is defined as $(\mathbf{k}_e - \mathbf{k}_h)/2$.[19, 36] While both direct and indirect band gap transitions are common with uncorrelated electron-hole pairs, in the excitonic picture generally $\Delta\mathbf{K}_{cm} \approx 0$ for all transitions because the particle motions must be correlated. Small deviations in this requirement for direct transitions at band minimum occur, but are generally no greater than that of the intrinsic momentum of the interacting photon.[38]

Depending upon the exciton spatial properties with respect to the host lattice, excitons can be generally divided into the two classifications of Frenkel and Mott-Wannier types.

Frenkel excitons are common in molecular solids, and are characterized by an effective exciton radius (a_{ex}) that is smaller than the lattice spacing.[39] Mott-Wannier excitons normally have smaller binding energies and have comparatively weak dielectric screening permitting a larger effective radius that can span many lattice sites.[17] For semiconducting SWNTs, the E_{11} exciton radius has been experimentally estimated to be 1-2 nm,[34] which is larger than tube diameter, and so they are generally classified at Mott-Wannier excitons.

The electronic properties of excitons can be roughly approximated by a two-particle Schrodinger equation with a Coulombic attractive potential.[37, 40] For SWNTs, the exciton properties in a dielectric environment can be estimated by a 1D model using the modified hydrogen-like Schrodinger equation shown below,

$$\left(\frac{\hbar^2}{2\mu_{ex}}\frac{d^2}{dx^2} - \frac{e^2}{\epsilon\,|x|}\right)\psi_n(x) = E_n\psi_n(x) \tag{2.16}$$

where μ_{ex} is the electron-hole effective mass, ϵ is the dielectric screening parameter, E_n is the minimum exciton energy, and $\psi_n(x)$ is a hydrogenic-like wavefunction. The solutions are obtained in a similar fashion to the hydrogen atom, except for the treatment of the singularity which arises near $|x| = 0$.[40] The resulting eigenvalues E_n, provide an effective exciton binding energy, which allows the overall dispersion relation for excitons to be expressed as

$$E_{n,ex}(\mathbf{K}_{cm}) = E_g - \frac{Ry^*}{\left(n^2 + \frac{d-3}{2}\right)} + \frac{\hbar^2\mathbf{K}_{cm}^2}{2(m_e + m_h)} \tag{2.17}$$

where E_g is the total band gap energy (i.e. $E_c(0) - E_v(0)$), and Ry^* =13.6 eV ($\mu_{ex}/m_e\epsilon^2$) is the effective Rydberg energy.[37] Here, a parabolic exciton band dispersion has been assumed similar to the schematic depicted for the E_{11} band in figure 2.7. Using this model the effective exciton radius is obtained directly from hydrogen Bohr radius(a_B) augmented by μ_{ex} and the dielectric screening coefficient ϵ,

$$a_{ex} = \left(n + \frac{d-3}{2}\right)^2 \frac{m_e\epsilon}{\mu_{ex}} a_B. \tag{2.18}$$

The resulting exciton radius varies markedly with system dimensionality(d), and with the dielectric constant of the nanotube and the local environment.[37, 39] For SWNTs, the dimensionality, $d = 1$ so we expect not only a larger exciton binding energy from enhanced Coulombic interactions, but also a larger exciton radius compared to solids of higher dimensionality as shown by equation 2.18. Notwithstanding the rough approximations made, this 1D hydrogenic model demonstrates how Mott-Wannier excitons with characteristic large radii of 1-2 nm[34] are realized in spite of the presence of remarkably large exciton binding energy.

2.4.3 Calculating electron-hole interaction

Long before conclusive experimental evidence for stable excitons in SWNTs, *ab initio* treatments showed the effective band gap for semiconducting tubes depends strongly on

how the electron-hole interaction is treated.[41, 28] In 2004, the seminal work by Spataru *et al.* calculated the band structure for metallic and semiconducting tubes.[29] Full details of the theoretical methods employed are presented elsewhere.[19, 29] Briefly, the electronic structure was modeled as $2p_z$ orbitals from a folded Brillouin zone of graphene, and a density-functional theory (DFT) approach was used to find the SWNT electronic ground state. DFT provided the required ground state wavefunction, and eigenvalues were obtained by solving the Kohn-Sham equations.[29]

Since Coulomb interaction localizes the wavefunction in real space, for strongly bound excitonic systems $\mathbf{k}$ is no longer a good quantum number, and a more sophisticated approach is required to obtain the coupled electron-hole excitation energy, Ω_n. Spataru *et al.* was able to explicitly include this electron-hole interaction using the powerful Bethe-Salpeter equation,

$$(E(\mathbf{k}_c) - E(\mathbf{k}_v))\psi_n(\mathbf{k}_c, \mathbf{k}_v) + \sum_{\mathbf{k}'_c\mathbf{k}'_v} \left\langle \mathbf{k}_c\mathbf{k}_v \left| K^{eh} \right| \mathbf{k}'_c\mathbf{k}'_v \right\rangle \psi_n(\mathbf{k}'_c, \mathbf{k}'_v) = \Omega_n\psi_n(\mathbf{k}_c, \mathbf{k}_v) \qquad (2.19)$$

where $E(\mathbf{k}_v)$ and $E(\mathbf{k}_c)$ are the quasi-electron and quasi-hole energies respectively, and $|\mathbf{k}_v\rangle$ and $|\mathbf{k}_c\rangle$ are the quasi-electron and quasi-hole states. K_{eh} is the electron-hole interaction kernel that contains both a repulsive Coulombic exchange term and an attractive screening contribution. Together, K_{eh} can effectively model electron-hole correlations through a two-particle Green's function.[19, 42] In Spataru *et al.*, solutions for Ω_n were obtained, and for the (8,0) SWNT a binding energy of $\sim$1 eV was reported after inclusion of electron-hole correlations.[29] This large exciton binding energy provided strong initial support for highly correlated electron-hole interactions in semiconducting SWNTs. From this work it was suggested that an enhanced Coulombic attraction between electron-hole pairs arises from confinement, dramatically altering effective band-gap to yield remarkable stable exciton states.[42, 29, 34]

2.5 Exciton Photophysics in Semiconducting Carbon Nanotubes

Ab initio calculations predict the existence of not only optically bright excitons transitions, but also a complex manifold of predominately dark exciton states.[29, 42] The results of one such calculation from the Louie group are shown figure 2.8 for the (11,0) tube.[43] This figure associated with the E_{11} exciton manifold, highlights the complexity of the fine structure. To simplify, the underlying symmetry of the carbon nanotube allows for excitonic wavefunctions of definite parity, that restricts interband, one-photon optical transitions to states of opposite parity only.[19] Using such arguments, the majority of the remaining states in figure 2.8 are either optically forbidden by symmetry selection rules or carry inherently low oscillator strength.[44, 45] The ${}_0A_0^-$ state shown results in particularly strong radiative transitions, and will be referred to as in this dissertation simply as the E_{11} transition.

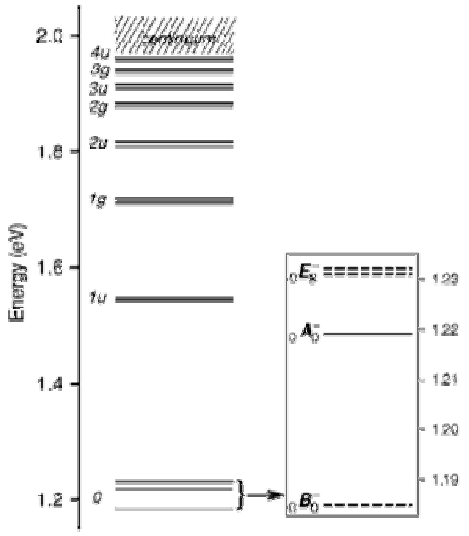

Figure 2.8. *Ab initio* energy diagram of the excitonic states for the (11,0) semiconducting tube. The states are labeled by their principle quantum number, followed by even (g) or odd (u) state symmetry. ${}_0A_0^-$ is commonly referred to as the (optically bright) E_{11} transition. *Reproduced with permission from Ma et al., Phys. Rev. B, 74, 085402, 2006.*

Owing to negligible momentum of the photon compared to the exciton, conservation rules requires that $\Delta K_{cm} \approx 0$ for an optical transition (see figure 2.9).[46] Once populated, the exciton is generally assumed to thermalize within the band according to Boltzmann statistics, resulting in broadening by amount k_bT. Assuming that the thermalization process is faster than the radiative transition, many excitons will be effective removed from the "radiative window" of $\Delta K_{cm} = k_{photon}$.[38, 47] As a consequence, this thermalization process is thought to contribute to the low photoluminescence yields (∼1-2%) commonly associated with semiconducting carbon nanotubes. [48]

Compared to conventional semiconductors where indirect and phonon assisted transitions are common, the requirement for $\Delta K_{cm} \approx 0$ is restrictive.[46] However, as shown in figure 2.9, the corresponding 1D joint density of states (JDOS) is expected to diverge near the exciton band minimum. So in stark contrast to the 3D case, the JDOS of the SWNT electron and hole bands, is inordinately large about the band minimum, allowing for multiple exciton population in the $\Delta K_{cm} \approx 0$ region. To demonstrate the importance of these multi-excitonic effects, a simple calculation for exciton population (n_{ex}) is carried out in figure 2.9. Using a recently reported absorption cross-section,[49] and a typical laser beam fluence, upwards of 60 exciton are expected to be populated for 600 nm long (6,5) SWNT. The ability to simultaneously populate such large number of excitons all initially localized near the band minimum can lead to markedly enhanced scattering among excitons.[50]

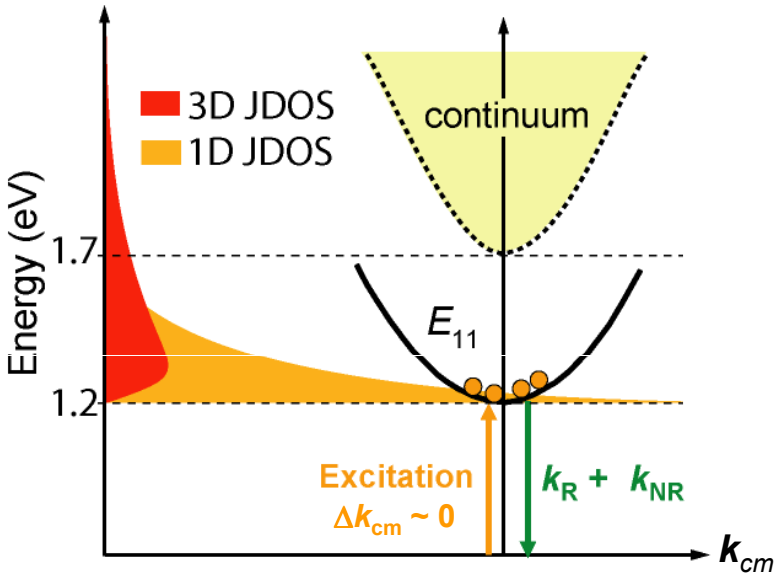

σ_C per C atom(cm^2)	N_C - for a 600 nm long (6,5) tube	I – typical excitation fluence (photons/pulse·cm^2)	n_{ex} - # of excitons
$(1 \pm 0.3) \times 10^{-17}$ [1]	5.31×10^4	1.2×10^{14}	64 ± 20 $n_{ex} = \sigma_C N_C I$

Figure 2.9. The requirement that $\Delta K_{cm} \approx 0$ restricts the E_{11} transition to the band minimum, where the one-dimensional joint DOS (JDOS) diverges, enabling multiple exciton populations. Using typical ultrafast beam fluences calculations suggests we can populate upwards of 60 excitons per 600 nm semiconducting tube.

2.6 Summary

This chapter provides a brief survey of the established physical properties of carbon nanotubes. While their structural, mechanical and electrical properties can be roughly understood through analogy to graphene, SWNTs optical processes are intrinsically more complex, and comparatively unexplored. The SWNT electronic properties can only be crudely approximated by the graphene band structure in the zone-folding approximation. Instead, it has been shown that quasi 1D confinement effects inherent to semiconducting SWNTs, greatly enhance electron-hole Coulombic interactions leading remarkably large exciton binding energies.[34, 33, 45] The ensuing optically bright excitonic transitions dominate all spectral features, and have important consequences for both the photoluminescence yield, and the time-resolved dynamics advanced in this dissertation through non-linear spectroscopy.

2.7 References

[1] S. Saito, G. Dresselhaus, and M.S. Dresselhaus. *Physical Properties of Carbon Nanotubes*. Imperial College Press, London, 1998.

[2] Laurent Cognet, Dmitri A. Tsyboulski, John-David R. Rocha, Condell D. Doyle, James M. Tour, and R. Bruce Weisman. Stepwise quenching of exciton fluorescence in carbon nanotubes by single-molecule reactions. *Science*, 316(5830):1465–1468, 2007.

[3] M.S. Dresselhaus, G. Dresselhaus, A. Jorio, A.G. Souza Filho, and S. Saito. Raman spectroscopy on isolated single wall carbon nanotubes. *Carbon*, 40:2043–2061, 2002.

[4] S. Saito, M. Fujita, G. Dresselhaus, and M.S. Dresselhaus. Electronic structure of chiral graphene tubules. *Appl. Phys. Lett.*, 60(18):2204–2206, 1992.

[5] S. Reich, C. Thomsen, and J. Maultzsch. *Carbon Nanotubes: Basic Concepts and Physical Properties*. Wiley-VCH Verlag GmbH & Co. kGaA, Weinheim, 2004.

[6] M.S. Dresselhaus, G. Dresselhaus, and P.C. Eklund. *Science of Fullerenes and Carbon Nanotubes*. Academic Press, San Diego, 1996.

[7] S. Reich, C. Thomsen, and J. Robertson. Exciton resonances quench the photoluminescence of zigzag carbon nanotubes. *Phys. Rev. Lett.*, 95:077402–077402, 2005.

[8] C. Kittel. *Introduction to Solid State Physics*. Wiley, New York, 1976.

[9] J.W. Mintmire and C.T. White. Universal density of states for carbon nanotubes. *Phys. Rev. Lett.*, 81(12):2506–2509, 1998.

[10] N. Hamada, S.-i. Sawada, and A. Oshiyama. New one-dimensional conductors: graphitic microtubules. *Phys. Rev. Lett.*, 68(10):1579–1581, 1992.

[11] Anton V. Naumov, Oleg A. Kuznetsov, Avetik R. Harutyunyan, Alexander A. Green, Mark C. Hersam, Daniel E. Resasco, Pavel N. Nikolaev, and R. Bruce Weisman. Quantifying the semiconducting fraction in single-walled carbon nanotube samples through comparative atomic force and photoluminescence microscopies. *Nano Letters*, 9(9):3203–3208, 2009.

[12] S. Iijima. Helical microtubules of graphitic carbon. *Nature*, 354:56–56, 1991.

[13] T. Ando, H. Matsumura, and T. Nakanishi. Theory of ballistic transport in carbon nanotubes. *Physica B*, 323:44–50, 2002.

[14] B. Kitiyanan, W.E. Alvarez, J.H. Harwell, and D.E. Resasco. Controlled production of single-wall carbon nanotubes by catalytic decomposition of co on bimetallic como catalysts. *Chem. Phys. Lett.*, 317(3-5):497–503, 2000.

[15] S.M. Bachilo, M.S. Strano, C. Kittrell, R.H. Hauge, R.E. Smalley, and R.B. Weisman. Structure-assigned optical spectra of single-walled carbone nanotubes. *Science*, 298:2361–2366, 2002.

[16] S.M. Bachilo, L. Balzano, J.E. Herrera, F. Pompeo, D.E. Resasco, and R.B. Weisman. Narrow (n,m)-distribution of single-walled carbon nanotubes grown using a solid supported catalyst. *J. Am. Chem. Soc.*, 125(37):11186–11187, 2003.

[17] N.W. Ashcroft and N.D. Mermin. *Solid State Physics*. Holt, Rinerhart and Winston, New York, 1976.

[18] S. Saito, G. Dresselhaus, and M.S. Dresselhaus. Trigonal warping effect of carbon nanotubes. *Phys. Rev. B*, 61(4):2981–2990, 2000.

[19] M.S. Dresselhaus, G. Dresselhaus, R. Saito, and A. Jorio. Exciton photophysics of carbon nanotubes. *Annu. Rev. Phys. Chem.*, 58:719–747, 2007.

[20] J. Lefebvre, D.G. Austing, J. Bond, and P. Finnie. Photoluminescence imaging of suspended single-walled carbon nanotubes. *Nano Lett.*, 6(8):1603–1608, 2006.

[21] M.S. Arnold, A.A. Green, J.F. Hulvat, S.I. Stupp, and M.C. Hersam. Sorting carbon nanotubes by electronic structure using density differentiation. *Nature Nanotech.*, 1:60–65, 2006.

[22] M.J. O'Connell, S. Sivaram, and S.K. Doorn. Near-infrared resonance raman excitation profile studies of single-walled carbon nanotube intertube interactions: A direct comparison of bundled and individually dispersed hipco nanotubes. *Phys. Rev. B*, 69:235415–235415, 2004.

[23] M.J. O'Connell, S.M. Bachilo, C.B. Huffman, V.C. Moore, M.S. Strano, E.H. Haroz, K.L. Rialon, P.J. Boul, W.H. Noon, C. Kittrell, J. Ma, R.H. Hauge, R.B. Weisman, and R.E. Smalley. Band gap fluorescence from individual single-walled carbon nanotubes. *Science*, 297:593–596, 2002.

[24] M.J. O'Connell, P.J. Boul, L.M. Ericson, C.B. Huffman, Y. Wang, E.H. Haroz, C. Kuper, J. Tour, K.D. Ausman, and R.E. Smalley. Reversible water-solubilization of single-walled carbon nanotubes by polymer wrapping. *Chem. Phys. Lett.*, 342:265–271, 2001.

[25] Matthew W Graham, Ying-Zhong Ma, and Graham R Fleming. Femtosecond photon echo spectroscopy of semiconducting single-walled carbon nanotubes. *Nano Lett.*, 8(11):3936–3941, 2008.

[26] H. Htoon, M.J. O'Connell, P.J. Cox, S.K. Doorn, and V. Klimov. Low temperature emission spectra of individual single-walled carbon nanotubes: multiplicity of subspecies within single-species nanotube ensembles. *Phys. Rev. Lett.*, 93(2):027401–027401, 2004.

[27] A. Jorio, M.A. Pimenta, A.G. Souza Filho, G.G. Samsonidze, A.K. Swan, M.S. Unlu, B.B. Goldberg, R. Saito, G. Dresselhaus, and M.S. Dresselhaus. Resonance raman spectra of carbon nanotubes by cross-polarized light. *Phys. Rev. Lett.*, 90(10):107403–107403, 2003.

[28] T. Ando. Excitons in carbon nanotubes. *J. Phys. Soc. Jpn.*, 66(4):1066–1073, 1997.

[29] C.D. Spataru, S. Ismail-Beigi, L.X. Benedict, and S.G. Louie. Quasiparticle energies, excitonic effects and optical absorption spectra of small diameter single-walled carbon nanotubes. *Appl. Phys. A*, 78:1129–1136, 2004.

[30] J. Shah. *Ultrafast spectroscopy of semiconductors and semiconductor nanostructures*. Berlin; New York: Springer Verlag, 1999.

[31] Yutaka Toyozawa. *Optical Processes in Solids*. Cambridge University Press, 2003.

[32] Y.-Z. Ma, J. Stenger, J. Zimmermann, S.M. Bachilo, R.E. Smalley, R.B. Weisman, and G.R. Fleming. Ultrafast carrier dynamics in single-walled carbon nanotubes probed by femtosecond spectroscopy. *J. Chem. Phys.*, 120(7):3368–3373, 2004.

[33] Y.-Z. Ma, L. Valkunas, S.M. Bachilo, and G.R. Fleming. Exciton binding energy in semiconducting single-walled carbon nanotubes. *J. Phys. Chem. B*, 109(33):15671–15674, 2005.

[34] Feng Wang, Gordana Dukovic, Louis E. Brus, and Tony F. Heinz. The optical resonances in carbon nanotubes arise from excitons. *Science*, 308(5723):838–841, May 2005.

[35] J. Maultzsch, R. Pomraenke, S. Reich, E. Chang, D. Prezzi, A. Ruini, E. Molinari, M.S. Strano, C. Thomsen, and C. Lienau. Exciton binding energies in carbon nanotubes from two-photon photoluminescence. *Phys. Rev. B*, 72:241402(R)–241402(R), 2005.

[36] Y.-Z. Ma, T. Hertel, Z.V. Vardeny, G.R. Fleming, and L. Valkunas. Ultrafast spectroscopy of carbon nanotubes. volume 111, pages 321–352. Springer-Verlag Berlin, Heidelberg, 2008.

[37] Charles Kittel. *Quantum Theory of Solids*. John Wiley and Sons, 1963.

[38] V. Perebeinos, J. Tersoff, and P. Avouris. Radiative lifetime of excitons in carbon nanotubes. *Nano Lett.*, 5(12):2495–2499, 2005.

[39] M. Fox. *Optical Properties of Solids*. Oxford University Press, 2001.

[40] R. Loudon. *Am. J. Phys.*, 27:649–649, 1959.

[41] H. Ando, H. Oohashi, and H. Kanbe. Carrier-induced optical nonlinear effects in semiconductor quantum well wire structure. *J. Appl. Phys.*, 70(11):7024–7032, 1991.

[42] J.B. Neaton, K.H. Khoo, C.D. Spataru, and S.G. Louie. Electron transport and optical properties of carbon nanostructures from first principles. *Comput. Phys. Comm.*, 169:1–8, 2005.

[43] Y.-Z. Ma, C.D. Spataru, L. Valkunas, S.G. Louie, and G.R. Fleming. Spectroscopy of zigzag single-walled carbon nanotubes: comparing femtosecond transient absorption spectra with ab initio calculations. *Phys. Rev. B*, 74(8):085402–085402, 2006.

[44] M. Damnjanovic, I. Miloevic, T. Vukovic, and R. Sredanovic. Full symmetry, optical activity, and potentials of single-wall and multiwall nanotubes. *Phys. Rev. B*, 60:2728–2739, 1999.

[45] J. Maultzsch, R. Pomraenke, S. Reich, E. Chang, D. Prezzi, A. Ruini, E. Molinari, M. S. Strano, C. Thomsen, and C. Lienau. Exciton binding energies in carbon nanotubes from two-photon photoluminescence. *Phys. Rev. B*, 72(24):241402–4, December 2005.

[46] J. Shaver and J. Kono. Temperature-dependent magneto-photoluminescence spectroscopy of carbon nanotubes: evidence for dark excitons. *Laser & Photonics Review*, 1(3):260–274, 2007.

[47] C.D. Spataru, S. Ismail-Beigi, R.B. Capaz, and S.G. Louie. Theory and ab initio calculation of radiative lifetime of excitons in semiconducting carbon nanotubes. *Phys. Rev. Lett.*, 95:247402–247402, 2005.

[48] Jacques Lefebvre, Shigeo Maruyama, and Paul Finnie. Photoluminescence: Science and applications. pages 287–319. Springer-Verlag Berlin, Heidelberg, 2008.

[49] Stephane Berciaud, Laurent Cognet, and Brahim Lounis. Luminescence decay and the absorption cross section of individual single-walled carbon nanotubes. *Phys. Rev. Lett.*, 101(7):077402–4, 2008.

[50] Y.-Z. Ma, L. Valkunas, S.L. Dexheimer, S.M. Bachilo, and G.R. Fleming. Femtosecond spectroscopy of optical excitations in single-walled carbon nanotubes: Evidence for exciton-exciton annihilation. *Phys. Rev. Lett.*, 94(15):157402–157402, 2005.

Chapter 3

Nonlinear Spectroscopy

3.1 Introduction: *time is our metric*

It takes on average 190 ms for a human to react to a visual stimulus, which is orders of magnitude slower than the neural, electrical and photonic processes involved.[1] The initial rate limiting process is a molecule's reaction time to light, which requires femtosecond (10^{-15} s) precision to resolve. To access this timescale, a wavepacket of photons can be squeezed down into bundles of energy only a few femtoseconds in duration. Following optical excitation, the absorbed wavepacket becomes electronic energy which in turn couples to molecular motions and will eventually dissipate on the picosecond (10^{-12} s) to nanosecond (10^{-9} s) timescale.[2] During this process, we can interrogate the system evolution in real-time, by applying subsequent probes pulses and measuring the resultant change in signal intensity.

In this chapter, the principles basic to the non-linear optical experiments described in subsequent chapters are introduced. To begin, the process of optical absorption is reviewed for both linear and non-linear interactions. The derived frequency-domain linear and non-linear optical susceptibilities are the re-cast into time dependent response functions, using the properties of the Fourier-Laplace transform. The resulting third-order polarization field, will then be used to provide the time-ordering necessary to describe the five types of four-wave mixing spectroscopy presented in this dissertation; transient absorption, transient grating, two-pulse photon echo, three-pulse photon echo peakshift and two-dimensional electronic spectroscopy.

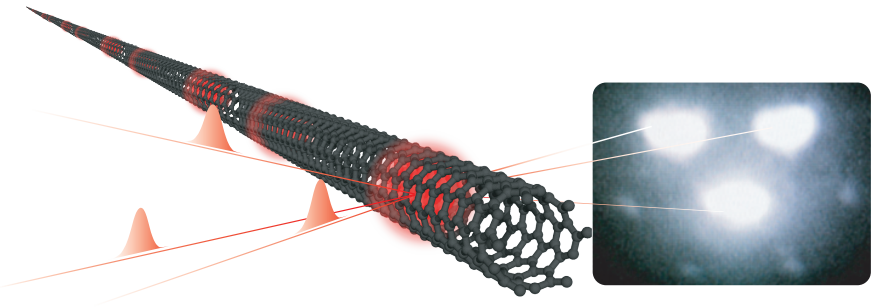

Figure 3.1. (6,5) SWNTs scatter intense nonlinear signals into momentum conserving directions, suggestive of an inherently large optical nonlinearity. Time-resolved detection of these signals enables the spectroscopic measurements presented in this dissertation. (see experimental photograph of nonlinear signals on right)

3.2 Light-Matter Interactions

3.2.1 Linear optical response

Given sufficient incident light intensity all materials will exhibit both linear and nonlinear optical response to light, however certain materials are more susceptible than others.[3] To explore how novel nanomaterials such as SWNTs respond to light and relax dynamically, the basic properties of light-matter interaction are reviewed. Optical absorption can be described by a material's linear susceptibility, which is derived by considering two-state transition (from state nk to $n'k'$) in the presence of an applied electromagnetic field. Beginning with the Hamiltonian for the motion of an electron of mass m, in an external electromagnetic field,[4] the terms involving the applied vector potential ($\mathbf{A}$) are treated as an applied perturbation, H_I.

$$H = \frac{1}{2}\sum_i \frac{1}{m_i}\left(\mathbf{p}_i + \frac{e\mathbf{A}}{c}\right)^2 + \sum_i V(\mathbf{r}_i) = H_o + H_I \tag{3.1}$$

$$H_I = \frac{e}{2c}\sum_i \frac{1}{m_i}\left(\mathbf{p}_i \cdot \mathbf{A} + \mathbf{A} \cdot \mathbf{p}_i\right) + \frac{1}{2c^2}\sum_i \frac{e^2A^2}{m_i.} \tag{3.2}$$

Using the definition of the momentum operator, the following expression is obtained for each electronic interaction i in our system.[5]

$$H_I^i = \frac{-ie\hbar\mathbf{A}\cdot\nabla_i}{mc} - \frac{ie\hbar}{2mc}\nabla_i \cdot \mathbf{A} + \frac{e^2}{2mc^2}A^2 \approx \frac{e}{mc}\mathbf{A}\cdot\mathbf{p}_i \tag{3.3}$$

For the Coulomb choice of gauge ($\nabla \cdot \mathbf{A} = 0$), the second term above vanishes. The last term varies nonlinearly with the applied field, and rigorously corresponds to a two photon

process mediated by a virtual state.[5] Such nonlinear processes are statistically small under ambient E-field sources such as the Sun. This approximation is known as the electric dipole approximation for electron-radiation interaction.[5, 3] Under the electric dipoles approximation, the imaginary dielectric coefficient ϵ_2 can be calculated to determine material absorption properties. Using Fermi's Golden Rule expression, the transition probability rate function $W_{tot}(\omega)$ is calculated for a direct band gap transition (labeled $nk \rightarrow n'k'$),

$$W_{tot}\left(nk \rightarrow n'k'\right) = \frac{2\pi}{\hbar}\left|\left\langle n'k'\left|H_I\right|nk\right\rangle\right|^2 \delta\left(E_{n'k'} - E_{nk} - \hbar\omega\right) \tag{3.4}$$

$$= \frac{2\pi\hbar e^2 A_o^2}{m^2\omega^2}\left|\hat{\mathbf{e}}\cdot\mathbf{M}_{nn'}(k',k)\right|^2 \delta\left(E_{n'k'} - E_{nk} - \hbar\omega\right) \tag{3.5}$$

where $\mathbf{M}_{nn'}(k',k)$ is the matrix element sandwiching the dipole operators from equation 3.3.[5] The resulting transition rate energy ($\hbar\omega W_{tot}$) can now be used to calculate the absorption coefficient ($n(\omega)$), by dividing it through by the energy incident on the sample per unit time which is given by $\frac{1}{2}\frac{n\omega^2 A_o^2}{\pi c}$.[5] Performing this substitution we obtain the absorption coefficient $n(\omega)$,

$$\begin{array}{l} n(\omega) \equiv \frac{\omega}{nc}\epsilon_2(\omega) = \frac{2\pi c}{n\omega^2 A_o^2}\hbar\omega W_{tot} \\ \Rightarrow \epsilon_2(\omega) = \frac{2\pi\hbar}{A_o^2}W_{tot} \end{array} \tag{3.6}$$

as well as an expression for ϵ_2 for direct-gap semiconductors like SWNTs. The corresponding real dielectric, ϵ_1 (for refractive processes) can be further calculated through substitution of ϵ_2 into the Kramers-Kronig relations.[3] Summing over all transitions k one obtains,

$$\begin{array}{l} \epsilon_2(\omega) = \left(\frac{2\pi\hbar e}{m\omega}\right)^2 \sum_k \left|\hat{\mathbf{e}}\cdot\mathbf{M}_{nn'}(k',k)\right|^2 \delta\left(E_{n'k'} - E_{nk} - \hbar\omega\right) \\ \epsilon_1(\omega) = 1 + \frac{4\pi\hbar^2 e^2}{m}\sum_k \left(\frac{2\left|\hat{\mathbf{e}}\cdot\mathbf{M}_{nn'}(k',k)\right|^2}{m(E_{n'k'} - E_{nk})}\right)\frac{1}{(E_{n'k'} - E_{nk})^2 - (\hbar\omega)^2} \end{array} \tag{3.7}$$

In equation 3.7 above, the first term in the sum is a dimensionless value that accounts for all the allowed dipole transitions, and is commonly referred to as the oscillator strength ($f_{E_{nk}}$),

$$f_{E_{nk}} = \frac{2\left|\hat{\mathbf{e}}\cdot\mathbf{M}_{nn'}(k',k)\right|^2}{m(E_{n'k'} - E_{nk})}. \tag{3.8}$$

One meaningful interpretation of a material's oscillator strength is that it is a measure of the number of dipole oscillators with energy $E_{n'k'} - E_{nk}$.[6] Thus the oscillator strength f_{Ek} is intrinsic to a particular material and accounts for the large variation in linear dielectric constants observed in condensed phase. Owing in part to the sheer number of carbon atoms (calculated in chapter 2 to be $\sim 5.5 \times 10^4$ atoms for most SWNTs in this dissertation), and the large absorption cross section per nanotube atom (5.5×10^{-17} cm^2)[7], carbon nanotubes have an inherently large linear absorption response. In the next section, the non-linear absorption response will be examined.

3.2.2 Nonlinear optical response

In developing the quantum mechanical description for the linear absorption in direct band gap semiconductors like SWNTs, higher order process such as two-photon absorption were neglected. In this section, higher orders are included by expanding the system wavefunction ($\psi(r,t)$) in the form of a power series,

$$\psi\left(r,t\right)=\psi^{(0)}\left(r,t\right)+\psi^{(1)}\left(r,t\right)+\psi^{(2)}\left(r,t\right)+... \tag{3.9}$$

For any desired order N, $\psi^{(n)}\left(r,t\right)$ can then be solved for perturbatively by again invoking the electric dipole approximation Hamiltonian ($H_I^i \approx \frac{e}{mc}\mathbf{A}\cdot\mathbf{p}_i \approx \mu\cdot\mathbf{E}$), and expanding the wavefunction in real space as,

$$\psi^{(n)}(r,t)=\textstyle\sum_l a_l^{(n)}(t)u_l(r)e^{-i\omega_l t} \tag{3.10}$$

The wavefunction is then substituted into the Schrodinger equation (below) and results up to some arbitrary order N can be solved for iteratively, i.e.

$$\begin{array}{l} i\hbar\frac{\partial\psi^{(n)}}{\partial t}=H_o\psi^{(n)}+H_I^i\psi^{(n-1)} \\ \Rightarrow i\hbar\sum_l\frac{\partial a_l^{(n)}(t)}{\partial t}u_l(r)e^{-i\omega_l t}=\sum_l a_l^{(n-1)}(t)H_I^i u_l(r)e^{-i\omega_l t}. \end{array} \tag{3.11}$$

Multiplying the both sides above by the orthonormal wavefunction u_m^* we obtain,

$$\frac{\partial a_m^{(n)}(t)}{\partial t}=(i\hbar)^{-1}\textstyle\sum_l a_l^{(n-1)}(t)\langle u_m|H_I^i|u_l\rangle e^{-i\omega_{ml}t}. \tag{3.12}$$

The coefficients ($a_m^{(1)}(t)$) for the first order wavefunction can be calculated by simple integration.[4, 2] The second (and higher) orders can then be obtained by iterative substitution back into equation 3.12, i.e.

$$\begin{array}{l} a_m^{(1)}=\frac{1}{\hbar}\sum_q\frac{\langle u_m|H_I^i|u_l\rangle}{\omega_{mg}-\omega_q}e^{i(\omega_{mg}-\omega_q)t} \\ \Rightarrow a_m^{(2)}=\frac{1}{\hbar^2}\sum_{qr}\sum_m\frac{\langle u_n|H_I^i|u_m\rangle\langle u_m|H_I^i|u_g\rangle}{(\omega_{ng}-\omega_q-\omega_r)(\omega_{mg}-\omega_q)}e^{i(\omega_{ng}-\omega_q-\omega_r)t} \end{array} \tag{3.13}$$

Equations 3.13 and 3.10 provide an expression for the second and first order wavefunctions ($\psi^{(1)}$ and $\psi^{(2)}$), from which the second order nonlinear susceptibility can be calculated from the corresponding second order polarization $P^{(2)}$,

$$P^{(2)}=N\left(\left\langle\psi^{(0)}\middle|\mu\middle|\psi^{(2)}\right\rangle+\left\langle\psi^{(1)}\middle|\mu\middle|\psi^{(1)}\right\rangle+\left\langle\psi^{(2)}\middle|\mu\middle|\psi^{(0)}\right\rangle\right). \tag{3.14}$$

Where here polarization is defined up to an arbitrary order with respect to the dipole operator μ, i.e., $P\equiv N\langle\psi|\mu|\psi\rangle=P^{(1)}+P^{(2)}+....$[4] Inserting in the calculated 0th, 1st and 2nd order

wavefuctions into equation 3.14, and making the substitution (which is permissible under the sum) that $\omega_q \to -\omega_q$ and $\omega_r \to -\omega_r$ we obtain,

$$P^{(2)} = \left(\frac{N}{\hbar^2}\right) \sum_{qr} \sum_{mn} \left(\frac{\langle u_g|\mu|u_n\rangle\langle u_n|H_I^i|u_m\rangle\langle u_m|H_I^i|u_g\rangle}{(\omega_{ng}-\omega_q-\omega_r)(\omega_{mg}-\omega_q)} + \frac{\langle u_n|H_I^i|u_g\rangle\langle u_n|\mu|u_m\rangle\langle u_m|H_I^i|u_g\rangle}{(\omega_{ng}+\omega_r)(\omega_{mg}-\omega_q)} \right. \\ \left. + \frac{\langle u_n|H_I^i|u_g\rangle\langle u_n|H_I^i|u_m\rangle\langle u_m|\mu|u_g\rangle}{(\omega_{ng}+\omega_r)(\omega_{mg}+\omega_q+\omega_r)} \right) e^{-i(\omega_q+\omega_r)t}. \tag{3.15}$$

The the second order polarization depends on the product of the applied E-fields i.e., $P_i^{(2)} = \sum_{j,k,l=x,y,z} \chi_{ijk}^{(2)} E_j E_k$.[4] As a consequence, the second order susceptibility can be read off immediately by dividing out the E-field contribution. Preforming this division and further assuming that the incident fields have identical frequencies (i.e., $\omega = \omega_q = \omega_r$), we obtain,

$$\chi_{ijk}^{(2)}(\omega) = \left(\frac{N}{\hbar^2}\right) \sum_{mn} \left(\frac{\mu_{gn}^i \mu_{nm}^j \mu_{mg}^k}{(\omega_{ng}-2\omega)(\omega_{mg}-\omega)} + \frac{\mu_{gn}^j \mu_{nm}^i \mu_{mg}^k}{(\omega_{ng}+\omega)(\omega_{mg}-\omega)} \right. \\ \left. + \frac{\mu_{gn}^k \mu_{nm}^k \mu_{mg}^i}{(\omega_{ng}+\omega)(\omega_{mg}+2\omega)} \right) \tag{3.16}$$

where $\mu_{gn} \equiv \langle u_n| H_I |u_m\rangle$. From the above expression it is observed that the second order nonlinear susceptibility tensor is resonantly enhanced both at the resonant frequency ($\omega_g = \omega$) and at half the transition frequency ($\omega_g = 2\omega$). The process is often employed as sum-frequency generation for materials with large $\chi^{(2)}$.[4, 3] Using the same derivation, analogous expressions for $\chi^{(3)}$ can also be formulated; which is the fundamental quantity enabling the four-wave mixing spectroscopic techniques used in this dissertation.

3.3 Nonlinear Spectroscopy

3.3.1 Intensity induced non-linearity

The linear dielectric function adequately describes a material's optical response under normal room light conditions, but will deviates markedly under high-fields ($|\mathbf{E}| > \sim 10^6$ V/cm).[4] In this regime, the approximation that the total dielectric function is independent of the magnitude of the incident field breaks down, and the nonlinearity (ϵ_{NL}) becomes significant.

$$\epsilon_{tot} = \epsilon + \epsilon_{NL} \cdot E \tag{3.17}$$

To see this dependence more explicitly it is useful to do a power series expansion of the total polarization in terms of the applied field,

$$P = \chi^{(1)} E + \chi^{(2)} EE + \chi^{(3)} EEE + ... \tag{3.18}$$

where here $\chi^{(1)}$ is the linear susceptibility tensor, $\chi^{(2)}$ and $\chi^{(3)}$ are the second and third order nonlinear susceptibility.[4] Higher-order nonlinear terms in the expansion become significant with increasing incident E-fields. For typical incident laser intensities investigate in this manuscript, only the third-order nonlinear susceptibility plays a dominant role. While the second order term in equation 3.18 should give the larger contribution, it vanishes identically for all centrosymmetric materials since $P^{(2n)}(E) = \chi^{(2)}(-E)(-E) = P^{(2n)}(-E)$. For expansion terms that are odd-order in E like $P^{(3)}$, a measurable response can be expected for sufficient applied field, as the sign change within the E-field will distinguish between the forward and reverse induced polarization processes.[4]

The magnitude of the nonlinear susceptibility tensorial elements determines the threshold intensity required for a particular polarization order to become significant in magnitude. For a centrosymmetric solid state system such as SWNTs, generally only the first and third order susceptibility need to be considered; all other orders either vanish under symmetry or will be statistically weak. Much like $\chi^{(1)}$, the fourth rank tensor $\chi^{(3)}$ must account for all possible Cartesian directions of the three applied E-fields and can be written as,

$$P^{(3)} = \epsilon_o \sum_{j,k,l=x,y,z} \chi^{(3)}_{ijkl} E_j E_k E_l. \tag{3.19}$$

Up to 81 different tensorial components of $\chi^{(3)}_{ijkl}$ are possible, however symmetry greatly reduces the components required to just a few elements,[4] that are required to explain the four-wave mixing spectroscopic techniques outlined in the subsequent sections.

3.3.2 Time-domain nonlinear spectroscopy

The work presented in this dissertation chiefly concerns time-resolved optical measurements. The experimentally controlled parameters are multiple applied fields ($E(t)$), in the form of ultrashort laser pulse (20 to 100 fs) that interact with a nanotube sample to produce the scattered third-order polarization field given by equation 3.19. By exploiting the properties of Fourier transform, the formalism for nonlinear processes developed in frequency domain, can be re-cast to describe time-dependent spectroscopic measurements.[8, 10] For example, in a first order process, $\chi^{(1)}(\omega)$ from equation 3.7, can be written as the Fourier transform of time-domain response function, $R^{(1)}(t)$, i.e.

$$\chi^{(1)}(\omega) = \int_0^\infty d\tau R^{(1)}(\tau) e^{i\omega\tau}. \tag{3.20}$$

The integration is from 0 to ∞, since by the principle of causality, before the applied electric field, $R^{(1)}(\tau) = 0$ for $\tau < 0$.[2] Inserting this susceptibility into equation 3.18, and absorbing the phase into applied E-field we obtain,

$$P^{(1)}(t) = \int_0^\infty d\tau R^{(1)}(\tau) E(t-\tau). \tag{3.21}$$

The resulting expression provides the first-order polarization produced at a time t, from an applied electric field (laser pulse) that interacted with a system at a time $t - \tau$.[4] This time-dependent formalism can be extended by analogy to polarizations of any order. In particular, the third-order susceptibility derived in equation 3.16, may be expressed as the Fourier transform of a time-dependent third-order response function $R^{(3)}(\tau_1, \tau_2, \tau_3)$,

$$\chi^{(3)}(\omega, \omega_2, \omega_3) = \int_0^\infty d\tau_1 \int_0^\infty d\tau_2 \int_0^\infty d\tau_3 R^{(3)}(\tau_1, \tau_2, \tau_3) e^{i(\omega_1\tau_1 + \omega_2\tau_2 + \omega_3\tau_3)}. \tag{3.22}$$

Inserting $\chi^{(3)}$ into equation 3.18 and absorbing the phase constants into the respective electric fields, the third-order polarization may be written as,

$$P^{(3)}(t) = \int_0^\infty d\tau_1 \int_0^\infty d\tau_2 \int_0^\infty d\tau_3 R^{(3)}(\tau_1, \tau_2, \tau_3) E(t - \tau_1) E(t - \tau_2) E(t - \tau_3). \tag{3.23}$$

The resulting expression depends upon the time-ordered delays (τ_1, τ_2 and τ_3) of the three applied E-fields pulses, and the material's third-order susceptibility which is effectively embedded in $R^{(3)}$.[8]

3.3.3 Four-wave mixing spectroscopy

The third-order polarization $P^{(3)}(t)$ expressed in equation 3.23 is often called a *four wave mixing* process. Three of these four "waves" refer to the applied E-fields, which in our case are temporally delayed femtosecond laser pulses labeled by their corresponding wavevectors $\mathbf{k}_1$, $\mathbf{k}_2$ and $\mathbf{k}_3$.[8, 2] The fourth wave is the $P^{(3)}$ polarization labeled $\mathbf{k}_s$, which scatters into momentum conserving directions of the combined incident pulses, i.e. $\mathbf{k}_s = \pm\mathbf{k}_1 \pm \mathbf{k}_2 \pm \mathbf{k}_3$. This scattered $P^{(3)}$ polarization, is refereed to as a photon echo when obtained with certain pulse time orderings such as those diagrammed in figure 3.2. To follow the time evolution of the quantum states involved, double-sided Feynman diagrams provide a convenient representation. As the applied fields ($\mathbf{k}_1$, $\mathbf{k}_2$ and $\mathbf{k}_3$) interact with the initial ground state density matrix, denoted $\rho = |g\rangle\langle g|$, state transitions will be induced to either an excited-state coherences such as $|e\rangle\langle g|$ or a population state such as $|e\rangle\langle e|$. The temporal evolution is represented by progression along the vertical axis. The arrows if figure 3.2 corresponds to E-field interactions with the density matrix; incoming arrows represent absorption, and upward pointing outgoing arrows represent photon emission. The wavy arrow $\mathbf{k}_s$ is an emissive $P^{(3)}$ polarization, and represents the trace operation over the time-dependent density matrix.[8]

The different pathways shown in figure 3.2 can be selectively measured by controlling the laser pulse time-ordering. Varying the population time (T, between $\mathbf{k}_2$ and $\mathbf{k}_3$) for instance can provide either transient grating (TG) or pump probe signals to measure the excited state lifetime and population dynamics. In contrast, scanning the coherence time (τ), provides the two-pulse photon echo (2PE) measurements, which provide the timescale of optical

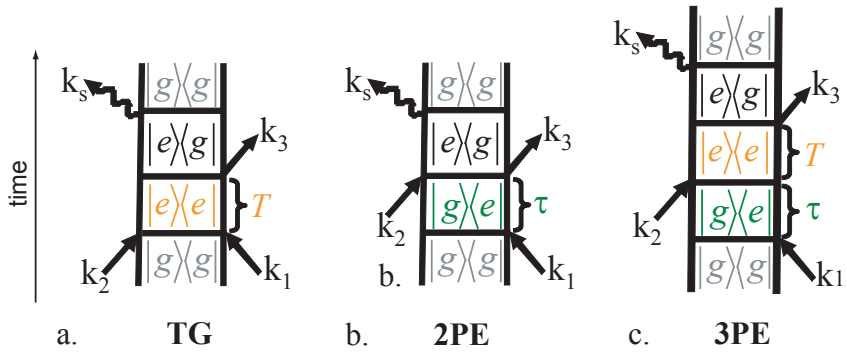

Figure 3.2. Selected double sided Feynman diagrams of $\chi^{(3)}$ processes showing the temporal evolution from the ground state of a two-level density matrix ($\rho = |g\rangle\langle g|$) in response to applied E-fields (labeled $\mathbf{k}_1$, $\mathbf{k}_2$ and $\mathbf{k}_3$). The resultant third order polarization field $P^{(3)}$, scatters into the momentum conserving direction, $\mathbf{k}_s$. Diagrams shown for (a) transient grating (TG) over a population delay time T, (b) two-pulse photon echo (2PE) over a coherence delay time τ, and (c) three-pulse photon echo (3PE) for both τ and T delays.

decoherence or dephasing. In a three pulse echo (3PE) experiment both the population and coherence times can be independently controlled.

Typically, the decay of an optical coherence (e.g. $|e\rangle\langle g|$) during time τ corresponds to a free-induction decay. To instead detect of the stimulated photon echo (SPE) signal, the two coherence states shown in figure 3.2b and c must be complex conjugates of each other (i.e. $|e\rangle\langle g|$ and $|g\rangle\langle e|$)), this causes a collective rephasing process in the ensemble of coherently excited chromophores, producing a macroscopic echo signal in direction $\mathbf{k}_s$(see figure 3.3). Full details details describing SPE and optical rephasing are discussed extensively in the literature,[11, 12, 13, 8] and are applied here to carbon nanotubes for the first time.

3.3.4 Four-wave mixing experiments; pump-probe to 2D electronic

The basic experimental configuration for a four wave-mixing experiment is shown schematically in figure 3.3. The applied laser pulses are temporally delayed by times τ and T, and overlap at the sample position to produce a scattered $P^{(3)}$ polarization field. Only the pulse combinations which produce a SPE give rise to macroscopic nonlinear signals such as those depicted in figure 3.3 showing 3PE signals emerging in the directions $\mathbf{k}_s = \pm(\mathbf{k}_1 - \mathbf{k}_3) + \mathbf{k}_2$ from an SWNT sample. Additionally, 2PE signal are also observed in the $-\mathbf{k}_1 + 2\mathbf{k}_3$ and $-\mathbf{k}_2 + 2\mathbf{k}_3$ directions.

In this dissertation four-mixing experiments on SWNTs are conducted by measuring the

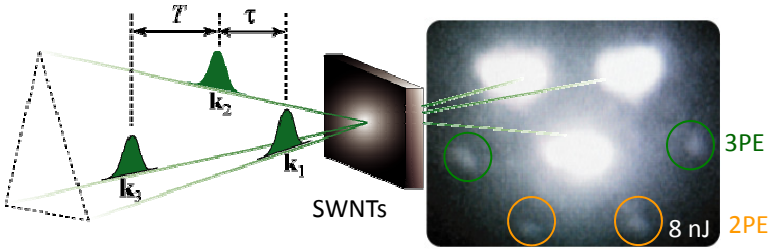

Figure 3.3. Experimental configuration for a four-wave mixing experiment upon resonant excitation of (6,5) SWNTs. Incident pulses $\mathbf{k}_1$, $\mathbf{k}_2$ and $\mathbf{k}_3$, produce a macroscopic third-order polarization $P^{(3)}$ that scatters in a direction $\mathbf{k}_s$ to produce remarkably intense nonlinear two-pulse echo (2PE) and three-pulse echo (3PE) signals shown in the photograph.

time-dependent intensity of the integrated $P^{(3)}(t)$ signals that are scattered into the different directions of $\mathbf{k}_s$. For measurements using a homodyne detection scheme, the collected signal (S_{SPE}) is simply the time-integrated response,

$$S_{SPE}(\tau, T) = \int_0^\infty dt \left| P^{(3)}(t) \right|^2 \tag{3.24}$$

of the scattered signal, measured at the variable time delays τ and T.[10] Alternatively, an analogous heterodyne measurement (S_{HSPE}) is obtained by interfering the scattered polarization with a local oscillator E-field, E^*_{LO}. In contrast to the homodyne case, the signal strength is linearly proportional to E^*_{LO}, and is given by,

$$S_{HSPE}(\tau, T) = -2\mathrm{Im} \int_{-\infty}^{\infty} dt E^*_{LO}(t - T) P^{(3)}(t). \tag{3.25}$$

Such a detection scheme is commonly used in transient absorption spectroscopy. For transient absorption, the resulting spectrum $\Delta A(t, \lambda)$ is be expressed as [14, 15],

$$\Delta A(t, \lambda) \propto n(t)[\sigma^{ESA}(\lambda) - \sigma^{SE}(\lambda) - \sigma_0(\lambda)], \tag{3.26}$$

where $\sigma_0(\lambda)$ is the ground state absorption spectrum (λ is the wavelength of the probe pulse), and $\sigma_i^{ESA}(\lambda)$ and $\sigma_i^{SE}(\lambda)$ are the cross-sections for excited state absorption and stimulated emission processes respectively.[15, 8] Unlike the homodyne detection case, pump interference with the local oscillator preserves both signal amplitude and phase. Such additional is information is particularly valuable for spectrally resolved measurements.

In chapter 12, spectrally resolved heterodyne detection is preformed on 3PE signals to produce a two-dimensional (2D) electronic spectrum for semiconducting SWNTs. Two-dimenensional Fourier-transform electronic spectroscopy is powerful technique that gives a

real-time picture of how an optical excitation distributes itself among it associated exciton states.[16] For SWNTs, this measurement characterized the lineshapes and dynamics of the E_{22} exciton manifold (see chapter 12).

3.4 Modeling Condensed Phase Dynamics

Upon optical excitation in SWNTs, strongly-bound electron-hole pairs or excitons are created, which initially have a fixed phase relationship amongst all the carbon atoms.[15] With time, the individual motions of the carbon atoms disrupts this phase relationship and causes the excitation to become localized within the nanotube. In condensed phase, such exciton-phonon coupling processes are commonly modeled by a two-level system that is linearly coupled to a phonon bath of harmonic oscillators.[8, 17] Following the first pulse interaction, the system is converted into a coherence which will oscillate at the system optical transition frequency ω_{eg}. In response to the coupled phonon bath, decoherence occurs over time τ, causing $\omega_{eg}(t)$ to fluctuate by an amount $\delta\omega_{eg}(t)$ (see figure 3.4). As such, the time-domain transition frequency for each member i of the molecular ensemble can be expressed as,

$$\omega_{i,eg}(t) = \langle\omega_{eg}\rangle + \delta\omega_{i,eg}(t) + \sigma_{i,inhomo} \tag{3.27}$$

where $\langle\omega_{eg}\rangle$ is the average transition energy within the ensemble and $\sigma_{i,inhomo}$ is the static frequency offset accounting for the different local environments of each absorbing chromophore.[18, 10] In figure 3.4, the right panel depicts three chromophores oscillating in phase($\omega_{eg} = \omega_{1,2,3}$) at $\tau = 0$, before each receives multiple perturbations in phase by amount $\delta\omega_{i,eg}$ in response to applied nuclear fluctuations. When all the component of ensemble are added, we obtain $\sum_i \delta\omega_{i,eg}(t) = \langle\omega_{eg}(t)\rangle$ whose phase envelope will decay exponentially for a strongly inhomogeneously broadened system at rate of $\exp(-4\tau/T_2)$.[19] As such, measurement of the photon echo signal ($S_{SPE}(\tau)$) permits extraction of the optical dephasing time (T_2) for $1/e$ of the coherently created excitations to dephase from electron-phonon coupling. T_2, thus becomes not only a measure on the exciton-phonon coupling strength, but also directly provides the spectral homogeneous spectral linewidth ($\Gamma_h = 2\hbar/T_2$).[19]

Alternatively, the transition frequency can be expressed in terms of a correlation function, $M(t)$

$$M(t) = \frac{\langle\delta\omega_{eg}(t)\delta\omega_{eg}(t)\rangle}{\langle\delta\omega_{eg}^2\rangle}. \tag{3.28}$$

As $t \to \infty$, the ensemble of chromophores will loose all frequency correlation due to exciton-phonon coupling, causing $M(t) \to 0$.[9, 10, 20] In later chapters this correlation function will be extracted from experimental results using 3PE peak-shift spectroscopy.[18, 21, 9] In order to simulate $M(t)$, the Spin-Boson Hamiltonian ($H_{HO} = H_o + H' = |g\rangle H_g \langle g| + |e\rangle H_e \langle e| + H'$) couples the electronic Hamiltonian H_o to a bath of harmonic oscillators given by H'. Application the fluctuation-dissipation theorem and statistical principles are then used to relate H_{HO} directly to the time-correlation function $M(t)$.[8, 10, 13, 22] From $M(t)$, various

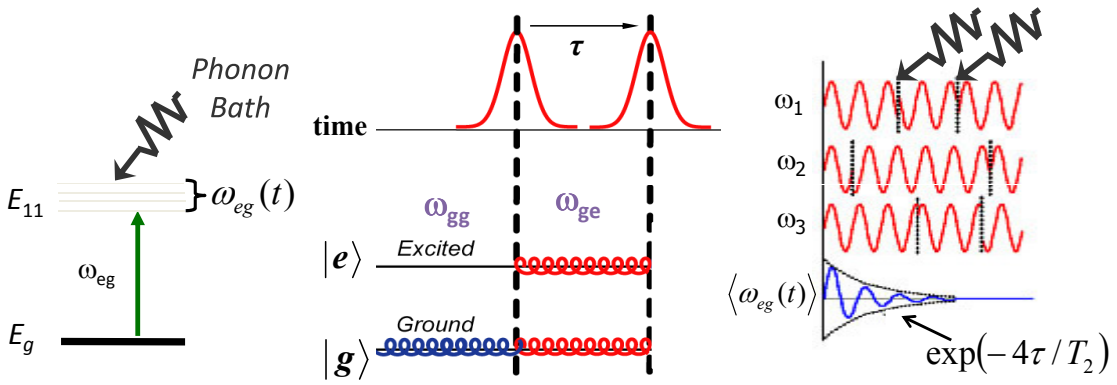

Figure 3.4. In SWNTs, the coherently excited E_{11} state (ω_{ge}) fluctuates in response to the phonon bath (left), these fluctuations cause decoherence over a time period τ (center). The coherent oscillations associated with each member of ensemble couple to the photon bath. When added together, the phase envelope $\langle\omega_{eg}(t)\rangle$ loses coherence exponentially for inhomogeneously broadened systems (right).

optical processes can be readily characterized from linear absorption to electron-phonon coupling strengths and timescales.[9]

$M(t)$ is also related to the lineshape function, $g(t)$ under the assumption that electron-phonon coupling can be modeled as multimode bath of harmonic oscillators linearly coupled to a a two-level system (by a Langevin like equation, for example).[9] Using this approximation, it can be shown that

$$g_i(t) = \left\langle \delta\omega_{i,eg}^2 \right\rangle \int_0^t dt_1 \int_0^{t_1} dt_2 M_i(t_2) - i\lambda_i \int_0^t dt_1 (1 - M_i(t_1)) \tag{3.29}$$

where $\sqrt{\left\langle \delta\omega_{i,eg}^2 \right\rangle}$ is the electron-phonon coupling strength, and λ_i is associated reorganizational energy with respects to the nuclear modes (commonly given as one half the total Stokes' shift). At high temperatures, when the phonon bath heavily populated, $\left\langle \delta\omega_{i,eg}^2 \right\rangle \approx 2\lambda_i k_b T$, where $k_b T$ is the Boltzmann thermal population.[8]

In more complex systems like SWNTs, multiple harmonic baths are required to sufficiently model $M(t)$, and so the total lineshape function becomes, $g(t) = \sum_i g_i(t)$. The spectral density is embedded in $g(t)$, and is can be shown that the real part of $g(t)$ gives the homogeneous spectral broadening from electron-phonon coupling, and the imaginary part provides the phonon induced spectral shift (e.g. Stokes's shift).[9, 8] As consequence,

knowledge of $g(t)$ and any inhomogeneous broadening is sufficient to provide the complete lineshapes of the linear absorption ($\sigma_{Abs}(\omega)$) and photoluminescence ($\sigma_{Em}(\omega)$) spectra [9, 8],

$$\sigma_{Abs}(\omega) = \frac{1}{\pi}\mathrm{Re}\int_0^\infty dt \exp\left[i(\omega - \omega_{eg})t\right] \exp\left[-g(t)\right] \tag{3.30}$$

$$\sigma_{Em}(\omega) = \frac{1}{\pi}\mathrm{Re}\int_0^\infty dt \exp\left[i(\omega - \omega_{eg} - 2\lambda)t\right] \exp\left[-g^*(t)\right]. \tag{3.31}$$

Knowledge of $g(t)$ is also sufficient to calculate the third-order response functions $R_i^{(3)}$, and hence $P^{(3)}$ by equation 3.23. Obtaining the explicit forms for these relations, requires carrying out a cumulant or Magnus expansion on response function $R^{(3)}(\tau_1, \tau_2, \tau_3)$, and is discussed in the literature in detail (see [9, 8] for example). In later chapters, the time-dependent photon echo signal $S_{SPE}(\tau, T)$ will be collected on semiconducting SWNTs, permitting the extraction of quantities such as $M(t)$, the homogeneous lineshape, and exciton-phonon coupling strength.

3.5 Summary and Outlook

The discovery in 2005 that semiconducting carbon nanotube spectroscopy is determined by stable exciton states, radically changed the understanding of the nanotube electronic structure and photophysics.[23, 15] While much progress has been made, there is still little clarity on basic questions, like the precise timescales and states involved in optical relaxation. Another significant bottleneck for carbon nanotube application development, is the still unexplained low fluorescence efficiency, and unknown exciton delocalization length. Measuring quantities such as the optical dephasing time using photon echo spectroscopy, permits selective access to the dynamics of coherent excitons, providing a fundamental basis to help tackle these questions.

In this dissertation, non-linear spectroscopy is employed as an incisive tool to time-resolve the journey from optical excitation to relaxation. In this chapter, we reviewed some the established principles of non-linear spectroscopy to enable the experiments which follow in the subsequent chapters. Beginning with Schrödinger equation, the linear ($\chi^{(1)}$) and non-linear ($\chi^{(3)}$) susceptibilities are derived in both the frequency and time-domain. The resulting expression for the third-order polarization $P^{(3)}(t)$ is then recast to describe various nonlinear spectroscopic processes such as the stimulated photon echo. Lastly, system-bath interactions were introduced by coupling the E_{11} transition to a bath of multimode harmonic oscillators to provide a complete model for the spectral dynamics of highly disordered systems such as semiconducting SWNTs.

3.6 References

[1] J. T. Brebner and T. A. Welford. *Reaction Times*. Academic Press, New York, 1980.

[2] N. Bloembergen. *Nonlinear Optics 4th Ed*. World Scientific Press, New York, 1996.

[3] M. Fox. *Optical Properties of Solids*. Oxford University Press, New York, 2001.

[4] R. Boyd. *Nonlinear Optics 2nd Ed.* Academic Press, San Diego, 2003.

[5] Y. Yu and M. Cardonna. *Fundamentals of Semiconductors: Physics and Materials Properties*. Spring Press, New York, 1996.

[6] Charles Kittel. *Quantum Theory of Solids*. John Wiley and Sons, New York, 1963.

[7] Stephane Berciaud, Laurent Cognet, and Brahim Lounis. Luminescence decay and the absorption cross section of individual single-walled carbon nanotubes. *Phys. Rev. Lett.*, 101(7):077402–4, 2008.

[8] S. Mukamel. *Principles of Nonlinear Optical Spectroscopy*. Oxford University Press, New York, 1995.

[9] Minhaeng Cho, and Graham R. Fleming. Chromophore-solvent dynamics. *Annu. Rev. Phys. Chem.*, 47:109–134, 1996.

[10] Minhaeng Cho, Jae-Young Yu, Taiha Joo, Yutaka Nagasawa, Sean A. Passino, and Graham R. Fleming. The integrated photon echo and solvation dynamics. *J. Phys. Chem.*, 100(29):11944–11953, 1996.

[11] T. Joo, Y. Jia, J.-Y. Yu, M.J. Lang, and G.R. Fleming. Third-order nonlinear time domain probes of solvation dynamics. *J. Chem. Phys.*, 104:6089–6108, 1996.

[12] T. Joo and A.C. Albrecht. Electronic dephasing studies of molecules in solution at room temperature by femtosecond degenerate four wave mixing. *Chem. Phys.*, 176(1):233–247, 1993.

[13] W.P. de Boeij, M.S. Pshenichnikov, and D.A. Wiersma. On the relation between the echo-peak shift and brownian-oscillator correlation function. *Chem. Phys. Lett.*, 253(53-60), 1996.

[14] R.M. Russo, E.J. Mele, C.L. Kane, I.V. Rubtsov, M.J. Therien, and D.E. Luzzi. One-dimensional diffusion-limited relaxation of photoexcitations in suspensions of single-walled carbon nanotubes. *Phys. Rev. B*, 74:041405(R)–041405(R), 2006.

[15] Y.-Z. Ma, T. Hertel, Z.V. Vardeny, G.R. Fleming, and L. Valkunas. Ultrafast spectroscopy of carbon nanotubes. volume 111, pages 321–352. Springer-Verlag Berlin, Heidelberg, 2008.

[16] T. Brixner, J. Stenger, H.M. Vaswani, M. Cho, R.E. Blankenship, and G.R. Fleming. Two-dimensional spectroscopy of electronic couplings in photosynthesis. *Nature*, 434:625–628, 2005.

[17] R. Kubo. *A Stochastic Theory of Line-shape and Relaxation*. Edinburgh, 1962.

[18] T. Joo, Y. Jia, J.-Y. Yu., M.J. Lang, and G.R. Fleming. Third-order nonlinear time domain probes of solvation dynamics. *J. Chem. Phys.*, 104:6089–6108, 1996.

[19] Mark A. Berg, K. D. Rector, and M. D. Fayer. Two-pulse echo experiments in the spectral diffusion regime. *J. Chem. Phys.*, 113(8):3233–3242, 2000.

[20] G.R. Fleming, S.A. Passino, and Y. Nagasawa. The interaction of solutes with their environments. *Phil. Trans. R. Soc. Lond. A*, 356:389–404, 1998.

[21] R. Jimenez, F. van Mourik, J.Y. Yu, and G.R. Fleming. Three pulse photon echo measurements on lh1 and lh2 complexes of rhodobacter sphaeroides: A nonlinear spectroscopic probe of energy transfer. *J. Phys. Chem. B*, 101:7350–7359, 1997.

[22] H. Fidder, J. Terpstra, and D.A. Wiersma. Dynamics of frenkel excitons in disordered molecular aggregates. *J. Chem. Phys.*, 94:6895–6907, 1991.

[23] Feng Wang, Gordana Dukovic, Louis E. Brus, and Tony F. Heinz. The optical resonances in carbon nanotubes arise from excitons. *Science*, 308(5723):838–841, May 2005.

Chapter 4

Femtosecond Infrared Spectroscopy Reveals Transient Mid-IR States

Femtosecond mid-infrared spectroscopy was applied to study the vibrational spectra and dynamics in the electronic excited-states of semiconducting single-walled carbon nanotubes. The experiments were performed by exciting the SWNTs dispersed individually in polymethylmethacrylate and polyvinyl alcohol polymer films with 40 fs laser pulses at 800 nm, and the resulting responses were monitored with broadband mid-infrared pulses ranging from 1510 to 1670 cm^{-1}. The structured spectra observed show vibrational bands with up-shifted frequencies by 10-50 cm^{-1} with respect to their ground state counterparts. The observation provides direct evidence for the theoretically predicted lattice distortions in the electronic excited-state. Analysis of the kinetics probed in the mid- and near-infrared regions provide an estimate of the time scales for the vibrational relaxation.

4.1 Introduction

The remarkable electronic properties of single-walled carbon nanotubes (SWNT) have stimulated enormous interests in studying their fundamental physics using both frequency- and time-domain spectroscopic methods (for an overview, see recent reviews[1–5]). Over the past a few years, application of ultrafast spectroscopy has revealed important information on fundamental dynamics, such as electron-phonon scattering, exciton-exciton annihilation,

intrinsic relaxation and some extrinsic effects (see the review by Ma *et al*[4] and the references therein). However, all these studies have been primarily focused on electronic excited-states.

It has been predicted theoretically that creation of an exciton in a semiconducting SWNT leads to a long-ranged distortion in its lattice[6–8] The resulting change in the bond length in the electronically excited SWNT can lead to different vibrational frequencies from the corresponding ground-state. The transition from this distorted lattice to a new equilibrium lattice geometry or vibrational relaxation in the electronically excited-state can further have profound effects on the relaxation of the electronic excited-state itself. This suggests that vibrational relaxation in the electronically excited-states is an integral part of the overall dynamical process. In this paper, we report a femtosecond mid-IR spectroscopic study on the vibrational spectra and dynamics of electronically excited semiconducting SWNTs.

4.2 Experimental Details

The experiments were performed on $\sim$100μm thick films of SWNTs fabricated using either polymethylmethacrylate (PMMA)[9] or polyvinyl alcohol (PVA) as the embedding matrix. Both polymers have good transmission in the mid-IR region necessary for the transient absorption (TA) measurements. Our starting material was a commercial H_2O suspension of CoMoCAT SWNTs (SouthWest Nano Tech.), which were dispersed individually with sodium dodecylbenzene sulfonate (NaDDBS) as a surfactant. The linear absorption spectra of these films and the starting aqueous solution are shown in Fig. 4.1. Although the spectra of the films exhibit a noticeable shift and a background change with respect to the solution spectrum, the main features associated with both the lowest and the second dominant exciton transitions (E_{11} and E_{22}) of the two most abundant tube types, the (6, 5) and (7, 5) tubes, are unchanged. This excludes the occurrence of any significant tube aggregation, which would have substantially washed out these distinct features.[10] This conclusion is further supported by the observed steady-state fluorescence emission spectra with a clearly weaker emission around 1150 nm than from those dominant tube species (data not shown)[11,12] Measurement of the fluorescence emission and excitation spectra further enabled us to determine the E_{11} (and E_{22}) transition wavelengths for both the (6, 5) and (7, 5) nanotubes.[13] For the SWNT/PMMA film we found 1004 and 1034 (572 and 647) nm, respectively. Blank PMMA and PVA films with NaDDBS surfactant were also prepared in order to experimentally quantify their potential contributions to the TA signals in the spectral region of interest.

We employed a light source that consists of a 1 kHz Ti:Sapphire regenerative amplifier and a mid-IR optical parametric amplifier (OPA). The former produces 800 nm pulses with typical duration of 40 fs (full-width at half maximum, FWHM), whereas the latter generates short pulses tunable between 3 and 7 μm (3300-1400 cm^{-1}) with a duration of 95 fs (FWHM) at 5 μm and a pulse energy of 1-2 μJ. The 800 nm pulses were used as the pump beam, and induced changes of sample absorbance were monitored with broadband mid-IR pulses. The detection system involves a Triax 180 imaging spectrometer with 4 cm^{-1} resolution, and

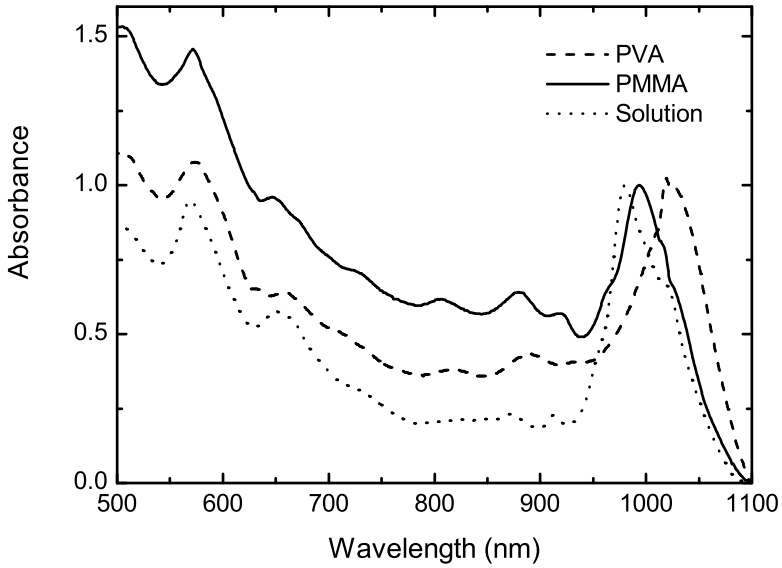

Figure 4.1. Linear absorption spectra of the aqueous suspension of CoMoCAT nanotubes (dotted line) and the nanotube films, which were prepared using this solution and PVA (dashed line) and PMMA (solid line) polymers.

a 64-element HgCdTe dual-array detector attached to an IR64-16 multichannel laser pulse integrator system. The pump beam was focused to a spot of ∼200 μm on the sample, and its polarization was set parallel to the probe beam. For a detailed description of the light source and the experimental setup, see ref. 14. The near-IR TA data were collected using a setup that consists of a 250 kHz Ti:Sapphire regenerative amplifier and a visible OPA. We refer to our previous papers for the experimental details.[15,16]

4.3 Results and Discussion

We found that a pump pulse intensity ranging from 0.64 to 3.2 mJ/cm^2 was necessary to acquire data with a satisfactory signal-to-noise ratio. Representative TA spectra recorded at a pump intensity of 2.5 mJ/cm^2 using the SWNT/PMMA film are shown in Fig. 4.2a. The TA spectra show positive-signed, induced absorption in the entire probe spectral region (1510 to 1670 cm^{-1}) with several distinct features. Besides the broad band peaking around 1600 cm^{-1}, distinct sidebands with peaks located at 1563 and 1633 cm^{-1} are prominent. Comparison of the TA spectra measured at other five pump intensities (0.38, 0.70, 1.12, 1.98 and 3.33 mJ/cm^2) shows that, upon normalizing at the maxima of the A bands, the spectral shape observed at any given delay time is independent of intensity. This invariance consequently leads to dynamics that are independent of pump intensity at all probe frequencies. As an example, Fig. 4.2b shows the normalized kinetic profiles obtained at 1603 cm^{-1} under

two different pump intensities. Fitting the kinetics by employing a sum of exponential terms as a model function and by taking into account the finite duration of the pump and probe pulses gives the following timescales (relative amplitudes): 0.21 ps (0.63), 1.66 ps (0.30) and 81 ps (0.07). Note that 81 ps is a rough estimate for the timescale of a long-lived decay component that persists over the entire range of our scan (700 ps). The maximum magnitude of the TA signal is further found to increase with pump intensity in a nonlinear, saturating manner (Fig. 4.2c). The independence of the kinetic decay on pump intensity (Fig. 4.2b) and the saturating behavior of its signal magnitude with increasing intensity (Fig. 4.2c) are qualitatively similar to what has been found in the near-IR region where the E_{11} transition of selected semiconducting SWNTs is probed following its direct optical excitation.[15]

Although the PMMA and PVA polymers as well as the NaDDBS surfactant have absorption in the spectral region of our measurements, none of them should contribute to the observed TA signals. The reason is that they are not excited by the 800 nm pump pulse, and the finite absorption of the mid-IR probe pulse is already subtracted off in the obtained TA data. This is confirmed by our test measurements performed at a pump intensity of 3.68 mJ/cm^2 on a reference PMMA film containing just the surfactant,. The result shows weak transients around time zero with either positive- or negative-signed signals depending on the probe frequency, arising most likely from a pulse overlapping effect (data not shown). Also, the maximum magnitude of the detected signal is less than 1.5% of the signal maximum observed from the SWNT/PMMA film at a similar pump intensity (3.33 mJ/cm^2). We therefore neglect this weak signal in the rest of the paper. We further found that use of the PVA polymer does not cause any significant changes in both TA spectra and kinetics (as an example, see Fig. 4.3b,c), suggesting that the results obtained are intrinsic to nanotubes. Furthermore, both the spectral and kinetic features are found to be independent of sample position for the SWNT/PMMA and SWNT/PVA films, even though the magnitudes of the TA signals can vary considerably from one location to another.

The positive-signed TA signals observed indicate that they must originate from electronic excited-state(s). A transition from such excited-state(s) in the frequency region of our measurements, in principle, can be either electronic or vibrational depending solely on the nature of the final state(s). From an energetic point of view, an electronic, intra-band excitonic transition appears plausible because of the presence of an exciton-manifold above the E_{11} state.[17] However, the line-widths observed in the TA spectra are too narrow for such an intra-band excitonic transition. Due to the short lifetime associated with an excitonic state lying above the E_{11} state, its involvement in the intra-band transition should result in a much broader spectrum than we observe. The well-studied E_{22} state can serve as a typical example here - its lifetime was determined to be in the order of 50 fs for several semiconducting tube species.[18,19] This short lifetime gives rise to a broad spectrum with a typical FWHM of 350 cm^{-1} or more.[20,21] This is in stark contrast to the narrow line-widths of the observed TA spectra. Analysis of the TA spectrum measured at a delay time of 100 fs shows that the spectrum can be decomposed into five Gaussian components with peaks (FWHM widths) at 1562 (20.1), 1588 (22.2), 1607 (18.5), 1628 (13.5) and 1640 (33.3) cm^{-1}, respectively (see Fig. 4.3b). The FWHM widths of the two major components peaking at 1588 and 1607 cm^{-1} are almost identical to the width of the G-band Raman spectrum measured using the same nanotube material in solution and embedded in polyvinylpyrrolidone (PVP) polymer

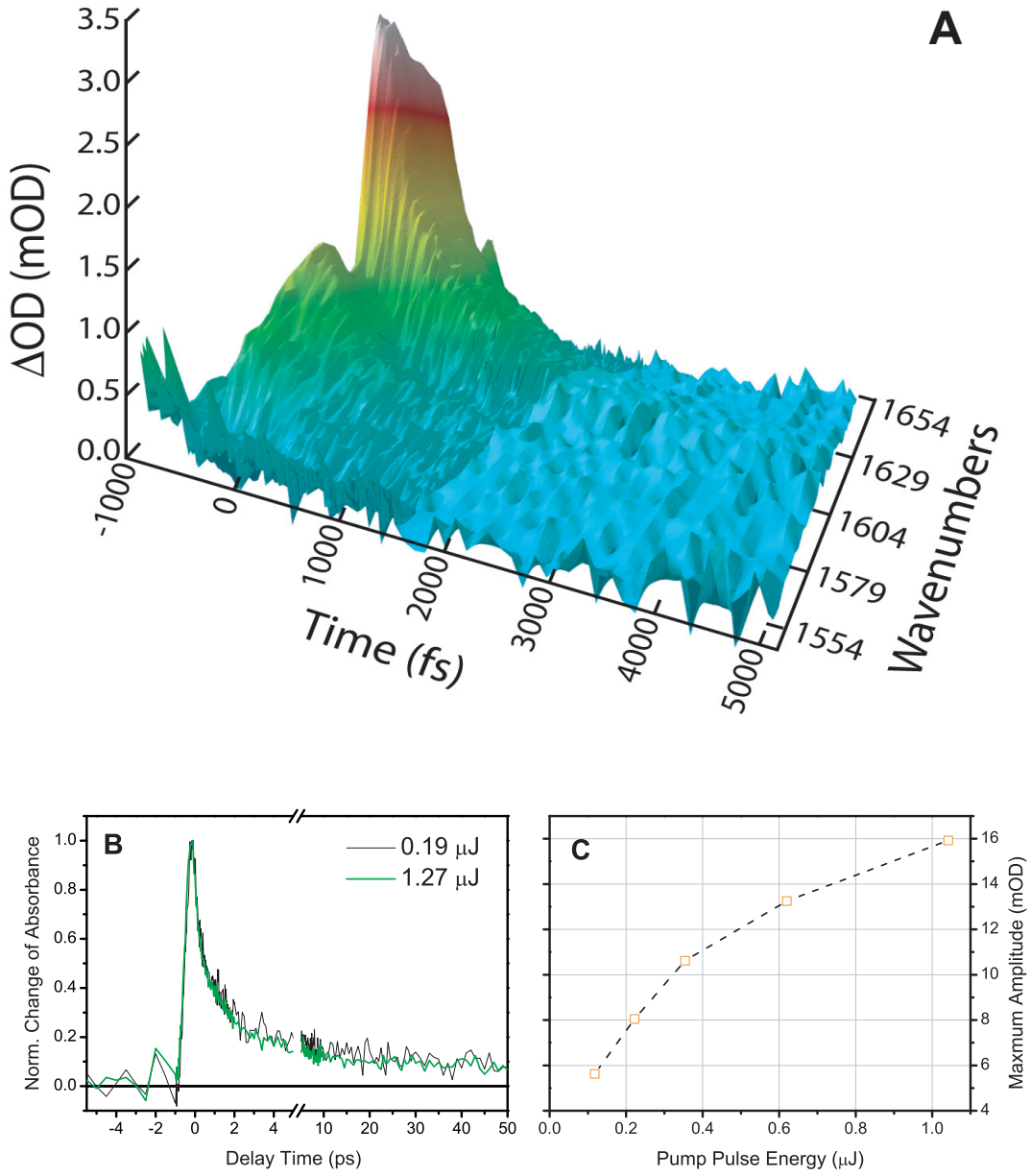

Figure 4.2. (a) Representative TA spectrum from 1554-1654 cm^{-1}, recorded at a pump intensity of 2.5 mJ/cm^2 at 800 nm. (b) The normalized ΔOD kinetic profiles obtained at 1603 cm^{-1} under two different pump intensities: 0.61 mJ/cm^2 (black line) and 4.1 mJ/cm^2 (dark green line). (c) Plot of the maximum magnitude of the TA signal at 1603 cm^{-1} as a function of pump intensity.

frequency(cm^{-1})	state	method	material	reference
1562	E_{11}	TA	individualized tubes	this work
1588	E_{11}	TA	individualized tubes	this work
1607	E_{11}	TA	individualized tubes	this work
1628	E_{11}	TA	individualized tubes	this work
1640	E_{11}	TA	individualized tubes	this work
1554	GS	Raman	isolated tubes	27
1563	GS	Raman	isolated tubes	27
1571	GS	Raman	isolated tubes	27
1591	GS	Raman	isolated tubes	27
1600	GS	Raman	isolated tubes	27
1541	GS	IR	isolated tubes	24
1564	GS	IR	isolated tubes	24
1585	GS	IR	isolated tubes	24
1587	GS	IR	isolated tubes	25

Table 4.1. Summary of the vibrational frequencies determined in this work and by Raman and infrared experiments.

(data not shown). Based on these considerations, we attribute the observed TA spectra to the transition between the levels of the tangential vibrations in the E_{11} excited-state(s).

Among the five spectral components shown in Fig. 4.3b for the E_{11} excited-state vibrations, three are characterized by a frequency that is up-shifted by 10-50 cm^{-1} with respect to the frequencies of the electronic ground-state vibrations. Electronic ground-state vibrations have been a subject of extensive studies by resonant Raman spectroscopy at both single-tube and ensemble levels (see the review by Dresselhaus *et al*[22]). Fewer investigations based on theoretical[23] and experimental[24,25] infrared spectroscopy have been also reported. In table 4.3, we summarize the vibrational frequencies determined in this work (for the excited state) together with the ground state frequencies reported in the literature of Raman and infrared measurements. Although some variations exist in the results reported for the tangential vibrations, the frequencies found from a majority of work are below 1590 cm^{-1}. The clearly up-shifted frequencies observed in this work provide a direct evidence for the occurrence of a long-ranged lattice distortion in the electronic excited-state.[6–8] We further speculate that the appearance of multiple spectral components as shown in Fig. 4.3b may be indicative of a bond-length variation in the distorted lattice. In the recent calculation by Tretiak *et al.*,[7] a corrugated tube surface arising from alternative lengthening and shortening of bond-length was predicted for a semiconducting SWNT. Note that such a bond-length alternation may give rise to both down- and up-shifted vibrational frequencies compared to the ground state.

Analysis of the temporal evolution of the TA kinetics probed in the mid- and near-IR regions enables us to estimate the time scale of the vibrational relaxation in the E_{11} state. Because the evolution of the mid-IR kinetics is governed by the relaxation from both the final vibrational state and the E_{11} electronic state, the contribution from the electronic relaxation must be removed. For this purpose, we performed separate experiments in the

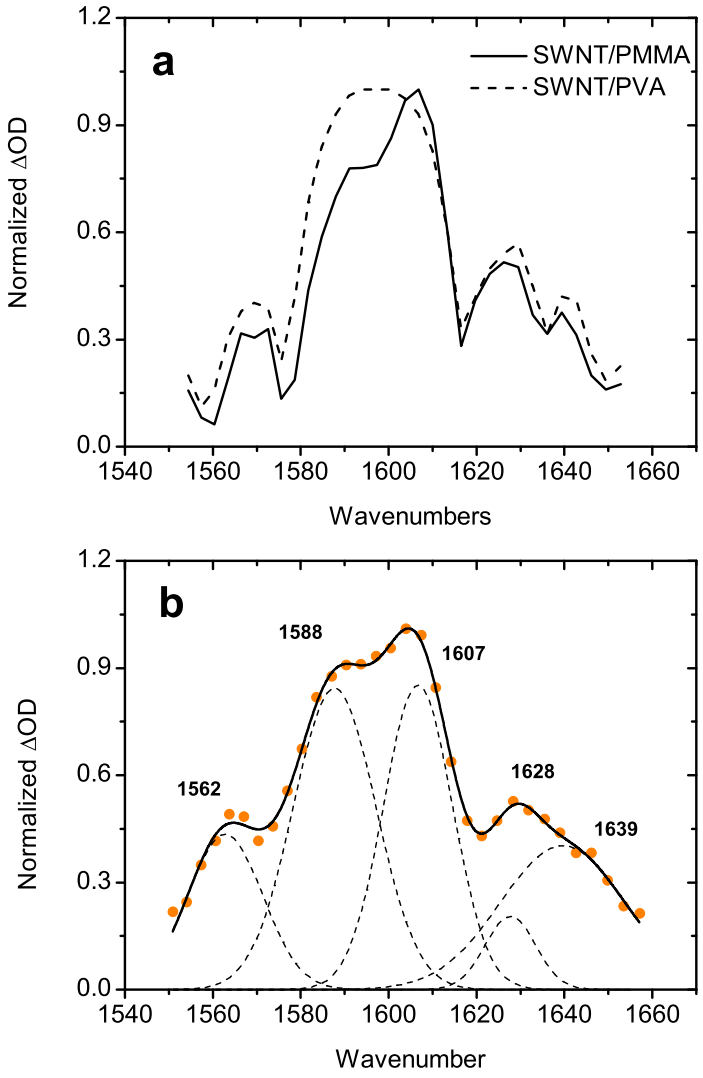

Figure 4.3. (a) Comparison of the TA spectra measured using the SWNT/PMMA (solid line) and SWNT/PVA (dashed line) films at a delay time of 100 fs. For ease of comparison, these spectra are scaled to equal amplitude at their maxima. (b) TA spectrum recorded for the SWNT/PMMA film at a delay time of 100 fs (symbols). The Gaussian components resulting from spectral deconvolution are shown as dashed lines and the fit spectrum is given by the solid line. The positions of the peaks are labeled on the figure.

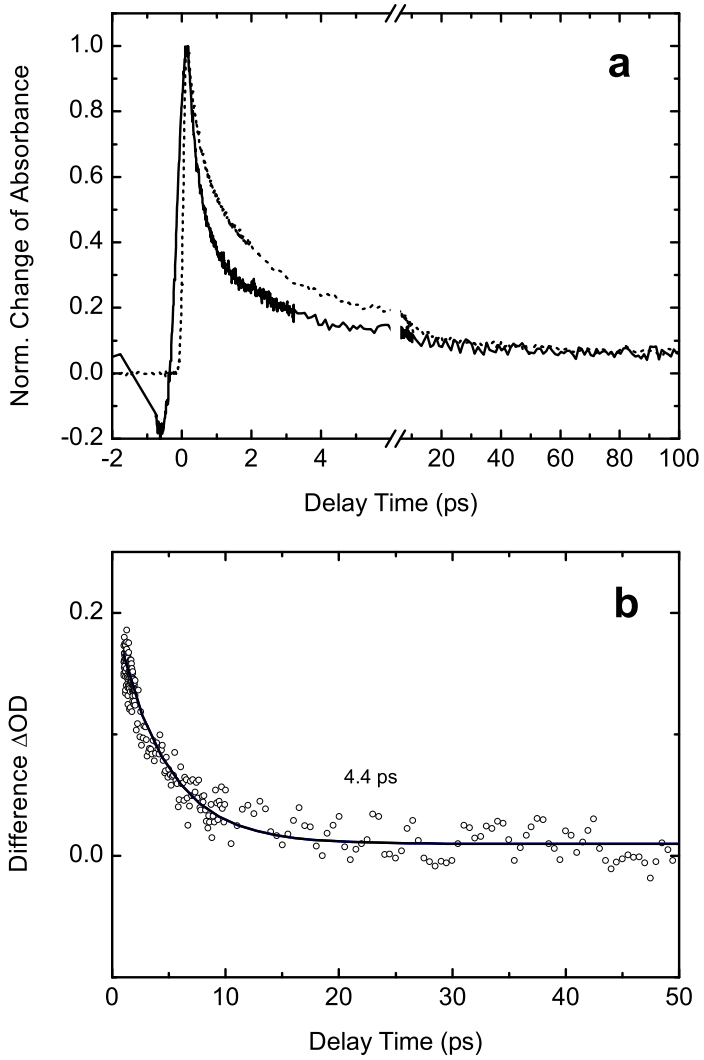

Figure 4.4. (a) Comparison of the TA kinetics detected at 1603 cm^{-1} (800 nm pump) (solid lines) and at 1018 nm (572 nm pump) (dashed lines) for the SWNT/PMMA film. For ease of comparison, the data collected at 1018 nm are inverted by multiplying (-1). The kinetic traces are normalized at the signal maxima. (b) The difference between the two kinetic profiles shown in (a) and its monoexponential decay fit (solid line).

near-IR region to characterize the exciton population relaxation from the E_{11} state and the concomitant recovery of ground state. The dashed-line curve in Fig. 4.4 shows the data obtained by from the same SWNT/PMMA film at 1018 nm, the E_{11} state of the (6, 5) tube, which is one of the dominant nanotube species in the sample. Selective detection of this particular tube type is accomplished by resonant excitation of its E_{22} state at 572 nm. As is evident from Fig. 4.4a, the kinetic profile probed at 1603 cm^{-1}exhibits a faster decay than the one measured at 1018 nm. The difference between these two kinetic profiles represents approximately the dynamics of the vibrational relaxation in the E_{11} state. As shown in Fig. 4.4b, this difference kinetics can be well described by a single time scale of 4.4 ps. A similar value was also obtained for the data measured using the SWNT/PVA film. Note that this time scale should be considered as a rough estimate as the mid- and near-IR data were measured under electronically non-resonant and resonant conditions, respectively.

As a final remark, we briefly discuss the work of Zhao *et al*[26] that covers a similar spectral range. The authors reported a TA spectrum measured on a film sample prepared by dispersing the HiPco tubes into a PVA matrix. The published spectrum is very different from ours in terms of the overall shape, due to the use of different tube materials (HiPco vs. CoMoCAT) and different spectral resolution (4 cm^{-1} in our case and roughly 160 cm^{-1} in the case of ref. 26). The authors attributed this band to intra-band excitonic transitions from both the lowest optically allowed and dark excitonic states to some higher-lying ones.

4.4 Conclusions

In summary, we demonstrated in this report that femtosecond TA spectroscopy employing 800-nm pump and mid-IR probe enables to access the vibrational spectra and dynamics in the E_{11} exciton states of semiconducting SWNTs. The observed induced absorption spectra exhibit prominent spectral structures, which can be decomposed into five Gaussian components. Three of these components are characterized by a frequency up-shifted by 10-50 cm^{-1} with respect to the frequencies of the electronic ground-state vibrations. This observation provides a direct evidence for the occurrence of a long-ranged lattice distortion in the electronic excited-state. Analysis of the TA kinetics probed in the mid- and near-IR regions enables us to extract an approximate time scale for the vibrational relaxation. Further studies employing single tube enriched samples in combination with resonant excitation are expected to provide a more accurate determination of the time scales.

4.5 References

[1] Hartschuh, A. New techniques for carbon-nanotube study and characterization. In *Topics Appl. Phys*; Jorio, A., Dresselhaus, G., Dresselhaus, M. S., Eds.; Springer-Verlag Berlin: Heidelberg, 2008; Vol. 111; pp 371.

[2] Heinz, T. F. Rayleigh scattering spectroscopy. In *Topics Appl. Phys*; Jorio, A., Dresselhaus, G., Dresselhaus, M. S., Eds.; Springer-Verlag Berlin: Heidelberg, 2008; Vol. 111; pp 353.

[3] Lefebvre, J.; Maruyama, S.; Finnie, P. Photoluminescence: science and applications. In *Topics Appl. Phys*; Jorio, A., Dresselhaus, G., Dresselhaus, M. S., Eds.; Springer-Verlag Berlin: Heidelberg, 2008; Vol. 111; pp 287.

[4] Ma, Y.-Z.; Hertel, T.; Vardeny, Z. V.; Fleming, G. R.; Valkunas, L. Ultrafast spectroscopy of carbon nanotubes. In *Topics Appl. Phys.*; Jorio, A., Dresselhaus, G., Dresselhaus, M. S., Eds.; Springer-Verlag Berlin: Heidelberg, 2008; Vol. 111; pp 321.

[5] Saito, R.; Fantini, C.; Jiang, J. Excitonic states and resonance Raman spectroscopy of single-wall carbon nanotubes. In *Topics Appl. Phys*; Jorio, A., Dresselhaus, G., Dresselhaus, M. S., Eds.; Springer-Verlag Berlin: Heidelberg, 2008; Vol. 111; pp 251.

[6] Perebeinos, V.; Avouris, P. *Phys. Rev. Lett.* **2005**, 94, 027402.

[7] Tretiak, S.; Kilina, S.; Piryatinski, A.; Saxena, A.; Martin, R. L.; Bishop, A. R. *Nano Lett.* **2007**, 7, 86.

[8] Kilina, S.; Tretiak, S. *Adv. Func. Mater.* **2007**, 17, 3405.

[9] Ma, Y.-Z.; Valkunas, L.; Bachilo, S. M.; Fleming, G. R. *Phys. Chem. Chem. Phys.* **2006**, 8, 5689.

[10] O'Connell, M. J.; Bachilo, S. M.; Huffman, C. B.; Moore, V. C.; Strano, M. S.; Haroz, E. H.; Rialon, K. L.; Boul, P. J.; Noon, W. H.; Kittrell, C.; Ma, J.; Hauge, R. H.; Weisman, R. B.; Smalley, R. E. *Science* **2002**, 297, 593.

[11] Torrens, O. N.; Milkie, D. E.; Zheng, M.; Kikkawa, J. M. *Nano Lett.* **2006**, 6, 2864.

[12] Tan, P. H.; Rozhin, A. G.; Hasan, T.; Hu, P.; Scardaci, V.; Milne, W. I.; Ferrari, A. C. *Phys. Rev. Lett.* **2007**, 99, 137402.

[13] Bachilo, S. M.; Balzano, L.; Herrera, J. E.; Pompeo, F.; Resasco, D. E.; Weisman, R. B. *J. Am. Chem. Soc.* **2003**, 125, 11186.

[14] van Tassle, A. J.; Prantil, M. A.; Fleming, G. R. *J. Phys. Chem. B* **2006**,110, 18989.

[15] Ma, Y.-Z.; Valkunas, L.; Dexheimer, S. L.; Bachilo, S. M.; Fleming, G. R. *Phys. Rev. Lett.* **2005**, 94, 157402.

[16] Ma, Y.-Z.; Valkunas, L.; Dexheimer, S. L.; Fleming, G. R. *Mol. Phys.* **2006**, 104, 1179.

[17] Ma, Y.-Z.; Spataru, C. D.; Valkunas, L.; Louie, S. G.; Fleming, G. R. *Phys. Rev. B* **2006**, 74, 085402.

[18] Ma, Y.-Z.; Stenger, J.; Zimmermann, J.; Bachilo, S. M.; Smalley, R. E.; Weisman, R. B.; Fleming, G. R. *J. Chem. Phys.* **2004**, 120, 3368.

[19] Manzoni, C.; Gambetta, A.; Menna, E.; Meneghetti, M.; Lanzani, G.; Cerullo, G. *Phys. Rev. Lett.* **2005**, 94, 207401.

[20] Lefebvre, J.; Fraser, J. M.; Finnie, P.; Homma, Y. *Phys. Rev. B* **2004**, 69, 075403.

[21] Miyauchi, Y.; Maruyama, S. *Phys. Rev. B* **2006**, 74, 035415.

[22] Dresselhaus, M. S.; Dresselhaus, G.; Saito, R.; Jorio, A. *Phys. Reports* **2005**, 409, 47.

[23] Sbai, K.; Rahmani, A.; Chadli, H.; Bantignies, J.-L.; Hermet, P.; Sauvajol, J.-L. *J. Phys. Chem. B* **2006**, 110, 12388.

[24] Kim, U. J.; Liu, X. M.; Furtado, C. A.; Chen, G.; Saito, R.; Jiang, J.; Dresselhaus, M. S.; Eklund, P. C. *Phys. Rev. Lett.* **2005**, 95, 157402.

[25] Bantignies, J.-L.; Sauvajol, J.-L.; Rahmani, A.; Flahaut, E. *Phys. Rev. B* **2006**, 74, 195425.

[26] Zhao, H.; Mazumdar, S.; Sheng, C.-X.; Tong, M.; Vardeny, Z. V. *Phys. Rev. B* **2006**, 73, 075403.

[27] Jorio, A.; Piamenta, M. A.; Souza Filhou, A. G.; Samsonidze, G. G.; Swan, A. K.; M. Unlu,; B. Goldberg,; R. Saito,; G. Dresselhaus,; and M. Dresselhaus *Phys. Rev. Lett.* **2004**, 90, 107403.

Chapter 5

Ultrafast Mid-Infrared Intra-Excitonic Response

We report a femtosecond mid-infrared study of the broadband low-energy response of individualized (6,5) and (7,5) single-walled carbon nanotubes. Strong photoinduced absorption is observed around 200 meV, whose transition energy, oscillator strength, resonant chirality enhancement and dynamics manifest the observation of quasi-1D intra-excitonic transitions. A model of the nanotube $1s$-$2p$ intra-excitonic cross section agrees well with the signal amplitudes. Our study further reveals a saturation of the photoinduced absorption with increasing phase-space filling of the correlated e-h pairs.

5.1 Introduction

The quasi-1D confinement of photoexcited charges in single-walled carbon nanotubes (SWNTs) gives rise to strongly enhanced Coulomb interactions and large exciton binding energies on the 100 meV energy scale. These amplified electron-hole (e-h) correlations are a key aspect of nanotube physics [1]. Following the availability of "individualized" SWNT ensembles, this strong excitonic behavior was independently confirmed by interband absorption-luminescence maps [2], two-photon excited luminescence [3, 4], and ultrafast spectroscopy [5]. Optical interband probes, however, are limited by symmetry and momentum to detect only a small subset of excitons.

As illustrated in Fig. 5.1(a) in a two-particle scheme, SWNT excitons are characterized by a center-of-mass momentum K and by an internal quantum state (designated here as $1s$, $2s$, $2p$, ...) that accounts for the relative charge motion. Each state splits into even (g) and odd (u) parity levels corresponding to different superpositions of the cell-periodic wavefunctions of the underlying graphene lattice [4]. This entails a series of optically "dark" excitons, including the $1s$-(g) lowest-energy exciton that lacks coupling in both single- and two-photon interband spectroscopy [3, 4]. Splitting into singlet and triplet spin states additionally restricts interband optical coupling [6]. Finally, interband transitions are limited to excitons around K ≈ 0 due to momentum conservation.

Intra-excitonic transitions between low-energy levels of excitons with the same cell-periodic symmetry [arrows, Fig. 5.1(a)] represent a fundamentally different tool, analogous to atomic absorption spectroscopy. In contrast to interband absorption that measures the ability to *generate* e-h pairs, intra-excitonic absorption detects existing excitons via transitions from the $1s$ ground state to higher relative-momentum states [7, 8]. Being independent of K, it is sensitive to genuine exciton populations across momentum space. As the cell-periodic component of the wavefunction remains unchanged, intra-excitonic absorption is also unrestricted by the exciton ground state symmetry [7]. Applied to individualized SWNTs,

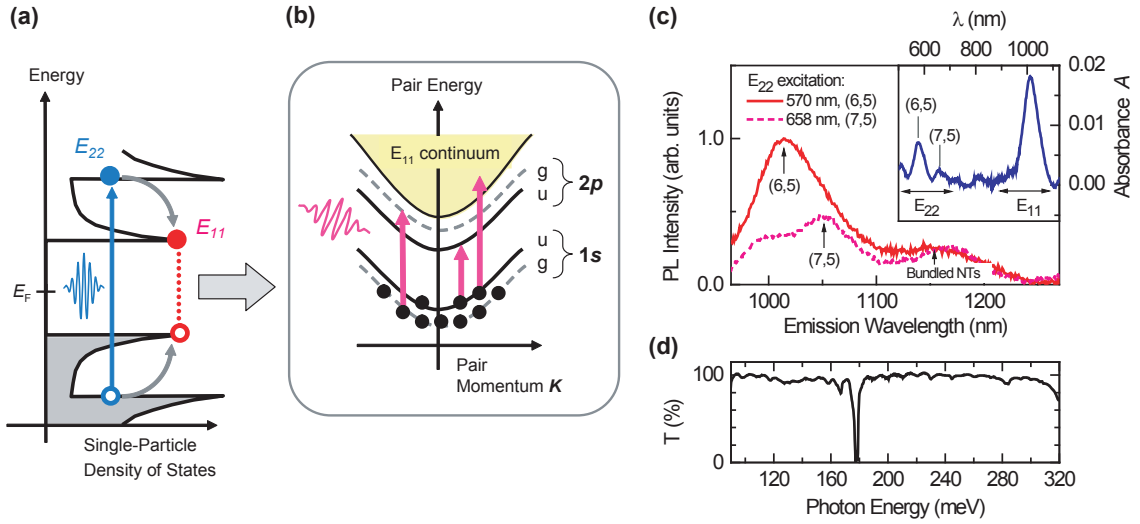

Figure 5.1. Electronic levels and optical properties of semiconducting SWNTs: (a) Optical interband transitions create quasi-1D e-h pairs that quickly relax to the lowest-energy (E_{11}) subband and form strongly-bound excitons. Excitons transcend a single-particle picture, but as superpositions of single-particle states occupy part of the available phase space. (b) Two-particle (e-h pair) dispersion illustrating exciton bands of odd (u) and even (g) symmetry, and 1s→ 2p intra-excitonic transitions (arrows). (c) Photoluminescence (PL) spectra of SWNTs embedded in a 50 μm thick polyethylene film, showing distinct (6,5) and (7,5) E_{11} nanotube emission after resonant E_{22} excitation. Curves are normalized to the emission at 1160 nm that indicates weak residual tube bundling. Inset: sample absorbance, after subtracting the scattering background. (d) equilibrium mid-IR transmission of the sample.

intra-excitonic resonances can thus measure both bright and dark excitons and should occur in the mid-infrared (mid-IR) after ultrafast excitation. In contrast to extensive interband nanotube studies [9, 10, 11, 12], only a few ultrafast intra-band experiments have been carried out which focus largely on nanotube bundles [13, 14, 15, 16]. THz experiments on photoexcited bundled tubes revealed a non-Drude response attributed to small-gap metallic tubes or inter-tube charge separation [13, 14]. Mid-IR transient absorption was also observed in bundled nanotubes and assigned to transitions from allowed to dipole-forbidden excitons [15, 16].

In this Letter, we report ultrafast optical-pump, mid-IR-probe studies of individualized (6,5) and (7,5) SWNTs. Transient spectra after photoexcitation evidence strong mid-IR absorption around 200 meV, in accordance with intra-excitonic transitions of strongly-bound e-h pairs in semiconducting nanotubes. The absorption cross section of $4 \cdot 10^{-15}$ cm^2 agrees closely with calculations of quasi-1D intra-excitonic $1s$-$2p$ dipole transitions presented here. The excitation-wavelength dependence and kinetics further underscore the excitonic origin of the transient mid-IR response, and its intensity dependence scales quantitatively with a model of phase-space filling expected for quasi-1D excitons. This intra-excitonic absorption represents a sensitive spectroscopic tool to probe correlated e-h pairs in SWNTs, unhindered by interband dipole or momentum restrictions.

5.2 Experimental Details

Ultrafast spectroscopy was carried out in transmission using widely tunable femtosecond (fs) pulses in the mid-IR and visible range. For this, two near-IR optical parametric amplifiers (OPAs) were pumped by a 1-kHz, 28-fs Ti:sapphire amplifier. Resonant and off-resonant interband excitation was achieved using the frequency-doubled OPA or a fraction of the fundamental. The output of the second OPA was difference-frequency mixed in GaSe to generate ≈100 fs mid-IR probe pulses tunable from 4-12 μm [17]. We study individualized Co-Mo-catalyst grown SWNTs of mainly (6,5) and (7,5) chiralities [18] embedded in 50-μm thick polyethylene (PE). Importantly, PE ensures wide transparency throughout our mid-IR probe range, except for a narrow CH-bend vibration at 178 meV. The films were fabricated by drying PE solutions in decalin mixed with micelle-dispersed SWNTs, after transferring individualized SWNTs suspended in water with NaDDBS surfactant to the PE solution via ultrasound and thermal treatments. In Fig. 5.1(b), the sample's photoluminescence (PL) spectra for resonant (6,5) and (7,5) E_{22} excitation clearly exhibit the distinct E_{11} emission of these individualized SWNT chiralities, with only weak emission from bundled tubes around 1160 nm [19]. The absorption spectrum [inset, Fig. 5.1(b)] also exhibits the distinct E_{11} and E_{22} absorption peaks.

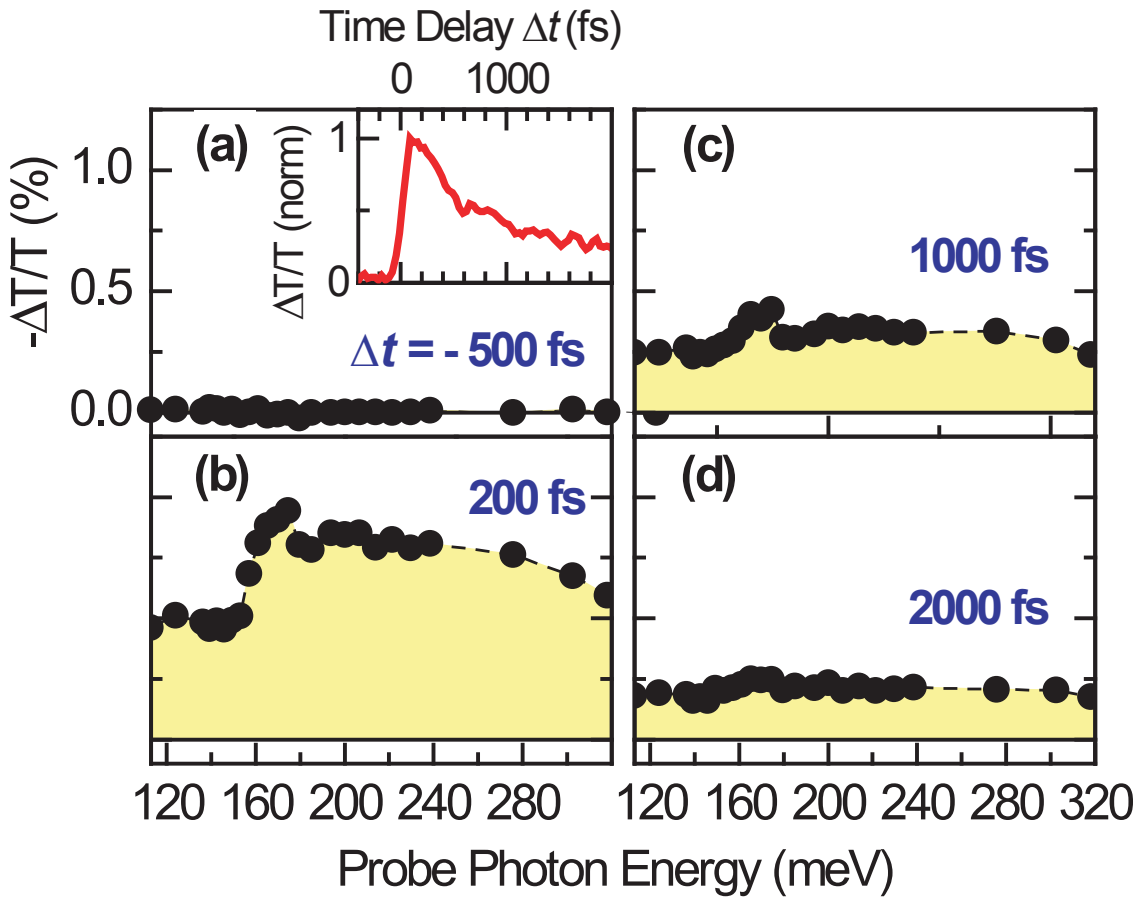

Figure 5.2. (a)-(d) Ultrafast spectrally-resolved mid-IR transmission changes after 800 nm excitation for four different delays Δt as indicated. The transient spectra are characterized by an asymmetric resonance that peaks above 160 meV and a low-frequency plateau measured down to 120 meV.Inset: normalized dynamics of the mid-IR transmission probed at 4.4 μm wavelength.

5.3 Results and Discussion

Ultrafast spectrally-resolved mid-IR transmission changes $\Delta T/T$ are shown in Fig. 5.2 for different time delays Δt after 800 nm photoexcitation at room temperature. A strong photo-induced absorption appears within the time resolution after photoexcitation [Fig. 5.2(b), Δt = 200 fs] and decays on a ps timescale [Fig. 5.2(c)-(d)]. The transient spectra are characterized by a broadly sloping, asymmetric resonance around 200 meV, with a step-like onset above 160 meV. This mid-IR resonance occurs in the transparent region far below the lowest interband exciton ($E_{11} \simeq 1.2$ eV) and intersubband transitions ($E_{22} - E_{11} \geq 0.6$eV). The peak energy is close to the (6,5) and (7,5) $1s$-$2p$ energy splitting in two-photon luminescence studies and calculations [3, 4, 20]. Thus, we associate this absorption with intra-excitonic transitions between $1s$ and $2p$ exciton levels of opposite parity. Both dipole-allowed and optically-dark $1s$ excitons can fundamentally contribute to this response. The dynamics exhibits a pulse-width limited rise of the photoinduced mid-IR absorption (inset, Fig. 5.2), which indicates rapid exciton formation.

We should comment on the asymmetric line shape observed in Fig. 2. The observed step-like onset points to a predominantly inhomogeneous broadening, and the asymmetry and large $\simeq$ 100 meV width both agree well with similar spectral features observed in the analogous two-photon PL experiments [3, 4]. We attribute the higher-energy tail of the mid-IR response to intra-excitonic transitions from the $1s$ into higher-lying np bound states and into the broad continuum of unbound pairs. This assignment is consistent with the asymmetric intra-excitonic spectra of quasi-2D e-h pairs [8]. Note that a much narrower peak seems to exist around 170 meV which we assign as an artifact [21]. Low-energy absorption is also observed below 160 meV which can arise e.g. from fluctuations of the dielectric environment around the nanotube and other chiral tube species associated with Co-Mo-catalyst-grown SWNT samples [22].

To further substantiate the nature of the response, Fig. 5.3(a) shows the excitation wavelength dependence. Resonant photoexcitation of the (6,5) and (7,5) interband E_{22} transitions, at 572 nm and 697 nm respectively, leads to significant enhancement of the transient mid-IR absorption. The amplitude closely tracks the PL-excitation spectrum [Fig. 5.3(b)], which clearly underscores the tube-specific origin of the transient mid-IR response. This conclusion is further supported by the disappearance of the photoinduced signal for excitation below the E_{11} transition [1250 nm, Fig. 5.3(a)]. Hence, the observed photo-induced absorption arises from intra-excitonic transitions of (6,5) and (7,5) SWNTs. The mid-IR dynamics after (6,5) E_{22} excitation is shown in Fig. 5.3(c) on an extended timescale, revealing a strongly non-exponential decay [dots, Fig. 5.3(c)] over several 10 ps. The dynamics closely follows the E_{11} exciton bleaching [solid line, Fig. 5.3(c)], confirming that the mid-IR signals originate from excitations in the E_{11} manifold. Thermal broadening $k_BT \simeq 26$ meV at 300 K entails comparable occupation of dark and bright excitons (split by $\simeq$ 10 meV), which enables this comparison. The decay has a bimolecular shape [dashed line, Fig 3(c)], similar to the fs kinetics of excitons in individualized SWNT suspensions explained by exciton-exciton annihilation [9], which further underscores the excitonic origin of the mid-IR response.

The mid-IR transmission changes can be used to estimate the absorption cross section

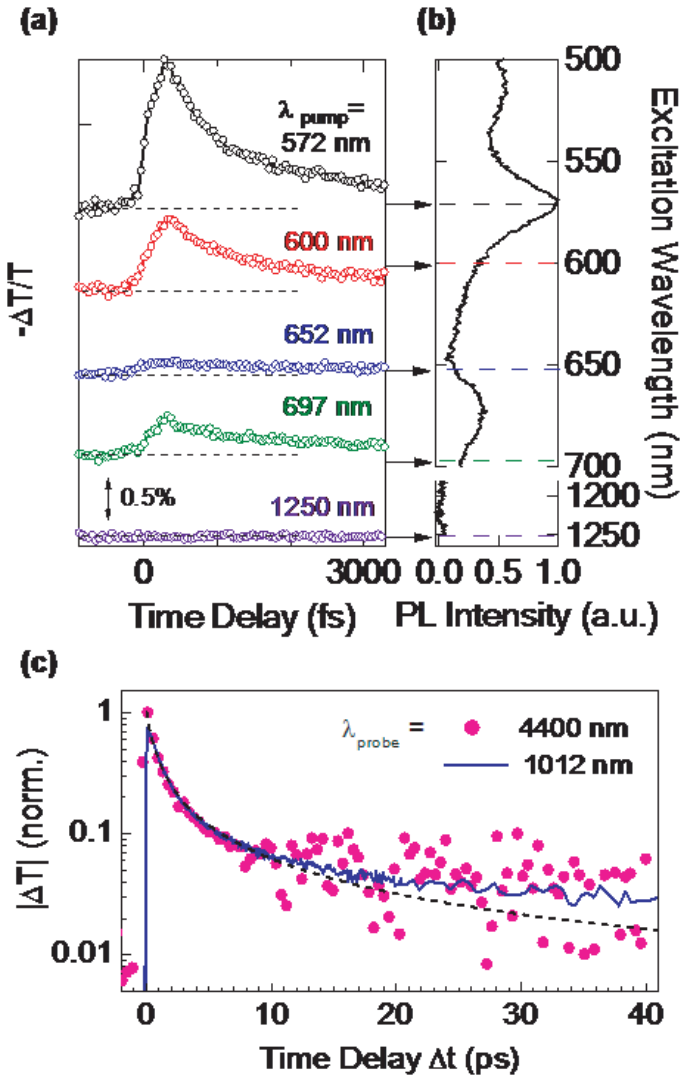

Figure 5.3. (a) Pump wavelength dependence on and off-resonant to the (6,5) and (7,5) E_{22} transitions. Traces are offset for clarity, and measured at 4.4 μm with 260 μJ/cm^2 excitation fluence. (b) PL-excitation spectrum for fixed E_{11} emission at 1012 nm. (c) Normalized mid-IR dynamics (dots) after 572 nm excitation. Thick line: E_{11} transmission change, scaled to the mid-IR signal at long delays. Dashed line: bimolecular decay $|\Delta T| \propto (1 + \gamma\ t)^{-1}$ with $\gamma = 1.5$ ps^{-1}.

$\sigma^{||}_{MIR}$ of the intra-excitonic transition, whose dipole is oriented parallel to the SWNT axis. It is defined as $\sigma^{||}_{MIR} = 3\ \ln(1-\Delta T/T)\,/\,n_{exc}$, where ΔT is the initial transmission change and n_{exc} the photoexcited density. The factor 3 accounts for the random SWNT orientation. Considering (6,5) E_{22} resonant excitation in Fig. 5.3(a) one has $\triangle T/T$ ≈1.7% and $n_{exc} = (F/\hbar\omega)\times\ln(10)A = 1.2\times10^{13}$ cm^{-2}, given $F = 260\ \mu$J/cm^2 and $A \simeq 0.007$ [inset, Fig. 5.1(b)]. This yields the experimentally-derived value for the cross section of $\sigma^{||}_{MIR} \simeq 4\times10^{-15}$ cm^2.

For comparison, we calculate the intra-excitonic $1s$-$2p$ cross section based on a model of Wannier-like excitons in SWNTs. The normalized $1s$ and $2p$ wavefunctions of Coulomb-bound e-h pairs on a cylindrical surface are [23]

$$\psi_{1s}(x) = \sqrt{\frac{8}{(a^*_B)^3\alpha^3_{1s}B_{1s}}}|x|e^{-\frac{|x|}{a^*_B\alpha_{1s}}}U(1-\alpha_{1s},2,\frac{2|x|}{a^*_B\alpha_{1s}}),$$
$$\psi_{2p}(x) = \sqrt{\frac{2}{(a^*_B)^3}}\ x\ e^{-\frac{|x|}{a^*_B}}, \tag{5.1}$$

where x measures the distance along the nanotube axis and $a^*_B = 4\pi\epsilon\epsilon_0\hbar^2/\mu e^2$ is the effective 3D Bohr radius with reduced mass μ and permittivity ϵ. Furthermore, U is Kummer's confluent hypergeometric function of the second kind and $B_{1s} \equiv 2\int_0^\infty y^2e^{-y}\left[U(1-\alpha_{1s},2,y)\right]^2 dy$ is a normalization constant. The binding energies are $E_{1s} = -\mathrm{Ry}^*/(\alpha_{1s})^2$ and $E_{2p} = -\mathrm{Ry}^*$, where $\mathrm{Ry}^* \equiv \hbar^2/(2\mu a^{*2}_B)$ is the 3D effective Rydberg energy. Also, α_{1s} is a scaling parameter that depends on the SWNT nanotube radius r_{NT} via $\ln(\alpha_{1s}) - \Psi(1-\alpha_{1s}) - (2\alpha_{1s})^{-1} \equiv \ln(r_{\mathrm{NT}}) - 2\Psi(1)$ where Ψ is the digamma function [23]. For the (6,5) and (7,5) SWNTs studied here, we have $r_{\mathrm{NT}} \simeq 0.4$ nm which entails $\alpha_{1s} = 0.33$, and $\mu \simeq 0.067$ from interpolated carrier effective masses [24]. The scale and shape of the resulting exciton wavefunctions are shown in Fig. 5.4(a). For this, the permittivity which depends on the local dielectric environment was adjusted to $\epsilon = 6$ to reproduce the intra-excitonic splitting $E_{2p} - E_{1s} \simeq 0.2\ eV$ from the experiment, which corresponds to a binding energy of 233 meV.

With the above wavefunctions, we obtain the $1s$-$2p$ intra-excitonic oscillator strength of quasi-1D excitons in SWNTs

$$f_{1s\to2p} \equiv \frac{128\,\mu\,a^2_B\alpha^5_{1s}}{\hbar^2B_{1s}}(E_{2p}-E_{1s}) \times\left(\int_0^\infty s^3e^{-s(1+\alpha_{1s})}U(1-\alpha_{1s},2,2s)ds\right)^2 \tag{5.2}$$

For our specific parameters, $f_{1s\to2p} = 0.41$. Transitions into higher bound np levels ($n > 2$) were also calculated but are very weak and add less than 15% in spectral weight. The *spectrally-integrated* absorption cross section is then determined as $\sigma^{\mathrm{Int}}_{1s\to2p} = 2\pi^2e^2/(4\pi\epsilon_0\,\mu c\,n)\times f_{1s\to2p} = 4.4\times10^{-13}$ cm^2 meV, where $n = 1.5$ is the polymer refractive index. Spreading this absorption across ≈100 meV results in an estimated $1s$-$2p$ intra-excitonic cross section of $\sigma_{1s\to2p} \simeq 4.4\times10^{-15}$ cm^2, in very close agreement with our experiment. We

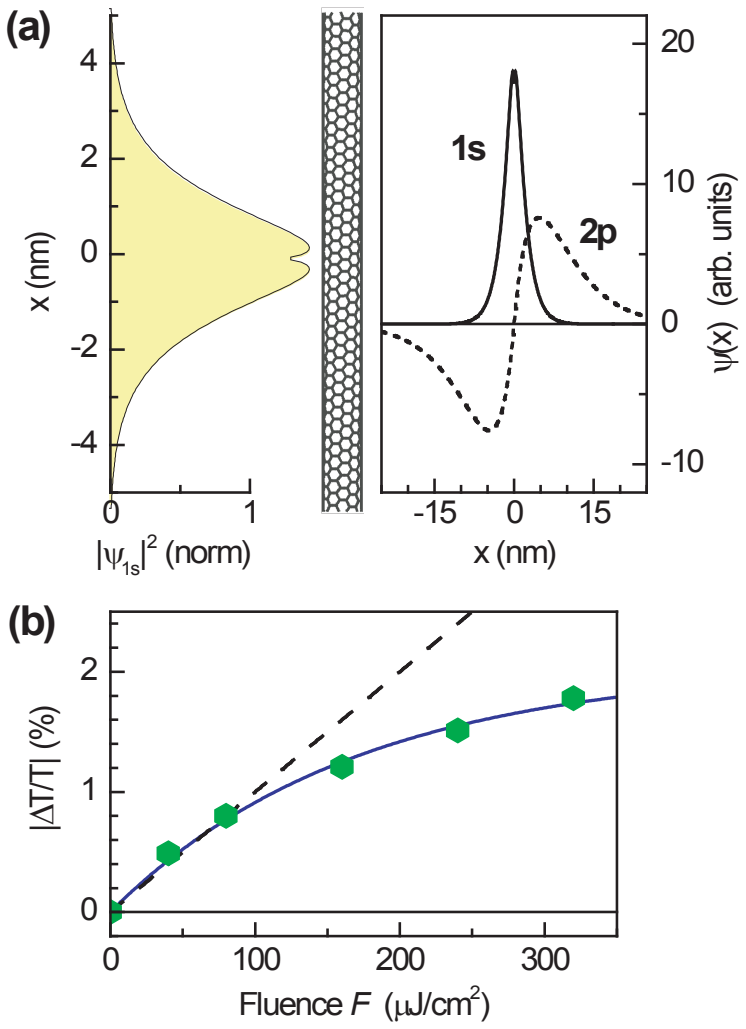

Figure 5.4. (a) Squared wavefunction amplitude $|\psi_{1s}(x)|^2$ compared to the (6,5) SWNT scale (left), and bare $1s$ and $2p$ wavefunctions (right). (b) pump fluence dependence of the initial mid-IR transmission change (dots) after resonant (6,5) E_{22} excitation. Solid line: model explained in the text, dashed line: linear scaling (guide to the eyes).

note that full modeling of the observed, asymmetric mid-IR intra-excitonic line shape in Fig. 2 is beyond the scope of the Wannier-exciton model. However, the above illustrates a general consistency between the observed mid-IR signal amplitude and the quasi-1D $1s$-$2p$ intra-excitonic cross section, motivating more sophisticated theory to calculate bound-bound and bound-continuum spectra with chirality-specific SWNT wave functions.

The transient mid-IR absorption represents a strong oscillator comparable to the interband absorption. In the photoexcited state, this low-energy oscillator strength is derived via transfer from the interband exciton peaks, i.e. from E_{11} bleaching [10, 11]. As plotted in Fig. 5.4(b), with increasing excitation fluence, the mid-IR amplitude $|\triangle T/T|$ exhibits a distinctly nonlinear behavior. This finding is well described by a saturation model $\triangle T \propto 1 - e^{-F/F_s}$, shown as the solid line in Fig. 5.4(b) for $F_S = 170$ μJ/cm^2. This corresponds to a 1D saturation density $n_s = \sigma_{22}^{\text{eff}} \times F_s/\hbar\omega$, where σ_{22}^{eff} is the effective E_{22} absorption cross section per unit nanotube length. The cross section of (6,5) SWNTs was recently demonstrated as $\sigma_{22}^{||} \simeq 85$ nm$^2/\mu$m for light polarized parallel to the nanotube axis, such that $\sigma_{22}^{\text{eff}} = 1/3 \times \sigma_{22}^{||}$ [25]. This yields from our experiment a saturation density $n_S = 1.4 \times 10^6$ cm^{-1} corresponding to an average exciton spacing $d_{XX} \approx 7$ nm. The value is close to the saturation density extrapolated from E_{11} interband bleaching at lower densities [11], while surpassing the saturation of time-averaged PL by more than an order of magnitude [12]. The difference occurs since PL depends on density-dependent decay times that saturate at lower densities, while our study detects the initial pair density. For comparison, we consider phase-space filling (PSF), i.e. the increasing occupation of the constituent Fermion states of the exciton many-particle wavefunction [26]. The PSF density is given by $N_S^{\text{PSF}} = L \,/\, [\sum_k \psi_k |\psi_k|^2 / \psi(x=0)]$, where ψ_k are the Fourier coefficients of the exciton wavefunction $\psi(x)$, and L is the normalization length [11, 26, 27]. For our quasi-1D $1s$ exciton wavefunction [Fig. 5.4(a)] this yields $N_S^{\text{PSF}} = 2.5 \times 10^6$ cm^{-1}. Hence, the mid-IR response approaches yet remains somewhat below the limit imposed by phase space filling.

5.4 Summary of Mid-IR SWNT Response

In conclusion, intra-excitonic transitions are both a direct consequence and a measure of e-h correlations. The experiments reported here provide new insights into the chirality-specific femtosecond mid-IR response of electronic excitations in individualized SWNTs. A photo-induced absorption around 200 meV was observed, manifesting quasi-1D intra-excitonic transitions in close agreement with the calculated $1s$-$2p$ oscillator strength. The non-exponential kinetics and (6,5)/(7,5) chirality-specific enhancement of the transient mid-IR absorption further underscores its excitonic origin. We believe that the mid-IR probe, extended e.g. into the low-temperature or low-density limit, will provide a versatile spectroscopic tool to investigate bound quasi-1D e-h pairs and their internal electronic structure independent of interband symmetry.

5.5 References

[1] see e.g. M. S. Dresselhaus, G. Dresselhaus, R. Saito, and A. Jorio, Annu. Rev. Phys. Chem. **58**, 719 (2007).

[2] M. J. O'Connell *et al.*, Science **297**, 593 (2002).

[3] F. Wang, G. Dukovic, L. E. Brus, and T. F. Heinz, Science **308**, 838 (2005).

[4] J. Maultzsch *et al.*, Phys. Rev. B **72** 241402 (2005).

[5] Y.-Z. Ma *et al.*, in: *Carbon Nanotubes*, edited by A. Jorio, G. Dresselhaus, and M. S. Dresselhaus, Topics Appl. Physics **111**, 321 (Springer Verlag, Berlin, 2008).

[6] J. Jiang *et al.*, Phys. Rev. B **75** 035407 (2007); E. B. Barros *et al.*, Phys. Rev. B **73**, 241406 (2006).

[7] T. Ideguchi, K. Yoshioka, A. Mysyrowicz, and M. Kuwata-Gonokami, Phys. Rev. Lett. **100**, 233001 (2008).

[8] R. A. Kaindl *et al.*, Nature **423**, 734 (2003); R. A. Kaindl *et al.*, Phys. Rev. B **79**, 045320 (2009).

[9] Y.-Z. Ma *et al.*, J. Chem. Phys. **120**, 3368 (2004); Y.-Z. Ma et al., Phys. Rev. Lett. **94**, 157402 (2005).

[10] F. Wang *et al.*, Phys. Rev. B **70**, 241403(R) (2004); G. N. Ostojic *et al.*, Phys. Rev. Lett. **94**, 097401 (2005); O. J. Korovyanko *et al.*, Phys. Rev. Lett. **92**, 017403 (2004).

[11] L. Luer *et al.*, Nature Phys. **5**, 54 (2009).

[12] Y. Murakami and J. Kono, Phys. Rev. Lett. **102**, 037401 (2009).

[13] L. Perfetti *et al.*, Phys. Rev. Lett. **96**, 027401 (2006); T. Kampfrath *et al.*, Phys. Rev. Lett. **101**, 267403 (2008).

[14] M. C. Beard, J. L. Blackburn, and M. J. Heben, Nano. Lett. **8**, 4238 (2008).

[15] H. Zhao *et al.*, Phys. Rev. B **73**, 075403 (2006).

[16] L. Luer et al., Phys. Rev. B **80**, 205411 (2009).

[17] The probe was spectrally resolved (10 nm resolution) with small photoinduced changes sampled by 500 Hz synchronous chopping coupled to shot-by-shot gated integration. Pump and probe diameters were ≈400 μm and 200 μm (full width at half maximum), respectively.

[18] S. M. Bachilo *et al.*, J. Am. Chem. Soc. **125**, 11186 (2003).

[19] O. N. Torrens, D. E. Milkie, M. Zheng, and J. M. Kikkawa, Nano Lett. **6**, 2864 (2006).

[20] Differences in this splitting can arise from the dissimilar embedding matrices i.e. dielectric constants.

[21] It appears due to a downward step at exactly the 178 meV vibrational resonance in the PE matrix.

[22] A. Jorio *et al*, Phys. Rev. B **72**, 075207 (2005).

[23] H. D. Cornean, T. G. Pedersen, and B. Ricaud, Cont. Math. **447**, 45 (2007).

[24] A. Jorio *et al.*, Phys. Rev. B **71**, 075401 (2005).

[25] S. Berciaud, L. Cognet, and B. Lounis, Phys. Rev. Lett. **101**, 077402 (2008).

[26] S. Schmittrink, D. S. Chemla, and D. A. B. Miller, Phys. Rev. B **32**, 6601 (1985).

[27] B. I. Greene, J. Orenstein, R. R. Millard, and L. R. Williams, Phys. Rev. Lett. **58**, 2750 (1987).

Chapter 6

Multi-Exciton Population Dynamics

Femtosecond transient absorption kinetics are obtained on semiconducting (6,5) single and (7,5)/(17,6) double-walled carbon nanotubes, and the relaxation dynamics are modeled with explicit inclusion of both phase space filling restrictions and nonlinear annihilation of coherent excitons. To holistically simulate the kinetics in all time regimes, both a continuum and a stochastic model of population probabilities are employed. The amplitude of E_{11} transient bleach signal is found to scale linearly with photon fluence for E_{22} excitation, but strikingly only with the square root for direct E_{11} excitation. Simulation of the peak amplitude dependence for both the E_{22} and E_{11} excitation, suggests the contrasting intensity dependence can be understood in terms of nonlinear annihilation of coherent excitons, and phase space filling at high photon fluences. Analysis of the kinetic decay curves, support a predominately diffusion-controlled mechanism for exciton-exciton annihilation at room temperature. However, at intermediate delays times ($<\tilde{}$1 ps) or at low temperatures ($<\tilde{}$200 K) multiexciton states of coherently delocalized excitons also contributes strongly to the E_{11} relaxation kinetics of (6,5) carbon nanotubes. While both the continuum and stochastic models could acceptably reproduce the kinetics and peak amplitude intensity dependences observed, markedly different branching ratios between the population decay pathways, and phase space filling restrictions are obtained. The stochastic model put forward highlights the importance of including contributions from coherent multiexciton states in modeling the optical relaxation dynamics of semiconducting single-walled carbon nanotubes.

6.1 Introduction

Depending on the strength of the Coulombic interaction, the elementary excitation in solid states can be either a neutral exciton, or a pair of electrons (e) and holes (h) with a weak mutual correlation.[1] A quantitative measure of the Coulombic interaction is the exciton

binding energy (E_b), defined as the energy difference between the *e-h* continuum and the lowest bound exciton state. As deduced experimentally[2,3] and from *ab initio* calculations[4,5], the E_b value determined for semiconducting single-walled carbon nanotubes (SWNTs) typically ranges from 0.3 to 1 eV, permitting assignment of the dominant absorption/emission spectral bands to excitonic transitions. Such large E_b values are possible because of greatly enhanced electron-hole Coulombic interactions owing to quasi-one-dimensional (quasi-1-D) confinement in SWNTs.[6]

Experimental studies of the excitation dynamics in the SWNT employing ultrafast transient absorption[7-10] and time-resolved fluorescence techniques with sub-100 femtosecond time resolution[11,12] reveal a very fast kinetic decay component on the time scale of a few hundreds of femtoseconds. Through analysis of both the non-exponential kinetic decay component and the dependence of the corresponding amplitude on excitation intensity it was concluded that exciton-exciton annihilation in semiconducting SWNTs is a dominant relaxation process.[10,11,13,14] This nonlinear annihilation process involves a pair of excitons whose interaction lead to rapid relaxation of one exciton whereas the other be promoted to a doubly excited-state $E_{nn} \cong 2E_{11}$ owing to momentum and energy conservation (see Fig. b).

For an exciton pair to annihilate they must first occupy the same physical space. This required overlap can occur from either from the delocalization of excitons or after diffusional motion along the tube length.[12,13] The energy and momentum of the annihilated exciton pair must also be conserved, requiring the newly created exciton to occupy a transient state $E_{nn}(=2E_{11})$ just above the E_{22} transition (see Fig. 6.1b). In general, these requirements make annihilation an inefficient process for most solid state systems. However, for quasi-1D systems like SWNTs, confinement inherently enhances the exciton-exciton scattering, inducing annihilation among either delocalized excitons or after 1D exciton diffusional motion. Further enhancing annihilation effects, the requirement of momentum conservation is thought to be relaxed because the translational symmetry along the tube is easily disrupted for nanoscale systems. For these reasons, it is perhaps not surprising that the exciton-exciton annihilation rate, γ(t) for a given excitation fluence is significantly greater than in comparable bulk semiconductors. While exciton-exciton annihilation in SWNTs is a well established process, a more general kinetic model is desirable to explicitly treat the dynamics of multiple exciton states associated with the E_{11} and E_{22} transitions. Such a kinetic model may provide important insight into how multiple exciton states are involved with annihilation and impact ionization processes in SWNTs, which are fundamental to such recently reported practical applications as the development highly-efficient SWNT photodiode devices [34].

The exciton energy, $E^n_{cv}(K_{CM})$, in semiconducting SWNTs is typically characterized by the translation wave number K_{CM}, which satisfies the translation symmetry of the center of mass of the *e-h* pair, and the quantum number n corresponding to their relative motion ($1s$, $2p$, ...states of the Hydrogen type spectrum).[1] The subscripts c and v refer to the corresponding van Hove singularities in the conduction and valence bands, respectively.[4,5] These exciton states are the eigen states of electronic excitation, which are qualify the excited states delocalized over the system under consideration. Thus, any exciton evolution should be determined by their interactions with phonons, impurities or by scattering with

other excitons resulting in exciton-exciton annihilation. A theoretical description of an exciton-exciton annihilation process would then define the transitions between the bands of the multiexciton manifolds resonantly coupled with other excited states, which decay by subsequent linear relaxation due to electron-phonon coupling.[13]

The evolution of the occupation probability of these multiexciton states and the annihilation rate constant are the main characteristics of a stochastic model. According to this description, exciton-exciton annihilation manifests itself as long as more than one exciton is present in the system but switches off when a single exciton is finally left.[15,16] Such a scheme is well suited for describing the exciton decay kinetics at the initial times, shorter than 10 ps.[10,11,14] On the other hand, it has been also demonstrated that the exciton decay kinetics on a longer timescale (up to 1 ns) follows the diffusion-controlled behavior.[17,18] In addition, calculations based on a diffusion-controlled exciton-exciton annihilation model enabled to reproduce the saturation behavior of photoluminescence emission with increasing excitation intensity.[19,20] Moreover, a recent study of the intensity-dependent exciton decay further suggested that exciton-exciton annihilation in semiconducting SWNTs is an inefficient process.[21] Apparently, these conclusions differ greatly from the conclusions derived from the earlier studies[7-12], and are also inconsistent with the conclusions drawn from recent four-wave-mixing spectroscopic experiments at different excitation intensities.[22,23] In order to provide clarity to these conflicting studies, analyses of the exciton decay kinetics at different timescales and at different excitation intensities will be presented in this paper.

6.2 Materials and Methods

The SWNT sample used in this study is highly enriched in a single semiconducting tube type, the (6, 5) nanotube, which was isolated through density-gradient ultracentrifugation [24]. The obtained aqueous solution contains individually separated nanotubes dispersed with sodium cholate as a surfactant. The experiments were performed directly on the aqueous suspensions in a 200 μm path length cell, or on a thin composite film fabricated by mixing the solution with appropriate amount of water soluble polyvinylpyrrolidone (PVP) polymer. Use of polymers films enabled low temperatures measurements, by placing the polymer in a temperature controlled Janis cryostat which operates under continuous liquid helium flow. Linear absorption and steady-state fluorescence emission spectra confirm that the nanotubes remain individualized and of optical quality after being transferred from the solution to the solid film. The double-walled carbon nanotubes (DWNTs) were prepared by chemical vapor deposition in combination with thermal oxidation to greatly reduce the presence of SWNTs[25]. The purified DWNTs were dispersed individually in D_2O solution using sodium dodecyl sulfate (SDS) as a surfactant, and have $\sim$90% content of double-walled carbon nanotubes. A quartz sample cell of 1 mm path length was used for measurements on DWNT samples. Here, only the results measured on the (7, 5) tube, the inner tube of a dominant DWNT species in the sample, will be presented.

The femtosecond transient absorption setup employed here has been described extensively

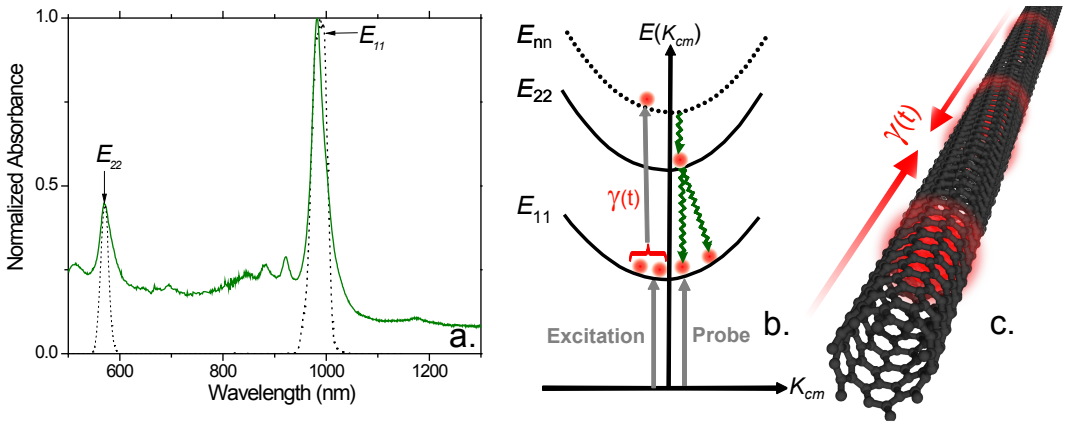

Figure 6.1. (a) Linear absorption spectrum of the (6, 5) tube-enriched aqueous solution and laser pulse spectra (dotted line) resonant with either its E_{22} or E_{11} transitions. (b) Schematic energy level diagram of a semiconducting SWNT with a dominant relaxation pathway mediated by exciton-exciton annihilation (with a rate constant γ(t)), shown for the direct E_{11} excitation case. c. Delocalized excitons can annihilate either from mutual overlap or after diffusion-controlled motion along the tube length (indicated by arrows).

elsewhere [13, 26]. In short, the light source was an optical parametric amplifier pumped by a 250 kHz Ti: sapphire regenerative amplifier, which enables resonant excitation at either the E_{11} or E_{22} transitions of the selected nanotube species with 60 and 45 fs laser pulses respectively. The pump beam was focused to a spot size of 161 μm at the sample. A single-filament white-light continuum served as the probe beam, and selection of the probe wavelength was realized using a single-grating monochromator with a typical band-width of 8 nm. The detection scheme consists of a photo-diode and a lock-in amplifier. The polarization of the pump beam was set to the magic angle (54.7^0) with respect to the probe beam. A combination of a waveplate and polarizer was used to control the intensity of the pump laser beam.

6.3 Results

6.3.1 Experimental observations

Fig. 6.1 shows the linear absorption spectrum of the (6, 5) tube-enriched, individualized SWNTs in aqueous solution. The two bands peaking at 982 and 570 nm correspond to the E_{11} and E_{22} excitonic transitions of the (6, 5) tube type, respectively. Upon resonant excitation of these bands with ultrashort laser pulses (see the dotted lines in Fig. 1 for the laser pulse spectra), a series of transient absorption kinetics were probed at 988 nm under different pump intensities. As observed previously, the transient absorption signals ($\Delta OD(t)$) are dominated by photobleaching and stimulated emission.[27] Also, in consistent with previous works, the kinetic profiles are, after normalizing at the signal maxima (ΔOD_0), largely invariant to the excitation intensity for each chosen pump wavelength.[10] However, the amplitudes of the signal maxima show strikingly different dependence on laser pump intensity for the E_{11} and E_{22} pump cases as shown in Fig. 6.2. A linear dependence of the amplitude on the intensity of the E_{22} excitation was found, whereas for the E_{11} excitation the corresponding amplitude scales linearly with the square root of the intensity. In both cases, the amplitudes of signal maxima exhibit saturation behavior when excitation intensity is greater than $\sim 1.4\times10^{13}$ photons/cm^2. The same intensity dependence was also found for the SWNT/PVP composite film (see the open circles in Fig. 6.2). In this case, the absence of the saturation behavior due to high sample optical density makes the different intensity dependence found for the E_{11} and E_{22} excitation even more distinct.

Quantitative data analysis employing a least square deconvolution fitting algorithm with explicit consideration of the finite temporal response shows that all the decay kinetics can be satisfactorily described with a model function consisting of three or four exponents. The component with the longest lifetime typically has a timescale of few hundreds picoseconds, which characterizes the relaxation associated with the last remaining exciton in the system. The kinetics probed at room temperature for the E_{11} transition of the (6, 5) tube upon excitation of its E_{22} state exhibits a slower initial decay than the corresponding kinetics measured with direct E_{11} excitation (Fig. 6.3a). In particular, the two fast decay components

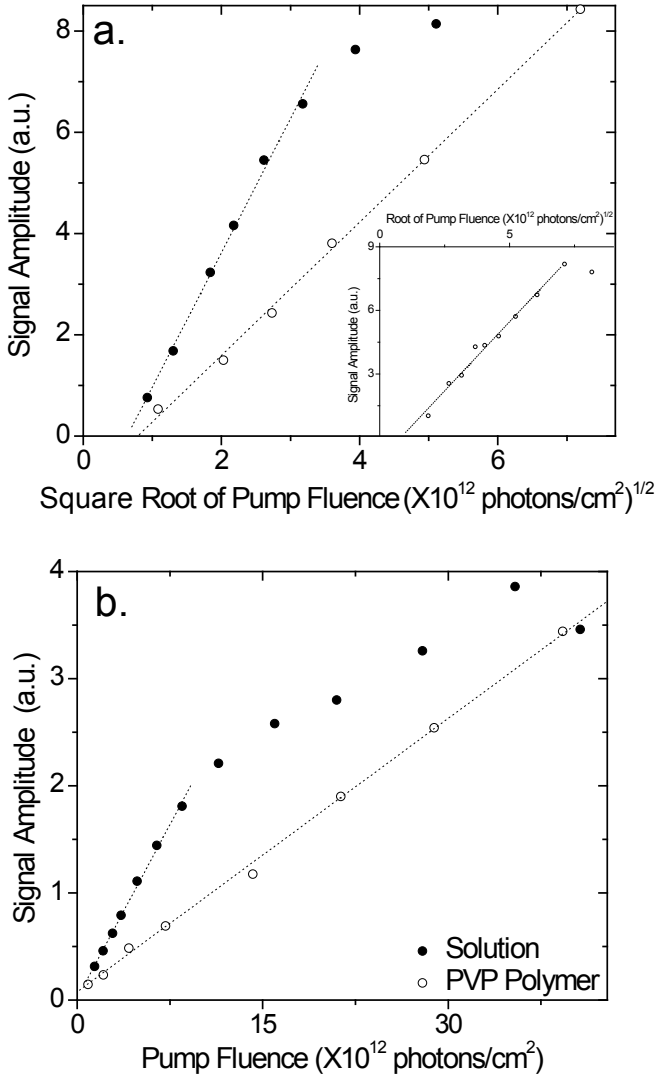

Figure 6.2. (a) Plots of the maximal transient absorption signals measured at 988 nm as a function of the square root of pump fluence for the (6, 5) tube species upon E_{11} excitation. The samples were either a polymer-SWNT composite film (open circles) or an aqueous solution (filled circles). (b) Plots of the maximal transient absorption signals measured at 988 nm as a function of the pump fluence for the (6, 5) tube species upon E_{22} excitation.

have considerably different decay timescales (and relative amplitude), which are 122 fs (55%) and 1.3 ps (29%) for the E_{11} excitation, and 350 fs (57%) and 2.4 ps (31%) for the E_{22} excitation. In contrast, the two slow decay components appear similar for the two pump scenarios, with decay times of ∼22 ps and ∼300 ps, respectively.

The kinetics measured at low temperatures until 4.4 K show a similar trend with the change of pump intensity as observed at 292 K (in Fig. 6.2) for both the E_{22} and E_{11} pump scenarios (data not shown). A representative set of transient absorption profiles measured at 110 K is plotted in Fig. 6.3b, where a remarkably faster decay is seen for the E_{11} pump case than the one obtained with the E_{22} pump. The lifetimes (relative amplitudes) determined from deconvolution fitting are 140 fs (63%), 1.5 ps (29%), and 19 ps (8%) for the $E11$ excitation data, whereas corresponding results are 310 fs (52%), 2.1 ps (28%), and 22.4 ps (20%) for the the E_{22} excitation case.

The need for multiple (three or four) exponential components to satisfactorily fit the transient absorption kinetics is partially due to occurrence of nonlinear exciton-exciton annihilation.[13] A qualitative justification can be obtained by assuming that the exciton-exciton annihilation process dominates the kinetic decay, and in this case a simple rate equation for exciton density $n(t)$ can be written as: $\frac{dn(t)}{dt} = -\frac{1}{2}\gamma t^{d/2-1} n^2(t)$, where g is the time-independent annihilation rate, and d is the dimensionality.11 As the transient absorption signal at a given delay time t, $\Delta OD(t)$, is proportional to $n(t)$, for a 1-D system ($d = 1$) the solution of the rate equation suggests a linear relation when the transient absorption signal is plotted in the form of $(\Delta OD_0/\Delta OD(t) - 1)^2$ versus delay time t (ΔOD_0 is the signal amplitude at $t = 0$). As shown in Fig. 6.3c, a good linear relation is indeed seen for the data collected with E_{11} excitation when t is approximately greater than 1 ps (green circles). This linear behavior suggests diffusion-limited annihilation in 1-D system. In comparison, the data obtained with E_{22} pump exhibit relatively large deviation from linearity (filled black circles), indicating possibly substantial contribution from linear relaxation to ground-state. Upon cooling, the data collected with the E_{22} pump at 110 K again show good linear relation in the plot of $(\Delta OD_0/\Delta OD(t) - 1)^2$ versus delay time within the experimental uncertainty (see Fig. 6.3d, black circles). In stark contrast, the result obtained with E_{11} pump at the same temperature exhibits an excellent linear relation between $\Delta OD_0/\Delta OD(t) - 1$ and delay time t (Fig. 3d, green circles). The latter linear relation can be derived from the same rate equation but for $d = 2$, and a resultant time-independent annihilation rate constant. As discussed in our earlier work, this time-independent annihilation rate arises from a rapid annihilation process involving coherently delocalized excitons.[13,28]

The difference between the kinetics probed at the E_{11} state upon excitation of the E_{11} and E_{22} states at room temperature is much more pronounced for the (7, 5) inner tube of the DWNT species (see Fig. 6.4a for the DWNT data). Here the dominant and fastest decay component has a lifetime of 110 fs for E_{11} pump, whereas it is 800 fs for the E_{22} pump. It is also noteworthy that the kinetics probed for the (7, 5) inner tube exhibits a substantially slower decay than the decay of the (7, 5) SWNT type measured under a comparable excitation intensity (see the black trace in Fig. 6.4a for example). However, our measurements under different excitation intensities for the (7, 5) inner tube of the DWNT species show linear dependence of the maximum transient absorption amplitude on the intensity of the E_{22}

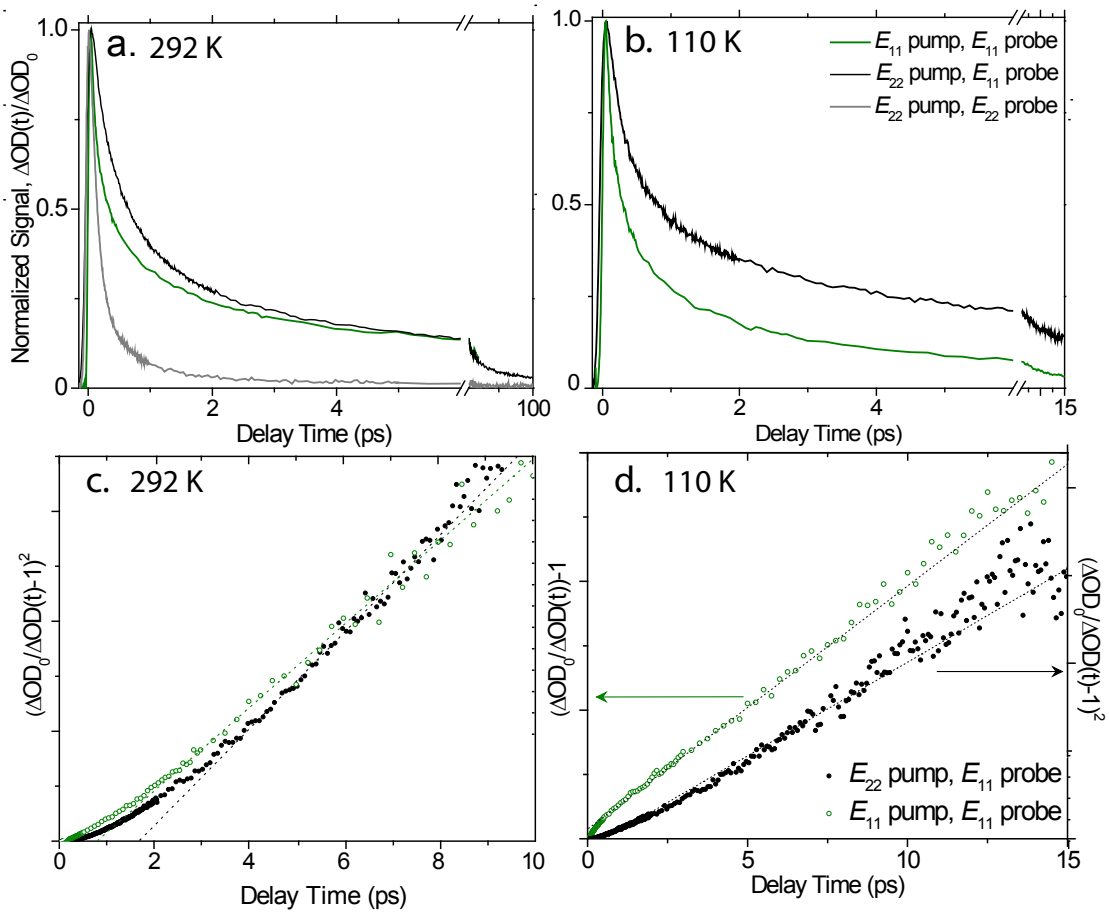

Figure 6.3. Transient absorption kinetics measured upon resonant excitation of the E_{11} state at 988 nm and the E_{22} state at 570 nm, respectively, for the (6,5) tube species. (a) Data acquired at 292 K for an aqueous solution sample, and (b) at 110 K for a PVP polymer composite film. (c) Plotting the same data shown in a as $(\Delta OD_0/\Delta OD(t) - 1)^2$ versus delay time. The dashed lines are linear fits to the majority of data points. (d) Plotting the same data shown in b as $\Delta OD_0/\Delta OD(t) - 1$ (left axis) or $(\Delta OD_0/\Delta OD(t) - 1)^2$ (right axis) versus delay time. Again, the dashed lines are linear fits to the majority of data points.

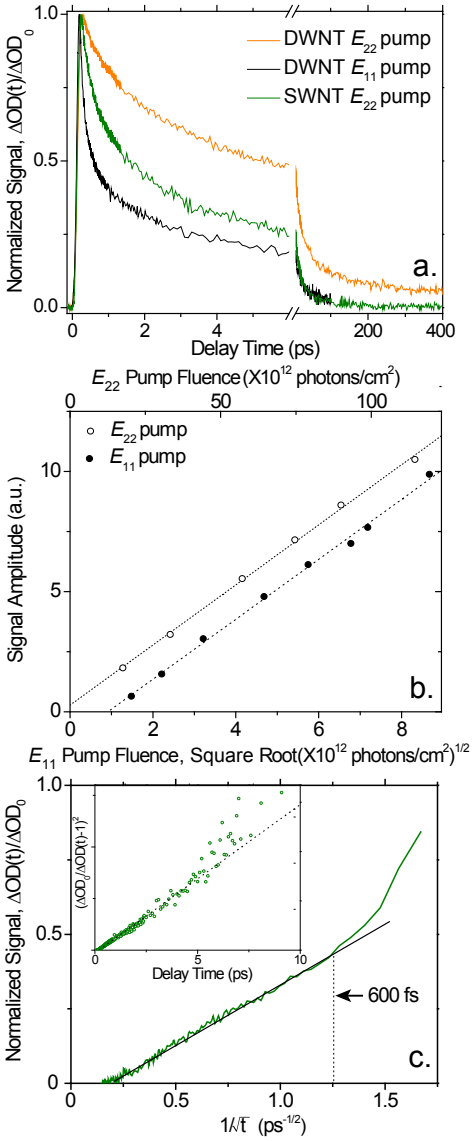

Figure 6.4. (a) Comparison of transient absorption kinetics obtained for the (7, 5) inner tube of a dominant DWNTs species upon E_{22} (orange) and E_{11} (black) excitation with the one measured for the (7, 5) SWNT (dark green) following excitation of its E22 state. (b) Plot of the peak amplitudes obtained upon the E_{11} (filled circles) or E_{22} (open circles) excitation for the (7, 5) inner tube of the dominant DWNT species as a function of the square root of pump fluence or pump fluence, respectively. (c) The data measured for the (7, 5) inner tube upon E_{11} excitation is plotted as a function of inverse of the square root of delay time. The inset shows the same data plotted as $(\Delta OD_0/\Delta OD(t) - 1)^2$ versus delay time.

excitation (Fig. 6.4b, open circles), whereas a square root dependence on the intensity of E_{11} excitation (Fig. 6.4b, filled circles). This observation is the same as what found the SWNTs such as the (6, 5) tube type as shown in Fig. 6.2, suggesting the observed distinct intensity dependence may be generic phenomenon for semiconducting nanotubes. Moreover, a plot of the kinetics measured for the (7, 5) inner tube upon its E_{11} excitation (black line in Fig. 4a) in the form of $(\Delta OD_0/\Delta OD(t) - 1)^2$ vs. delay time t gives rise to good linear relationship for the first a few picoseconds (see Fig. 6.4c, inset). As for the (6, 5) tube type (see Fig. 6.3c, d), this linear relation again suggests occurrence of diffusion-limited annihilation. However, at short times deviation from the linearity is again noticed, which can be more clearly seen from an alternative plot of the same data as a function of the inverse of the square root of delay time, $1/\sqrt{t}$ (see Fig. 6.4c). The initial decay within the first 600 fs does not follow the linear dependence (indication of diffusion-controlled annihilation) seen at longer delay times.

6.4 Theoretical description of exciton-exciton annihilation

The key findings of out transient absorption measurements on the (6, 5) SWNT species and the (7, 5) inner tube of a dominant DWNT type are as follows. First, we found that the initial decay of the kinetics probed at the E_{11} state of the (6, 5) tube species upon excitation of its corresponding E_{22} transition is clearly slower than that measured with its direct E_{11} excitation (see Fig. 6.3a,b), and this difference appears much more pronounced for the (7, 5) inner tube type (Fig. 6.4a). Second, the maximal signal amplitudes scale linearly with the intensity of the E_{22} excitation, but with the square root of the E11 excitation intensity (see Figs. 6.2 and 6.4b). Our qualitative analysis further shows occurrence of a diffusion-limited annihilation process except for the data collected at 110 K and with a direct E_{11} excitation (Fig. 6.3d, dark green circles). In order to gain insights into these strikingly different temporal and intensity behaviour in response to the different excitonic states initially excited, we will develop detailed theoretical description with explicit consideration of exciton-exciton annihilation.

6.4.1 Continuum model.

Exciton-exciton annihilation (Auger recombination) is typically described in terms of a simple scheme, which is well justified for extended systems [10, 13, 29]. The time evolution

of excitons in this approach can be determined by the following kinetic equations:

$$\begin{aligned}
\frac{dn_1}{dt} &= G_1(t)f_1(n_1) - Kn_1 - \gamma(t)n_1^2 + k_{21}f_1(n_1)n_2, \\
\frac{dn_2}{dt} &= G_2(t)f_2(n_2) + k_{n2}f_2(n_2)n_n - k_{21}f_1(n_1)n_2, \\
\frac{dn_n}{dt} &= \tfrac{1}{2}\gamma(t)n_1^2 - k_{n2}n_n f_2(n_2),
\end{aligned} \tag{6.1}$$

where n_i is the exciton concentration populating the i-th exciton state (the E_{ii} state), $G_i(t)$ is the generation function of the pump pulse (depending on the resonance condition corresponding to the E_{ii} state), $f_i(t) = 1 - \frac{n_i}{N_i}$ is the phase space-filling factor (N_i determines the maximal amount of the excitations, which could be generated in the i-th state), $\gamma(t)$ is the rate of exciton-exciton annihilation (on the E_{11} exciton state), and the linear relaxation terms determine the dominant relaxation pathways. K is the relaxation rate for the E_{11} exciton, k_{21} determines the rate of the relaxation from the E_{22} state to the E_{11} state. Here the E_{nn} state corresponds to the excited state, which is involved in the process of exciton-exciton annihilation ($E_{nn} \cong 2E_{11}$ shown in Fig. 6.1b), and k_{n2} determines the rate of the exciton transfer between the corresponding states. In the case of the short pump pulses (when the pump pulse duration is shorter than $1/k_{21}$ and $1/k_{n2}$ the excitation intensity dependence of the initial populations will be different for different pump conditions. If the pump pulse is in resonance with the E_{11} exciton state, then $G_2(t) = 0$, and if also the time dependence of the annihilation rate can be discarded, at high excitation conditions (when the nonlinear exciton relaxation due to exciton-exciton annihilation is dominating) but not so high that the phase filling starts manifest itself, i.e. when $n_1 << N_1$ is still fulfilled and, thus, $f_1(n_1) \approx 1$, from Eq. 6.1 it follows that:

$$n_1(0) = \sqrt{\frac{G_{1,max}}{\gamma}}, \tag{6.2}$$

where $G_{1,max}$ is the maximal value of the generation function. Due to the short pulse duration (in comparison with $1/k_{21}$ and $1/k_{n2}$ the E_{22} state is not populated at the initial times, i.e. $n_2(0) \approx 0$. In the opposite case, when the pump pulse is in resonance with the E_{22} exciton state, we have $G_1(t) = 0$, and then

$$n_2 \approx \frac{G_{2,max}}{k_{21}}, \tag{6.3}$$

while $n_1(0) \approx 0$. Here $G_{2,max}$ is the maximal value of the generation function.

The transient spectrum $\Delta A(t, \lambda)$ is defined by the exciton populations and, thus, can be given by [13, 27]:

$$\Delta A(t, \lambda) \propto \sum_i n_i(t)[\sigma_i^{ESA}(\lambda) - \sigma_i^{SE}(\lambda) - \sigma_0(\lambda)], \tag{6.4}$$

where $\sigma_0(\lambda)$ is the ground state absorption spectrum (λ is the wavelength of the probe pulse), $\sigma_i^{ESA}(\lambda)$ and $\sigma_i^{SE}(\lambda)$ are the cross-sections for excited state absorption and stimulated emission of the i-th excited state, respectively, $n_i(t)$ determines the time evolution of the i-th

excited state population according to Eq. 6.1 (i enumerates the exciton states populated by excitation pulses, relaxation from higher states and via exciton-exciton annihilation). Thus, by substituting Eq. 6.2 into Eq. 6.4 we will get that the transient bleaching amplitude should be proportional to $\sqrt{G_{1,max}}$, while by substituting Eq. 11.3 into Eq. 6.4 we will get the result proportional to $G_{2,max}$. This qualitatively is in line with the experimental dependences shown in Fig. 6.2.

Due to the finite rate k_{21} of the exciton relaxation from the E_{22} exciton state to the E_{11} state (in comparison with the pump pulse duration), the situation corresponding to the pumping conditions into the E_{22} exciton state can be considered in a similar way as in the case when pumping into the E_{11} exciton state but with longer pulses. This should evidently slow down the excitation kinetics in accord to the experimental observations shown in Fig. 6.3.

The ground state bleaching should be proportional to $(n_1 + n_2)_{max}$, where the subscript indicates the maximal value, as follows from Eq. 6.4. For modeling let us assume the Gaussian pump pulse with amplitude A and FWHM duration of 50 fs. Also taking typical values such as $k_{21}^{-1} \approx 50$ fs [30], $\gamma^{-1} \approx 800$ fs [12] (the latter value corresponds to normalization of the amount of excitons per nanotube), $K^{-1} \approx 10$ ps, and also assuming that $k_{n2} > k_{21}$, we cannot obtain the intensity dependence as shown in Fig. 6.2 (to compare the pulse duration of the order of tens of fs with k_{21}^{-1}. At high intensities of excitation usually $n_{2max} > n_{1max}$ independent of either E_{11} or E_{22} state is initially excited. Furthermore, in both cases the amplitude of the bleaching signal always follows almost linear intensity dependence, and change of the parameters used in our calculations does not alter this result. This clear discrepancy from the experimental data can be improved by modifying the annihilation kinetic scheme described by Eq. 6.1 through assuming existence of two pathways of the exciton relaxation from the $E_{nn} \cong 2E_{11}$ state: one via population of the E_{22} exciton state and another directly to the E_{11} exciton state bypassing the E_{22} exciton state. Such branching scheme for the exciton relaxation from the $E_{nn} \cong 2E_{11}$ state in combination with an assumption of similarly high relaxation rates can be described by slightly modifying kinetic equations given by Eq. 6.1:

$$\begin{aligned} \frac{dn_1}{dt} &= G_1(t)f_1(n_1) - Kn_1 - \tfrac{1}{2}(1+\alpha)\gamma(t)n_1^2 + k_{21}f_1(n_1)n_2, \\ \frac{dn_2}{dt} &= G_2(t)f_2(n_2) + \tfrac{1}{2}\alpha\gamma(t)n_1^2 - k_{21}f_1(n_1)n_2, \end{aligned} \tag{6.5}$$

where α determines the branching ratio. The intensity dependence of the $(n_1 + n_2)_{max}$ value obtained by neglecting the phase-filling effects and assuming relatively small α values, e.g. $\alpha = 0.1$, resembles the experimental observations for both excitation conditions (Fig. 6.5a). However, the same set of parameters produces much faster decay behavior than the kinetics observed experimentally as shown in Figure 6.3. Better agreement at least for the initial delay times can be obtained assuming that the relaxation rate, k_{21}, is up to 10 times slower. The best fit of the experimental kinetics measured at 292 K is obtained for the following parameters, which are treated to be variable: $\alpha = 0.4$, $\gamma^{-1} = 1040$ fs, $k_{21}^{-1} = 480$ fs (Fig. 6.5b). An excitation intensity of $G_{max} \equiv A = 8$ is used for our calculations. Similarly, for the kinetics measured at 110 K we get $\alpha = 0.5$, $\gamma^{-1} = 3760$ fs and $k_{21}^{-1} = 410$ fs for the same excitation intensity (Fig. 6.5c). We further found that an increase of the A value

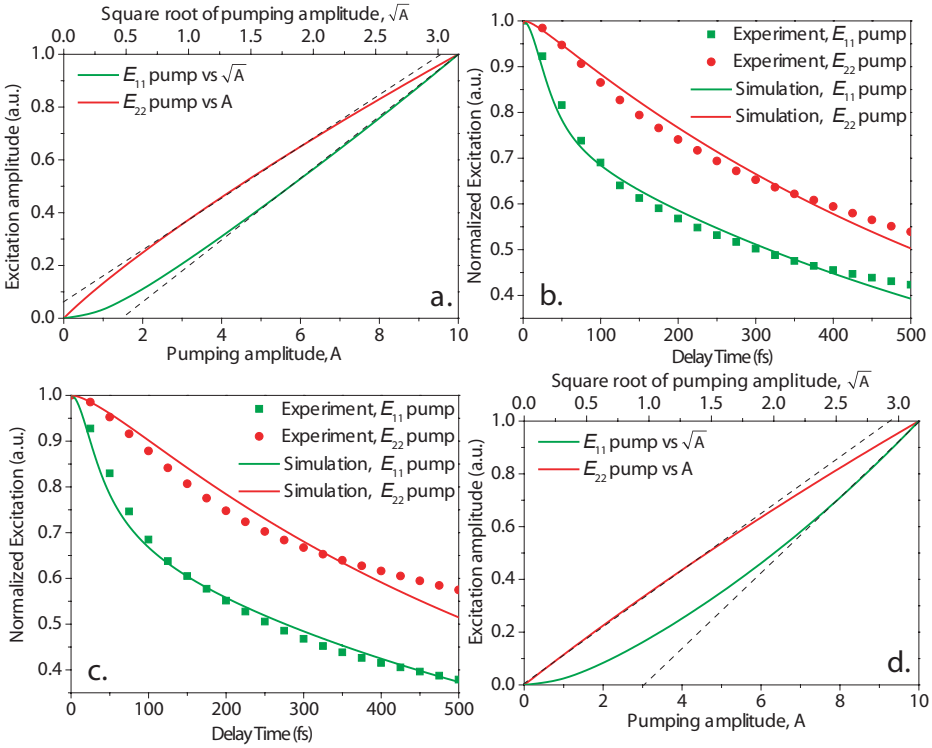

Figure 6.5. a. The dependence of $(n_1+n_2)_{max}$ calculated according to the continuum model (Eq. 6.5) with typical values $\gamma^{-1} = 800$ fs, $k_{21}^{-1} = 50$ fs, and assuming $\alpha = 0.1$ on the pump pulse intensity Ain the case of pumping to the E_{22} band (red curve, lower x-axis) and of its square root $\sqrt{A}$ in the case of pumping to the E_{11} band (green curve, upper x-axis). b. The best fit for the both experimental kinetics measured at room temperature (292 K) upon excitation of the E_{11} or E_{22} band (green and red curves, respectively) is obtained using the following parameters: $\alpha = 0.4$, $\gamma^{-1} =$ 1040 fs, $k_{21}^{-1} = 480$ fs, and an amplitude of the generation function $A \equiv G_{max} = 8$. c. The best fit for the corresponding kinetics measured at 110 K is obtained by assuming the same intensity of the generation function, A, and using the following parameters: $\alpha = 0.5$, $\gamma^{-1} = 3760$ fs, and $k_{21}^{-1} = 410$ fs. d. The dependence of the $(n_1 + n_2)_{max}$ on the pump pulse intensity Ain the case of the E_{22} excitation (red curve, lower x-axis) and on its square root $\sqrt{A}$ in the case of the E_{11} excitation (green curve, upper x-axis) calculated using the same set of parameters. It is almost the same for the kinetics measured at different temperatures.

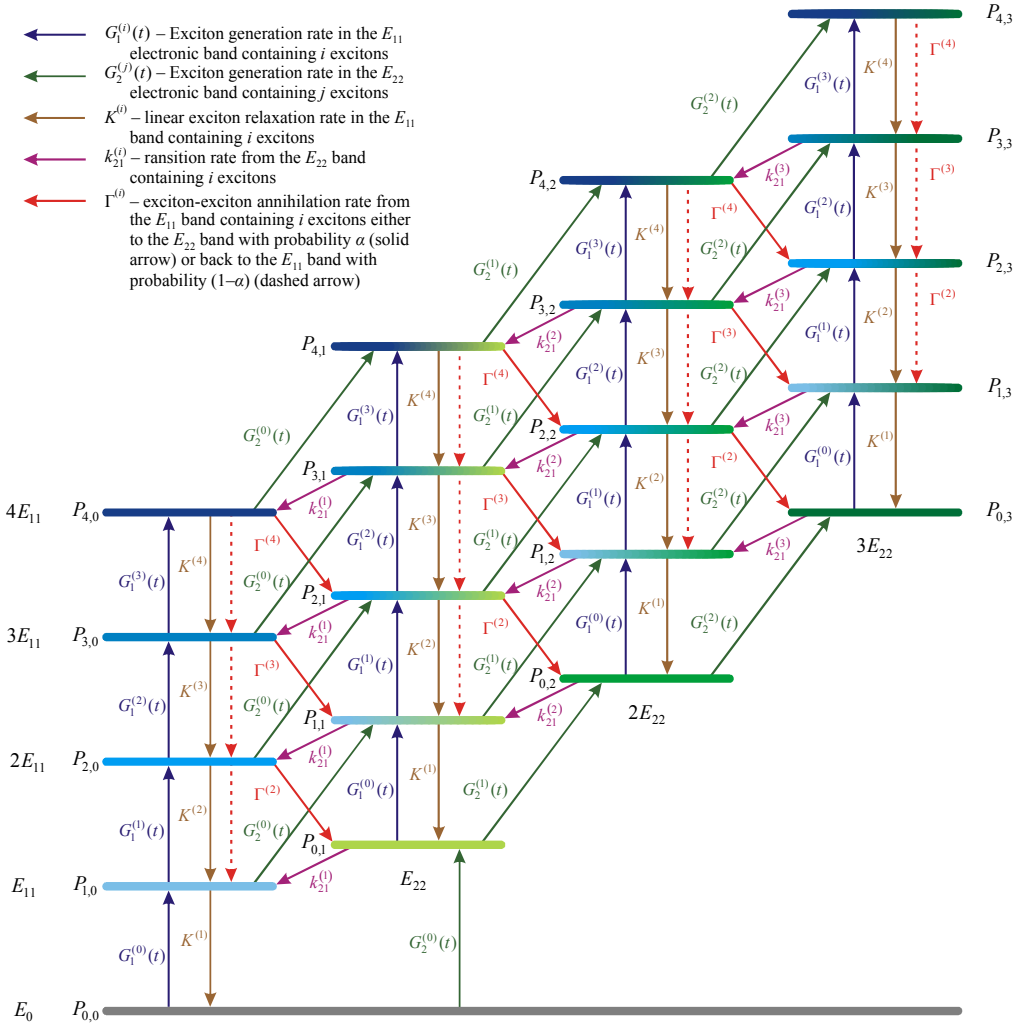

Figure 6.6. The kinetic scheme for the system with multiple exciton population of both E_{11} and E_{22} exciton states. The lowest energy level E_0 (grey bar) indicates the ground state. The population of the E_{11} exciton band is reflected in the upward direction with the corresponding energies of E_{11}, 2 E_{11}, 3 E_{11}, ... (shown up to 4 E_{11}), while the population of the E_{22} exciton band is indicated rightwards (with the corresponding energies of E_{22}, 2 E_{22}, ... (shown up to 3 E_{22})). In addition, the levels of the combined population corresponding to energies $E_{i,j} = i \cdot E_{11} + j \cdot E_{22}$ are also shown. The probabilities of the occupation of these energy levels are denoted as $P_{i,j}$, and the possible transition pathways between different states are indicated with arrows (for the labeling see the legend in the kinetic scheme). For clarity, the upper electronic band $E_{nn} \approx 2E_{11}$ involved in exciton-exciton annihilation is not shown since the excitons relax form this state almost instantaneously (comparing with other characteristic rates in this model) either to the E_{22} or back to the E_{11} band.

from 1 to 30 leads to almost linear variation of the corresponding $1/\gamma$ value with A. The intensity dependences of the $(n_1 + n_2)_{max}$ calculated using the same sets of parameters are very similar for both cases and qualitatively agree to the experimental observations as shown in Fig. 6.5d.

The calculated kinetics, however, start to substantially deviate from the experimental kinetics on a longer time scale (>400 fs). The much faster decays than our experimental data can be considered as indication of overestimation of the efficiency of the exciton-exciton annihilation processes on longer time scales. To avoid such fast excitation decay, a stochastic description of the exciton-exciton annihilation process should be used [13].

6.4.2 Stochastic model.

This model describes the population probabilities [13] according to the scheme shown in Fig. 6.6. In the case of multiple excitons in the system they can populate both E_{11} and E_{22} states in the course of their generation/relaxation. To reflect these relaxation/generation pathways, various energy levels $E_{i,j} = i \cdot E_{11} + j \cdot E_{22}$ have to be taken into account as shown in Fig. 6.6, where i and j prescribe the amount of excitons in the E_{11} and E_{22} bands, respectively. The possible transition pathways between various energy levels determining the evolution of probabilities, $P_{i,j}$, are depicted by arrows. Time-dependent rates of the exciton generation in the E_{11} and E_{22} bands already containing i and j excitons are defined as $G_1^(i)(t)$ and $G_2^(i)(t)$, respectively, while the relaxation rates k_{21}^j determines the relevant transition from the E_{22} band containing j excitons to the relevant E_{11} band. The rate constants for the linear relaxation $K^{(i)}$ and nonlinear annihilation $\Gamma^{(i)}$ determine the exciton loss from the E_{11} band already containing i excitons. It is also assumed that after annihilation the excitons from the $E_{nn} \cong 2E_{11}$ electronic band can relax either to the E_{22} band (with probability α) or directly back to the E_{11} band with probability (1 – α). According to the scheme shown in Fig. 6.6, the following Master equations for the occupation probabilities $P_{i,j}$ are derived:

$$\frac{dP_{0,0}}{dt} = -\left\{G_1^{(0)}(t) + G_2^{(0)}(t)\right\} P_{0,0} + K^{(1)} P_{1,0}, \tag{6.6}$$

$$\begin{aligned} dP_{1,0}dt = G_1^{(0)}(t)P_{0,0} - \left\{G_1^{(1)}(t) + G_2^{(0)}(t) + K^{(1)}\right\} P_{1,0} + k_{21}^{(1)} P_{0,1} \\ + \left\{K^{(2)} + (1-\alpha)\,\Gamma^{(2)}\right\} P_{2,0} \end{aligned}, \tag{6.7}$$

$$\frac{dP_{0,1}}{dt} = G_2^{(0)}(t)P_{0,0} - \left\{G_1^{(0)}(t) + G_2^{(1)}(t) + k_{21}^{(1)}\right\} P_{0,1} + \alpha\Gamma^{(2)} P_{2,0} + K^{(1)} P_{1,1}, \tag{6.8}$$

etc. For $P_{i,j}$ when $i \geq 2$ and $j \geq 1$ the relevant equations can be given by:

$$\begin{aligned} \frac{dP_{i,0}}{dt} = G_1^{(i-1)}(t)P_{i-1,0} - \left\{G_1^{(i)}(t) + G_2^{(0)}(t) + K^{(i)} + \Gamma^{(i)}\right\} P_{i,0} + k_{21}^{(1)} P_{i-1,1} + \\ + \left\{K^{(i+1)} + (1-\alpha)\,\Gamma^{(i+1)}\right\} P_{i+1,0}, \end{aligned} \tag{6.9}$$

$$\frac{dP_{0,j}}{dt} = G_2^{(j-1)}(t)P_{0,j-1} - \left\{G_1^{(0)}(t) + G_2^{(j)}(t) + k_{21}^{(j)}\right\} P_{0,1} + \alpha\Gamma^{(2)}P_{2,j-1} + K^{(1)}P_{1,j}, \quad (6.10)$$

$$\begin{aligned}\frac{dP_{1,j}}{dt} = G_2^{(j-1)}(t)P_{1,j-1} + G_1^{(0)}(t)P_{0,j} - \left\{G_1^{(1)}(t) + G_2^{(j)}(t) + K^{(1)} + k_{21}^{(j)}\right\} P_{1,j} \\ +k_{21}^{(j+1)}P_{0,j+1} + +\alpha\Gamma^{(3)}P_{3,j-1} + \left\{K^{(2)} + (1-\alpha)\,\Gamma^{(2)}\right\} P_{2,j},\end{aligned} \quad (6.11)$$

$$\begin{aligned}\frac{dP_{i,j}}{dt} = G_2^{(j-1)}(t)P_{i,j-1} + G_1^{(i-1)}(t)P_{i-1,j} - \left\{G_1^{(i)}(t) + G_2^{(j)}(t) + K^{(i)} + k_{21}^{(j)} + \Gamma^{(i)}\right\} P_{i,j} \\ + + k_{21}^{(j+1)}P_{i-1,j+1} + \alpha\Gamma^{(i+2)}P_{i+2,j-1} + \left\{K^{(i+1)} + (1-\alpha)\,\Gamma^{(i+1)}\right\} P_{i+1,j}.\end{aligned} \quad (6.12)$$

Since the annihilation process corresponds to the two-exciton relaxation, the following relationship for the annihilation rates can be deduced if the statistical number of possible relaxation pathways are taken into account:

$$\Gamma_1^{(i)} = \frac{i\,(i-1)}{2}\Gamma_1^{(2)} \equiv i\,(i-1)\,\frac{\gamma}{2}. \quad (6.13)$$

Similarly, for the linear relaxation rates we obtain:

$$k_{21}^{(i)} = ik_{21}^{(1)} \equiv ik_{21} \quad (6.14)$$

and

$$K^{(i)} = iK^{(1)} \equiv iK. \quad (6.15)$$

Substituting Eqs. 6.13-6.15 into Eqs. 6.6-6.12 and also assuming that the exciton generation rate is independent of $i$and j, i.e. $G_1^{(i)}(t) \equiv G_1(t)$ and $G_2^{(j)}(t) \equiv G_2(t)$, we get:

$$\frac{dP_{0,0}}{dt} = -\left\{G_1(t) + G_2(t)\right\} P_{0,0} + KP_{1,0}, \quad (6.16)$$

$$\frac{dP_{1,0}}{dt} = G_1(t)P_{0,0} - \left\{G_1(t) + G_2(t) + K\right\} P_{1,0} + k_{21}P_{0,1} + \left\{2K + (1-\alpha)\cdot\gamma\right\} P_{2,0}, \quad (6.17)$$

$$\begin{aligned}\frac{dP_{i,0}}{dt} = G_1(t)P_{i-1,0} - \left\{G_1(t) + G_2(t) + iK + i\,(i-1)\,\tfrac{\gamma}{2}\right\} P_{i,0} + k_{21}P_{i-1,1} + \\ + \left\{(i+1)\,K + (1-\alpha)\,(i+1)\,i\tfrac{\gamma}{2}\right\} P_{i+1,0},\end{aligned} \quad (6.18)$$

$$\frac{dP_{0,j}}{dt} = G_2(t)P_{0,j-1} - \left\{G_1(t) + G_2(t) + jk_{21}\right\} P_{0,j} + \alpha\cdot\gamma P_{2,j-1} + KP_{1,j}, \quad (6.19)$$

$$\begin{aligned}\frac{dP_{1,j}}{dt} &= G_2(t)P_{1,j-1} + G_1(t)P_{0,j} - \{G_1(t) + G_2(t) + K + jk_{21}\}\, P_{1,j} \\ &+ (j+1)\, k_{21}P_{0,j+1} + +\alpha \cdot 3 \cdot \gamma P_{3,j-1} + \{2K + (1-\alpha)\cdot\gamma\}\, P_{2,j},\end{aligned} \tag{6.20}$$

$$\begin{aligned}\frac{dP_{i,j}}{dt} &= G_2(t)P_{i,j-1} + G_1(t)P_{i-1,j} - \left\{G_1(t) + G_2(t) + iK + jk_{21} + i\,(i-1)\,\tfrac{\gamma}{2}\right\} P_{i,j} \\ &+ (j+1)\, k_{21}P_{i-1,j+1} + \alpha\,(i+2)\,(i+1)\,\tfrac{\gamma}{2}P_{i+2,j-1} \\ &+ \left\{(i+1)\,K + (1-\alpha)\,(i+1)\,i\tfrac{\gamma}{2}\right\} P_{i+1,j}\end{aligned} \tag{6.21}$$

for $i \geq 2$, $j \geq 1$.

The amount of excitons in the E_{11} and E_{22} bands can be also defined accordingly as:

$$n_1(t) = \sum_{i,j} i \cdot P_{i,j}(t), n_2(t) = \sum_{i,j} j \cdot P_{i,j}(t). \tag{6.22}$$

Thus, to determine the temporal evolution of the excitations in the system, the set of differential equations (equations 6.16-6.21) have to be solved. The amount of these equations increases with the excitation intensity but is restricted when population is reaching the limits due to the phase space filling. If the amount of exciton states in the phase space (N_1 for the E_{11} manifold and N_2 for the E_{22} manifold) is taken into account, the set of equations to be solved reaches the finite number, which equals to $(N_1 + 1) \times (N_2 + 1)$. As a result, the exciton kinetics should become intensity-independent for excitation intensities large enough to approach the limit of the phase space filling.

According to the experimental conditions, we assume a Gaussian pump pulse with an amplitude A and a FWHM duration of 50 fs. The maximum amounts of exciton states in the phase space for the E_{11} and E_{22} manifolds are assumed to be $N_1 = N_2 = 50$, and the amplitude A of the excitation pulse is chosen to ensure the occurrence of the phase space saturation effect. In our case, the excitation kinetics become independent of A when it is greater than $\sim$1.2 (when neglecting phase space filling factors and when the exciton relaxation/annihilation processes are switched off, this would results in generation of about 60 excitons per nanotube). The linear relaxation rate from the E_{11} manifold is assumed to be equal $K^{-1} = 10$ ps. We find that both kinetics measured at room temperature with either E_{11} or E_{22} excitation can be well described for their initial part by assuming the following set of parameters: $\alpha = 0.5$, $\gamma^{-1} = 460$ fs, and $k_{21}^{-1} = 400$ fs (Fig. 6.7a). On the other hand, for the data collected at 110 K the best fit is obtained when $\alpha = 0.5$, $\gamma^{-1} = 770$ fs, and $k_{21}^{-1} = 390$ fs are chosen (Fig 6.7b). With these parameters we are also able to obtain the intensity dependences for the maximum value of the bleaching signal, as defined by Eq. 6.4, close to the experimental observations, which appear almost the same for the two temperatures (110 and 292 K) (Fig. 6.7c).

It is noteworthy that in opposite to the continuous model, the calculated kinetics obtained within the frame of the statistical model are less sensitive to the changes of the α parameter, the branching ratio. In this case, sensitivity of the kinetics to the excitation intensity is controlled by an appropriate phase space filling factor.

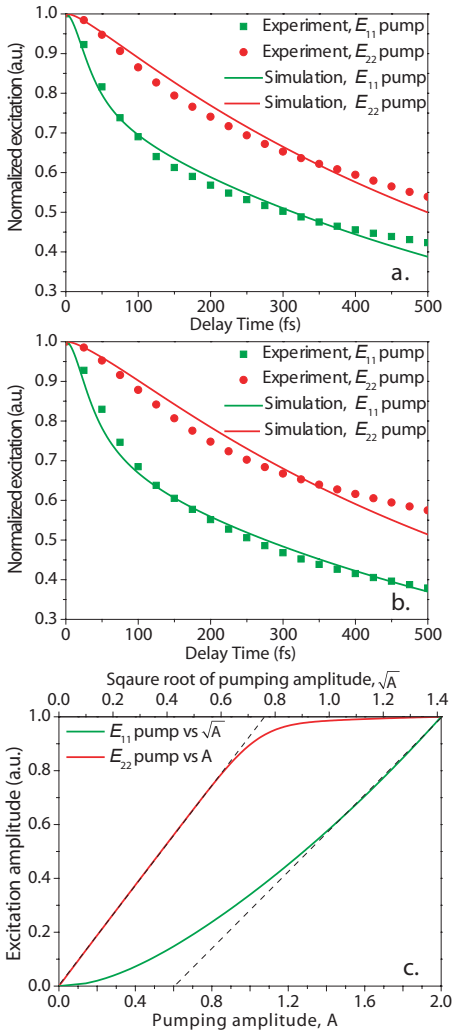

Figure 6.7. a. The best fit for the excitation kinetics of SWNT calculated according to the stochastic model (solid curves) with the experimental data measured at 292 K (squares and circles) obtained using the following parametres: $\alpha = 0.5$, $\gamma^{-1} = 460$ fs, $k_{21}^{-1} = 400$ fs. b. The best fit for the same excitation kinetics measured at 110 K, obtained using $\alpha = 0.5$, $\gamma^{-1} = 770$ fs and $k_{21}^{-1} = 390$ fs c. The dependence of the $(n_1 + n_2)_{max}$ upon intensity of the pumping signal defined as Ain the case of pumping to the E_{22} band (red curve) and upon its square root $\sqrt{A}$ in the case of pumping to the E_{11} band (green curve) calculated using the same parameter set. The intensity dependencies demonstrate almost the same behavior at both temperatures.

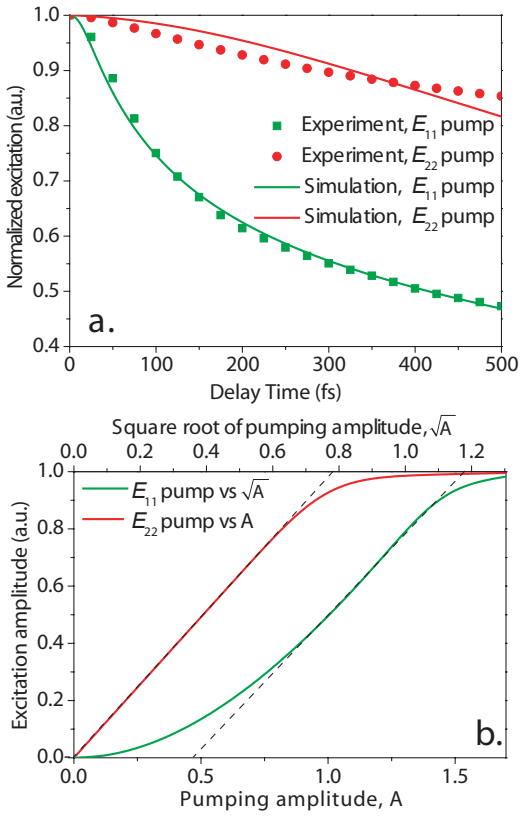

Figure 6.8. a. The best fit for the excitation kinetics of DWNT calculated according to the stochastic model (solid curves) with the experimental data (squares and circles) obtained using the following parametres: $\alpha = 0.5$, $\gamma^{-1} = 3930$ fs, $k_{21}^{-1} = 800$ fs. b. The dependence of the $(n_1 + n_2)_{max}$ upon intensity of the pumping signal defined as Ain the case of pumping to the E_{22} band (red curve) and upon its square root $\sqrt{A}$ in the case of pumping to the E_{11} band (green curve) calculated using the same parameter set.

Within the same annihilation scheme, the much larger differences in the kinetics measured with E_{11} and E_{22} excitation for the DWNTs (see Fig. 6.4) could be attributed to much slower rates of the annihilation γ and the relaxation k_{21}, which may be caused by the presence of the outer nanotube. Indeed, the best fit of the kinetics is obtained assuming $\alpha = 0.5$, $\gamma^{-1} =$ 3930 fs, $k_{21}^{-1} = 800$ fs (Fig. 6.8a). Using these parameters, the intensity dependence of the resulting maximal bleaching signal also provides a trend similar to the experimental results (Fig. 6.8b). It is evident that our chosen value $A = 1.7$ corresponds to a situation when both intensity dependences exhibit some saturation effect. As a result, by increasing the A value above $\sim$1.5 the obtained value of γ^{-1} remains almost invariant.

6.5 Discussion

Through numerical simulations presented above, we found that the strikingly different dependence of the maximal bleaching signal on the excitation intensity observed for E_{11} and E_{11} excitation (square root dependence vs. linear dependence as shown in Figs. 6.2 and 6.4b) could be understood in terms of nonlinear annihilation of coherent excitons. In order to reproduce these intensity dependences, we proposed two relaxation pathways from the doubly excited states that are populated in the course of nonlinear exciton-exciton annihilation. One of them takes into account a sequential relaxation from these high-lying excited states via the band to the lowest E_{11} band, while the other pathway corresponds to a direct exciton relaxation to the E_{11} band that bypasses the E_{22} band. The branching ratio α between these two pathways, the values of the linear relaxation rate k_{21} and nonlinear annihilation rate γ are all sensitive to the phase space filling factors. Through fitting the same experimental data based on the continuum model (Fig. 6.5b) and the stochastic model (Fig. 6.7a), we found that all these values are markedly different.

It is noteworthy that the phase space filling factors used in the two theoretic model are also very different: N_1 and N_2were chosen to be 2000 and 50 for the continuum model and the stochastic model, respectively. Since the initial kinetics have to be independent of the model used for calculations (either the continuum or stochastic model), use of different phase space filling factors result in differences in α, k_{21} and γ values needed for the best fits of the experimental data. Moreover, the annihilation rates determined according to the optimum model is dependent on excitation intensity, and the defined value of $1/\gamma$ varies linearly with A. However, this is not the case for the stochastic model, where the annihilation rate is found to be almost independent of the excitation intensity. Indeed, for the chosen phase space filling factors, $N_1 = N_2 = 50$, the saturation of the maximal bleaching signal occurs at very similar excitation intensities for the (7, 5) inner tube of a DWNT species upon pumping its E_{11} or E_{22} state (see Fig. 6.8b). When the excitation intensity exceeds this limiting value, the calculated kinetics remain almost invariant, and the obtained rate parameters (γ and k_{21}) are no longer dependent on the intensity. On the other hand, our calculations for the (6, 5) SWNT species with the same assumption for the phase space filling factors ($N_1 = N_2 = 50$) show that the maximal bleaching signal starts to saturate at a much lower excitation intensity in the case of the E_{22} excitation than the corresponding intensity

for the E_{11} excitation (Fig. 6.7c). As a result, the calculated kinetics still depend on the excitation amplitude for the chosen intensity in our simulations ($A = 1.7$), although to a lesser extent than what seen at lower intensities. For much higher excitation intensities when the maximal bleaching signal calculated for the E_{11} excitation starts to saturate, the rate parameters become intensity independent. However, the maximal bleaching signal calculated for the $E22$ excitation would remain invariant within a very wide region of $A > 1.5$. This difference in the intensity dependence for the E_{11} and E_{22} excitation could be overcome by assuming different phase space filling factors for the two excitonic bands ($N_1 < N_2$).

The kinetics measured experimentally can be reasonably well fitted using either the continuum or stochastic models. However, our calculations using the same sets of parameters lead to distinct differences in the dependence of the bleaching signal amplitude on the excitation intensity. The phase space filling factors $f_i(n_i)$ introduced in the equations of the continuum model (Eqs. 6.1 and 6.5) can partly account for the saturation effect found experimentally, and thus such modifications allow us to obtain the similar restriction effect. By taking the phase space filling restriction into account, we obtain from Eq. 6.5 (instead of Eqs. 6.2 and 11.3) that:

$$n_1(0) \approx \frac{G_{1,\max}}{(1+\alpha)\gamma N_1}\left(\sqrt{1+\frac{2N_1^2(1+\alpha)\gamma}{G_{1,\max}}}-1\right), \quad n_2(0) \approx 0 \tag{6.23}$$

when the pump pulse is in resonance with the E_{11} exciton state, whereas

$$n_1(0) \approx 0, \quad n_2(0) \approx \frac{G_{2,\max}}{k_{21}+\frac{G_{2,\max}}{N_2}} \tag{6.24}$$

when the E_{22} exciton state is excited. From Eqs. 6.23 and 6.24, it is clear that the saturation of the bleaching signal amplitude with increasing the excitation intensity is very gradual (see Fig. 6.5a,d), and the discrepancies from Eqs. 6.2 and 11.3 are obvious even at the intermediate intensities of excitation. On the other hand, in stochastic model the phase space filling appears naturally when the number of excitons reaches the maximum number of the energy states that are available in the system. This provides a much stronger (abrupt) saturation (Fig. 6.7c), which does not manifest itself at the intermediate values of the excitation intensity, and thus is in better agreement with experimental observations.

With the same stochastic model, we are able to reproduce quantitatively the initial portion of the kinetics and qualitatively the intensity dependence of the maximal bleaching signals by assuming only slower rates k_{21} and γ (Figs. 6.7 and 6.8). The nonlinear annihilation kinetics calculated in the frame of the stochastic model exhibit slower decay for delay times > 400 fs than the corresponding kinetics obtained according to the continuum model.[15,16,31] However, this slow-down is still insufficient to describe the kinetics observed experimentally. This is in contrast to the data from our previous studies on aqueous solutions of semiconducting SWNTs, where nonlinear annihilation of coherent excitons as the leading relaxation process is well identified at room temperature.[10,13,14] This discrepancy between our present and previous results suggests a possible sample dependence of exciton relaxation dynamics. In view of the strong environmental effects on exciton dynamics observed

by both single-tube and ensemble time-resolved experiments,[8,32] it may be not surprising that the variation of nanotube surroundings can affect the mechanisms of exciton-exciton annihilation.

As follows from qualitative analysis of the experimental data, a plot of the transient absorption kinetics measured at room temperature as $(\Delta OD_0/\Delta OD(t) - 1)^2$ scales linearly with time on a long delay times (picoseconds and longer), and thus can be attributed to the 1D diffusion-limited annihilation.[29] It indicates a change of the physical mechanism of exciton-exciton annihilation from involving delocalized coherent excitons to localized ones at the intermediate time scale, from a few hundreds of fs up to 1 ps (see Figs. 6.3c and 6.6b). This possible change of physical mechanisms of exciton-exciton annihilation can be understood in a following way. Initially the exciton density is high enough so that the wavefunctions of coherent excitons are overlapping in the nanotube. As a result, the nonlinear annihilation process involving coherent excitons dominates. The resulting exciton relaxation leads to decrease of the concentration of excitons, and consequently their wavefunctions will no longer overlap. In this case, exciton diffusion becomes a dominant factor in the nonlinear exciton annihilation.[29] Evidently, this mechanistic change in the nonlinear annihilation process will result in a corresponding rate decrease owing to the finite exciton diffusion timescale. Therefore the kinetics on the intermediate and long times should be attributed to nonlinear annihilation between excitons which are affected by their scattering on the lattice imperfections caused by the external conditions. These external conditions could also stimulate the spontaneous symmetry breaking or so-called Peierls distortion expected in 1-D systems.[33] As the result of these processes, the exciton diffusion starts to dominate. On the other hand, the data collected at temperatures below ∼200 K, such as at 110 K (Fig. 6.3d) indicates an annihilation process involving long-lived coherent excitons. This observation is qualitatively in line with the long exciton dephasing times found at low temperatures.[22]

6.6 Summary

A new picture is emerging of excitons in semiconducting SWNTs in which the character of the excitation and its dynamical behavior vary remarkably as a function of time following excitation. Using femtosecond transient absorption measurements on the (6, 5) SWNT type and the (7, 5) inner tubes of a dominant DWNT species we found that the dynamics of exciton relaxation depends strongly on their method of preparation - either directly into E_{11} or via ultrafast relaxation from E_{22}. For excitons created directly in E_{11} the initial state comprises multiple overlapping coherent excitons. As exciton-exciton interaction does not require exciton motion, rapid exciton-exciton scattering and exciton-exciton annihilation ensues. Following this initial annihilation phase, the remaining excitons may still be coherent for timescales of 1 ps.[28] Qualitative analysis of the E_{11} transient decay kinetics at longer delay times (¿ 1 ps) indicates occurrence of diffusion-limited exciton-exciton annihilation, and therefore these results support the concept based on the diffusion type of exciton-exciton annihilation as observed on long time scales.[17,18]

The exciton annihilation process produces complex behavior in the optical response that is sensitive to how the E_{11} state is populated. When E_{22} is initially populated, the subsequent phonon-mediated relaxation leads to exciton occupation at the E_{11} state with various momenta. Relaxation of all these excitons is 'visible' in transient absorption experiments: those with close to zero momenta are through stimulated emission of the E_{11} state and its excited-state absorption, and the rest with finite momenta are through ground state recovery. In contrast, direct excitation of the E_{11} state will create excitons with negligible momentum and subsequent relaxation is expected to be more rapid, provided that this process is faster than the thermalization. Experimentally, a clearly slower decay is indeed observed when the E_{22} state of the (6, 5) tubes is excited than the one measured with its E_{11} excitation. This difference is even more pronounced for the (7, 5) inner tube species. Striking differences in the excitation intensity dependence are further found for the maximal bleaching signals obtained for both the (6, 5) and (7, 5) tubes upon excitation of their corresponding E_{22} or E_{11} states. The former exhibits a linear dependence on the E_{22} excitation intensity, whereas the latter scales linearly with the square root of the E_{11} excitation intensity. This complex picture is not fully included in our theoretical model yet. The E_{22} to E_{11} transition is present in our scheme while population distribution in the K_{CM}-space of the E_{11} excitons arising from this relaxation is not taken into account.

In order to better understand these experimental findings, we develop the continuum model and stochastic model by explicit consideration of the annihilation of coherent excitons and a branching parameter. Our numerical simulations show that both models can reproduce reasonably well the initial portion of decay kinetics measured upon the E_{22} and E_{11} excitation of the chosen tube species but with significantly different sets of adjustable parameters. In particularly, our calculations based on the stochastic model give qualitatively better agreement with the intensity dependence observed experimentally than those obtained with the continuum model. However, it should be pointed out that the complex behavior in the optical response depending on how the E_{11} state is populated is not fully included in our theoretical model yet. While the E_{22} to E_{11} transition is present in our scheme, population distribution in the K-space of the E_{11} excitons arising from this relaxation is not taken into account. Nevertheless, we believe the kinetic models developed here may provide important insight into how multiple exciton states are involved in the annihilation and impact ionization processes in SWNTs, which may play a key role in practical applications such as development highly-efficient SWNT photodiode devices.[34]

6.7 References

[1] C. Kittel, Quantum Theory of Solids. John Willey and Sons New York-London, 1963.

[2] F. Wang, G. Dukovic, L. E. Brus, T. F. Heinz, *Science* **308**, 838 (2005).

[3] Y.-Z. Ma, L. Valkunas, S. M. Bachilo, G. R. Fleming, *J. Phys. Chem. B* **109**, 15671 (2005).

[4] C. D. Spataru, S. Ismail-Beigi, L. X. Benedict, S. G. Louie, *Appl. Phys. A* **78**, 1129 (2004).

[5] C. D. Spataru, S. Ismail-Beigi, L. X. Benedict, S. G. Louie, *Phys. Rev. Lett.* **92**, 077402 (2004).

[6] X.-F. He, *Phys. Rev. B* **43**, 2063 (1991).

[7] O. J. Korovyanko, C.-X. Sheng, Z. V. Vardeny, A. B. Dalton, R. H. Baughman, *Phys. Rev. Lett.* **92**, 017403 (2004).

[8] G. N. Ostojic, S. Zaric, J. Kono, M. S. Strano, V. C. Moore, R, H, Hauge, R. E. Smalley, *Phys. Rev. Lett.* **92**, 117402 (2004).

[9] L. Huang, H. N. Pedrosa, T. D. Krauss, *Phys. Rev. Lett.* **93**, 017403 (2004).

[10] Y.-Z. Ma, L. Valkunas, S. L. Dexhemer, S. M. Bachilo, G. R. Fleming, *Phys. Rev. Lett.* **94**, 157402 (2005).

[11] Y.-Z. Ma, J. Stenger, J. Zimmermann, S. M. Bachilo, R. E. Smalley, R. B. Weisman, G. R Fleming, *J. Chem. Phys.* **120**, 3368 (2004).

[12] F. Wang, G. Dukovic, E. Knoesel, L. E. Brus, T. F. Heinz, *Phys. Rev. B* **70**, 241403 (2004).

[13] L. Valkunas, Y.-Z. Ma, G. R. Fleming, *Phys. Rev. B* **73**, 115432 (2006).

[14] L. Huang, T. D. Krauss, *Phys. Rev. Lett.* **96,** 057407 (2006).

[15] A. V. Barzykin, M. Tachiya, *Phys. Rev. B* **72**, 075425 (2005).

[16] A. V. Barzykin, M. Tachiya, *J. Phys. - Cond. Matter* **19**, 065105 (2007).

[17] R. M. Russo, E. J. Mele, C. L. Cane, I. V. Rubcov, J. M. Therien, D. E. Luzzi, *Phys. Rev. B* **74**, 041405 (2006).

[18] Zhu et al., JPC C 111 3831 2007.

[19] A. Srivastava, J. Kono, *Phys. Rev.* B 79, 205407 (2009).

[20] Y. Murakami, J. Kono, *Phys. Rev. Lett.* 102, 037401 (2009).

[21] L. Lüer, S. Hoseinkhani, D. Polli, J. Crochet, T. Hertel, G. Lanzani, *Nature Physics* DOI: 10.10.38 (2008).

[22] Y.-Z. Ma, M. W. Graham, G. R. Fleming, A. A. Green, M. C. Hersam, *Phys. Rev. Lett.* **101**, 217402 (2008).

[23] D. Abramavicius, Y.-Z. Ma, M. W. Graham, L. Valkunas, G. R. Fleming, *Phys. Rev. B* **79**, 195445 (2009).

[24] M. S. Arnold, A. A. Green, J. F. Hulvat, *et al.*, Nature Nanotech. 1, 60, 2006

[25] N. Kishi *et al.*, *J. Phys. Cham B* 110, 24816, 2006.

[26] Y.-Z. Ma, L. Valkunas, S. L. Dexheimer, G. R. Fleming, Mol. Phys. 104, 1179, 2006.

[27] Ma, Y.-Z.; Hertel, T.; Vardeny, Z. V.; Fleming, G. R.; Valkunas, L. Ultrafast spectroscopy of carbon nanotubes. *In Topics Appl. Phys.*; Jorio, A., Dresselhaus, G., Dresselhaus, M. S., Eds.; Springer-Verlag Berlin: Heidelberg, 2008; Vol. 111; pp 321.

[28] M. W. Graham, Y.-Z. Ma, A. A. Greeen, M. C. Hersam, G. R. Fleming, *Proc. of SPIE*, **7600**, 76001F,1 2010.

[29] L. Valkunas, G. Trinkunas, V. Liuolia, in *Resonance Energy Transfer*, eds. D. L. Andrews and A. A. Demidov, John Wiley & Sons, Chichester, 1999.

[30] C. Manzoni, A. Gambetta, E. Menna, M. Meneghetti, G. Lanzani, G. Cerullo, *Phys. Rev. Lett.* **94**, 207401 (2005).

[31] V. Barzda, V. Gulbinas, R. Kananavicius, V. Cervinskas, H. van Amerongen, R. van Grondelle, L. Valkunas, Biophys. J. **80**, 2409 (2001).

[32] Hertel, T.; Hagen, A.; Talalaev, V.; Arnold, K.; Hennrich, F.; Kappes, M.; Rosenthal, S.; McBride, J.; Ulbricht, H.; Flahaut, E. *Nano Lett.* 2005, 5, 511.

[33] S. Tretiak, S. Kilina, A. Piryatinski, A. Saxena, R. L. Martin, A. R. Bishop, Nano Lett. **7**, 87 (2007).

[34] N. M. Gabor, Z. Zhong, K. Bosnick, J. Park, P. L. McEuen, Science 325, 1367, 2009.

Chapter 7

Ultrafast Exciton Dephasing

Femtosecond two-pulse degenerate four-wave mixing spectroscopy was applied to study the exciton dephasing in a broad range of excitation intensity and lattice temperature. We find that both exciton-exciton and exciton-phonon scattering have profound effects on the dephasing process. The dominant phonon mode involved in the dephasing is identified as the out-of-plane, transverse optical mode with a frequency of 847 cm^{-1}. The extracted homogeneous linewidths at all measured temperatures are in excellent agreement with the results of a single tube photoluminescence experiment.

7.1 Introduction

A single-walled carbon nanotube (SWNT) is a one-dimensional (1-D) seamless cylinder of a one-atom thick graphitic sheet. Depending on its structure defined by two indices (n, m), it can exhibit either metallic or semiconducting characteristics [1]. The spatial confinement in the transverse direction gives rise to markedly enhanced Coulomb correlations and many-body interactions[2, 3]. An unambiguously identified effect is the formation of neutral excitons in semiconducting SWNTs upon optical excitation, which are characterized by an anomalously large binding energy which is a substantial fraction of the bandgap energy ($\sim$0.4 eV [4, 5]). These excitons determine essentially all the optical properties of semiconducting SWNTs [6].

In general, the excitons created in semiconductors with an ultrashort laser pulse initially posses a definite phase relationship among themselves and with the electromagnetic radia-

tion creating them [7]. Subsequent scattering among themselves and with charged carriers, phonons, impurities and defects will lead to decoherence or dephasing, and eventually deexcitation or exciton population relaxation. Investigations of exciton dynamics in this coherent regime employing coherent transient spectroscopy [7] have offered an excellent opportunity of learning fundamental physics in a variety of systems, including many quantum-confined materials such as quantum wells [8-10], wires [11, 12] and dots [13, 14]. Determination of the time scales of various dephasing processes has further provided a wealth of information about the intrinsic homogenous linewidths of specific exciton transitions directly through an ensemble measurement [9, 11, 12].

Ultrafast dynamics of exciton population relaxation in semiconducting SWNTs is an active field and has recently been reviewed [15]. The coherent behavior of SWNTs, however, has not been explored experimentally. Studies of exciton dynamics in the coherent regime are important for understanding the complex interactions among various quasi-particles in this strongly confined, 1-D system, and for identifying their potential contributions to the exciton dephasing process. The spectroscopic information gained from such studies is also particularly valuable, because the substantial heterogeneity in all currently available samples leads to significant inhomogeneous broadening of spectral lines, and because the data obtained from single-tube spectroscopy is currently very limited and gives highly variable results even for the same tube type [16-18]. Here, we present an experimental study of ultrafast exciton dephasing in semiconducting SWNTs. The exciton dynamics in the coherent regime is investigated by femtosecond two-pulse degenerate four-wave mixing (FWM) experiments. Our measurements for a broad range of excitation intensity and lattice temperature enable us to separate the effects of exciton-exciton and exciton-phonon scattering on exciton dephasing. Quantitative analyses of our data further allow us to identify the dominant phonon mode involved in the dephasing process, to determine the decay timescales of the FWM signals, and to estimate the corresponding homogeneous linewidth of the lowest exciton transition of selected tube species.

7.2 Experimental Details

The sample used in this study is highly enriched in a single semiconducting tube type, the (6, 5) nanotube, which was isolated through density-gradient ultracentrifugation [19]. The obtained aqueous solution was mixed with appropriate amount of water soluble polyvinylpyrrolidone (PVP) polymer to fabricate a thin composite film. Use of this solid sample greatly suppresses the light scattering arising from motion of nanotubes in the solution. Measurements of linear absorption and steady-state fluorescence emission spectra confirm that the nanotubes remain individualized after being transferred from the solution to the solid film.

We studied the coherent exciton dynamics using femtosecond two-pulse degenerate FWM spectroscopy. The light source was an optical parametric amplifier pumped by a 250 kHz Ti:Sapphire regenerative amplifier [20], which was tuned to a central wavelength of 990 nm

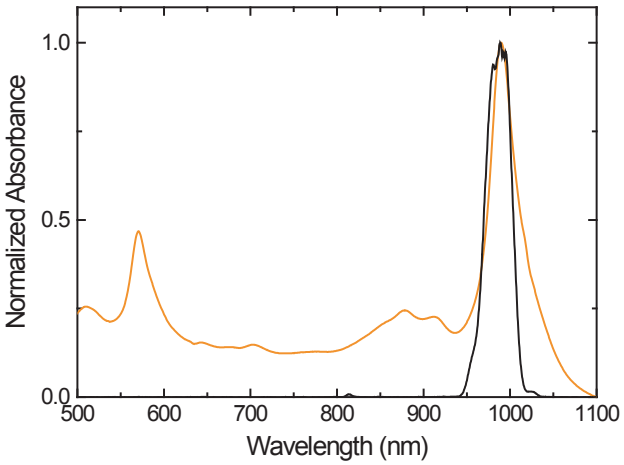

Figure 7.1. Linear absorption spectrum of the SWNT/PVP film (orange). The peaks at 571 and 990 nm correspond to the second and the first excitonic transitions of the dominant tube species in the sample, the (6, 5) tube. The back line is the laser pulse spectrum. Both spectra are normalized at the maxima.

in order to resonantly excite the lowest excitonic transition (E_{11}) of the (6, 5) tube (see Fig. 7.2). In this experiment, two nearly equal intensity laser pulses of 45 fs duration with a variable decay t_{12} are focused to the sample. The first pulse with wavevector $\mathbf{k}_1$ generates a coherent macroscopic polarization of the exciton ensemble, and when the second pulse with wavevector $\mathbf{k}_2$ arrives before the dephasing of the induced polarization an interference grating is produced. This transient grating diffracts photons into the background-free, phase-matching direction $2\mathbf{k}_2$-$\mathbf{k}_1$. A schematic of the FWM geometry is shown in Fig. 7.3a. As the time delay t_{12} increases, the amplitude of the grating decays and the diffracted signal decreases. Measurement of the diffracted signal as a function of t_{12} yields a time scale that is directly proportional to the dephasing time T_2 (see following discussion). The diffracted signal was detected in a time-integrated manner with an InGaAs photodiode and a lock-in amplifier.

7.3 Results and Discussion

We performed measurements at seven lattice temperatures ranging from 77 to 292 K, and at each temperature several different excitation intensities between 1.74 and 12.21 μJ/cm^2 were employed. Fig. 7.3b shows the data collected at 100 K for five different excitation intensities. Here, the intensity of the FWM signal is plotted as a function of the time decay t_{12}. The decay of the diffracted signal depends strongly on the intensity, manifesting by a significantly faster decay with increasing intensity. Quantitative analysis employing a least square deconvolution fitting algorithm with explicit consideration of the finite temporal response shows that the decay time (τ_{decay}) decreases from 71 fs at 1.74 μJ/cm^2 to 36 fs at

12.21 μJ/cm^2. Such a trend of the decay time change with excitation intensity is also observed at other lattice temperatures measured (77, 130, 160, 200, 250 and 292 K). Furthermore, a comparison of the data collected at $\sim$1.74 μJ/cm^2, the lowest intensity used in this work, demonstrates a clear temperature effect (see Fig. 7.3c). The decay time extracted from the data decreases from 77 fs at 77 K to 35 fs at 292 K. The observed strong dependence on temperature and excitation intensity provides the direct evidence for the involvement of both excitons and phonons in the exciton dephasing process.

The markedly enhanced contribution of phonons to the exciton dephasing with increasing temperature results in strikingly distinct excitation intensity effects on the FWM decays at different temperatures. For the given seven-fold increase of excitation intensity, we find that the reduction of τ_{decay} at 292 K (from 35 to 22 fs) is three times smaller than that observed at 77 K (from 77 to 36 fs). This temperature-dependent phonon contribution further leads to a prominent difference in the intensity dependence of the corresponding dephasing rate, $1/T_2$, or equivalently the homogeneous linewidths [full width at half maximum (FWHM)] Γ_h of the E_{11} transition, at different lattice temperature. Here, the dephasing time T_2 is calculated from the τ_{decay} by assuming $T_2 = 4\tau_{decay}$, which is strictly valid for a strongly inhomogeneously broadened, independent two-level system[21]. The corresponding $\Gamma_h$value is then obtained from $\Gamma_h = 2\hbar/T_2$, and is indicated by the label on the right-side of Fig. 7.3. As shown in Fig. 7.3, the dephasing rate (or the homogeneous width) at 77, 100 and 130 K increases linearly with intensity. Such linear dependence has been observed in quantum wells [9, 10] and wires [11, 12]. However, at higher temperatures, the dependence found for the same intensity change deviates obviously from linearity. This obvious deviation strongly suggests a pronounced phonon contribution at high temperature.

The linear intensity dependence of $1/T_2$ (or Γ_h) observed at 77, 100 and 130 K represents a typical characteristics of dominant exciton-exciton collision broadening. The linear dependence can be described by $1/T_2(N_x) = 1/T_2(0) + \beta N_x$, with N_x the excitation density, β the exciton-exciton scattering parameter, and $1/T_2(0)$ the temperature-dependent zero-density dephasing rate. N_x is estimated from an absorption cross section (5.2×10^{-14} cm^2 per tube), a mean tube length of 600 nm, the measured $1/e^2$ beam diameter (148 μm) and the excitation intensity, and is depicted by the labels of the top axes of Fig. 7.3. The linear fits shown in Fig. 7.3a give a β value of 0.84, 0.85 and 0.78 ps$^{-1}\cdot\mu$m at 77, 100 and 130 K, respectively. The corresponding $1/T_2(0)$ values are 2.84, 3.01 and 3.67 ps^{-1}. As the absorption cross section employed in the calculation represents a lower limit of the actual value, the resulting N_x must be underestimated. Consequently, this suggests that the β values are an upper limit. Note that these β values are several times smaller than those determined from 1-D quantum wires[11, 22], suggesting a reduced exciton-exciton scattering in semiconducting nanotubes.

By extrapolating the decay times determined at different intensities to the limit of zero intensity for each temperature, we can examine the contribution of the phonons to the dephasing without other effects. This extrapolation involves a nonlinear regression using an empricial function $\tau_{decay} = c_1 \exp(-I/I_0) + c_2$ (I is the intensity, c_1, c_2 and I_0 are the variables). Similar results were also obtained using a hyperbolic function $\tau_{decay} = 1/(c_1 + c_2 I)$ for the data measured at 77, 100 and 130 K. The dephasing rate $1/T_2$ and the corresponding homogeneous width Γ_h are plotted in Fig. 7.3 as a function of temperature. The resulting

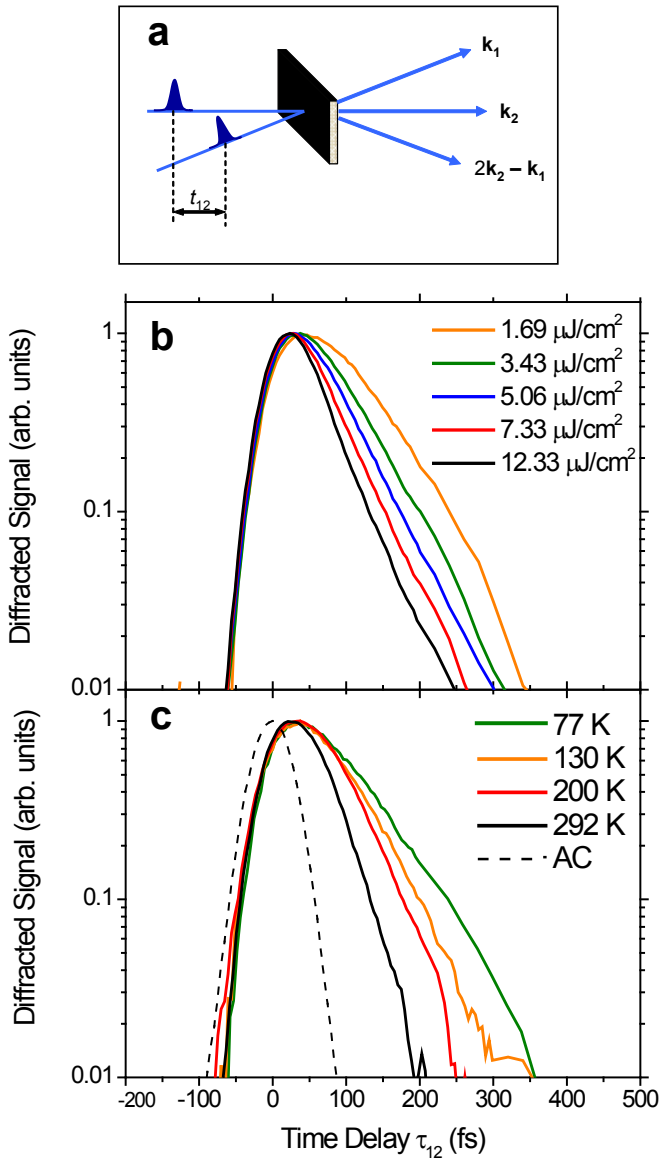

..

Figure 7.2. (a) Schematic of the geometry of four-wave mixing. Here t_{12} is considered positive (negative) when pulse 1 (2) precedes pulse 2 (1). (b) FWM signals measured at 100 K for five different excitation intensities. (c) FWM signals measured at 77, 130, 200 and 292 K under the lowest excitation intensity used for this experiment, which was 1.74 μJ/cm^2. The dashed line is the auto-correlation function of the two laser pulses. All the data have been normalized at the signal maxima.

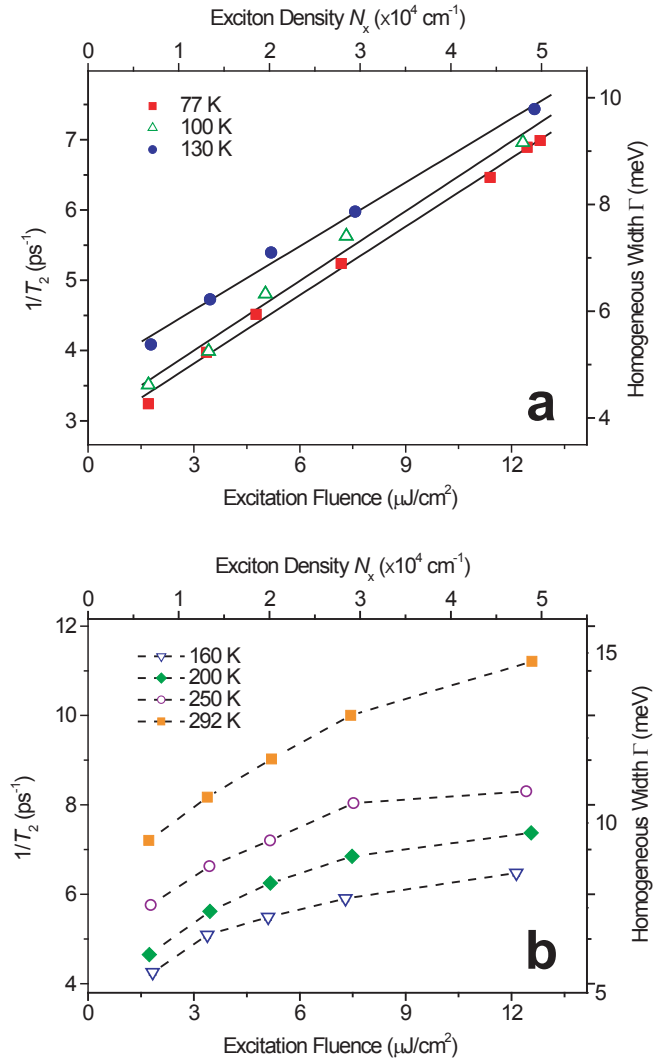

Figure 7.3. Dependence of the dephasing rates and the corresponding homogeneous linewidths on excitation intensity at different lattice temperatures. (a) 77, 100, and 130 K, (b) 160, 200, 250, and 292 K. The solid lines in (a) are the linear fits to the data obtained at 77, 100 and 130 K. The dashed lines in (b) are drawn to guide the eye. The corresponding exciton densities estimated from the absorption cross section, mean tube length, laser beam size at the focus and the excitation intensities are depicted by the scales on the top of the plots.

temperature dependence can be best described by the function: $\Gamma_h = a + b\exp(-\Delta E/k_B T)$, where T is the lattice temperature, and ΔE denotes an energy scale. The solid line in Fig. 7.3 is obtained with $a = 4.2$ meV, $b = 254$ meV, and $\Delta E = 847$ cm^{-1}. Note that the second term in the fitting function is equivalent to the thermal occupation function of optical phonons after neglecting the constant term of 1 in the denominator[7, 10], which is negligible for the given ΔE value and the temperature range. Thus from the fitting result we deduce a frequency of 847 cm^{-1}for the phonon mode involved in the dephasing. This frequency matches well with the frequency of the out-of-plane, transverse optical (TO) phonon mode found in the Raman spectra of both SWNT bundles and single tubes as a broad and weak feature[23, 24]. We therefore conclude that this TO phonon mode plays a dominant role in the exciton dephasing process. As this TO mode has an atomic displacement along the tube axis[25], it can effectively modulate both the exciton binding energy and E_{11} energy, and thus induce dephasing. We found no evidence for contribution from much stronger G-band mode ($\sim$1590 cm^{-1}), which was predicted to dominate the exciton dephasing in recent calculations[26].

It is interesting to note that the homogeneous widths determined in the zero-intensity limit are in excellent agreement with the results of a single tube photoluminescence (PL) measurement at all lattice temperatures we studied[27]. This agreement justifies the applicability of the simple relation $T_2 = 4\tau_{decay}$. We therefore can confidently deduce in the zero-intensity limit an exciton dephasing time of 380 and 162 fs at 77 and 292 K, respectively. The dephasing time obtained at 77 K is very close to the result (350 fs) of a recent frequency domain, single tube PL experiment at 90 K [28]. Literature values for the homogeneous width vary substantially[16-18]. However, the experiments reported in refs. 27 and 28 were performed on as-grown, air-suspended nanotubes. In comparison to those experiments employing the tubes subjected to rigorous post-growth processing, these results should be least affected by environment [15, 29], defects [16] and unintentional doping [18], and therefore we expect them to more closely reflect the intrinsic spectral properties of individual tubes. Moreover, the homogeneous width appears much narrower than the FWHM width of linear absorption spectrum, with room temperature FWHM widths of 8.1 and 50.3 meV, respectively. Clearly, the absorption spectrum shown in Fig. 7.2 is dominated by inhomogeneous broadening. Assuming a Gaussian distribution of the E_{11} energies, we estimate an inhomogeneous width of 49.7 meV. This gives a ratio of inhomogeneous to homogeneous widths of 6.1.

7.4 Conclusions

In summary, we have demonstrated that both exciton-exciton and exciton-phonon scattering processes have profound effects on exciton dephasing in semiconducting SWNTs. We find that both the dephasing rates and the corresponding homogeneous linewidths increase with excitation intensity. These intensity dependences vary markedly with lattice temperature. At 77, 100 and 130 K, the intensity dependence is linear, whereas a clear deviation from linearity is observed at higher temperatures. Analysis of the temperature dependence

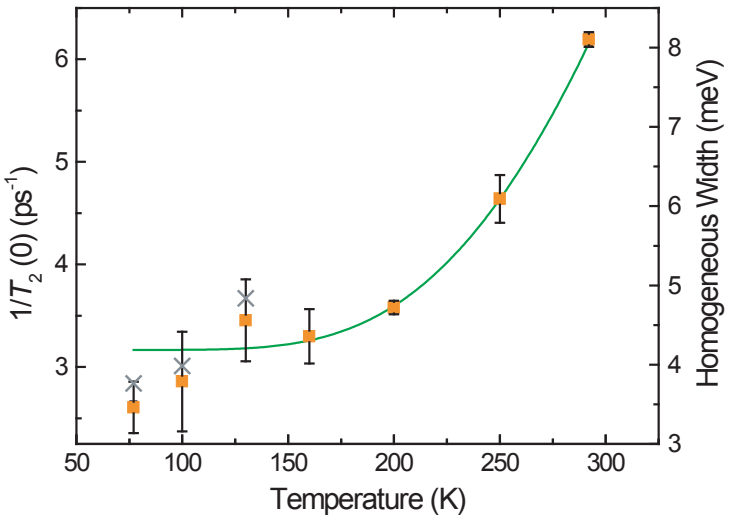

Figure 7.4. The dephasing rates in the zero-intensity limit versus temperature. The solid line is a least squares fit. The corresponding homogeneous linewidths are depicted by the scales on the right side. See text for details. The crosses at 77, 100 and 130 K show the $1/T_2(0)$ values obtained through linear extrapolation.

of homogeneous linewidth in the zero-intensity limit further enable us to identify the dominant phonon mode as the out-of-plane TO mode with a frequency of 847 cm^{-1}. Moreover, the estimated homogeneous linewidths are in excellent agreement with the results of a single tube PL experiment. A large ratio of the inhomogeneous to homogeneous widths of 6.1 is estimated for the room temperature absorption spectrum, consistent with the presence of substantial sample heterogeneity. The observation of exciton coherence in semiconducting SWNTs that persists over 162 fs at room temperature and almost 400 fs at 77 K provides a sufficient window of studying many-body effects in real time, along with the resulting dynamical and spectroscopic signatures. Our finding may also stimulate exploration of potential applications such as in ultrafast all-optical devices.

7.5 References

[1] S. Saito, G. Dresselhaus, and M. S. Dresselhaus, *Physical Properties of Carbon Nanotubes* (Imperial College Press, London, 1998).

[2] T. Ando, J. Phys. Soc. Jpn. **66**, 1066 (1997).

[3] C. D. Spataru, S. Ismail-Beigi, L. X. Benedict, et al., Phys. Rev. Lett. **92**, 077402 (2004).

[4] F. Wang, G. Dukovic, L. E. Brus, et al., Science **308**, 838 (2005).

[5] Y.-Z. Ma, L. Valkunas, S. M. Bachilo, et al., J. Phys. Chem. B **109**, 15671 (2005).

[6] M. S. Dresselhaus, G. Dresselhaus, R. Saito, et al., Annu. Rev. Phys. Chem. **58**, 719 (2007).

[7] J. Shah, *Ultrafast spectroscopy of semiconductors and semiconductor nanostructures* (Berlin; New York: Springer Verlag, 1999).

[8] L. Schultheis, A. Honold, J. Kuhl, et al., Phys. Rev. B **34**, 9027 (1986).

[9] A. Honold, L. Schultheis, J. Kuhl, et al., Phys. Rev. B **40**, 6442 (1989).

[10] D.-S. Kim, J. Shah, J. E. Cunningham, et al., Phys. Rev. Lett. **68**, 1006 (1992).

[11] H. P. Wagner, W. Langbein, J. M. Hvam, et al., Phys. Rev. B **57**, 1797 (1998).

[12] W. Langbein, H. Gislason, and J. M. Hvam, Phys. Rev. B **60**, 16667 (1999).

[13] R. W. Schoenlein, D. M. Mittleman, J. J. Shiang, et al., Phys. Rev. Lett. **70**, 1014 (1993).

[14] A. E. Colonna, X. Yang, and G. D. Scholes, Phys. Stat. Sol. (b) **242**, 990 (2005).

[15] Y.-Z. Ma, T. Hertel, Z. V. Vardeny, et al., in *Topics Appl. Phys.*, edited by A. Jorio, G. Dresselhaus and M. S. Dresselhaus (Springer-Verlag Berlin, Heidelberg, 2008), Vol. 111, p. 321.

[16] A. Hagen, M. Steiner, M. B. Raschke, et al., Phys. Rev. Lett. **95**, 197401 (2005).

[17] J. Lefebvre, D. G. Austing, J. Bond, et al., Nano Lett. **6**, 1603 (2006).

[18] H. Htoon, M. J. O'Connell, P. J. Cox, et al., Phys. Rev. Lett. **93**, 027401 (2004).

[19] M. S. Arnold, A. A. Green, J. F. Hulvat, et al., Nature Nanotech. **1**, 60 (2006).

[20] Y.-Z. Ma, L. Valkunas, S. L. Dexheimer, et al., Mol. Phys. **104**, 1179 (2006).

[21] T. Joo and A. C. Albrecht, Chem. Phys. **176**, 233 (1993).

[22] E. J. Mayer, J. O. White, G. O. Smith, et al., Phys. Rev. B **49**, 2993 (1994).

[23] A. M. Rao, E. Richter, S. Bandow, et al., Science **275**, 187 (1997).

[24] M. S. Dresselhaus, G. Dresselhaus, and A. Jorio, Annu. Rev. Mater. Res. **34**, 247 (2004).

[25] S. Reich, C. Thomsen, and J. Maultzsch, *Carbon Nanotubes: Basic Concepts and Physical Properties* (Wiley-VCH Verlag GmbH & Co. kGaA, Weinheim, 2004).

[26] B. F. Habenicht, H. Kamisaka, K. Yamashita, et al., Nano Lett. **7**, 3260 (2007).

[27] J. Lefebvre, P. Finnie, and Y. Homma, Phys. Rev. B **70**, 045419 (2004).

[28] K. Matsuda, T. Inoue, Y. Murakami, et al., Phys. Rev. B **77**, 033406 (2008).

[29] H. Hirori, K. Matsuda, Y. Miyauchi, et al., Phys. Rev. Lett. **97**, 257401 (2006).

Chapter 8

Photon Echo Spectroscopy and Absorption Lineshape Properties

Three-pulse photon echo peak shift measurements were performed on semiconducting single-walled carbon nanotubes embedded in polymer matrix at room temperature. The peak shifts exhibit a striking dependence on the excitation intensity and an exceptionally large initial value. Simultaneous modeling of the peak shift data in the limit of zero-intensity and the linear absorption spectrum enable us to extract intrinsic spectral lineshap information through ensemble measurements. We found that the overall width of the choosen absorption band is dominated by inhomogeneous broadening with a full width at half maximum (FWHM) of 698 cm^{-1}. The intrinsic homogeneous linewidth is determined to be 178 cm^{-1}. From the simulation parameters, we further calculated a Huang-Rhys factor of 0.04 for the radial breathing mode vibration. This value suggests weak exciton-phonon coupling in semiconducting nanotubes, and is fully consistent with the observed large initial peak shift. Two-pulse photon echo experiments were also conducted for independent verification of the homogeneous linewidth and for direct quantification of the dephasing time scale. Finally, the exciton population relaxation dynamics were simultaneously measured using either transient grating or pump-probe experiments.

8.1 Introduction

Semiconducting single-walled carbon nanotubes (SWNTs) are one of most intriguing nano-materials due to their large aspect ratios, size-tunable properties, and recent progress in fabrication and purification techniques[1–3] The scope of optoelectronic applications for SWNTs depends critically on a detailed understanding of their underlying physical mechanisms, spectral features and excited-state dynamics[4] Recent advances in the optical spectroscopy of semiconducting SWNTs have revealed specific spectral characteristics of structurally distinct tube species,[5] the excitonic nature and binding energy of elementary excitations,[6,7] and ultrafast dynamics at both the single tube and ensemble levels[8].

One of the greatest challenges in the spectroscopic studies is the substantial heterogeneity in the samples currently available, which contain a variety of tube species with different indexes (n, m). Besides metallic tubes, the samples typically contain variable amounts of semiconducting species with diameter distribution depending critically on the synthetic conditions[5,9–11]. Even for the same tube type, the length, curvature, defect and surfactant wrapping can vary substantially from one tube to another. As a result, the frequency of a given excitonic transition varies accordingly, giving rise to significant inhomogeneous broadening of spectral lines. Assessment of the intrinsic, homogeneous linewidth is not possible from linear spectroscopic measurements of nanotube ensembles due to their inherent limitation in differentiating fast fluctuations of the transition frequencies (homogeneous broadening) from the static distributions (inhomogeneous broadening). Although such information should in principle be accessible by single tube spectroscopy, the reported results so far differ remarkably even for the same tube type, owing presumably to occurrence of defects,[12,13] unintentional doping,[14] and/or differences in tube environments.[12,13]

In this paper, we report an experimental study of the spectral line broadening of the lowest allowed excitonic transitions of semiconducting SWNTs by exploiting two femtosecond four-wave mixing (FWM) techniques. Application of three-pulse stimulated photon echo peak shift (3PEPS) spectroscopy[15,16] in combination with data simulations enable a clear separation of the homogeneous and inhomogeneous broadening of the selected spectral line directly through measurements on nanotube ensembles, and provides estimates of the strength and timescales of electron-phonon coupling. A complimentary technique employing degenerate two-pulse FWM spectroscopy or two-pulse photon echo (2PE) allows for quantification of the timescale of exciton dephasing and independent determination of the corresponding homogeneous linewidth. Furthermore, transient grating (TG) and pump-probe (PP) spectroscopy permit measurement of exciton population relaxation dynamics under the excitation intensities used for 3PEPS and 2PE experiments, respectively.

8.2 Experimental Methods

The sample used for this study is a nanotube-polymer composite film of $\sim$200 μm thickness. Use of such a sample greatly suppresses scattering arising from slow tube motion in an

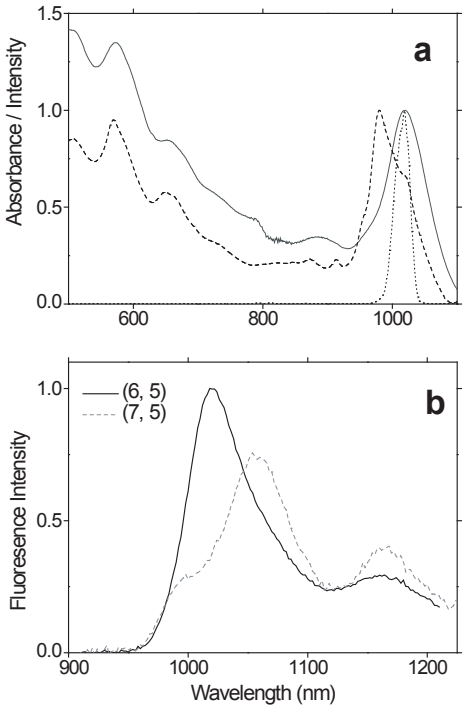

Figure 8.1. a) Linear absorption spectra of the SWNT/PVP composite film (solid line) and the D_2O solution of the NaDDBS dispersed SWNTs (dashed line), which was used to fabricate the SWNT/PVP film. The dotted line is the laser pulse spectrum. Both absorption spectra are normalized at the peaks of the E_{11} transitions, and the laser pulse spectrum is scaled to match the E_{11} peaks. (b) Steady-state fluorescence emission spectra measured for the SWNT/PVP film upon resonant excitation of the E_{22} transitions of the (6, 5) and (7, 5) tubes at 572 and 655 nm, respectively.

aqueous solution, and enables measurement of photon echo signals at low excitation powers and long population times with a high signal-to-noise ratio. The starting material is a commercial D_2O suspension of the CoMoCAT nanotubes dispersed individually with surfactant sodium dodecylbenzene sulfonate (NaDDBS, SouthWest Nano Technologies, Inc.). The suspension was mixed with appropriate amount of water-soluble polyvinylpyrrolidone (PVP) polymer, drop-cast in layers into a Teflon mold and slowly dried in a desiccator to yield an optical quality sample with no visible aggregation. Although the linear absorption spectrum of the polymer film exhibits a clear red-shift and enhanced background with respect to the spectrum of the corresponding aqueous solution (Fig. 8.2a), the steady-state fluorescence emission spectra of the film show no sign of significant tube aggregation. As shown in Fig. 8.2b, upon resonant excitation of the second allowed excitonic states (E_{22}) of the (6, 5) and (7, 5) tubes, the emission from the corresponding E_{11} states is much stronger than the emission band around 1150 nm. The presence of a broad, intense emission in the 1150 nm spectral region has been shown to indicate tube bundling.[17,18]

The 3PEPS technique employed here has been described extensively elsewhere.[15,16,19,20] In short, the light source was a 250-kHz Ti:Sapphire regenerative amplifier pumped optical parametric amplifier that generates 62 fs pulses with a central wavelength of 1018 nm. The laser pulse spectrum is indicated by the dotted line in Fig. 8.2a. This excitation wavelength was chosen to resonantly excite the lowest transition-allowed excitonic states (E_{11}) of the (6, 5) as well as the (7, 5) nanotubes, with the majority of absorption coming from the (6, 5) tubes. The laser beam was split into three replicas of equal intensity with wave vectors $\mathbf{k}_1$, $\mathbf{k}_2$ and $\mathbf{k}_3$, and focused to the sample with a 15-cm singlet lens. Time-integrated photon echo signals at the two phase-matching directions $\mathbf{k}_1$ - $\mathbf{k}_2$ + $\mathbf{k}_3$ and -$\mathbf{k}_1$ + $\mathbf{k}_2$ + $\mathbf{k}_3$ were detected simultaneously with two InGaAs photodiodes connected to separate lock-in amplifiers. The intensity of the incident light was controlled with a waveplate and polarizer combination, and monitored with a reference photodiode. TG signals were measured using the same setup by setting the time delay between the $\mathbf{k}_1$ and $\mathbf{k}_2$ pulses to zero.

Separate 3PEPS measurements were also performed at selected excitation intensities on an aqueous suspension of individualized SWNTs. A quartz cell with a path length of 100 μm was employed in order to minimize laser light scattering and thermal lensing effects. As the measurements on the aqueous solution produced similar results to those obtained from the polymer film at similar intensities, we will focus on the data collected using the film which is of higher signal to noise ratio. All measurements were performed at room temperature (294 K).

The same setup was used for the two-pulse FWM experiment by blocking the third beam ($\mathbf{k}_3$), and the diffracted signal was detected at the phase-matching direction $2\mathbf{k}_2$ - $\mathbf{k}_1$. In order to directly time resolve the exciton dephasing process from the diffracted signal, a shorter laser pulse with duration of 45 fs was employed. Simultaneous detection of the $\mathbf{k}_1$ beam after passing through the sample further enabled measurement of the PP signals.

8.3 Results and Discussion

Representative time-integrated photon echo profiles collected in the two phase matching directions $\mathbf{k}_1$ - $\mathbf{k}_2$ + $\mathbf{k}_3$ (open circles) and -$\mathbf{k}_1$ + $\mathbf{k}_2$ + $\mathbf{k}_3$ (filled circles) are shown in Fig. 8.2 for the population times T = 0, 50, 500 and 900 fs. The echo signals are symmetric along the axis of coherence time (τ). The peak shift (τ^*) at each population time T are obtained by fitting each of the echo signals to a Gaussian function and then calculating half the difference between their maxima. This calculation gives peak shifts of 26.7, 18.2, 12.8 and 12.6 fs for the data shown in Fig. 8.2, which progressively decreases with T in response to electronic dephasing induced by nuclear motions.[21,22] As discussed extensively in previous studies on molecular systems and quantum dots,[19,21,23] the echo peak shift (τ^*) plotted as a function of the population time is related to the time correlation function of the electronic transition frequencies $M(t)$,[16,22]

$$M(t) = \frac{\langle \delta\omega_{eg}(0)\delta\omega_{eg}(t)\rangle}{\langle \delta\omega_{eg}^2\rangle} \tag{8.1}$$

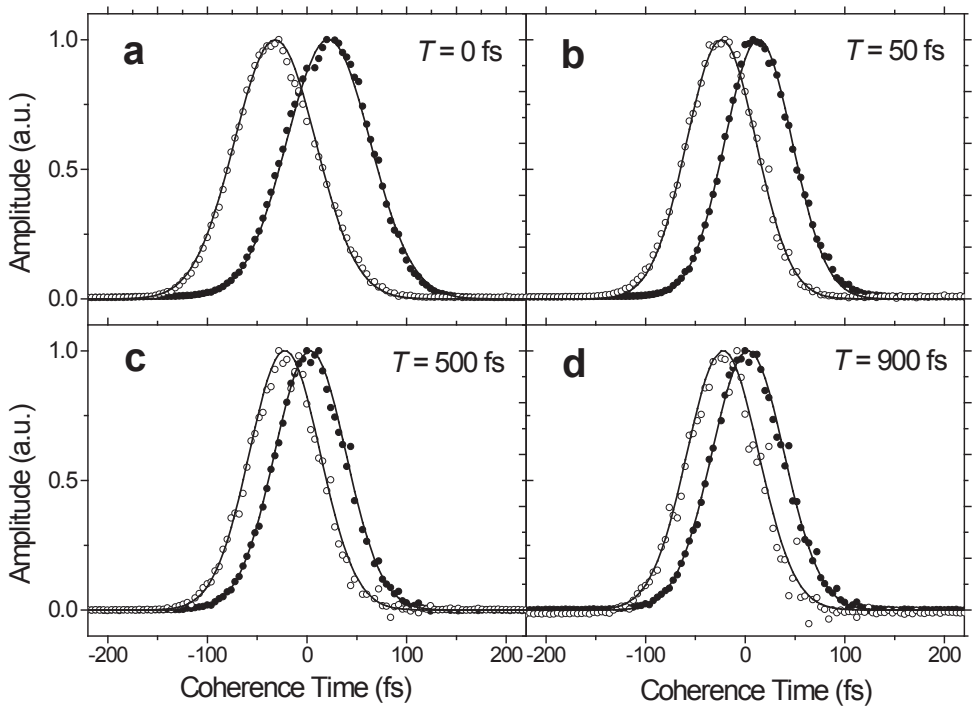

Figure 8.2. Normalized integrated photon echo profiles collected in the two phase matching directions $\mathbf{k}_1$ - $\mathbf{k}_2$ + $\mathbf{k}_3$ (open circles) and -$\mathbf{k}_1$ + $\mathbf{k}_2$ + $\mathbf{k}_3$ (filled circles) for the population times $T = 0$ (a), 50 (b), 500 (c) and 900 fs (d), respectively. The solid lines are the fits to Gaussian functions.

where $\delta\omega_{eg}$ is the transition frequency from the ground to the E_{11} state.

Measurements on aqueous SWNT suspensions produced essentially identical 3PEPS results (see Fig. 8.3a, open squares) to those obtained using the PVP polymer film at comparable excitation intensities. This similarity indicates that the dynamics detected using 3PEPS spectroscopy are highly insensitive to the environment outside the nanotube and surfactants, and thus are in stark contrast to the dynamics of exciton population relaxation.[24–26] More importantly, the similarity between the results measured from the aqueous solution and the PVP films confirms that embedding SWNT into PVP polymer films does not induce additional broadening of the spectral line-width. Otherwise, the residual peak shift at long population time ($T > 300$ fs) would be larger than that observed from the aqueous suspension. Moreover, this similarity provides further additional support for the absence of substantial tube aggregation in the polymer film samples.

One surprising finding of our 3PEPS studies is the strong dependence of peak shift on excitation intensity. As shown in Fig. 8.3a, the peak shift at a given population time increases sharply with decreasing excitation intensity. When the intensity is decreased 27 times, the peak shift increases at all population times by ~ 25 fs. To the best of our knowledge, such a dependence has not been observed for molecular systems or other nanoscale materials. While the observed peak shifts depend strongly on excitation intensity (see Fig. 8.3b), the decay timescale of the 3PEPS profiles themselves are largely invariant to intensity effects. This invariance is best illustrated by overlaying the peak shift profiles (Fig. 8.3b, inset) onto the curve collected at the lowest intensity. Each of the 3PEPS profiles can be satisfactorily described by a mono-exponential decay with a 60 fs decay constant and a time-independent non-zero offset. This time constant is very different from the time scales of exciton population relaxation, which were determined through TG measurements at the corresponding excitation intensities (see Fig. 8.3b). The TG signals measured at different intensities exhibit essentially identical kinetics, with their peak amplitudes linearly proportional to the excitation intensity. This behavior is fully consistent with the results of previous PP measurements.[27] To extract the time scales of population relaxation from the TG data, we preformed deconvolution fitting by explicitly considering the finite laser pulse width and the E-field squared nature of the TG signal. This fitting gives two time scales of 130 and 790 fs, both are much longer than the 60 fs decay time of the 3PEPS profiles.

The intensity dependence of peak shifts arises from exciton-exciton scattering and annihilation, and its analysis will be described elsewhere. Instead, we focus our analysis on extracting absorption lineshape information from the 3PEPS profile in the limit of zero-intensity, where complications from exciton-exciton interactions can be neglected. The invariance in the decay behavior of the 3PEPS profiles with excitation intensity (see Fig. 8.2b, inset) enables us to construct a zero-intensity 3PEPS profile. This construction involves measuring the peak shifts under different excitation intensities at selected population times, and then extrapolating the experimental data to the limit of zero-intensity. This extrapolation gives a $\tau^*(T= 0) = 52$ fs, which is only marginally higher than the $\tau^*(T= 0) = 50$ fs measured at the lowest experimental excitation energy (0.60 μJ/cm^2 for all three beams). The constructed zero-intensity profile shown in Fig. 8.3 is obtained by shifting the entire 3PEPS

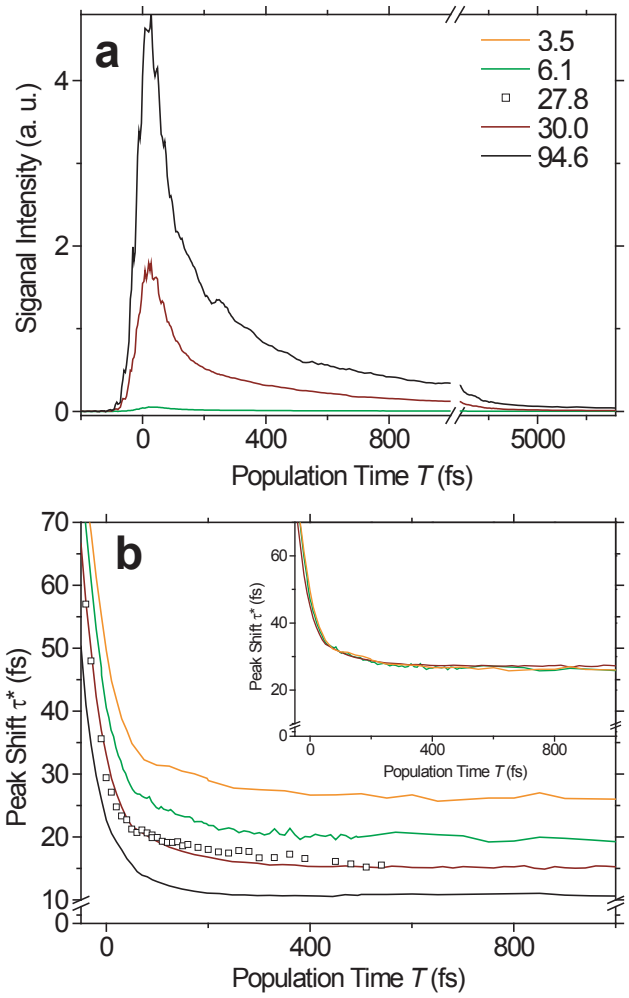

Figure 8.3. (a) Transient grating signals measured on the SWNT/PVP films (line colors match with corresponding 3PEPS excitation intensities in μJ/cm^2). (b) Three-pulse echo peak shifts measured on the SWNT/PVP film at four different excitation intensities (in μJ/cm^2). The inset shows that the 3PEPS profile collected at different intensities can all be superimposed by means of a linear shift in peak shift. The open squares depict the data collected from the aqueous solution at an excitation intensity of 27.8 μJ/cm^2. Due to pronounced scattering, measurement was possible only for a limited range of population times.

profile measured at the lowest excitation intensity by a 2 fs increment in peak shift. The resulting 3PEPS profile can then be modeled by conventional methods, since all the effects from the exciton-exciton interactions which dominate at higher intensities become negligible.

Our data simulation involves constructing an $M(t)$ that is capable of reproducing both the peak shift curve and the experimental linear absorption spectrum in the high-temperature limit ($2k_B^T \gg \hbar\omega$, ω is the frequency of vibrations).[15,22,28] A detailed description of the general procedure and the related theoretical background can be found in references 22,23,29 We begin our simulations with a simple form of $M(t)$, composed of a gaussian, exponential and static inhomogeneity terms. This simulation is found to capture the overall features of the extrapolated 3PEPS profiles except the weak oscillatory behavior. To improve the match between the simulation and the extrapolated zero-intensity 3PEPS profile, we add an additional term to simulate a damped vibrational frequency present in our data. The $M(t)$ can be written as,

$$M(t) = A_g \exp\left[-\left(\frac{t}{\tau_g}\right)^2\right] + A_e \exp\left(\frac{-t}{\tau_e}\right) + A_c \exp\left(\frac{-t}{\tau_c}\right)\cos(\omega_c t + \phi_c) + \sigma_{in}^2, \qquad (8.2)$$

where A and τ are the corresponding coupling strengths and time constants, respectively. Static inhomogeneity σ_{in} is also included, which is defined as the standard deviation of the inhomogeneous distribution of transition frequencies. The simulated curve is in excellent agreement with the extrapolated zero-intensity 3PEPS profile (see the solid line in Fig. 8.3a). The parameters determined from this simulation areA_g = 2 cm^{-1}, τ_g= 20 fs, A_e = 18 cm^{-1}, τ_e= 200 fs and σ_{in} = 300 cm^{-1}. Note that $A_e + A_g$ = 20 cm^{-1} is approximately one half the Stokes shift of the (6, 5) tubes, which equals to the total reorganization energy according to the fluctuation-dissipation theorem. Among the four additional parameters A_c, τ_c, ω_c and ϕ_c; ω_c was predetermined by independent curve-fitting employing an algorithm based on singular-value decomposition. The extracted frequency of 245 cm^{-1} is fairly close to the frequency of the radial breathing mode (RBM) of 282 cm^{-1} observed from a resonant Raman measurement on the PVP film sample (data not shown). The rest of the vibrational parameters extracted from our simulations are A_c = 10 cm^{-1}, τ_c = 120 fs and a phase factor ϕ_c= 4.5 rad.

To verify that the simulation parameters used are physically reasonable, we simulated the linear absorption spectrum via the relation

$$\sigma(\omega) = \frac{1}{\pi} Re \int_0^\infty dt \exp[i(\omega - \omega_{eg})t - g(t)], \qquad (8.3)$$

where ω_{eg} is the transition frequency of the system and $g(t)$ is the line-broadening function that is obtained from $M(t)$.[22] As shown in Fig. 8.3b, the simulated spectrum fits rather well to the experimental absorption spectrum, with an overall full width of half maximum (FWHM) of 720 cm^{-1}. The corresponding homogenous linewidth is calculated by setting σ_{in} to zero in eq. 2, resulting in a value of 178 cm^{-1}. These results give a ratio of overall to homogeneous widths of 4.1. Note that the total width is an overestimate of the E_{11} band associated with the (6, 5) tube because of the contribution from the (7, 5) tube and

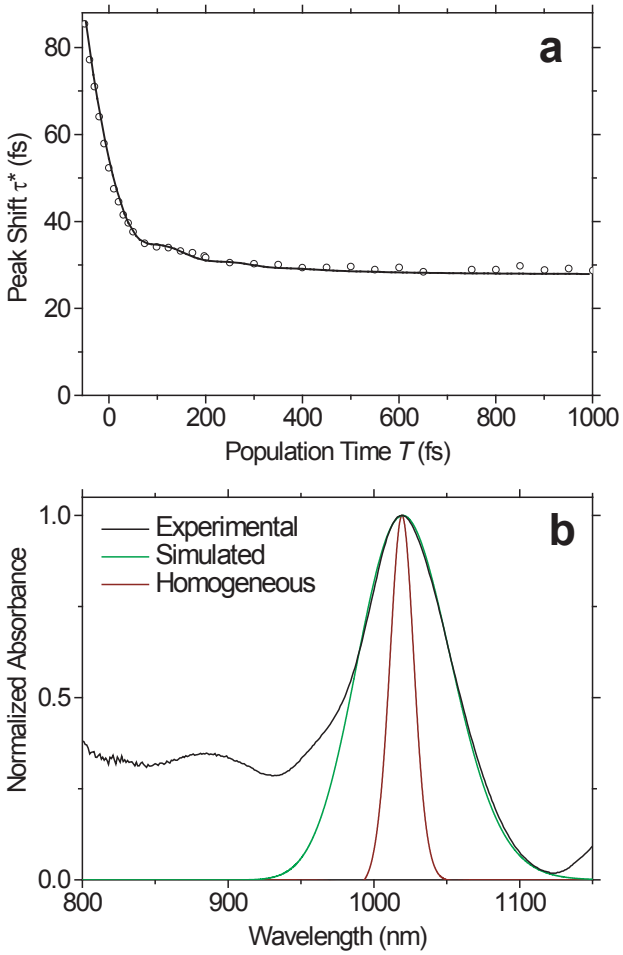

Figure 8.4. (a) Zero-intensity three-pulse echo peak shift profile obtained by extrapolating the experimental data collected at 0.6 μm/cm^2. The solid line is the simulated curve based on the $M(t)$ described in eq. 2. (b) Measured (black line) and simulated (green line) absorption spectra. The red line represents the homogenous line shape calculated by setting σ_{in} to zero (see text for details).

others. Based on Gaussian decomposition of the broad featureless absorption band of the PVP sample in the E_{11} region, we estimate that the contribution from the (7, 5) and other tubes should not be greater than 25 % of the total width. The homogeneous width may be also overestimated by a similar amount.

From the frequency and coupling strength of the vibrational contribution, we can further calculate the Huang-Rhys factor$S = \Delta^2/2 = A_c/\hbar\omega_c = 0.04$, where Δ is the dimensionless displacement between potential minima of the ground state and the resonant electronic state.[21] This value is fully consistent with the results of recent *ab initio* calculations[30] and Raman experiments,[31] and provides further evidence for weak exciton-phonon coupling in semiconducting SWNTs. Our simulations further provide one of the first experimental estimates for the time scale ($\tau_c = 120$ fs) for the damping of the RBM vibrational mode. The damping time is significantly shorter than the overall exciton population relaxation times, but is comparable to the timescale obtained for pure dephasing.

The exceptionally large values of the initial peak shift $\tau^*(T= 0$ fs) make semiconducting SWNTs distinct from all previously studied molecular systems studied with similar pulse durations.[15,32,33] At the lowest excitation intensity possible (0.60 μm/cm^2), we measured a initial peak shift of 50 fs. A slightly larger value of 52 fs is obtained by extrapolating the experimental data to the limit of zero intensity. Generally, large initial peak shift values are indicative of weak electron-phonon coupling.[16,20] This is fully consistent with the small Huang-Rhys factor calculated using the simulation parameters. It is also in line with the rather small Stokes shift and reorganization energy, the latter was required for simulating our 3PEPS results. Further work is required, however, to determine the influence of the delocalization length of the coherent excitons on the effective exciton-phonon coupling. The extent to which exchange narrowing related effects, such as seen in molecular aggregates,[34] reduces the apparent exciton phonon coupling strength is not yet clear.

As an independent verification of the homogeneous linewidth extracted from the simulation, we performed two-pulse FWM measurements on the same film sample. Fig. 8.3a shows the time-integrated FWM signal measured at an excitation intensity of 4.2 μJ/cm^2, along with the auto-correlation profile of the two laser pulses (dotted line) and the fitting result (solid line). The FWM signal exhibits an essentially instantaneous rise for the negative delay times and reaches a maximum at a positive delay of + 37 fs. This shift from the zero delay time corresponds well to the peak shift at $T = 0$ determined at a similar intensity. The decay of the FWM signal is best characterized by a timescale of τ_d= 19.5 fs, obtained through a least squares fit with explicit consideration of the finite temporal response. From the extracted timescale τ_d, we calculate the FWHM homogeneous linewidth Γ_h through a simple relation $\Gamma_h = 2\hbar/T_2$, where the dephasing time T_2 is obtained from τ_d by $T_2 = 4\tau_d$[35] Although the latter relation is strictly valid only for a strongly inhomogeneously broadened, independent two-level system, our recent study on a sample that is highly enriched in a single tube species shows that the homogeneous linewidths obtained with this expression at different temperatures agree very well with the results of a single tube photoluminescence experiment[36] Calculation based on the same relation gives an homogeneous linewidth of 136 cm^{-1}at room temperature, which is fairly close to the value (178 cm^{-1}) determined from our 3PEPS simulation.

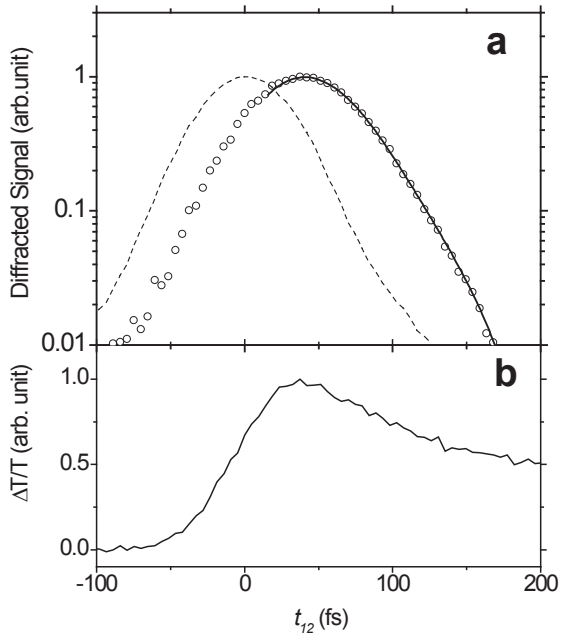

Figure 8.5. (a) Two pulse echo signal measured at an excitation intensity of 4.2 μJ/cm^2. The solid line is the result of least squares deconvolution fitting, and the dotted line is the auto-correlation of laser pulses measured using thin nonlinear BBO crystal. (b) Pump-probe signal recorded simultaneously.

A simultaneously measured PP signal has a much slower decay (see Fig. 8.3b) and excludes any significant contribution from exciton population relaxation to the observed FWM signal decay. Based on the well-known relation between the dephasing time T_2, pure dephasing time T_2^* and the population relaxation time T_1 for a two-level system

$$\frac{1}{T_2} = \frac{1}{T_2^*} + \frac{1}{2T_1}, \tag{8.4}$$

we can deduce a T_2^* value of 78 fs at room temperature. This result suggests that a proper description of ultrafast exciton dynamics in semiconducting SWNTs should take exciton coherence into account even at room temperature.

8.4 Conclusions

In summary, we have demonstrated that photon echo spectroscopy is an incisive technique for elucidating spectral lineshape information through ensemble measurements of semiconducting SWNTs. We observed a strong dependence of the peak shift on excitation intensity owing to simultaneous creation of multiple excitons and their mutual interactions. To overcome these multi-exciton complications, and to extract absorption lineshape information, we simulate the 3PEPS profile obtained in the limit of zero-excitation intensity. We find that the linear absorption spectrum associated with the transitions from the ground-states to the E_{11} excitonic states of the abundant tube species is dominated by inhomogeneous broadening with a FWHM of 698 cm^{-1}. A much narrower homogeneous linewidth with a FWHM of 178 cm^{-1} is obtained, which is close to the value (136 cm^{-1}) determined from a separate two-pulse degenerate FWM experiment at low but finite excitation intensity. The total width (720 cm^{-1}) is overestimated for the spectral band of the (6, 5) tube because of the contribution from the (7, 5) and other tubes, which amount to no greater than 25 %. Determination of the very short decay time of the two-pulse FWM signal compared with the exciton population relaxation further enables us to conclude that the obtained finite homogeneous width arises primarily from a pure exciton dephasing process. Moreover, the exceptionally large initial peak shift observed at$T = 0$ suggests weak exciton-phonon coupling. This is further supported by the small Huang-Rhys factor calculated for the RBM using the simulated parameters. Future study employing ultrashort laser pulses of < 20 fs should enable assessment of the coupling strengths of high-frequency vibrational modes and excitons.

8.5 References

[1] Saito, S.; Dresselhaus, G.; Dresselhaus, M. S. *Physical Properties of Carbon Nanotubes*; Imperial College Press, London, 1998.

[2] Odom, T. W.; Huang, J.-L.; Kim, P.; Lieber, C. M. *J. Phys. Chem. B* **2000**, 104, 2794.

[3] Baughman, R. H.; Zakhidov, A. A.; de Heer, W. A. *Science* **2002**, 297, 787.

[4] Dresselhaus, M. S.; Dresselhaus, G.; Saito, R.; Jorio, A. *Annu. Rev. Phys. Chem.* **2007**, 58, 719.

[5] Bachilo, S. M.; Strano, M. S.; Kittrell, C.; Hauge, R. H.; Smalley, R. E.; Weisman, R. B. *Science* **2002**, 298, 2361.

[6] Wang, F.; Dukovic, G.; Brus, L. E.; Heinz, T. F. *Science* **2005**, 308, 838.

[7] Ma, Y.-Z.; Valkunas, L.; Bachilo, S. M.; Fleming, G. R. *J. Phys. Chem. B* **2005**, 109, 15671.

[8] Ma, Y.-Z.; Hertel, T.; Vardeny, Z. V.; Fleming, G. R.; Valkunas, L. Ultrafast spectroscopy of carbon nanotubes. In *Topics Appl. Phys.*; Jorio, A., Dresselhaus, G., Dresselhaus, M. S., Eds.; Springer-Verlag Berlin: Heidelberg, 2008; Vol. 111; pp 321.

[9] Bachilo, S. M.; Balzano, L.; Herrera, J. E.; Pompeo, F.; Resasco, D. E.; Weisman, R. B. *J. Am. Chem. Soc.* **2003**, 125, 11186.

[10] Lebedkin, S.; Schweiss, P.; Renker, B.; Malik, S.; Hennrich, F.; Neumaier, M.; Stoermer, C.; Kappes, M. M. *Carbon* **2002**, 40, 417.

[11] Miyauchi, Y.; Chiashi, S.; Murakami, Y.; Hayashida, Y.; Maruyama, S. *Chem. Phys. Lett.* **2004**, 387, 198.

[12] Hagen, A.; Steiner, M.; Raschke, M. B.; Lienau, C.; Hertel, T.; Qian, H.; Meixner, A. J.; Hartschuh, A. *Phys. Rev. Lett.* **2005**, 95, 197401.

[13] Lefebvre, J.; Austing, D. G.; Bond, J.; Finnie, P. *Nano Lett.* **2006**, 6, 1603.

[14] Htoon, H.; O'Connell, M. J.; Cox, P. J.; Doorn, S. K.; Klimov, V. *Phys. Rev. Lett.* **2004**, 93, 027401.

[15] Joo, T.; Jia, Y.; Yu, J.-Y.; Lang, M. J.; Fleming, G. R. *J. Chem. Phys.* **1996**, 104, 6089.

[16] Cho, M.; Yu, J.-Y.; Joo, T.; Nagasawa, Y.; Passino, S. A.; Fleming, G. R. *J. Phys. Chem.* **1996**, 100, 11944

[17] Torrens, O. N.; Milkie, D. E.; Zheng, M.; Kikkawa, J. M. *Nano Lett.* **2006**, 6, 2864.

[18] Tan, P. H.; Rozhin, A. G.; Hasan, T.; Hu, P.; Scardaci, V.; Milne, W. I.; Ferrari, A. C. *Phys. Rev. Lett.* **2007**, 99, 137402.

[19] Jimenez, R.; van Mourik , F.; Yu, J. Y.; Fleming, G. R. *J. Phys. Chem. B* **1997**, 101, 7250.

[20] Agarwal, R.; Yang, M.; Xu, Q.-H.; Fleming, G. R. *J. Phys. Chem. B* **2001**, 105, 1887.

[21] Salvador, M. R.; Hines, M. A.; Scholes, G. D. *J. Chem. Phys.* **2003**, 118, 9380.

[22] Mukamel, S. *Principles of Nonlinear Optical Spectroscopy*; Oxford University Press: New York, 1995.

[23] Fleming, G. R.; Passino, S. A.; Nagasawa, Y. *Phil. Trans. R. Soc. Lond. A* **1998**, 356, 389.

[24] McDonald, T. J.; Engtrakul, C.; Jones, M.; Rumbles, G.; Heben, M. J. *J. Phys. Chem. B* **2006**, 110, 25339

[25] Hertel, T.; Hagen, A.; Talalaev, V.; Arnold, K.; Hennrich, F.; Kappes, M.; Rosenthal, S.; McBride, J.; Ulbricht, H.; Flahaut, E. *Nano Lett.* **2005**, 5, 511.

[26] Ostojic, G. N.; Zaric, S.; Kono, J.; Strano, M. S.; Moore, V. C.; Hauge, R. H.; Smalley, R. E. *Phys. Rev. Lett.* **2004**, 92, 117402.

[27] Ma, Y.-Z.; Valkunas, L.; Dexheimer, S. L.; Bachilo, S. M.; Fleming, G. R. *Phys. Rev. Lett.* **2005**, 94, 157402.

[28] de Boeij, W. P.; Pshenichnikov, M. S.; Wiersma, D. A. *Chem. Phys. Lett.* **1996**, 253.

[29] Fleming, G. R.; Cho, M. *Annu. Rev. Phys. Chem.* **1996**,47, 109.

[30] Tretiak, S.; Kilina, S.; Piryatinski, A.; Saxena, A.; Martin, R. L.; Bishop, A. R. *Nano Lett.* **2007**, 7, 86.

[31] Shreve, A. P.; Haroz, E. H.; Bachilo, S. M.; Weisman, R. B.; Tretiak, S.; Kilina, S.; Doorn, S. K. *Phys. Rev. Lett.* **2007**, 98, 037405.

[32] Homoelle, B. J.; Edington, M. D.; Diffey, W. M.; Beck, W. F. *J. Phys. Chem. B* **1998**, 102, 3044.

[33] Lee, J.-H.; Min, C.-K.; Joo, T. *J. Chem. Phys.* **2001**, 114, 377.

[34] Fidder, H.; Terpstra, J.; Wiersma, D. A. *J. Chem. Phys.* **1991**, 94, 6895.

[35] Shah, J. *Ultrafast spectroscopy of semiconductors and semiconductor nanostructures*, 2nd ed.; Berlin; New York: Springer Verlag, 1999.

[36] Ma, Y.-Z.; Graham, M. W.; Fleming, G. R.; Green, A. A.; Hersam, M. C. **2008**, 101, 217402.

Chapter 9

Exciton-Exciton Annihilation Induced Dephasing

Three-pulse photon echo peak shift measurements were performed on semiconducting single-walled carbon nanotubes embedded in a polymer matrix at room temperature. We found a striking dependence of the peak shift on the excitation intensity. Numerical simulations based on a newly developed interacting-boson model demonstrate that the intensity dependence originates from a highly-nonlinear optical response initiated by exciton-exciton annihilation.

9.1 Introduction

The optical properties of semiconducting single-walled carbon nanotubes (SWNTs) are governed by excitons with anomalously large binding energies [1, 2, 3]. Understanding of exciton dynamics is important from the prospective of both fundamental research and potential applications [4]. Recently, investigations on the coherent phenomena of the excitons have emerged [5, 6]. Experiments in the time domain reveal that the dependence of the exciton dephasing rate ($1/T_2$) on excitation intensity changes markedly with temperature [6]. At 77, 100 and 130 K, a linear dependence on intensity is found, whereas a clear deviation is evident at higher temperature. This deviation indicates possible contributions from inelastic exciton-exciton scattering processes. A significant shortening of exciton population

relaxation times, T_1, with increasing temperature [7, 8] can enhance exciton dephasing at high temperature through the well-known relation: $1/T_2 = 1/T_2^* + 1/2T_1$ ($1/T_2^*$ is the pure dephasing rate). The results of recent single tube photoluminescence spectroscopy lend support to this inference, where a nonlinear dependence of homogeneous linewidth on excitation intensity was observed and attributed to exciton-exciton annihilation [5].

To unambiguously identify the effect of population relaxation on exciton dephasing, we employ time-integrated three-pulse photon echo peak shift (3PEPS) spectroscopy [9], which is capable of detecting simultaneously exciton dephasing and population relaxation. A key distinction of this incisive tool from conventional two-pulse photon echo or, equivalently, two-pulse degenerate four-wave mixing spectroscopy, is the presence of a population period. It offers the capability of elucidating directly the electronic dephasing induced by population transfer processes within the bandwidth of employed laser pulses. We present 3PEPS data for selected semiconducting SWNTs embedded in a solid polymer film. Surprisingly, we find a strong dependence of the photon echo peak shift on excitation intensity, which increases approximately exponentially with decreasing intensity. Note that previous intensive studies on molecules, molecular complexes and aggregates, and polymeric systems have shown that the peak shift is highly insensitive to the processes taking population out of the laser bandwidth [9].

To identify the origin of this striking intensity dependence, we carried out theoretical model simulations. Third order nonlinear response theory predicts that a plot of the peak shift as a function of population time T follows closely the correlation function of transition energy fluctuation [10, 11], and its signal amplitude is proportional to the cube of excitation intensity. The strong dependence on the intensity observed in this study thus goes beyond the third order nonlinearity. We use a Mean-Field-Approximation (MFA) combined with non-perturbative numerical simulations to convert a complex many-exciton problem into a single exciton problem, and most importantly to calculate the contributions of induced polarizations beyond the usual third-order response. By extracting up to the 10th order contributions we show that the exciton-exciton annihilation process contributes substantially to the observed intensity dependent photon echo peak shift [12].

9.2 Experimental Methods

A commercial D_2O solution of the CoMoCAT nanotubes wrapped with surfactant sodium dodecylbenzene sulfonate (NaDDBS) was used to fabricate a thin SWNT-PVP (polyvinylpyrrolidone) composite film of $\sim$ 200 μm thickness. Use of this solid sample enables significant suppression of the light scattering arising from the motion of nanotubes in the solution sample. A dichloroethane solution of laser dye IR26 was used for reference measurements, which was circulated through a 200 μm thickness flow cell with a peristaltic pump.

The 3PEPS technique employed here has been described extensively elsewhere [13]. In short, the light source was an optical parametric amplifier pumped by a 250-kHz Ti:Sapphire

regenerative amplifier, generating 62 fs pulses at 1018 nm. This wavelength was chosen in order to excite resonantly the lowest transition-allowed excitonic state (E_{11}) of the dominant semiconducting species, the (6,5) tube. The laser beam was split into three replicas of equal intensity with wave vectors $\boldsymbol{k_1}$, $\boldsymbol{k_2}$ and $\boldsymbol{k_3}$, and focused to the sample by a 15-cm focal length singlet lens. Time-integrated photon echo signals at the two phase matching directions $\boldsymbol{k_1} - \boldsymbol{k_2} + \boldsymbol{k_3}$ and $-\boldsymbol{k_1} + \boldsymbol{k_2} + \boldsymbol{k_3}$ were detected simultaneously with two InGaAs photodiodes connected to separate lock-in amplifiers.

Representative time-integrated photon echo profiles collected in the two phase matching directions for a population time $T = 50$ fs are plotted as a function of coherence time τ in the inset of Fig. 9.1. The peak shift at each T is obtained by calculating half the difference between their maxima. The 3PEPS data collected at three different excitation intensities are plotted in Fig. 9.1 as a function of T. The most intriguing feature of the data is that the peak shift, $\tau^*(T)$, strongly depends on excitation intensity. For a given T, an increase of the intensity leads to an approximately exponential decrease of $\tau^*(T)$. This dependence is illustrated in Fig. 9.1a through the peak shift measured at $T = 0$. By contrast the data obtained from a IR26 solution (filled orange circles in Fig. 9.2a) shows a very small increase (< 4 fs) in accord with third order nonlinear response theory.

Fig. 9.2b compares dependence of the peak amplitude on intensity for SWNTs and IR26. The latter exhibits the expected cubic dependence, whereas the former saturates at very low intensity. A similar saturation behavior was also observed previously for the amplitude of the pump-probe signal and was identified unambiguously as originating from exciton-exciton annihilation [12]. Clearly, the photon echo signal from the SWNTs is no longer governed by the third-order induced polarization, and thus higher-order contributions must be taken into account in order to adequately simulate the unusual intensity-dependent peak shift data.

9.3 Simulations

Theoretical description of the correlations of multiple excitons in semiconductors is a challenging many-body problem [14, 15]. At the third order in the field, description of a two-exciton scattering process must account for not only the Coulomb interactions between the electrons and holes but also their Pauli exclusion.

The simplest tight-binding model Hamiltonian of electrons and holes in a semiconductor (no phonons) in real space is [21]

$$\begin{aligned}\hat{H} = &\sum_i [\varepsilon_i^{(c)} \hat{c}_i^\dagger \hat{c}_i + \varepsilon_i^{(d)} \hat{d}_i^\dagger \hat{d}_i] + \sum_{ij}^{i \neq j} [V_{ij}^{(c)} \hat{c}_i^\dagger \hat{c}_j + V_{ij}^{(d)} \hat{d}_i^\dagger \hat{d}_j] \\ &+ \sum_{ij} [\frac{1}{2} W_{ij}^{(cc)} \hat{c}_i^\dagger \hat{c}_j^\dagger \hat{c}_j \hat{c}_i + \frac{1}{2} W_{ij}^{(dd)} \hat{d}_i^\dagger \hat{d}_j^\dagger \hat{d}_j \hat{d}_i - W_{ij}^{(cd)} \hat{c}_i^\dagger \hat{d}_j^\dagger \hat{d}_j \hat{c}_i]. \end{aligned} \tag{9.1}$$

Here $\hat{c}_i^\dagger$ is an electron creation operator at site i, $\hat{d}_i^\dagger$ is a hole creation operator; the operators without daggers are the conjugate annihilation operators. The electron on-site energies are

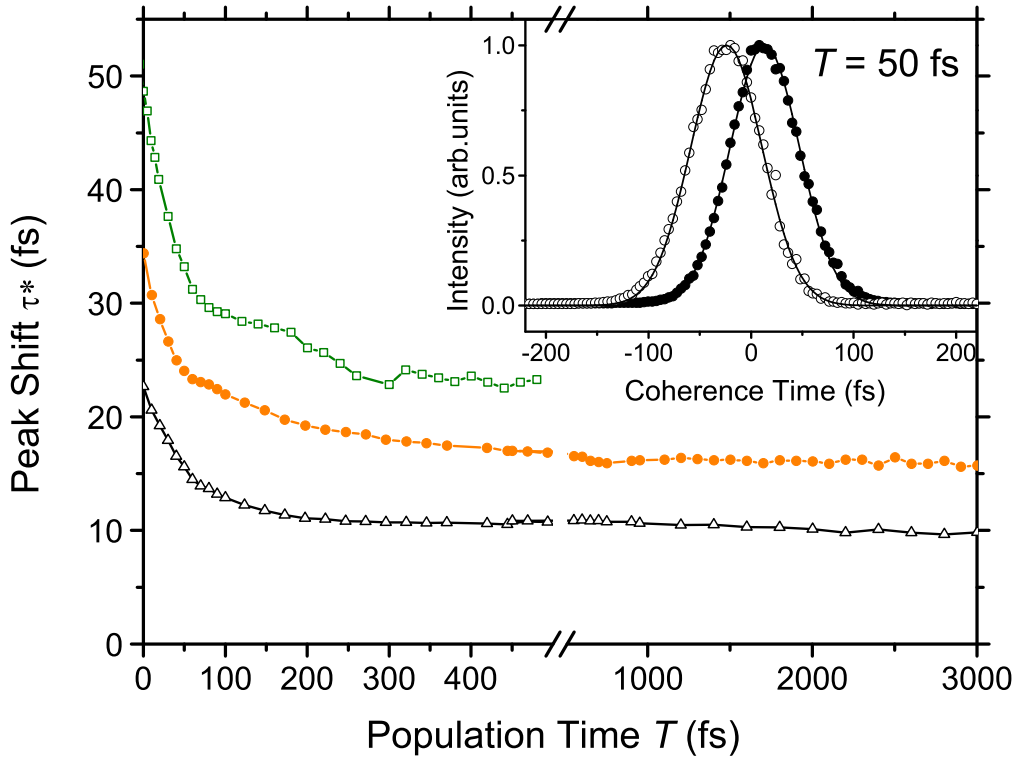

Figure 9.1. 3PEPS data obtained at three excitation intensities: 3.3 (green), 16.4 (orange) and 92.4 μJ/cm^2 (black). The inset shows the normalized time-integrated photon echo profiles collected in the two phase matching directions $\boldsymbol{k_1} - \boldsymbol{k_2} + \boldsymbol{k_3}$ (open circles) and $-\boldsymbol{k_1} + \boldsymbol{k_2} + \boldsymbol{k_3}$ (filled circles) for the population time $T = 50$ fs and an excitation intensity of 18.9 μJ/cm^2. The solid lines are the fits to Gaussian functions.

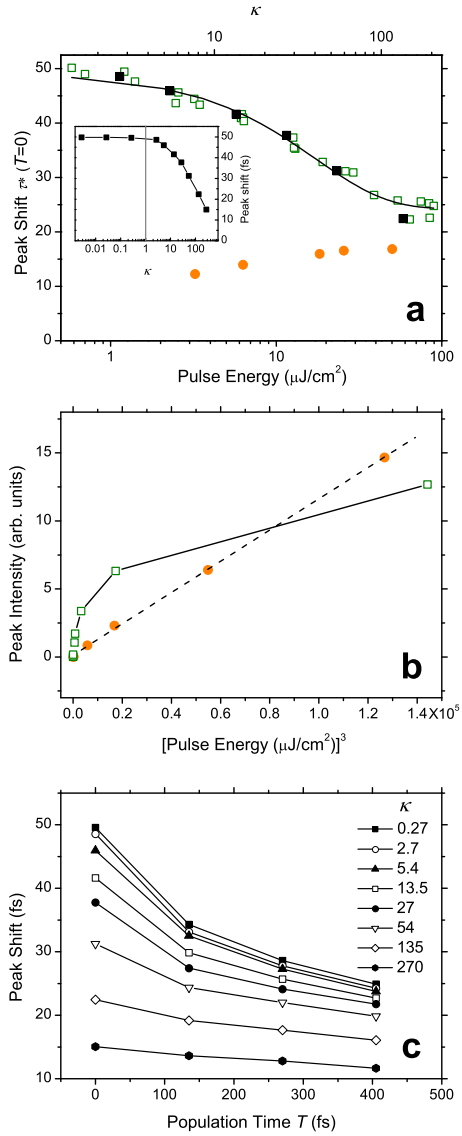

Figure 9.2. (a) The intensity dependence of the peak shifts at $T = 0$ fs obtained for the SWNT-PVP film (open green squares) and the IR26 solution (filled orange circles). The solid line is a mono-exponential fit. Black squares are the simulated result as a function of κ depicted by the scale on the top of the plot (see text). This simulated result is also shown in the inset for a broad range of κ values, and the vertical gray line is drawn for $\kappa = 1$, which separates the two intensity regimes. (b) Plot of the corresponding peak amplitudes of the time-integrated photon echo signals versus the cube of the excitation pulse energy. The dotted line is a linear fit to the IR26 data (orange), whereas the solid line through the SWNT data (green) is drawn to guide the eye. (c) Simulated 3PEPS decays at different intensities using Eq. 9.6. The solid lines connecting the symbols are for visual purposes.

$\varepsilon_i^{(c)}$, while those of holes are $\varepsilon_i^{(d)}$. Electron and hole hopping parameters are $V_{ij}^{(c)}$ and $V_{ij}^{(d)}$ respectively. These parameters characterize non interacting electrons and holes. The rest of the parameters are the Coulomb monopole-monopole interation energies: $W_{ij}^{(cc)}$ between two electrons on sites i and j, $W_{ij}^{(dd)}$ between two holes and $W_{ij}^{(cd)}$ between an electron and a hole. This Hamiltonian neglects exchange and four-point Coulomb integrals, however it captures the main exciton properties. The electrons and holes are fermions with nonzero anticommutators:

$$\hat{c}_i\hat{c}_j^\dagger + \hat{c}_j^\dagger\hat{c}_i = \delta_{ij}, \tag{9.2}$$

$$\hat{d}_i\hat{d}_j^\dagger + \hat{d}_j^\dagger\hat{d}_i = \delta_{ij}. \tag{9.3}$$

This Hamiltonian has been used to derive equations of motion for electrons and holes in semiconductors, where each atom is taken as a site. A hierarchy of equations of motion for electron and hole variables is obtained using the Heisenberg equation of motion. The hierarchy is truncated exactly at four-particle correlation functions when considering third order nonlinear optical signals. In this case only two electron-hole pairs need to be considered. Such an approach has been successfully used for semiconductors with the Hamiltonian parameters obtained from ab-initio simulations [14, 16, 17].

The nonlinear behavior of the final equations of motion originate from two sources: the Coulomb interaction and the Pauli exclusion resulting from the Fermion commutation relations. Instead of using the Fermion particle commutation relations for deriving equations of motion, the Pauli exclusion requirements in real space may be mapped into the nonlinear interaction potential of bosons as basic particles. While the boson commutation relations allow the existence of unphysical states, where two electrons (or two holes) as bosons may occupy the same state, such states may be excluded later by forcing their energies out of physical detection window, e. g. to infinity. The only anharmonic potential containing such divergencies is then solely responsible for nonlinear signals.

The four-point particle correlation truncation is approximate for our problem of high excitation intensities, because high-order many-body correlations may be important at these conditions. Their inclusion expands the hierarchy of necessary equations and the number of parameters considerably. The 3PEPS signal does not directly reveal the many-body resonances, instead it is most sensitive to various dephasing processes. Therefore instead of a full microscopic model, in this paper we develop a phenomenological model of delocalized interacting bosonic excitons representing exciton bands in momentum k space, as inspired by effective bosonization techniques[18, 19]. On the basis of delocalized excitons, we treat the exciton bands as an anharmonic ladder of single-exciton, two-exciton, etc delocalized exciton bands, which is a sufficient level of sophistication for calculating the 3PEPS signal. The starting point of our modeling is the Hamiltonian of interacting single-type bosons, which are excitons in our case, coupled to a phonon bath and an optical field $E(t)$:

$$\hat{H} = \sum_{mn}^{m\neq n}(\delta_{mn}h_{mm} + h'_{mn}(Q))(\hat{b}^\dagger)^m(\hat{b})^n - \hat{P}E(t) + \hat{H}_B, \tag{9.4}$$

where $h_{00} \equiv 0$, $\hat{b}^\dagger$ is the exciton creation operator, and $\hat{b}$ is the conjugate annihilation operator ($[\hat{b}, \hat{b}^\dagger] = 1$). $h_{11} \equiv \varepsilon$ is the energy of a single exciton, $h'_{mn}(Q)$ describes the

fluctuations induced by phonon coordinate Q, characterized by the bath Hamiltonian $\hat{H}_B$. Higher-orders of h determine nonlinear exciton properties, such as biexciton binding energies (h_{22}) and resonances, etc. In principle the h_{mm} parameter may be required for describing nonlinear signals up to mth order in the optical field. For isolated excitons ($h'_{mn} = 0$, $E = 0$), the Hamiltonian (9.4) conserves the number of particles. Since in the following we consider a resonant optical signal, where the laser is tuned to a single system resonance, this model of a single-type boson is sufficient to capture essential intensity-related effects. The interaction of the system with the optical field is represented by a polarization operator:

$$\hat{P} = \mu(\hat{b}^\dagger + \hat{b}), \tag{9.5}$$

where μ is the transition dipole.

This system response to the optical field is described by using perturbation theory with respect to the optical field. The Heisenberg equation is used to determine time evolution of the polarization operator, $i\hbar\dot{\hat{P}} = [\hat{H}, \hat{P}]$ [20, 21]. Since $\langle\hat{P}\rangle$ is proportional to $\langle\hat{b}\rangle$, we obtain the equations of motion for the expectation values of products of operators $\hat{b}$. The lowest-order exciton variable is $b \equiv \langle\hat{b}\rangle$; the induced polarization is then $P = \mu b + c.c.$. System nonlinearities lead to an infinite hierarchy of coupled differential equations. These can be closed at a certain order in the incoming field [20]. In the MFA at the third-order in the field a single equation is obtained [20, 21]:

$$\frac{d}{dt}b = -i(\varepsilon - i\frac{\gamma}{2})b - i(\Delta - i\frac{3}{2}\bar{\gamma})b|b|^2 + i\mu E(t), \tag{9.6}$$

where $\Delta \equiv h_{22}/2$ is the biexciton binding energy, γ is the linear exciton decay rate, and $\bar{\gamma}$ represents the nonlinear decay of excitons. These rates can be derived using second-order perturbation theory in the Markovian approximation from the off-diagonal fluctuation parameters h'_{10} and h'_{21}. They are given by the Fermi-Golden rule:

$$\gamma = \frac{2\pi}{\hbar}|h'_{10}|^2\rho(\varepsilon), \tag{9.7}$$

$$\bar{\gamma} = \frac{2\pi}{\hbar}|h'_{21}|^2\rho(\varepsilon + \Delta), \tag{9.8}$$

where $\rho(\omega)$ represents the bath spectral density. The term proportional to $\bar{\gamma}$ is cubic in $\hat{b}$ and thus describes the transition from two excitons into a single exciton, i.e., reflects exciton-exciton annihilation.

The optical field in a 3PEPS experiment consists of three Gaussian pulses:

$$E(t) = \sum_j \mathcal{E}_j(t - \tau_j)\exp[ik_j r - i\omega_0(t - \tau_j)] + c.c. \tag{9.9}$$

where k_j and τ_j are the wavevector and the central time of pulse j with a Gaussian envelope $\mathcal{E}_j(t-\tau_j)$. We consider the same carrier frequency, resonant to the excitation energy, $\omega_0 = \varepsilon$. For convenience it is useful to consider chronologically ordered pulses with $\boldsymbol{k}_1$ first, and delayed by times τ (between pulses 1 and 2) and T (between 2 and 3). This set of pulses

generates a four-wave-mixing signal characterized by the induced nonlinear polarization, $P(t)$. It is given by the expectation value of the polarization operator and its time evolution may be calculated from Eq. (9.6) for a certain configuration of pulse delay times.

The photon-echo signal, $P_s(t)$ is detected in the $-\boldsymbol{k}_1+\boldsymbol{k}_2+\boldsymbol{k}_3$ phase matching direction [22]. We do numerical non-perturbative propagation of Eq. (9.6) to calculate the induced polarization at strong excitations. However, numerically propagated quantities continuously depend on the excitation intensity and all phase-matching contributions are entangled. Thus the photon echo contributions up to the 10th order in the field are extracted using phase cycling [23, 24], which is equivalent to spacial Fourier transformation. The general procedure to extract a certain phase-matching signal at high excitation intensities is as follows. The 2π interval of a j-th pulse phase $\Phi_j = k_j r$ is divided into N points, $\Phi_j = \phi n$, $n = (0, ..., N-1)$, with a step $\phi = 2\pi/N$; N is the order of the signal at which the phase-matching contributions are extracted exactly. The time evolution of the variable b is calculated for a certain pulse delay configuration according to Eq. (9.6) as a function of phases $b(\Phi_3, \Phi_2, \Phi_1)$ of three pulses. The $u\boldsymbol{k}_1 + v\boldsymbol{k}_2 + w\boldsymbol{k}_3$ phase matching exciton variable may then be obtained using

$$\bar{b}_{uvw} = \sum_{\Phi_3\Phi_2\Phi_1} b(\Phi_3, \Phi_2, \Phi_1) e^{-iu\Phi_3 - iv\Phi_2 - iw\Phi_1}. \tag{9.10}$$

Only homogeneous dephasing is included in Eq. (9.6) via parameters γ and $\bar{\gamma}$ corresponding to the off diagonal bath fluctuations. Thus the phase-matched homogeneous photon-echo induced polarization is given by

$$P_h(t) = \mu b_{-1,1,1}. \tag{9.11}$$

Structural fluctuations on various timescales induce motional narrowing (additional homogeneous contribution) and inhomogeneous broadening through *diagonal* Hamiltonian fluctuations h'_{11} (for simplicity we neglect h'_{22} and higher terms). Using the time correlation functions of these fluctuations their action is expressed through the line-shape functions $g(t)$ by cumulant expansion techniques [22]. We consider the transition frequency fluctuations ($\tilde{\varepsilon} \equiv h'_{11}$). They are characterized by Gaussian statistics and the corresponding correlation function is

$$\langle \tilde{\varepsilon}(\tau)\tilde{\varepsilon}(0)\rangle = 2\Gamma\delta(\tau) + \sigma_e^2 \exp(-\tau/\tau_c), \tag{9.12}$$

where $\tau > 0$. Here Γ and σ_e are the strengths of fast and slow phonon modes, respectively, and τ_c is the correlation time of the slow mode. The line-shape function for this type of fluctuations is [22]

$$g(t) = \Gamma t + (\sigma_e\tau_c)^2[\exp(-t/\tau_c) + t/\tau_c - 1], \tag{9.13}$$

where for slow modes we use $\tau_c^{-1} \ll k_B T/\hbar$ (high temperature) and $\tau_c\sigma_e \gg 1$ (slow limit). This model for $\tau_c \to \infty$ leads to an absorption linewidth of $\sigma_e\sqrt{8\ln(2)}$. The *third-order* induced polarization at the $-\boldsymbol{k_1}+\boldsymbol{k_2}+\boldsymbol{k_3}$ phase-matching direction for the real line-shape function may be written in the form [22]

$$\begin{aligned} P_s(t_4) &= P_h(t_4)\exp[-g(t_{21}) - g(t_{43}) \\ &+g(t_{32}) - g(t_{42}) - g(t_{31}) + g(t_{41})], \end{aligned} \tag{9.14}$$

where $t_{jj'} = t_j - t_{j'}$ are the delays between time-ordered pulses with t_4 standing for the signal detection time. P_h and P_s are the homogeneous and inhomogeneous signals, respectively. In

our simulations, even though they go beyond third order theory, we use Eq. (9.14) on top of the homogeneous signal extracted using Eq. (9.11) to account for diagonal fluctuations.

The photon-echo signal in the 3PEPS spectroscopy is a time-integrated intensity at a certain pulse delay configuration

$$I_s(T,\tau) = \int dt_4 |P_s(t_4)|^2. \tag{9.15}$$

This is simulated for a grid of T and τ values and the peak shift is extracted by the value of τ, where $I_s(T,\tau)$ has its maximum amplitude, as a function of T. In our simulations the maximum τ value is determined using a parabolic interpolation procedure.

We choose the fundamental transition frequency $\varepsilon = 9800$ cm^{-1}, and the parameter Δ, which characterizes the shift of the two-exciton resonances from ε, is set to zero by assuming that the exciton binding effect in 3PEPS signal is a secondary effect compared to exciton annihilation at high exciton intensities. The dephasing parameter γ and the annihilation parameter $\bar{\gamma}$ are set to $\gamma/\varepsilon = 5.4 \cdot 10^{-5}$ (10 ps) and $\bar{\gamma}/\varepsilon = 6.75 \cdot 10^{-4}$ (800 fs) [25], respectively, and the inhomogeneous linewidth is chosen to be $\sigma_e/\varepsilon = 0.02$. The diagonal fluctuation parameters τ_c and Γ were tuned to best reproduce the experimental data: $\tau_c\varepsilon = 4000$, $\Gamma/\varepsilon = 4.5 \cdot 10^{-3}$.

The annihilation rate $\bar{\gamma}$ controls the system susceptibility to different excitation intensities (see Eq. 9.6). When the ratio $\bar{\gamma}|b|^2/\gamma \ll 1$, the linear decay dominates. The annihilation is the main relaxation pathway in the opposite limit. This ratio can be estimated by linear response theory, which gives the maximum $|b^{(1)}| = \mu\bar{\mathcal{E}}$, where $\bar{\mathcal{E}} = \int d\tau \mathcal{E}(\tau)$ is the time-integrated field amplitude. We approximate the polarization decay by σ_e which is usually much larger than γ and introduce an intensity parameter

$$\kappa = \frac{\bar{\gamma}}{\sigma_e}\mu^2\bar{\mathcal{E}}^2. \tag{9.16}$$

The regime where exciton annihilation becomes important is uniquely defined by the excitation intensity and the ratio of the annihilation rate to the full linewidth.

In the inset of Fig. 9.2a we present the calculated dependence of initial peak-shift at $T = 0$ on the pulse intensity κ (black squares). It clearly shows transition behavior from an intensity-independent regime $\kappa \ll 1$ into a regime where the peak shift rapidly decreases when $\kappa \gg 1$. The same calculated values are also plotted in Fig 9.2a for a narrower range of κ values (from 1.2 to 230), showing very good agreement with experiment. Note that this comparison allows an estimate of the degree of system excitation in the experiment. The calculated 3PEPS decays at different intensities are shown in Fig. 9.2c. These decays describe the trend of the observed intensity dependence rather well.

9.4 Discussion

The experimental data demonstrate an unusual and striking effect of excitation intensity on photon echo peak shift. Our simulations capture the main feature of the experimental

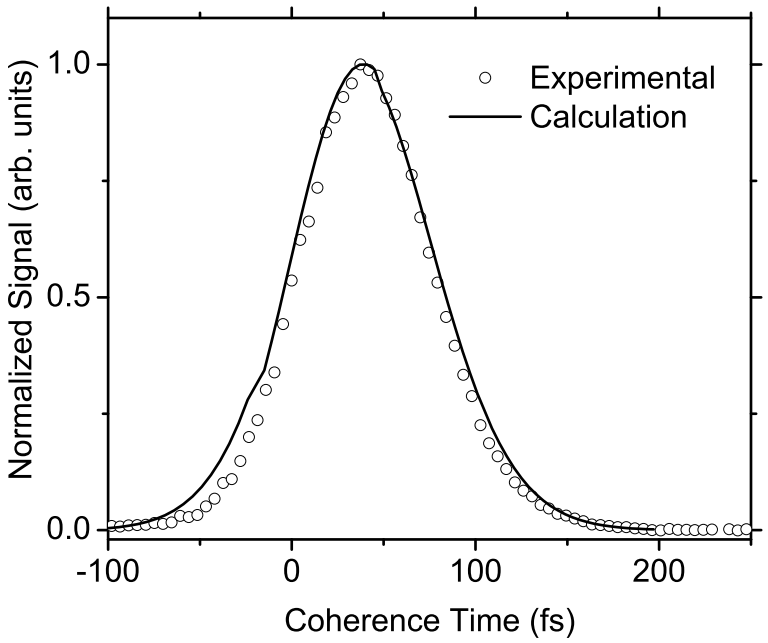

Figure 9.3. Measured (symbols) and simulated (line) two-pulse photon echo profiles. The measured data was taken from Fig. 5 of ref. [27], where a full account of the experimental details can be found. The calculated data was horizontally shifted by $-15fs$ to account the effect of finite excitation intensity used to collect the experimental data.

findings - the intensity dependence of peak shift, and also offer insights into the physical mechanism underlying this unusual phenomenon. With current level of simplifications, our simulations still can not satisfactorily reproduce the decay behavior of the 3PEPS traces (compare the results shown in Fig. 9.1 and Fig 9.2c). To improve the match between the experimental data and simulated results, it may be important to consider a full atomistic model of the nanotube. The simplifications we used include: (i) the MFA (no biexciton resonances [26]), (ii) neglect of multiple exciton scattering pathways by electrons/holes/excitons beyond phonon-induced annihilation, and (iii) the phenomenological spectral broadening scheme. However, since the 3PEPS (unlike pump-probe or two dimensional photon echo) does not directly resolve the many-body resonances but instead reveals dephasing processes, the phenomenological interacting-boson model built directly for delocalized excitons is adequate to explain our 3PEPS data and the physical phenomena behind them. The qualitative agreement between our simulations and the experimental results demonstrates that at high excitation intensities the system behaves as a simple nonlinearly damped oscillator.

The correlation time of slow bath fluctuations, $\tau_c = 2253fs$, determined here is about one order of magnitude longer than the timescale ($\tau_e = 200fs$) extracted from our previous simulations for an exponential decay term in the correlation function $M(t)$ [27]. This difference, at first glance, seems to indicate inconsistency between our previous and current work. However, direct comparison of these timescales is inappropriate because the forms of the correlation functions used are different (compare Eq. (9.12) above with Eq. 2 in ref. [27]). Instead, consistency between our previous and current simulations is verified through calculations of both 3PEPS and two-pulse photon echo signals using these $M(t)$ functions, and confirmed by the similar results for both cases (data not shown). We further find that the correlation function given by Eq. (9.12) can reproduce very well the decay behavior of an experimental two-pulse photon echo profile acquired using a similar SWNT-PVP film (see Fig. 11.4). This long τ_c timescale accounts for both the slow bath fluctuations and the peak shift offset at population times longer than $\approx 300fs$ (see Fig. 9.1). This offset was modeled by an additional term describing static inhomogenity in our previous paper [27]. The present correlation function thus constitutes the simplest model, which agrees approximately with the 3PEPS data.

9.5 Summary

The remarkable intensity dependence of the photon echo peak shift sets SWNTs apart from almost all other systems studied by this technique to date. Although a decrease of the photon echo peak shift with increasing excitation intensity was reported by Cundiff and coworkers for GaAs quantum wells, no analysis was presented and therefore the cause leading to the observed dependence remains unknown [28]. The strong dependence of the initial peak shift value (Figs. 9.1 and 9.2a), the absence of a dependence on population time [27], and the marked derivation from the typically observed cubic dependence on excitation intensity (Fig. 9.2b) found from the semiconducting SWNTs all imply the existence of a new dephasing mechanism dependent on the creation of multiple excitons.

According to our simulations the observed intensity dependence of peak shift arises from two levels of electronic dephasing - a characteristic, intensity-independent dephasing of single exciton and an intensity-dependent dephasing owing to an enhanced exciton-exciton scattering in this spatially confined system [6]. These dephasing processes are described in our simulations by the dephasing parameter γ and the pulse intensity parameter κ, respectively. Since we let Δ=0 in our simulations, we find that exciton-exciton annihilation makes a major contribution to the intensity dependence compared to other possible elastic and inelastic exciton-exciton scattering pathways.

9.6 References

[1] F. Wang, G. Dukovic, L. E. Brus, T. F. Heinz, Science 308, 838 (2005).

[2] J. Maultzsch, R. Pomraenke, S. Reich, E. Chang, D. Prezzi, A. Ruini, E. Molinari, M. S. Strano, C. Thomsen, C. Lienau, Phys. Rev. B 72, 241402(R) (2005).

[3] Y.-Z. Ma, L. Valkunas, S. M. Bachilo, G. R. Fleming, J. Phys. Chem. B 109, 15671 (2005).

[4] Y.-Z. Ma, T. Hertel, Z. V. Vardeny, G. R. Fleming, L. Valkunas, in Carbon Nanotubes, Topics Appl. Phys., A. Jorio, G. Dresselhaus, M. S. Dresselhaus, Eds. (Springer-Verlag Berlin, Heidelberg, 2008), vol. 111, pp. 321.

[5] K. Matsuda, T. Inoue, Y. Murakami, S. Maruyama, Y. Kanemitsu, Phys. Rev. B 77, 033406 (2008).

[6] Y.-Z. Ma, M. W. Graham, G. R. Fleming, A. A. Green, M. C. Hersam, Phys. Rev. Lett., 101, 217402 (2008).

[7] Y.-Z. Ma, L. Valkunas, S. M. Bachilo, G. R. Fleming, Phys. Chem. Chem. Phys. 8, 5689 (2006).

[8] S. Berger, C. Voisin, G. Cassabois, C. Delalande, P. Roussignol, X. Marie, Nano Lett. 7, 398 (2007).

[9] G. R. Fleming, S. A. Passino, Y. Nagasawa, Phil. Trans. R. Soc. Lond. A 356, 389 (1998).

[10] G. R. Fleming, T. Joo, M. Cho, Adv. Chem. Phys. 101, 141 (1997).

[11] M. Cho, J.-Y. Yu, T. Joo, Y. Nagasawa, S. A. Passino, G. R. Fleming, J. Phys. Chem. 100, 11944 (1996).

[12] Y.-Z. Ma, L. Valkunas, S. L. Dexheimer, S. M. Bachilo, G. R. Fleming, Phys. Rev. Lett. 94, 157402 (2005).

[13] T. Joo, Y. Jia, J.-Y. Yu, M. J. Lang, G. R. Fleming, J. Chem. Phys. 104, 6089 (1996).

[14] V. M. Axt, S. Mukamel, Rev. Mod. Phys. 70, 145 (1998).

[15] H. Huag, S. W. Koch,*Quantum Theory of the Optical and Electronic Properties of Semiconductors* (World Scientific, Singapore, 2004), 4th ed.

[16] G. Khitrova, H. M. Gibbs, F. Jahnke, M. Kira, S. W. Koch, Rev. Mod. Phys. 71, 1591 (1999).

[17] R. Oszwałdowski, M. Reichelt, T. Meier, S. W. Koch, M. Rohlfing, Phys. Rev. B 71, 235324 (2005).

[18] A. O. Gogolin, A. A. Nersesyan, A. M. Tsvelik, *Bosonization and Strongly Correlated Systems* (Cambridge University Press, 1998).

[19] S. Okumura, T Ogawa, Phys. Rev. B 65, 035105 (2001).

[20] V. Chernyak, W. M. Zhang, S. Mukamel, J. Chem. Phys. 109, 9587 (1998).

[21] R. Oszwaldowski, D. Abramavicius, S. Mukamel, J. Phys.: Condens. Matter 20 045206 (2008).

[22] S. Mukamel, *Principles of Nonlinear Optical Spectrscopy* (Oxford University Press, New York, 1995).

[23] P. Tian, D. Keusters, Y. Suzaki, W. S. Warren, Science 300, 1553 (2003).

[24] T. Mancal, A. V. Pisliakov, G. R. Fleming, J. Chem. Phys. 124, 234504 (2006).

[25] F. Wang, G. Dukovic, E. Knoesel, L. E. Brus, T. F. Heinz, Phys. Rev. B 70, 241403 (2004).

[26] M. R. Salvador, P. S. Nair, M. Cho, G. D. Scholes, Chem. Phys. 350, 56 (2008).

[27] M. W. Graham, Y.-Z. Ma, G. R. Fleming, Nano Lett., 8, 3936 (2008).

[28] S. G. Carter, Z. Chen, S. T. Cundiff, Phys. Rev. B 76, 121303(R) (2007).

Chapter 10

Exciton Annihilation and Dephasing Dynamics

Semiconducting single-walled carbon nanotubes (SWNTs) are one of the most intriguing nanomaterials due to their large aspect ratios, size tunable properties, and dominant many body interactions. While the dynamics of exciton population relaxation have been well characterized, optical dephasing processes have only been examined indirectly through steady-state measurements such as single-molecule spectroscopy that can yield highly variable estimates of the homogeneous linewidth. To bring clarity to these conflicting estimates, a time-domain measurement of exciton dephasing at an ensemble level is necessary. Using two-pulse photon echo (2PE) spectroscopy, comparatively long dephasing times approaching 200 fs are extracted for the (6,5) tube species at room temperature. In this contribution, we extend our previous study of 2PE and pump-probe spectroscopy to low temperatures to investigate inelastic exciton-exciton scattering. In contrast to the population kinetics observed upon excitation of the second transition-allowed excitonic state (E_{22}), our one-color pump-probe data instead shows faster relaxation upon cooling to 60 K when the lowest transition-allowed state (E_{11}) is directly excited for the (6,5) tube species. Analysis of the kinetics obtained suggests that the observed acceleration of kinetic decay at low temperature originates from an increasing rate of exciton-exciton annihilation. In order to directly probe exciton-exciton scattering processes, femtosecond 2PE signal is measured as a function of excitation fluence and temperature. Consistent with the observed enhancement of exciton-exciton scattering and annihilation at low temperatures, the dephasing rates show

a correlated trend with the temperature dependence of the population lifetimes extracted from one-color pump-probe measurements.

10.1 Introduction

Semiconducting single-walled carbon nanotubes (SWNTs) have recently shown strong potential for use as efficient fluorophores[1, 2] and photodiodes[3]. The development of such promising optoelectronic applications requires an understanding of the dominant many-body photophysics of these nanomaterials. Inherent one-dimensional confinement in nanotubes, greatly enhances electron-hole Coulombic interactions which give rise to strongly bound (0.4 to 1.1 eV binding energy) excitons whose transitions (E_{11}, E_{22}, etc.) dominate the optical spectra (figure 10.2).[4, 5, 6] These stable Mott-Wannier type excitons have yet to be fully characterized optically. In particular the short-time coherent behavior of excitons delocalized in SWNTs is an often overlooked property that determines important physical observables such as spectral line-broadening.[7] Coherent excitons occur when incident photons create delocalized excitations that have a definite phase relationship between themselves and the absorption of electromagnetic radiation creating them.[8] In the site basis, such delocalized excitons can extend for length scales up to the wavelength of the resonant excitation pulse. As time evolves, the nuclear modes of the nanotube and its surroundings couple to the coherent exciton causing both rapid dephasing and exciton localization toward its inherent radius of 1-2 nm.[4] In this contribution we use time-resolved spectroscopy as an incisive probe of inelastic exciton-exciton scattering and annihilation to investigate how these many-body scattering processes contribute to the overall dynamics of the E_{11} transition.

The timescale of coherence between the ground and E_{11} state is characterized by the dephasing time (T_2) required for $1/e$ of the coherence to decay from exciton scattering with phonons and other quasi-particles. In pump-probe experiments, E_{11} population relaxation and annihilation processes overwhelm the contribution of the rapidly decaying coherent dynamics.[9] In order to directly access the timescales of optical dephasing, 2PE spectroscopy is used. 2PE measures the collective ability of an excited ensemble of SWNTs to maintain coherence after a variable time delay over which dephasing occurs. This process generates a macroscopic polarization or photon echo signal which decays primarily from exciton-phonon coupling, allowing direct extraction of the dephasing time.[9] For most molecular and solid state systems at room temperature, the electron-phonon coupling will dephase electronic coherence within 10s of femtoseconds. Recent determination of comparatively long T_2 times approaching 200 fs at room temperature in semiconducting (6,5) SWNTs highlights the important role of coherent excitons for the fundamental photophysics of this quasi one-dimensional nanomaterial.[10, 11] To better understand the long T_2 times recently observed in SWNTs,[10] we will review existing work and present new data acquired at low temperature to examine the contribution of multi-excitonic effects to optical dephasing.

The exciton dynamics associated with population relaxation from the E_{11} state have been investigated through femtosecond transient absorption and time-resolved fluorescence

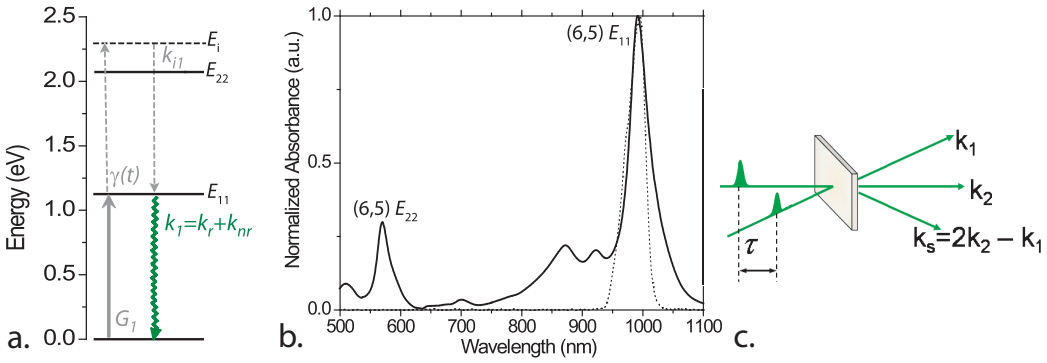

Figure 10.1. a. Simplified kinetic relaxation pathways from the lowest E_{11} excitonic state with inclusion of exciton depletion by annihilation. b. Corresponding linear absorption and laser pulse spectra (dotted line) showing resonant excitation of the (6,5) tube species embedded in PVP polymer. c. Two-pulse photon echo beam geometry on SWNT sample with emitted echo signal.

measurements.[7] While fluorescence-based results have already quantified the temperature-dependent relaxation kinetics, these measurements rely on indirect excitation of the E_{11} state via relaxation from the corresponding E_{22}, vibronic bands or off-resonant excitation.[12, 13, 14] Such indirect measurement of E_{11} kinetics are usually justified since the $E_{22} \rightarrow E_{11}$ relaxation occurs with approximately 80% efficiency on a roughly 40 fs timescale.[15, 16] However, because the electronic and phonon processes which couple the E_{11} state to higher-lying states are not clearly understood, an E_{11} transition excited directly may for instance be substantially more delocalized than one that relaxed from a higher lying state. This subtle question comparing E_{11} relaxation dynamics for E_{22} versus E_{11} resonant excitation is investigated in detail elsewhere.[17] Instead, here we avoid such complications by using transient absorption spectroscopy where the E_{11} state is excited directly. Previously, such one-color pump-probe measurements have been conducted at room temperature only, and reported that the E_{11} population dynamics are dominated by depletion through rapid exciton-exciton annihilation.[18] After reviewing the established kinetics for exciton-exciton anhilation in SWNTs, we will describe the characteristics of annhilation at low temperature through pump-probe experiments. To understand the origin of the observed low temperature enhancement of exciton annihilation, we will discuss the correlation between the annihilation kinetics and the coherent dynamics of exciton-exciton scattering processes probed through 2PE measurements.

10.2 Sample Characteristics and Experimental

To unambiguously probe the E_{11} exciton dynamics associated with a specific nanotube species using femtosecond pump-probe and 2PE spectroscopic techniques, a sample highly

enriched in a single SWNT chirality is desirable. We employed a sample highly enriched in the (6,5) tube species (see figure 10.2b for the linear absorption spectrum), which was prepared using a density gradient enrichment method.[1] The starting material was synthesized through the cobalt-molybdenum catalyst (CoMoCAT) technique, and the obtained SWNTs were subsequently dispersed via sonication in bile salts followed by ultracentrifugation.

Our measurements at room temperature were performed using aqueous suspensions of SWNTs with a quartz sample cell with a path length of 100 μm. For measurements at lower temperatures, we fabricated thin SWNT-polymer composite films of approximates 200 μm thickness by mixing the suspensions with either polyvinylpyrolidone (PVP) polymer or gelatin and drop casting layer-wise into teflon molds. After drying in a dessicator, the solid films are removed from molds for spectral characterization and time-resolved experiments. Steady-state photoluminescence measurements on these films upon the E_{22} excitation gives a sharp E_{11} peak whose intensities are an order of magnitude stronger than the emission band around 1150 nm. The presence of a broad, intense emission in the 1150 nm spectral region has been shown to indicate tube-bundling.[20, 21] A Janis ST-100 cryrostat with a Lakeshore temperature controller was used for measurement at low temperature, and a temperatures as low as 2.5 K could be realized using continuous flow liquid helium under reduced pressure.

The experimental setup for femtosecond 2PE and pump-probe spectroscopy have been described in detail previously and only a brief account will be given here.[22] The light source was an optical parametric amplifier pumped with a 250 kHz Ti:Sapphire regenerative amplifier. The 2PE experiments were performed by directly exciting the E_{11} state of the (6,5) tube with 45 fs laser pulses centered at 995 nm for SWNT-PVP films, and 998 nm for SWNT-gelatin films in order to account for the spectral shift induced by different tube environment. The laser beam was split into two nearly equal intensity replicas and focused on the sample to a spot diameter of 148 μm (see figure 10.2c). The first pulse with wavevector $\mathbf{k}_1$ creates a coherent macroscopic polarization of the exciton ensemble that is allowed to dephase over a variable delay time or coherence time (τ). After time τ, a second pulse $\mathbf{k}_2$ arrives producing an interference grating with respect to the partially dephased coherent polarization created by $\mathbf{k}_1$. The time integral of the photon echo signal is detected in the phased-matched direction $2\mathbf{k}_2$-$\mathbf{k}_1$, with an InGaAs photodiode and a lock-in amplifier. A plot the diffracted signal as function of positive τ delay time shows a nearly monoexponential decay and the corresponding timescale (τ_{decay}) can be accurately extracted through a least square deconvolution fitting algorithm with explicit consideration of finite pulse duration. For strongly inhomogeneously broadening systems, this will further allow us to determine the dephasing time through the simple relation: $T_2 = 4\tau_{decay}$.[9, 22] One-color pump-probe measurements were performed concurrently with 2PE experiments by directly detecting the $\mathbf{k}_1$ beam as shown in figure 10.2c. The detection consists of an InGaAs photodiode and a lock-in amplifier. Parallel polarization between the pump and probe beams were used, and the pump beam fluence was controlled by a combination of a waveplate and a polarizer.

10.3 Kinetics of exciton-exciton annihilation

The exceptionally large absorption cross sections, which is estimated to be 5.1×10^{-13} cm^2 for the E_{11} transition of a 600 nm long (6,5) tube,[23] indicates the creation of an average of 1.4 excitons even under the lowest laser excitation fluence employed in this work (0.1 μJ/cm^2). As revealed in previous studies, the interaction of these simultaneously created excitons will result in rapid annihilation leading to depletion of the E_{11} state.[24, 25] For a one-color pump-probe experiment with resonant E_{11} excitation, the exciton relaxation can be described by following rate equation,

$$\frac{dn_1(t)}{dt} = G_1(t) - \frac{1}{2}\gamma(t)n_1^2(t) - k_1 n_1(t) + k_{i1}n_i(t) \tag{10.1}$$

where $n_1(t)$ is the population of the excitons, $G_1(t)$ is the exciton generation rate, k_1 is the linear relaxation rate to ground state, and $\gamma(t)$ is the exciton-exciton annihilation rate.[18, 26] In the annihilation process, a new exciton is created in a higher-lying state ($n_i(t)$) according to energy-momentum conservation, and its subsequent relaxation to the E_{11} state is denoted by k_{i1}. This simplified kinetic model is outlined schematically in figure 10.2a.

For diffusion-limited annihilation in an extended system whose size is comparable with or larger than the exciton diffusion radius, the annihilation rate becomes time-dependent for systems with dimensionality (d) less than two. This rate can be expressed by $\gamma(t) = \gamma_0/t^{1-d/2}$, where γ_0 is the time-independent annihilation rate.[24] For one-dimensional systems like SWNTs and under high excitation intensity where the annihilation term dominates, equation 10.1 can be approximated by,[24]

$$\frac{dn_1(t)}{dt} \cong -\frac{1}{2}\gamma_0 t^{-1/2} n_1^2(t). \tag{10.2}$$

This equation can be solved analytically,

$$\frac{n_1(0)}{n_1(t)} - 1 = n_1(0)\gamma_0\sqrt{t}. \tag{10.3}$$

As the pump-probe signal amplitude is proportional to $n_1(t)$, this equation suggests a linear dependence can be obtained when the signal amplitude is instead plotted as $\left(\frac{n_1(0)}{n_1(t)} - 1\right)^2$. Kinetics obeying this rate law with d=1 correspond to the annihilation arising from exciton diffusion along the nanotube axis.[24, 25] In figure 10.3 (inset), the one-color pump-probe signal for the E_{11} state is plotted, where the change in normalized optical density ($\Delta OD(t)/\Delta OD_0$) is analogous to ($n_1(t)/n_1(0)$), and the negative signed signal indicates dominant contribution of photobleaching and/or stimulated emission. Three exponentials are necessary to fit the kinetic decay with corresponding lifetimes (and relative amplitudes) of 0.1 (60%), 1.6 (28%) and 38 ps (12%). The multiexponential decay orginates from the nonexponential kinetics described by equation 10.2 owing to dominant contribution from exciton annhililation.[24] For laser intensities typical to pump-probe spectroscopy, exciton-exciton annihilation has been observed to dominate relaxation kinetics.[24, 25] Exponential relaxation is expected

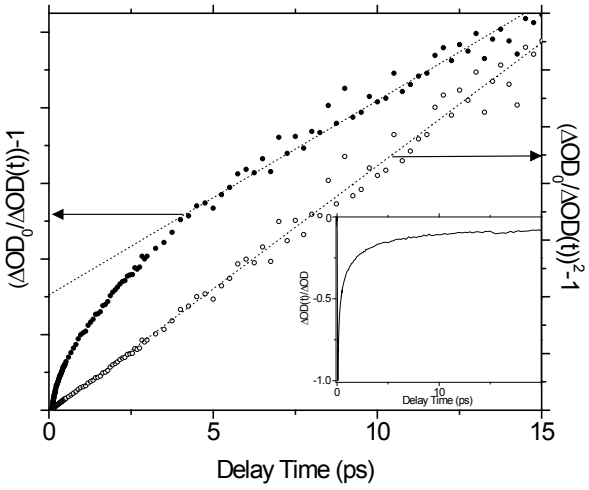

Figure 10.2. One-color pump-probe signal resonant with the E_{11} band at 995 nm (inset) for the (6,5) SWNTs in aqueous solution at room temperature. The decay is linear for times longer than 2 ps when plotted according to the square of equation 10.3 (see text). This suggests that the kinetic decay occurs predominately by annihilation via one-dimensional exciton diffusion at room temperature.

only for the longest decay components, when optically excited nanotubes are likely to have only one exciton left per tube.

Assuming one-dimensional diffusion-limited annihilation is the predominant decay mechanism, equation 10.3 can be used to fit the room temperature kinetics. Figure 10.3 shows the experimental data plotted as $(\Delta OD_0/\Delta OD(t) - 1)^2$ versus time, and gives a good linear fit, suggesting dominant one-dimensional diffusion-limited annihilation with a rate coefficient $\Delta OD_0\gamma_0 = 4.1$ ps$^{-1/2}$. For comparison we also consider the case of annihilation in two-dimensions. Solving equation 10.2 using a time-independent annihilation rate obtained for $d = 2$,[24] we obtain

$$\frac{n_1(0)}{n_1(t)} - 1 = \frac{1}{2} n_1(0)\gamma_0 t. \tag{10.4}$$

Plotting $(\Delta OD_0/\Delta OD(t) - 1)$ versus delay time in figure 10.3 results in a nonlinear dependence on time. While this supports that annihilation occurs predominately by one-dimensional diffusion of excitons, for shorter timescales on the order of T_2 an annihilation process involving delocalized excitons may also contribute.

Previous time-resolved fluorescence and two-color pump-probe at room temperature showed that a model involving diffusion-limited exciton annihilation provides an excellent description for the kinetics obtained.[18, 24, 25] However, at shorter delay times substantial deviation from this behavior was observed. For instance, time-resolved fluorescence kinetics reported for (9,5) tube type were more consistent with time-independent annihilation rates associated with two-dimensional diffusion of excitons described by equation 10.4.[24] The Bohr radius, however is reported to be larger than the tube diameter,[27] negating the possibility of two-dimensional diffusion of excitons in semiconducting SWNTs. Conse-

quently, Valkunas *et al.* suggested that at shorter times the necessity of time-independent annihilation rate may be because the excitons involved are sufficiently delocalized along the nanotube axis, and annihilate without diffusive motion.[24] Corroborating the involvement of delocalized excitons was the observation that the E_{11} pump-probe signal amplitude scales only linearly with the square root of the excitation fluence, suggesting virtually instantaneous annihilation of excitons instead of slow diffusional transport.[18] These early results suggested that the coherent properties of excitons are an important component of the overall exciton dynamics in SWNTs. To further elucidate the importance of coherent excitons, we will examine how the dynamics of exciton annihilation change at lower temperatures by analyzing the one-color pump-probe data acquired upon resonant excitation of the E_{11} state of the (6,5) tube species.

10.4 Temperature dependent exciton annihilation kinetics

For many molecular and solid state systems, the population lifetime is observed to increase as temperature is lowered. The excited state relaxation of such systems often involve highly localized Frenkel type excitons,[26] that relax non-radiatively primarily by exciton-phonon scattering. The temperature dependence of such a kinetic rate (k_{NR}) can be approximated as,

$$k_{NR} = k_c + Cexp(-\theta_k/k_bT) \tag{10.5}$$

where k_c is the temperature independent decay rate, C is a rate coefficient, k_b is the Boltzmann constant and θ_k is the energy of the coupled phonon mode.[28, 29] For semiconducting SWNTs, equation 10.5 has been used to justify the overall decrease in the fluorescence decay rate when temperature is lowered moderately from ambient conditions.[30] Below approximately 80 K, a more complex dependence of population lifetime on temperature has been reported that requires a more detailed model.[12, 30, 31, 32] Two-color, E_{22} pump and E_{11} probe transient absorption measurements have also been reported down to 77 K on (6,5) and (7,5) SWNTs.[14] An increasing kinetic decay rate with temperature was reported, consistent with predominately non-radiative E_{11} population relaxation suggested by the earlier time-resolved fluorescence results.[12, 33]

Previous temperature-dependent studies investigated the population relaxation from the E_{11} state only indirectly through resonant E_{22} excitation. Here, we report a one-color pump-probe measurement of the E_{11} state of the (6,5) SWNTs, and the obtained decay rates increase upon cooling to 80 K (see figure 10.4). Our measurements were conducted for at least four different pump intensities for each sample temperature. Consistent with previous results obtained at room temperature, the peak amplitude of the pump-probe signal detected at low-temperature scales linearly with the square root of pump fluence. This observation again supports that the initial population relaxation is dominated by annihilation of excitons.[24, 6] Figure 10.4a (inset) shows the normalized pump-probe kinetics measured at three different

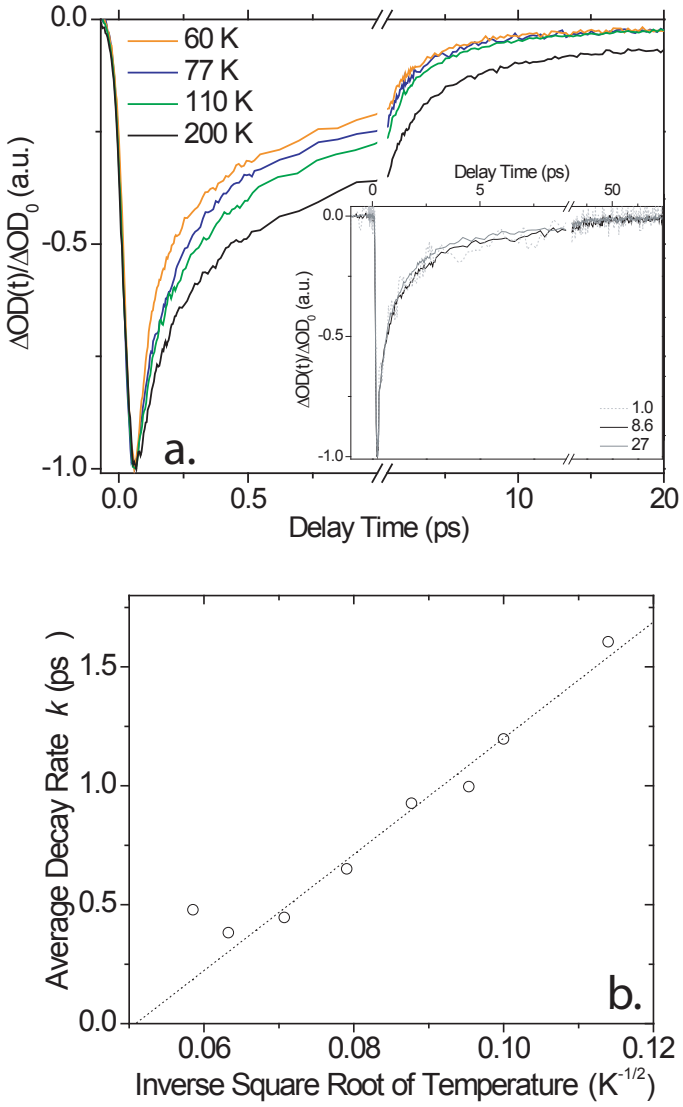

Figure 10.3. a. One-color pump-probe data collected for the (6,5) SWNTs embedded in PVP polymer at four different temperatures. The experiment was performed at 998 nm excitation with pump fluence of 4.0 μJ/cm^2. All the data were normalized at peak amplitudes of the signals, and the resulting decay profiles appear largely independent of the pump fluence (see inset, units in μJ/cm^2) b. Plot of the amplitude weighted decay rate for the dominant two fast decay components versus the inverse square root of temperature gives a nearly linear relaxation.

pump fluences, and the resulting decay profiles appear largely independent of the pump fluence. A similar observation was reported previously by Valkunas *et al.* for the data collected at room temperature and was attributed to pronounced exciton annihilation at longer delay times.[24]

We extract the population decay timescales though fitting the one-color pump-probe data to a model function consisting of three exponential terms by employing a least square deconvolution fitting algorithm. The two shorter lifetimes contain dominant contributions from exciton-exciton annihilation. From these two lifetimes, we calculate a mean decay rate (k) by weighting the decay times with corresponding relative amplitudes. The obtained k values increase three fold upon cooling to 80 K. The resulting change of this mean decay rates with temperature is shown in figure 10.4, and is discordant with previous results obtained from resonant excitation of the E_{22} transition.[30, 12] Further support to the observed increase of mean decay rate with decreasing temperature was obtained by pump-probe measurements on both SWNT-PVP and SWNT-gelatin composite films. Possible complications from thermal induced spectral shifts were eliminated by repeating measurements at the red side of the E_{11} absorption band where the laser pulses were detuned by 18 nm. While considerable variations in the decay rate are observed for different embedding polymers and excitation wavelengths, in all cases the decay of the pump-probe kinetics accelerates upon cooling. These results show that for direct E_{11} excitation of the (6,5) tube species in polymer environments, the exciton population relaxation accelerates upon decreasing temperature.

To understand the one-color pump-probe results reported above, we first consider the contribution of the temperature dependent radiative rate. While k_{NR} is expected to decrease (equation 10.5), an increasing E_{11} radiative rate (k_R) has been reported upon cooling to the 80 K region.[12, 34] Early theoretical treatments by Spataru *et al.* showed that for moderately low temperatures, the radiative rate can be approximately described by the standard temperature-dependent rate equation for one-dimensional systems,

$$k_R = k_o \sqrt{\frac{\Delta_r}{k_b T}} \tag{10.6}$$

where k_o is the rate coefficient, and Δ_r represents the maximum energy an exciton can occupy in the E_{11} band and still decay radiatively according to momentum conservation restrictions.[35, 27] This radiative decay gives a $1/\sqrt{T}$ dependence similar to the rates extracted from our one-color pump-probe experiments (see figure 10.4b). The very low fluorescence yield however, makes it implausible that the temperature dependence of the pump-probe signal arises from changes in the radiative rate, even though Spataru *et al.* suggest a $1/\sqrt{T}$ dependence for k_R.[35, 27] This is in contrast to GaAs quantum wires where the temperature dependence of the decay rate is attributed to the variation of the radiative rate.[36] In the case of SWNTs evidence suggests that exciton annihilation is the dominant relaxation pathway in ultrafast spectroscopic studies, and therefore we must consider the temperature dependence of this process.[7, 12, 33]

The strong signatures of exciton annihilation observed at all temperatures enabled us to identify annihilation as the dominant relaxation pathway for pump intensities employed in ultrafast experiments. The corresponding temperature dependence associated with the

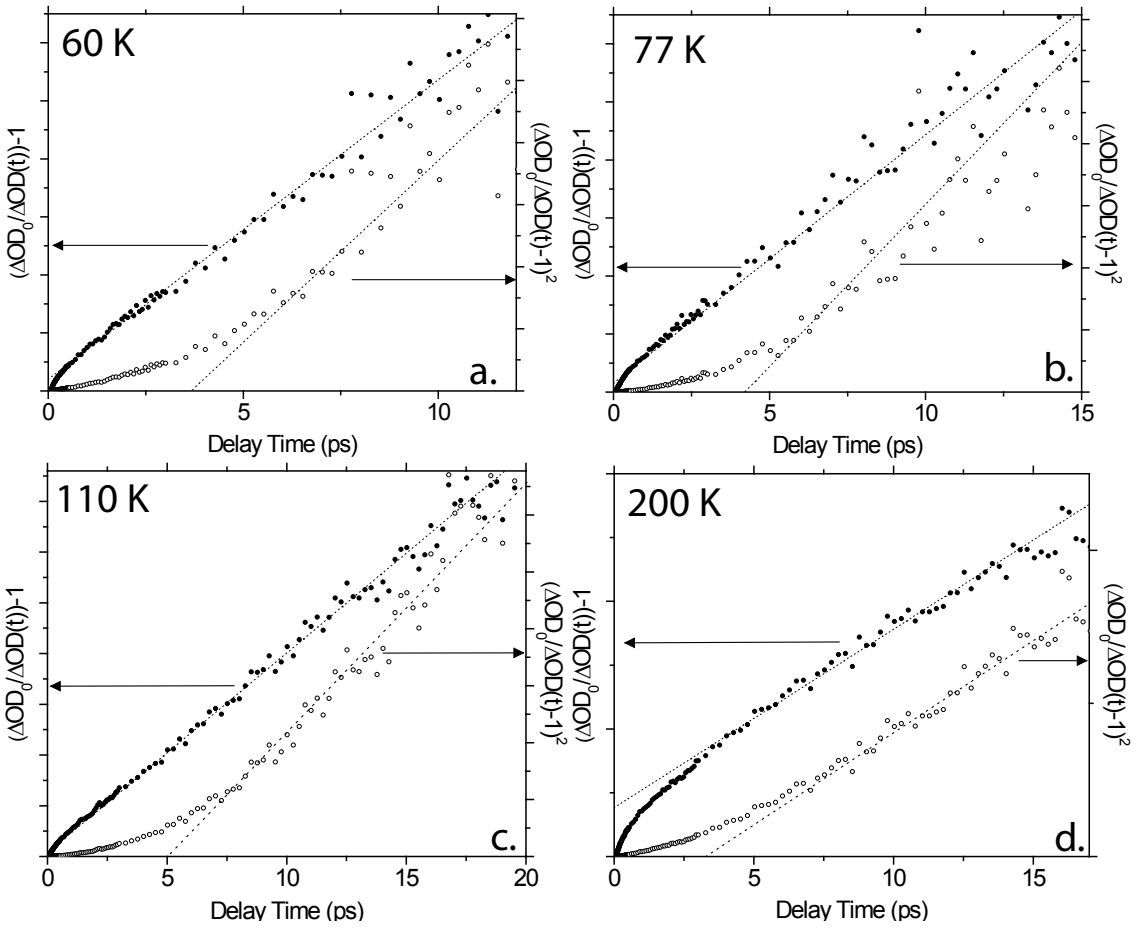

Figure 10.4. a. Pump-probe data collected at 60 (a), 77 (b), 110 (c) and 200 K (d) are plotted as $(\Delta OD_0/\Delta OD(t) - 1)$ (left axis) and $(\Delta OD_0/\Delta OD(t) - 1)^2$ (right axis) versus delay times, respectively. The dashed lines are fits to the linear portion of the data. Note a gradual shift of the linearity towards the predominately one-dimensional diffusion-limited annihilation model is observed upon warming sample toward ambient conditions.

exciton annihilation rate ($\gamma(t,T)$) for the E_{11} state has not been investigated. Approximate temperature-dependent annihilation rates can be obtained through plotting the pump-probe data by assuming either a time-dependent or a time-independent annihilation rate according to equations 10.3 and 10.4 respectively, and then fitting the linear portion of the data (see figure 10.4). The same approach is used for the results obtained at room temperature (figure 10.3). As shown in figure 10.4, for temperatures ranging from 60 to 180 K we observe a remarkably linear relationship in the plots of $(\Delta OD_0/\Delta OD(t)-1)$ versus time, suggesting that the E_{11} exciton annihilation rate at low temperatures is predominately time-independent. Upon further increase in temperature, a gradual transition toward a linear relationship in the plot of $(\Delta OD_0/\Delta OD(t)-1)^2$ versus time is found, favoring one-dimensional diffusion-limited annihilation. This temperature-activated transition is further evidenced by a progressively decreasing slope upon warming (see figure 10.4). From equation 10.4, one can see the slope ($\frac{1}{2}\Delta OD_0\gamma_0$) is directly proportional to the time independent annihilation rate γ_0. This parameter $\Delta OD_0\gamma_0$ is found to decrease from 5.2 ps^{-1} at 60K to 3.6 ps^{-1} at 150 K, in accord with the enhanced exciton-exciton annihilation accelerating the one-color pump-probe decay rate at low temperature. Since the corresponding pump-probe data in figure 10.4 exhibits better linearity applying the time-independent (d=2) annihilation rate model at low temperature, it implies the involvement of coherently delocalized excitons in exciton-exciton annihilation. In order to investigate the role of coherent dynamics in exciton annihilation, we will discuss femtosecond 2PE results in the following section.

10.5 Optical dephasing and exciton-exciton scattering

2PE spectroscopy provides an indirect measure of coherent exciton scattering dynamics by quantifying the dephasing time, T_2. Recently, dephasing times of the E_{11} state at room temperature and selected low temperatures were reported through extrapolating the temporal offset of photon echo signals (peak-shift)[11, 37], and direct determination from the 2PE signal decay (down to 77 K).[10] In figure 10.5a, 2PE profiles are plotted for resonant E_{11} excitation of the (6,5) SWNTs with a total fluence of 2.0 $\mu J/cm^2$, and essentially mono-exponential decays are found with T_2 times decreasing from 280 to 135 fs as temperature is raised from 60 K to room temperature. These results are consistent with our previous data obtained for temperatures ranging from 77 and 292 K.[10] The long T_2 times are supportive of a weak exciton-phonon coupling at low temperature that permits longer exciton coherences.[8]

The measured dephasing rates are directly proportional to the homogeneous linewidth ($\Gamma_h = 2\hbar/T_2$), which were recently shown to vary markedly as function of total excitation fluence.[10, 11] This strong intensity effect is also observed at lower temperatures, and as an example, figure 10.5b shows the 2PE data measured at 50 K. Increasing the excitation intensity by three fold leads to a significantly faster decay. As previously found for quantum wells and wires,[38, 39, 40] and more recently SWNTs[10, 41], this intensity-induced dephasing arises from exciton-exciton scattering processes and affects not only 2PE decays but also three-pulse photon echo peak shifts as recently reported. Abramavicius *et al.*[41] used

a non-perturbative phase cycling approach to calculate the contribution of exciton-exciton scattering and annihilation processes to the E_{11} exciton dephasing dynamics. A qualitative agreement with experiments was obtained by the inclusion of higher than third-order polarizations, suggesting the involvement of multi-exciton states induce optical dephasing predominately through annihilation pathways.[41]

The homogeneous linewidth (Γ_h) contains contributions from the broadening induced by exciton-phonon coupling processes (Γ_{ex-ph}), and from dephasing induced by exciton-exciton scattering (Γ_{ex-ex}).[11, 10, 42] If separable, the two broadening mechanisms sum to give the full-width at half maximum (FWHM) of the overall homogeneous lineshape according to,

$$\Gamma_h(N_x, T) = \Gamma_0 + \Gamma_{ex-ex}(N_x, T) + \Gamma_{ex-ph}(T), \tag{10.7}$$

where Γ_0 is defect related intrinsic spectral diffusion broadening, Γ_{ex-ex} is a function of both temperature and the exciton density per tube (N_x) and $\Gamma_{ex-ph}(T)$ varies with temperature only.[11, 42] N_x was estimated from the absorption cross-section (1×10^{-17} cm^2 per carbon atom)[23], a mean tube length of 600 nm,[1] the measured $1/e^2$ beam diameter (148 μm) and the total excitation intensity. The strong contribution of Γ_{ex-ex} to the linewidth has also been observed in the frequency domain, where the linewidths of single-tube photoluminescence spectra increase markedly at high excitation fluences. The reported Γ_h values from the single-tube experiment are similar to our time-domain estimates for comparable tube types.[43]

By incrementally lowering the excitation intensity, we can extrapolate the $\Gamma_h(N_x, T)$ values determined at different intensities to the zero intensity limit where the contribution from exciton-exciton scattering (i.e. Γ_{ex-ex}) can be neglected. The E_{11} exciton dephasing rates at selected temperatures for the (6,5) tubes embedded in a gelatin matrix are plotted in figure 11.6a. The overall homogeneous linewidth scales linearly with excitation density (N_x) below 220 K for the data obtained using SWNT-gelatin films, and below 180 K for the SWTN-PVP polymer films (data not shown). The ordinate intercepts of figure 11.6a give the zero intensity linewidth, $\Gamma_h(N_x = 0, T) = \Gamma_0 + \Gamma_{ex-ph}(T)$. This linear extrapolation further allows the $\Gamma_{ex-ex}(N_x, T)$ contribution to be determined using equation 10.7. For instance, at 80 K the Γ_{ex-ex} contribution to Γ_h increases from 4 to 16 meV as the estimated mean number of E_{11} excitons per tube changes from 2 to 17. This linear dependence[8] on N_x has also been observed in quantum wells and wires[44, 40, 45] where it is fit to,

$$\Gamma_h(N_x) = \Gamma_h(0) + \beta N_x \tag{10.8}$$

where β (units in ps$^{-1}\mu$m) is the exciton-exciton collisional broadening parameter. For the (6,5) SWNTs, we determine the β values directly from the slopes of the linear dependences shown in figure 11.6a, which appear strongly temperature dependent for the SWNTs embedded in both gelatin and PVP matrices. For temperature above the 200 K region, the dephasing rates begin to deviate from linearity, indicating that equation 10.7 cannot be used because the contributions from exciton-phonon and exciton-exciton scattering to the overall linewidth are no longer separable.

There is no obvious physical meaning ascribed to the β parameter, however work by May *et al.* shows that the β parameter approximates the relative magnitude of the the exciton-exciton scattering potential ($V_x(q)$), where q is the one-dimensional momentum space

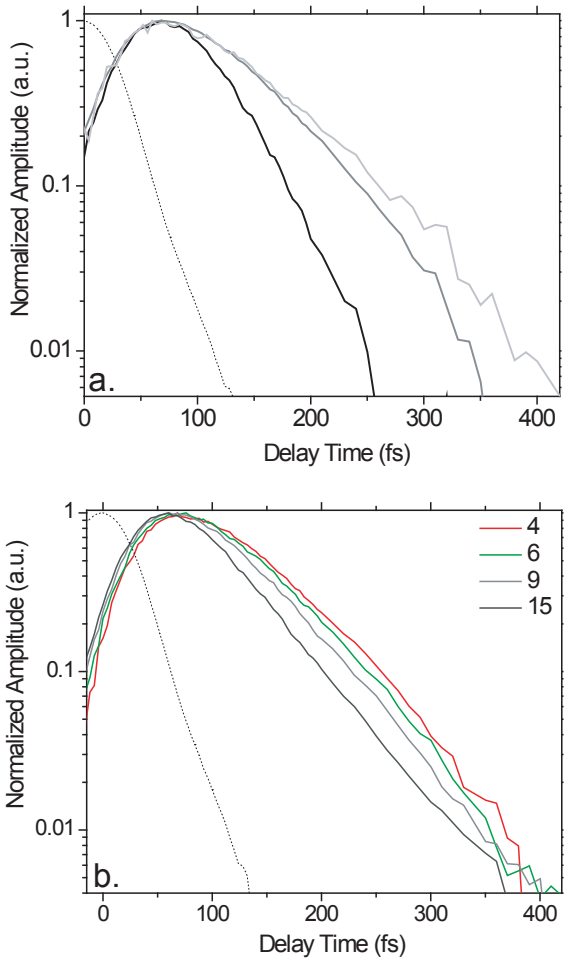

Figure 10.5. a. Temperature dependence of 2PE signals measured at 60, 110 and 292 K (top to bottom) under the lowest excitation intensity used for this experiment, which was 2 μJ/cm^2 in PVP polymer films. The dashed line is the autocorrelation function of the laser pulse. b. Excitation intensity dependence of the 2PE signals measured from 4 to 15 μJ/cm^2 for SWNT-PVP polymer film at 50 K.

scattering coordinate.[46, 47]. An approximate relationship is derived in Boldt *et al.*[47] for a two-dimensional system, which is trivially simplified here for a one-dimensional excitonic system as,

$$\Gamma_h(N_x) = \Gamma_h(0) + \left(\sum_q |V_x(q)|^2 \frac{\Gamma_h(0)}{[E_0 - E(q)]^2 + \Gamma_h(0)^2} \right) N_x, \tag{10.9}$$

where the energy $E(q)$ is approximated as an E_{11} parabolic band dependence, and E_0 is the free exciton energy. Comparing equations 10.8 and 10.9, it is readily seen that β provides the evaluation of sum over q. While our data does not permit extraction of $V_x(q)$, the observation that β decreases over two-fold with temperature does imply that the strength of the E_{11} exciton scattering potential must also decrease with temperature. Since the exciton kinetic energy at low temperatures is smaller, an enhancement of exciton-exciton scattering potential further suggests the effective exciton mean free path is longer either due to fewer phonon scattering events or longer coherence lengths. Further analysis including calculation of β from the one-dimensional exciton wavefunctions is still needed to understand the precise origin of the low temperature enhancement in the exciton-exciton scattering potential.

10.5.1 Exciton-exciton scattering and E_{11} population relaxation

In the absence of complications from annihilation of excitons, a decreasing E_{11} population decay rate is expected upon cooling as bath fluctuations that induce relaxation are frozen out.[30] However, this expectation is opposite to what we found in this work. Instead, the temperature dependent kinetics obtained are consistent with a low temperature enhancement in the exciton annihilation rate $\gamma(t)$. This is further supported by a strong correlation between the temperature-dependent k and β parameters plotted in figure 11.6b. This correlation links the observed acceleration in E_{11} population decay at low temperatures to an enhancement in the exciton-exciton scattering rate. Enhanced scattering among coherent excitons provides a likely pathway which enables more efficient annihilation of exciton population out of the E_{11} state as the nanotube temperature is lowered.

10.6 Summary

Previous studies using ultrafast spectroscopy show that exciton-exciton annihilation is a dominant process governing both population relaxation and exciton dephasing of the E_{11} state in semiconducting SWNTs.[18, 10, 41, 25] Through examining both processes as a function of temperature, we find a correlation between coherent exciton-exciton scattering (characterized by β or $V_x(q)$) and population depletion by annihilation (characterized by γ_0). This correlation suggests an important contribution from coherent exciton scattering to the observed rapid population decay of the E_{11} state. Further evidence is obtained by careful analysis of one-color pump-probe data which reveals a temperature-activated transition from exciton-exciton annihilation kinetics requiring a time-independent rate constant to one

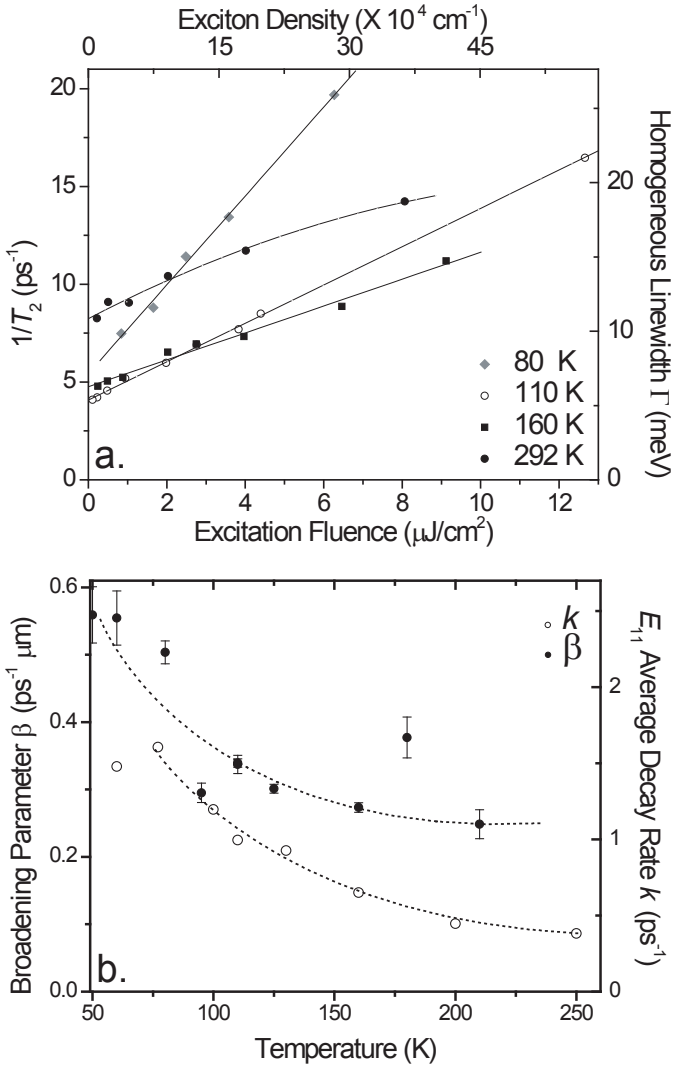

Figure 10.6. a. Dependence of the dephasing rates and the corresponding homogeneous linewidths on excitation intensity at different lattice temperatures for the (6,5) tube in a gelatin matrix. The solid lines are fits to the selected data taken at 4.4, 80, 110, 160 and 292 K, from which the β broadening parameters are obtained. b. Comparison of temperature dependence of the β parameter (filled circles) and the mean decay rate of the E_{11} population relaxation (open circles). Dashed lines are fits to the two data sets.

that needs a time-dependent annihilation rate. Below 180 K, the pump-probe data can be satisfactorily modeled by a time-independent rate γ_0, indicating annihilation occurs without diffusion, but instead involving extensively delocalized excitons. The extracted annihilation

rates γ_0 decreased two-fold with increasing temperature. Collectively, the marked decrease in γ_0, temperature activated transition to diffusion-limited kinetics, and the correlation between the mean population decay rate and the exciton-exciton scattering potential for the E_{11} state (figure 11.6), all support that a strongly temperature dependent annihilation rate is the origin of the unexpected acceleration in the population decay rate at low temperatures. The reported temperature dependence of the exciton-exciton annihilation and scattering rate also presents new challenges to understand the more commonly applied two-color E_{22} pump and E_{11} probe results. The starkly different E_{22} pump kinetics compared with direct E_{11} excitation suggests that the $E_{22} \rightarrow E_{11}$ relaxation remains a poorly understood process requiring careful investigation.

10.5 References

[1] Kevin Welsher, Zhuang Liu, Sarah P. Sherlock, Joshua Tucker Robinson, Zhuo Chen, Dan Daranciang, and Hongjie Dai. A route to brightly fluorescent carbon nanotubes for near-infrared imaging in mice. *Nature Nano*, 4(11):773–780, 2009.

[2] Sang-Yong Ju, William P. Kopcha, and Fotios Papadimitrakopoulos. Brightly Fluorescent Single-Walled Carbon Nanotubes via an Oxygen-Excluding Surfactant Organization. *Science*, 323(5919):1319–1323, 2009.

[3] Nathaniel M. Gabor, Zhaohui Zhong, Ken Bosnick, Jiwoong Park, and Paul L. McEuen. Extremely Efficient Multiple Electron-Hole Pair Generation in Carbon Nanotube Photodiodes. *Science*, 325(5946):1367–1371, 2009.

[4] F. Wang, G. Dukovic, Louis E. Brus, and Tony F. Heinz. The optical resonances in carbon nanotubes arise from excitons. *Science*, 308:838–841, 2005.

[5] J. Maultzsch, R. Pomraenke, S. Reich, E. Chang, D. Prezzi, A. Ruini, E. Molinari, M.S. Strano, C. Thomsen, and C. Lienau. Exciton binding energies in carbon nanotubes from two-photon photoluminescence. *Phys. Rev. B*, 72:241402(R), 2005.

[6] Y.-Z. Ma, L. Valkunas, Sergei M. Bachilo, and Graham R. Fleming. Exciton binding energy in semiconducting single-walled carbon nanotubes. *J. Phys. Chem. B*, 109(33):15671–15674, 2005.

[7] Y.-Z. Ma, T. Hertel, Zahid V. Vardeny, Graham R. Fleming, and L. Valkunas. Carbon nanotubes– ultrafast spectroscopy of carbon nanotubes. volume 111, pages 321–352. Springer-Verlag Berlin, Heidelberg, 2008.

[8] J. Shah. *Ultrafast spectroscopy of semiconductors and semiconductor nanostructures.* Berlin; New York: Springer Verlag, 1999.

[9] T. Joo and Albert C. Albrecht. Electronic dephasing studies of molecules in solution at room temperature by femtosecond degenerate four wave mixing. *Chem. Phys.*, 176(1):233–247, 1993.

[10] Ying-Zhong Ma, Matthew W. Graham, Graham R. Fleming, Alexander A. Green, and Mark C. Hersam. Ultrafast exciton dephasing in semiconducting single-walled carbon nanotubes. *Phys. Rev. Lett.*, 101(21):217402, 2008.

[11] Masao Ichida, Yumie Kiyohara, Shingo Saito, Yasumitsu Miyata, Hiromichi Kataura, and Hiroaki Ando. Phase-relaxation processes of excitons in semiconducting single-walled carbon nanotubes. *Phys. Stat. Sol. (b)*, 245(12):2712–2715, 2008.

[12] S. Berger, C. Voisin, G. Cassabois, C. Delalande, P. Roussignol, and X. Marie. Temperature dependence of exciton recombination in semiconducting single-wall carbon nanotubes. *Nano Lett.*, 7(2):398–402, 2007.

[13] Y.-Z. Ma, J. Stenger, J. Zimmermann, Sergei M. Bachilo, Robert E. Smalley, Robert B. Weisman, and Graham R. Fleming. Ultrafast carrier dynamics in single-walled carbon nanotubes probed by femtosecond spectroscopy. *J. Chem. Phys.*, 120(7):3368–3373, 2004.

[14] Y.-Z. Ma, L. Valkunas, Sergei M. Bachilo, and Graham R. Fleming. Temperature effects on femtosecond transient absorption kinetics of semiconducting single-walled carbon nanotubes. *Phys. Chem. Chem. Phys.*, 8:5689–5693, 2006.

[15] C. Manzoni, A. Gambetta, E. Menna, M. Meneghetti, G. Lanzani, and G. Cerullo. Intersubband exciton relaxation dynamics in single-walled carbon nanotubes. *Phys. Rev. Lett.*, 94(20):207401, 2005.

[16] Sergei Lebedkin, Frank Hennrich, Oliver Kiowski, and Manfred M. Kappes. Photophysics of carbon nanotubes in organic polymer-toluene dispersions: Emission and excitation satellites and relaxation pathways. *Phys. Rev. B*, 77(16):165429, 2008.

[17] Matthew W. Graham, Y.-Z. Ma, J. Chmeliov, L. Valkunas, and Graham R. Fleming. Exciton dynamics in carbon nanotubes. in preparation:–, 2009.

[18] Y.-Z. Ma, L. Valkunas, Susan L. Dexheimer, Sergei M. Bachilo, and Graham R. Fleming. Femtosecond spectroscopy of optical excitations in single-walled carbon nanotubes: Evidence for exciton-exciton annihilation. *Phys. Rev. Lett.*, 94(15):157402, 2005.

[19] Mark S. Arnold, Alex A. Green, Jared F. Hulvat, Steve I. Stupp, and Mark C. Hersam. Sorting carbon nanotubes by electronic structure using density differentiation. *Nature Nanotech.*, 1:60–65, 2006.

[20] Oscar N. Torrens, David E. Milkie, M. Zheng, and Jim M. Kikkawa. Photoluminescence from intertube carrier migration in single-walled carbon nanotube bundles. *Nano Lett.*, 6(12):2864–2867, 2006.

[21] Phillip H. Tan, Adam G. Rozhin, T. Hasan, P. Hu, V. Scardaci, Walter I. Milne, and Albert C. Ferrari. Photoluminescence spectroscopy of carbon nanotube bundles: evidence for exciton energy transfer. *Phys. Rev. Lett.*, 99:137402, 2007.

[22] Mark A. Berg, K. D. Rector, and M. D. Fayer. Two-pulse echo experiments in the spectral diffusion regime. *J. Chem. Phys.*, 113(8):3233–3242, 2000.

[23] S. Berciaud, L. Cognet, P. Poulin, Robert B. Weisman, and B. Lounis. Absorption sectroscopy of idividual single-wlled crbon nanotubes. *Nano Lett.*, 7(5):1203–1207, 2007.

[24] L. Valkunas, Y.-Z. Ma, and Graham R. Fleming. Exciton-exciton annihilation in single-walled carbon nanotubes. *Phys. Rev. B*, 73:115432, 2006.

[25] Yoichi Murakami and Junichiro Kono. Nonlinear photoluminescence excitation spectroscopy of carbon nanotubes: Exploring the upper density limit of one-dimensional excitons. *Phys. Rev. Lett.*, 102(3):037401, 2009.

[26] H. van Amerongen, L. Valkunas, and R. van Grondelle. *Photosynthetic Excitons*. World Scientific, Singapore, New Jersey, London, Hong Kong, 2000.

[27] Catalin D. Spataru, S. Ismail-Beigi, L.X. Benedict, and Steven G. Louie. Quasiparticle energies, excitonic effects and optical absorption spectra of small diameter single-walled carbon nanotubes. *Appl. Phys. A*, 78:1129–1136, 2004.

[28] Mario F. Lin and Kim W.-K. Shung. Plasmons and optical properties of carbon nanotubes. *Phys. Rev. B*, 50(23):17744–17747, 1994.

[29] Sharon H. Lin and R. Bersohn. Effect of partial deuteration and temperature on triplet-state lifetimes. *J. Chem. Phys.*, 48(23):2732–2738, 1968.

[30] Gregory D. Scholes, Sergei Tretiak, Timothy J. McDonald, Wyatt K. Metzger, Chaiwat Engtrakul, Garry Rumbles, and Michael J. Heben. Low-lying exciton states determine the photophysics of semiconducting single wall carbon nanotubes. *J. of Phys. Chem. C*, 111(30):11139–11149, 2007.

[31] Walter K. Metzger, Timothy J. McDonald, C. Engtrakul, Jacob L. Blackburn, Greg D. Scholes, G. Rumbles, and Michael J. Heben. Temperature-dependent excitonic decay and multiple states in single-wall carbon nanotubes. *J. Phys. Chem. C*, 111(9):3601–3606, 2007.

[32] V. Perebeinos, J. Tersoff, and Ph. Avouris. Radiative lifetime of excitons in carbon nanotubes. *Nano Lett.*, 5(12):2495–2499, 2005.

[33] A. Hagen, M. Steiner, Mohab B. Raschke, C. Lienau, T. Hertel, H. Qian, Adam J. Meixner, and A. Hartschuh. Exponential decay lifetimes of excitons in individual single-walled carbon nanotubes. *Phys. Rev. Lett.*, 95:197401, 2005.

[34] V. Perebeinos, J. Tersoff, and Ph. Avouris. Scaling of excitons in carbon nanotubes. *Phys. Rev. Lett.*, 92:257402, 2004.

[35] Catalin D. Spataru, S. Ismail-Beigi, Robert B. Capaz, and Steven G. Louie. Theory and ab initio calculation of radiative lifetime of excitons in semiconducting carbon nanotubes. *Phys. Rev. Lett.*, 95:247402, 2005.

[36] M. Lomascolo, P. Ciccarese, R. Cingolani, R. Rinaldi, and Finnigan K. Reinhart. Free versus localized exciton in gaas v-shaped quantun wires. *J. Appl. Phys.*, 83(1):302–305, 1998.

[37] Matthew W Graham, Ying-Zhong Ma, and Graham R Fleming. Femtosecond photon echo spectroscopy of semiconducting single-walled carbon nanotubes. *Nano Lett*, 8(11):3936–3941, 2008.

[38] Ernest J. Mayer, Janet O. White, George O. Smith, H. Lage, D. Heitmann, K. Ploog, and J. Kuhl. Femtosecond coherent spectroscopy of etched quantum wires. *Phys. Rev. B*, 49(4):2993–2996, 1994.

[39] A. Honold, L. Schultheis, J. Kuhl, and C.W. Tu. Collision broadening of two-dimensional excitons in a gaas single quantum well. *Phys. Rev. B*, 40(9):6442–6445, 1989.

[40] D.-S. Kim, J. Shah, Jed E. Cunningham, Ted C. Damen, W. Schfer, M. Hartmann, and S. Schmitt-Rink. Giant excitonic resonance in time-resolved four-wave mixing in quantum wells. *Phys. Rev. Lett.*, 68(7):1006–1009, 1992.

[41] Darius Abramavicius, Ying-Zhong Ma, Matthew W. Graham, Leonas Valkunas, and Graham R. Fleming. Dephasing in semiconducting single-walled carbon nanotubes induced by exciton-exciton annihilation. *Phys. Rev. B*, 79(19):195445, 2009.

[42] Kazunari Matsuda, Tadashi Inoue, Yoichi Murakami, Shigeo Maruyama, and Yoshihiko Kanemitsu. Exciton fine structure in a single carbon nanotube revealed through spectral diffusion. *Phys. Rev. B*, 77(19):193405, 2008.

[43] Kohei Yoshikawa, Ryusuke Matsunaga, Kazunari Matsuda, and Yoshihiko Kanemitsu. Mechanism of exciton dephasing in a single carbon nanotube studied by photoluminescence spectroscopy. *Appl. Phys. Lett.*, 94(9):093109, 2009.

[44] L. Schultheis, A. Honold, J. Kuhl, K. Khler, and Carl W. Tu. Optical dephasing of homogeneously broadened two-dimensional exciton transitions in gaas quantum wells. *Phys. Rev. B*, 34(12):9027–9030, 1986.

[45] Henry P. Wagner, W. Langbein, Jared M. Hvam, G. Bacher, T. Kammell, and A. Forchel. Exciton dephasing in znse quantum wires. *Phys. Rev. B*, 57(3):1797–1800, 1998.

[46] G. Manzke, K. Henneberger, and V. May. Many-exciton theory for multiple quantum-well structures. *Phys. Stat. Sol. (b)*, 139:233–239, 1987.

[47] F. Boldt, K. Henneberger, and V. May. Many-body theory for the dense exciton gas of direct semiconductors. *Phys. Stat. Sol. (b)*, 130(2):675–687, 1985.

Chapter 11

Pure Exciton Dephasing Dynamics

A room temperature E_{11} optical dephasing time (T_2) of 205 fs is measured for aqueous (6,5) single-walled carbon nanotubes (SWNTs), which is longer than comparable molecular systems or nanostructures. T_2 was extracted directly from the decay rate of the femtosecond two pulse photon echo response that was measured as a function of both excitation fluence and temperature. Longer dephasing times of 320 fs were obtained at 70 K, but upon further cooling to 2.5 K the extracted T_2 time decreased to 265 fs. This unexpected temperature dependence is explained with the aid of transient absorption measurements, which contain a dominant fast initial E_{11} population relaxation component which accelerates below 80 K. By accounting for population relaxation, the corresponding pure optical dephasing rates $1/T_2^*$ are calculated and found to increase monotonically from 225 fs at room temperature to 508 fs at 4.4 K fs. Below $\sim$180 K, $1/T_2^*$ is found to scale linearly with temperature with a slope of 6.7$\pm$0.6 μev/K, indicative dephasing arising from one-phonon scattering from acoustic modes. Corroborating measurements using three-pulse photon echo peakshift (3PEPS) independently reproduced dephasing times obtained from the 2PE decay. To better understand how long room temperature pure dephasing times are realized in view of the large dynamic disorder of the surrounding environment, the nonexponential component of the photon echo decay was fitted. The extracted 2PE curvature suggests that the actual strength of exciton-phonon coupling is mitigated by motional narrowing which effectively averages over applied nuclear fluctuations. This further suggests the occurrence of remarkable initial exciton delocalization, and makes nanotubes ideal to study many-body effects in spatially confined systems.

11.1 Introduction

Semiconducting single-walled carbon nanotubes (SWNTs) are one of the most intriguing nanomaterials due to their large aspect ratios, size tunable properties, and dominant many body interactions.[1, 2] While SWNT electrical and mechanical properties have been well studied, fundamental optical properties are continuously emerging with new synthetic and purification developments enabling advancements such as great enhancements in fluorescence yields (up to 20%) and demonstration of highly efficient carbon nanotube photodiodes.[3, 4] The photophysical properties of this quasi-one dimensional(1D) material are determined by strongly-bound Mott-Wannier type excitons, which arise from an electron-hole Coulombic interaction that is greatly enhanced from 1D confinement effects.[5, 6, 7] Since the corresponding exciton binding energy composes a large fraction of the overall band-gap ($\sim$30% for (6,5) SWNTs), excitonic transitons completely determine the optical properties of semiconducting SWNTs. As a consequence, the linear abosorption and photoluminesence spectra produce relatively sharp peaks from transitions directly with the bound exciton states(see Figure 11.1a). *Ab initio* calculations show each such transiton (denoted E_{11}, E_{22}, and so on) occurs within a manifold of both optically bright and dark states, the latter of which are believed to play a critical role in exciton population relaxation processes[8, 9] and in determining the overall photoluminescence yield.[10, 11]

The excitons initially possess a definite phase relationship among themselves and with the electromagnetic radiation creating them.[12] The resulting coherent excitons can be spatially delocalized on an extended scale limited in principle only by the wavelength of the laser light. For semiconducting SWNTs with a length scale of $\sim$1 μm or shorter, this would suggest that E_{11} excitons may be initially delocalized up to the length of nanotube. Subsequent scattering with phonons, defects and impurities, etc. will lead to an exponential loss of coherence within an ensemble of SWNTs, and eventually exciton localization to a finite spatial length equal to its inherent radius of $\sim$1-2 nm.[5] A quantitative measure of this timescale where exciton coherence persists is the dephasing time(T_2), and its determination also provides a time-domain based measurement of the homogeneous linewidth though the inverse proportionality, $\Gamma_h = 2\hbar/T_2$.[13] During the dephasing time both population and ensemble phase will decay and the remaining excitons may be extensively delocalized. Currently, available estimates for the exciton delocalization lengths vary greatly from 10 to 100s of nm.[14, 10]

The homogeneous linewidths of SWNT ensembles were first measured by femtosecond three-pulse photon echo peak shift (3PEPS) spectroscopy, which provided an indirect estimation of the T_2 timescales.[15] Shortly after, direct determination of the dephasing timescales was preformed using a femtosecond two-pulse photon echo (2PE) technique on a sample highly enriched in the (6,5) tube species. Using 2PE, long-lived E_{11} coherences with a T_2 of 170 fs were reported at room temperature.[16] Similar dephasing times have been also reported for other tube types using indirect two-pulse photon peak shift measurements.[17] Observation of long electronic dephasing times at room temperature is striking in comparison to molecules, molecular complexes and aggregates which typically dephase on a sub 10 fs timescale.[18, 19] Crystalline systems such as two-dimensional GaAs quantum wells have moderately longer dephasing times approaching $\sim$95 fs at 294 K.[12, 20, 21] In addition,

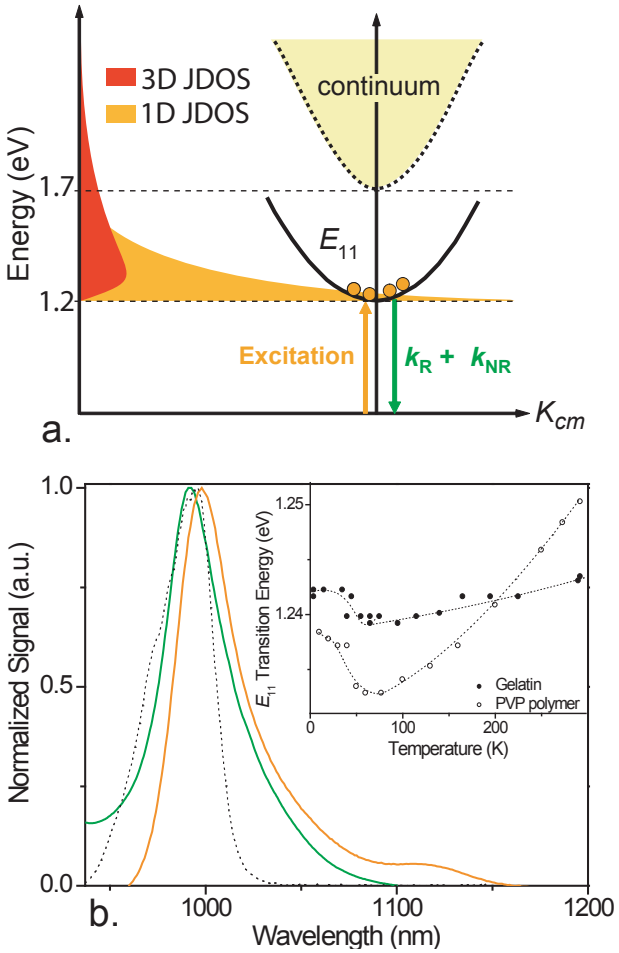

Figure 11.1. (a) Simplified electronic energy diagram for a semiconducting SWNT showing only the bright strongly bound E_{11} exciton state with respect to the continuum. The corresponding 1D joint density of states (JDOS) diverges at band minimum, allowing for direct excitation of multiple excitons. Subsequent relaxation pathways can be both radiative (k_R) and non-radiative (k_{NR}) and may also involve a low-lying state (not shown). (b) E_{11} linear absorption(green line) and steady-state fluorescence emission(orange line) spectra of (6,5) tube embedded in PVP polymer, together with a spectrum of a 45 fs laser pulse (dotted line). The inset shows the energies of the absorption maxima plotted as a function of temperature for two polymer-SWNT composites prepared using gelatin (filled circles) and PVP (open circles) polymer SWNT composites, respectively.

previous measurements at different excitation intensities and lattice temperatures (77-292 K) showed that both exciton-exciton and exciton-phonon scattering profoundly influence the dephasing timescales and the homogeneous linewidths of the E_{11} transition.[16, 17]

Together the 3PEPS and 2PE results independently report that the homogeneous linewidth associated with the (6,5) E_{11} transition is at least 4 fold smaller than the inhomogeneous contributions.[16, 15] Similar homogeneous linewidths have been also obtained from frequency-domain single-tube measurements.[22, 23, 24] One advantage of the ensemble based approach of photon echo spectroscopy, is its inherent averaging accounts for the differences in (6,5) tube characteristics (length, defects, etc.) and local environmental disorder. While correspondence can be found between the results obtained from time-domain ensemble measurements and frequency-domain single-tube spectroscopy, direct comparison is hampered by the often highly variable linewidths obtained from single-tube measurements even for the tubes with same chirality. In addition, reported single-tube fluorescence experiments employ indirect excitation of the E_{11} band through its corresponding E_{22} manifold, vibronic bands or off-resonance. The ensuing relaxation to the radiative E_{11} state is typically accompanied by multi-phonon emission, which can cause additional dephasing not present in time-domain photon-echo measurements employing direct E_{11} excitation.[25]

Although both time-domain photon echo and frequency-domain single-tube approaches are powerful tools to quantify the dephasing times (T_2), neither of them can directly provide the pure dephasing time (T_2^*), which is related to the dephasing time T_2 and the population lifetime (T_1) through the well-known relation:

$$\frac{1}{T_2} = \frac{1}{2T_1} + \frac{1}{T_2^*} \tag{11.1}$$

While the T_2 timescales can be readily obtained from 2PE measurements, proper determination of the T_1 values is not straightforward owing to the general existence of complicated multiexponential decays in SWNTs. The shortest component of the population relaxation can approach the corresponding T_2 times,[2] and in this case a substantial contribution to broadening from the population lifetime broadening is expected. Here simultaneous measurement of both population and exciton dephasing timescales are crucial to elucidate the pure dephasing timescale (T_2^*) for E_{11} exciton decoherence from exciton-phonon scattering.

In this contribution, we employ complimentary femtosecond spectroscopic techniques including pump-probe, 2PE and 3PEPS spectroscopy to determine pure optical dephasing times associated with the E_{11} transition. Our experiments were conducted across a broad temperature range (2.5 to 292 K) and at various excitation intensities, and on samples highly enriched in the (6,5) tube type dispersed individually either in aqueous solution or polymer composite films. Analysis of the resulting data further permitted us to distinguish specific contributions to homogeneous linewidth from longitudinal optical and acoustic phonons, and to observe an intrinsically large linewidth in the low temperatures limit given by the environmental disorder.

11.2 Experimental

Optical spectrocscopic investigations of SWNTs are often complicated by the existence of multiple structurally distinct tube species and by a variable amount of bundles being present. Central to all experiments reported in this paper is the use of a sample highly enriched in a single semiconducting tube species, the (6,5) tube. In combination with resonant excitation/dexcitation of the E_{11} or E_{22} excitionic bands, this allows us to access the ultrafast dynamics associated with a single tube type. A sample enriched in a single tube type was obtained using a density-gradient ultracentrifuguation procedure.[26] The resulting chirality enriched aqueous suspensions of individualized SWNTs were mixed with water-soluble gelatin or polyvinylpryrolidone(PVP) polymer and then cast into thin (roughly 500 μm) polymer composite films. Use of such polymer films greatly suppress laser light scattering arising from slow tube motions occurring in aqueous solution, and enables measurements at sufficiently low excitation intensities with good signal-to-noise ratio and across a broad temperature range.

The linear absorption and steady-state fluorescence emission spectra measured for SWNTs embedded in a PVP film at room temperature are shown in Figure 11.1b. Upon excitation of the E_{22} transition at 572 nm, similar relative fluorescence yields are obtained compared with the starting aqueous samples. Additionally, the absence of a broad, intense emission in the 1150 nm spectral region indicates that tube bundling is insignificant.[27, 28] Measurements at low temperatures were carried out by placing the SWNT-polymer composite films in direct contact with a Janis ST-100 cold finger which operates under continuous liquid helium flow. The sample temperature was continuously controlled by interfacing the cryostat with a Lakeshore temperature controller. To ensure high optical quality and resonant excitation of the (6,5) tubes at all measured temperatures, linear absorption spectra were recorded from 4.4 to 292 K, and the resulting E_{11} peak positions are shown in Figure 11.1b (inset). Upon cooling, the PVP composite films showed a maximum 5 nm redshift, which may be attributed to hydrostatic tube strain effects.[29, 30] In contrast, gelatin films yielded a comparatively small redshift (maximum 2 nm), suggesting a somewhat weaker hydrostatic effect. Moreover, a small spectral blueshift was observed for both composite films at temperature below $\sim$70 K. Similar low temperature blueshifts have been previously reported experimentally and predicted theoretically for selected tube types.[31] In addition to the measurements conducted on the composite films, we also performed experiments using the aqueous solution at room temperature. In this case, a thin quartz cell of 100 μm quartz cell was used, which helps minimize the thermal lensing effects induced by laser beams.

The experimental setups for femtosecond 2PE, 3PEPS and transient absorption spectroscopy have been described in detail previously and only a brief account will be given here.[12, 32, 13] The light source was an optical parametric amplifier pumped by a 250 kHz Ti:Sapphire regenerative amplifier, which can produce 40 to 65 fs laser pulses tunable in the visible and near-infrared regions. A combination of a waveplate and a polarizer was used to control the intensity of laser pulse from 0.3 to 15 μJ/cm^2 for all experiments described in this paper.

The 2PE experiments were performed by directly exciting the E_{11} state of the (6,5)

tube with 45 fs laser pulses centered at 998 nm for the SWNT-gelatin film, 995 nm for the SWNT-PVP film (see Figure 11.1b for the laser laser pulse spectrum), and 990 nm for aqueous solution sample. Additional experiments were also performed at 1012 nm to excite the red-edge of the E_{11} absorption band for the PVP-SWNT composite films. In these experiments, two nearly equal intensity laser pulses were focused to a spot of 148 μm diameter. The first pulse with wavevector $\mathbf{k}_1$ creates a coherent macroscopic polarization of the exciton ensemble that is allowed to dephase over a variable delay time or coherence time(τ_{12}). After time τ, a second pulse $\mathbf{k}_2$ arrives producing an interference grating with respect to the partially dephased coherent polarization created by $\mathbf{k}_1$. This transient grating diffracts incident photons into phased-matched direction $2\mathbf{k}_2$-$\mathbf{k}_1$ as shown in Figure 11.2, which is detected in a time-integrated manner with an InGaAs photodiode and a lock-in amplifier. A measurement of the diffracted signal as function of positive τ delays gives a nearly monoexponential decay, and the corresponding timescale (τ_{decay}) can be accurately extracted through a least squares deconvolution fitting algorithm with explicit consideration of finite pulse duration. For strongly inhomogeneously broadened systems such as semiconducting SWNTs,[15] the dephasing time T_2 can be obtained directly from the following relation $T_2 = 4\tau_{decay}$.[33]

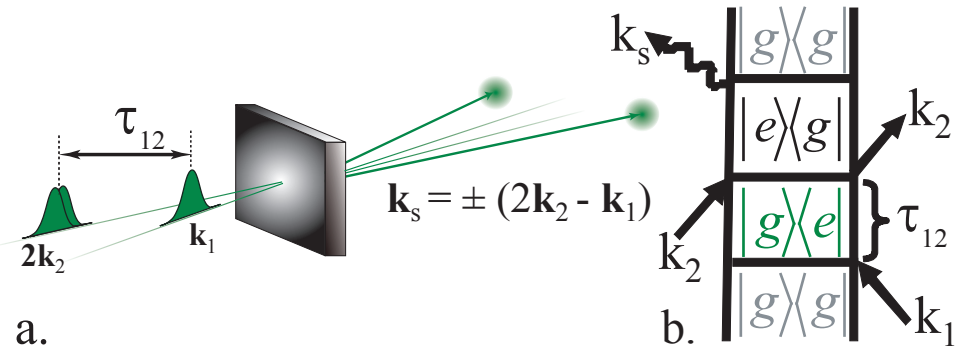

Figure 11.2. (a) The laser beam geometry of the 2PE experiment. (b) A double-sided Feynman diagram shows the temporal state evolution, laser pulse $\mathbf{k}_1$ prepares a coherent superposition ($|g\rangle\langle e|$) between ground and the E_{11} excited state, which subsequently dephases over time τ_{12}. The detected 2PE scattering signal($\mathbf{k}_s$) is stimulated by the remaining two interactions ($\mathbf{k}_2$).

The dynamics of exciton population relaxation was monitored by femtosecond transient absorption spectroscopy. Upon excitation of the E_{22} transition with 48 fs laser pulses centered at 570 nm and subsequent rapid interband relaxation[34], the dynamics of the resulting E_{11} excitons is probed selectively at chosen wavelengths with a white-light continuum. The detection unit consists of a single-grating monochromator, an InGaAs photodiode and a lock-in amplifier. The polarization of the pump beam was set to the magic angle (54.7^o) with respect to probe beam, to suppress tube orientation contributions. The measurements were performed at several sample temperatures which was chosen to be same as used for our 2PE experiments. A least squares deconvolution algorithm was applied to extract the timescales of the decay kinetics employing a model function that consists of sum of multiple exponents.

To investigate both optical dephasing and spectral diffusion processes, 3PEPS was used as an extension of the 2PE approach where the laser pulse was instead divided into three replicas ($\mathbf{k}_1, \mathbf{k}_2, \mathbf{k}_3$).[35] The details of this technique and its application to SWNTs at room temperature has been previously described at room temperature.[15, 33] The 3PEPS signal were simultaneously detected in two phase-matching directions ($\mathbf{k}_1-\mathbf{k}_2+\mathbf{k}_3$ and $-\mathbf{k}_1+\mathbf{k}_2+\mathbf{k}_3$) as a function of coherence time (τ_{12}) and an additional delay between pulses 2 and 3, the population time(t_{23}). At a given population time, the two photon echo profiles were measured and the corresponding peak-shift (τ^*) is defined as half of the temporal offset of the two signal maxima. A plot of the peak shift τ^* as a function of population time allowed us to examine both optical dephasing (for $t_{23} = 0$) and spectral diffusion processes ($t_{23} > 0$) for temperatures ranging from 4.4 to 292 K.

11.3 Results and Discussion

11.3.1 Exciton-exciton scattering dynamics

The large absorption cross-section of semiconducting SWNTs facilitates the creation of multiple excitons per tube, which will experience enhanced mutual interactions because of one-dimensional confinement.[2] A quantitative estimate for the number of excitons created can be obtained using an absorption cross-section ($\sim 1 \times 10^{-17}$ cm^2 per SWNT carbon atom)[36], the mean tube length of 600 nm for our samples,[26] a measured beam waist (148 μm) and the total incident excitation intensity used. Varying the excitation intensity over fifty fold, corresponds to a mean exciton population of 0.8 to 42 per tube, or alternatively an exciton density(N_x) ranging from 1.3 to 70 cm^{-1}. One consequence of populating many spatially confined excitons is a significant enhancement in exciton-exciton scattering events along the nanotube axis.[25] Previous work has shown that such exciton-exciton scattering and annihilation leads to additional optical dephasing in SWNTs.[37]

Figures 11.3a and b show the 2PE data measured for different excitation fluences at 4.4 and 292 K respectively (semi-log scale plotted). At all temperatures, the decay follows monoexponential behavior very closely. The 2PE profile decays markedly faster with increasing excitation fluence, providing direct evidence for exciton dephasing induced by exciton-exciton scattering. While a similar intensity dependence has been recently reported[16, 17], the results obtained here extract dephasing rate directly from the echo decay profile and are reported down to temperatures as low as 2.5 K. As has been discussed previously[25, 38], the exciton dephasing rate ($1/T_2$) or equivalently, the homogeneous linewidth, contains contributions from line broadening induced by both inelastic exciton-phonon ($\Gamma_{ex-ph}(T)$) and exciton-exciton scattering ($\Gamma_{ex-ex}(N_x, T)$).[37, 15, 17] These contributions sum to give the overall effective homogeneous linewidth,

$$\Gamma_h(N_x, T) = \Gamma_0 + \Gamma_{ex-ex}(T)N_x + \Gamma_{ex-ph}(T) \tag{11.2}$$

where Γ_0 is the intrinsic linewidth at T=0 K.[38] As exciton density is increased, the expo-

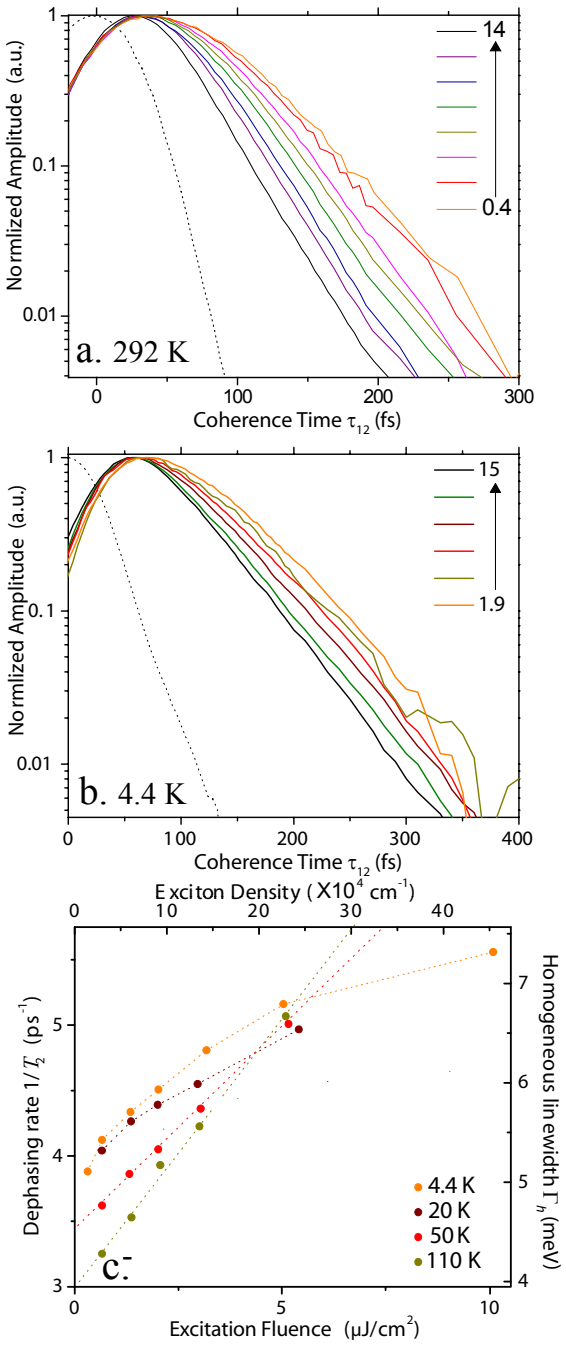

Figure 11.3. 2PE decays profile showing the excitation intensity dependence for (6,5) SWNTs collected at (a) 292 K in aqueous solution and (b) 4.4 K in PVP polymer under various excitation fluences as indicated in the plots (in μJ/cm^2) (c) Plot of the extracted dephasing rate, $1/T_2$ as a function of excitation fluence shown at four different temperatures. Dashed lines are used to extrapolate to the zero-intensity limit where contributions from exciton-exciton scattering are negligible.

nential decay rate of the 2PE signal increases by one fold across all temperatures measured (see Figure 11.3, note the semilog intensity scale). Other spatially confined systems such as quantum wires[39] and CdSe quantum dots [40] also exhibit clear signatures of intensity induced dephasing. A substantial Γ_{ex-ex} contribution to the linewidth is consistent with exciton confinement effects leading to enhanced exciton-exciton scattering. Carbon nanotubes in particular are not only strongly confined 1D systems, but have large absorption cross sections ($\sim 5.5\times10^{13}$ cm^2 per 600 nm (6,5) tube), making them an ideal systems to observe such intensity dependent contributions to the exciton dephasing rate. In order to reach a limit where scattering from multi-exciton interactions (i.e. Γ_{ex-ex}) can be safely neglected, the beam fluence was incrementally lowered, permitting extrapolation to the zero intensity limit (see Figure 11.3c). The resulting intensity-independent dephasing rate (or intrinsic homogeneous linewidth) is then obtained. For the majority of temperatures measured the dephasing rate varied linearly with the exciton density(N_x) according to equation 11.2. Below ~20 K and above ~200 K however, the dephasing rates obtained have significant curvature with excitation intensity, suggesting the exciton-exciton (Γ_{ex-ex}) and exciton-phonon (Γ_{ex-ph}) dephasing contributions may be coupled. In these cases, a polynomial expression was used to extrapolate to the zero intensity limit. The results obtained are in good accord with measurements published earlier reporting the intensity-dependent exciton dephasing rate down to 77 K.[16] Detailed studies examining the contributions from exciton-exciton scattering to exciton dephasing can be found elsewhere.[25, 37] In the following sections we instead focus on the extrapolated results in the zero intensity limit, which effectively eliminates the contributions from the Γ_{ex-ex} term that broaden the homogeneous linewidth.

11.3.2 Temperature-dependent contributions from E_{11} population relaxation

Pure optical dephasing times are often considered to be identical to the T_2 time obtained directly from 2PE experiments, and the contributions from population relaxation are neglected by assuming that its lifetime is significantly long (i.e., $1/2T_1 \ll 1/T_2$). The population relaxation detected for the (6,5) nanotubes by pump-probe experiments however, contains a dominant decay component with a timescale similar to the T_2 time. This means that explicit account of the population decay time (T_1) is crucial to correctly obtain the pure optical dephasing time T_2^*.

To account for the contributions from population decay, we performed pump-probe measurements for the (6,5) tubes embedded in both PVP polymer and gelatin composites at different temperatures (see Figure 11.4a). For the PVP composites, the same temperatures were chosen as used for our 2PE measurements. Extraction of the decay timescales from the pump-probe data involves use of a least-squares deconvolution algorithm and a model function consisting of multi-exponential components. We obtained satisfactory fits for a majority of our data with a model function with three exponents, but for those measured near room temperature ($T \geq 250$ K), an additional exponential component was needed. Among these three or four components, the fastest decay component is always dominant, and has

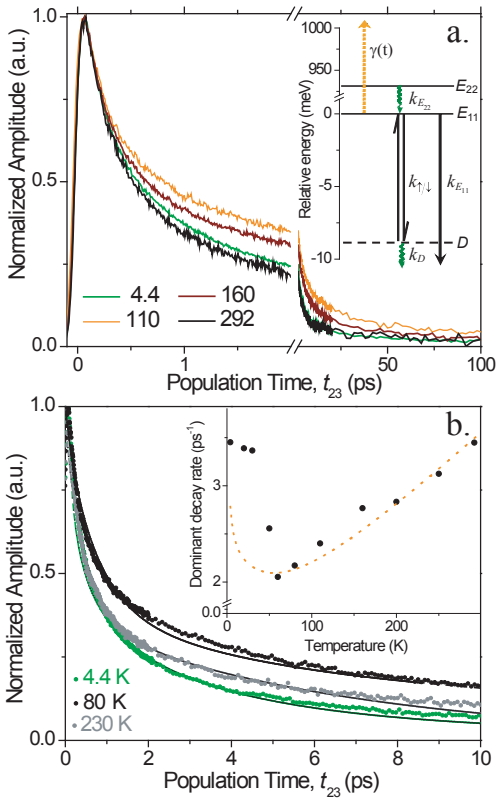

Figure 11.4. (a) Pump-probe data collected for the (6,5) tube embedded in PVP polymer matrix at four different temperatures (in K). The experiments were performed by exciting the E_{22} transition at 570 nm, and probing the E_{11} state at 998 nm. All the data were normalized at peak amplitudes of the pump probe signals, and the resulting decay profile appears largely independent of the pump fluence. The inset shows the three-state model used to model our data, where a radiative decay occurs from the E_{11} state to ground and all other rate constants represent non-radiative pathways. (b) Temperature dependence of the extracted population decay rates (black circles) for the fastest (and dominant) decay component of a multiexponential fit. The dotted line (orange) show the simulated temperature dependence. Simulated decay kinetics (solid lines) using the three-state model captures the main components of E_{11} dynamics for the temperatures shown.

an approximate relative weight of 60% of the total amplitude. The extracted lifetime for this fastest lifetime component ranged from 290 to 460 fs as temperature was lowered from room temperature to 80 K. The lifetime associated with the second decay component ranged form 2.7 to 5.6 ps over the same temperature range with a relative ampliteude of 30%, and the slowest decay component has a lifetime of 140 ps with about 10% relative amplitude. It is clear from equation 11.1, that the two slower decay components will not contribute appreciably to the pure dephasing rate. Also, their significantly smaller amplitudes in combination with their relatively weak temperature dependence further reduce their influence on the obtained pure dephasing times T_2^*. Thus, we will instead focus primarily on modelling the initial, fast decay portion of the pump-probe data collected at various temperatures.

The inset in Figure 11.4b shows the dominant population decay rates extracted from the fastest exponential relaxation component at each temperature measured. Upon cooling from 292 to 80 K, a roughly linear dependence of the population decay rate on temperature is found. Such a rate increase with temperature is normally expected for systems dominated by non-radiative decay primarily mediated by exciton-phonon scattering.[41] On cooling below the 80 K threshold, a marked increase in the E_{11} population decay rate is observed, which can be seen from the kinetics shown in Figure 11.4a. To model if such an acceleration in the initial decay component for (6,5) SWNTs, a phenomenological three state model previously used to describe temperature dependence of steady-state and time-resolved fluorescence kinetics of semiconducting SWNTs is adopted.[42, 43, 10] This three-state model allows for rapid thermalization of the optically bright E_{11} state with a third state state low-lying state (labeled D, see the energy level diagram in the inset of Figure 11.4a). At sufficiently low temperatures, the acoustic phonon modes mediating the $E_{11} \leftrightarrow D$ thermalization are no longer excited, which will effectively halt the uphill energy transfer from D to E_{11}. This consideration suggests that an enhancement in exciton population decay will occur when temperature approaches a certain value, which is qualitatively in line with the accelerated decay of the fastest decay component observed below 80 K in our pump-probe measurements (see Figure 11.4a,b).

To quantitatively simulate the population relaxation dynamics, we begin with the following coupled differential rate laws that describe the $n_{E_{11}}$ and n_D state populations (refer to Figure 11.4a(inset)).

$$\frac{dn_{E_{11}}}{dt} = k_{E_{22}} n_{E_{22}} - (k_{E_{11}} + k_{\downarrow}) n_{E_{11}} + k_{\uparrow} n_D - \gamma_0 t^{-1/2} [n_{E_{11}}]^2 \tag{11.3}$$

$$\frac{dn_D}{dt} = -(k_D + k_{\uparrow}) n_D + k_{\downarrow} n_{E_{11}} \tag{11.4}$$

Since, $E_{22} \rightarrow E_{11}$ relaxation is known to be fast (roughly 40 fs)[34] compared to our pulse width, we assume that the E_{11} band is impulsively populated (i.e., $k_{E_{22}}$=0). A major distinction of our model from the previous work is the explicit inclusion of an exciton-exciton annihilation process allowing for an additional population depletion pathway out of the E_{11} state. The corresponding annihilation rate is assumed to be $\gamma(t) = \gamma_0 t^{-(1-d/2)}$ using $d = 1$ for diffusion-controlled annihilation in the nanotubes.[44, 41] Using equations 11.3 and 11.4 we were able to satisfactorily show that such a three-state model can roughly reproduce the

temperature dependent rate coefficients shown in Figure 11.4b (inset, compare with orange dotted line).

For the above simulation, we assumed that that E_{11} exciton band is parabolic and band thermalization occurs according to Boltzmann statistics. In order to explicitly include the temperature dependence, a phonon assisted scattering process between the E_{11} and the low lying state D was included in equations 11.3 and 11.4, along with radiative decay ($k_{E_{11}}$) from the optically bright E_{11} state and non-radiative relaxation (k_{NR}) from D to ground state. Owing to momentum conservation, the radiative relaxation can occur only from excitons located within a region $\Delta \cong 0.37$ μeV above the band minimum, which is accessible by a photon's momentum.[43, 45] According to Spataru *et al.*,[46] for an infinite length tube, the E_{11} radiative decay rate at finite temperatures can be approximated as,

$$k_{E_{11}} = k^o \sqrt{\frac{\Delta}{k_b T}} \tag{11.5}$$

where k^o is an intrinsic radiative decay parameter (at $K_{cm} = 0$) and k_b is the Boltzmann constant. A corresponding intrinsic radiative lifetime of 2.5 ps was used. The actual effective radiative lifetime measured ($k_{E_{11}}$) will be orders of magnitude larger at all temperatures because of the exciton momentum distribution, and potential thermalization with the low-lying state, D. This intrinsic lifetime value is somewhat shorter than the ∼10 ps *ab initio* result predicted for the (8,0) tube type.[46] Above ∼80 K, excitation of acoustic phonons enables a constant thermal exchange between the E_{11} and the lower lying state D. The corresponding uphill and downhill rates ($k_\uparrow$ and $k_\downarrow$) can be approximately related by detailed balance as follows,

$$k_\uparrow = k_\downarrow \exp(-\Delta E_D / k_b T) \tag{11.6}$$

where ΔE_D is the energy difference from E_{11} to D, which our model suggests is approximately 9 meV. Recent measurements have identified low lying electronic states under high magnetic fields that have similar energy separations (5-8 meV) to the one we extracted.[11] The potential involvement of this low-lying state D, has been shown to further increase the effective radiative lifetime, particularly in $T <$∼80 K region.[43, 47]

The the downhill rate ($k_\downarrow$) and subsequent decay from the low lying D state (k_D) are assumed to be non-radiative. The corresponding temperature-dependence associated with non-radiative rates is approximated as,[48, 49]

$$k_{NR} = k_c + C \exp(-\theta_k / k_b T) \tag{11.7}$$

where $k - c$, C and θ_k are fitted constants determined to be 0.06 ps^{-1}, 0.6 ps^{-1} and 90 K for the $k_\downarrow$ phonon-mediated transition. For the relaxation from k_D, 0.15 ps^{-1} was used with no temperature dependence required for our temperature range. If we assume the exciton annihilation rate is largely temperature independent we can set $\gamma_0 = 0$ to get the initial rate dependence on temperature; our analysis then follows one presented by Scholes *et al.* applied to temperature dependent photoluminescence rates.[43] Using the fitted parameters to compute the initial decay rate, the three-state model reproduces the temperature-dependent trend observed for the dominant E_{11} kinetic relaxation rate (see Figure 11.4b, inset dashed line)).

The above model (with $\gamma_0 = 0$) gives a biexponential decay for E_{11} kinetics, whereas at least three exponential decay components were required to numerically approximate our pump-probe measurements. Inclusion of exciton-exciton annihilation introduces a nonexponential component which allows us to roughly model the temperature-dependent kinetic decay. Using γ_0 values ranging from 0.2 to 0.8 $ps^{-1/2}$, we solved the differential system of equation 11.3 and 11.4 numerically for temperatures ranging from 4 to 290 K. At most temperatures, the resulting simulated decay curves (solid lines) could reproduce the experimental decay well (see Figure 11.4b).

The involvement of low-lying states such as the phenomenological D state included here, has also been used extensively to model temperature dependent SWNT quantum yields. These studies report a precipitous decrease in quantum yield below 80 K, and suggests that any radiative decay out of low-lying state must be comparatively small.[42, 47, 50] Accompanying this marked decrease in yield, a significant decrease in total effective radiative rate has been reported.[47] In many works, low-lying states such as the D state has been commonly ascribed to the *1g* state originally proposed from calculations using a 1D hydrogenic model exciton wavefunction.[5, 43] The *1g* state is expected to be optically dark from parity selection rules for a one-dimensional SWNT.[10] However for intra-excitonic transitions from the optically bright E_{11} *1u* state to *1g*, rapid scattering and thermalization between states of different parity is allowed.[51, 52, 50]

Previous pump probe measurements on individually separated SWNTs have been reported down to 77 K only, and the measured E_{11} population lifetimes also increased in a roughly linear fashion upon cooling.[53] A linearly decreasing decay rate is reported down to $\sim$80 K in the time-resolved photoluminescence (PL) studies by Hagen *et al.* and Berger *et al.* on (9,4) and (6,4) SWNTs.[47, 54] In the $T <\sim 80$ K region, the overall PL decay rate was reported to plateau, and remained roughly constant down to 4 K. In contrast to the pump probe measurements reported here, the previously reported PL single photon counting measurements have intrinsically lower (ps) time resolution.[47, 43] As a result, a rate acceleration occurring on the $\sim$100 fs timescale may not be detected.

Modeling of the temperature dependent pump-probe decay curves, suggests the low temperature rate acceleration is physically consistent with involvement of a low-lying state. While a similar temperature-dependent trend was also observed for (6,5) SWNTs in a gelatin composite environment (data not shown), we nonetheless cannot completely rule out unforeseen environmental considerations as an alternate explanation. Regardless of the precise physical origin of the observed acceleration in E_{11} population decay rate at low temperatures, we can use the dominant initial decay rates plotted in Figure 11.4b (inset) to effectively remove the contributions of population relaxation from our 2PE results, allowing us to determine T_2^* directly.

11.3.3 Pure optical dephasing timescales

Semiconducting SWNTs generally have weak exciton-phonon coupling, an observation that was first suspected from both the associated small Stokes shift (e.g. $\sim$4 nm in Figure

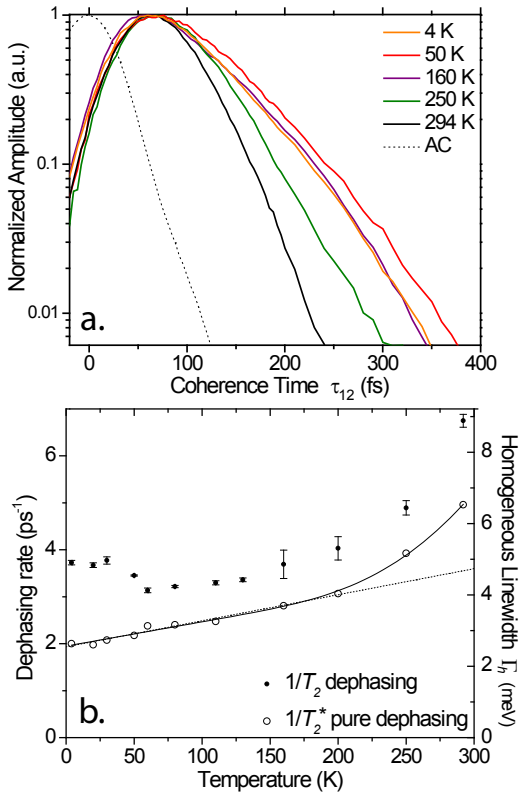

Figure 11.5. (a) Temperature-dependent 2PE collected at 6.0 μJ/cm^2 total excitation fluence for (6,5) SWNTs in a PVP polymer composite. Below ~80 K, T_2 decreases. (b) Population decay rates ($1/T_1$) are used to calculate pure dephasing times, revealing a predominately linear slope (dotted line) consistent with optical dephasing from one-phonon processes.

11.1a) and from *ab initio* calculations.[55] A 205 fs dephasing time (low intensity limit) is extracted for (6,5) SWNTs in aqueous solution at 294 K (Figure 11.3a). Such long dephasing times at room temperature are indicative of weak exciton-phonon coupling strength. To better understand the physical origin of this weak coupling, 2PE traces were measured as a function of excitation fluence at fixed temperature increments down to temperature of 2.5 K. Consistent with previous T_2 times reported down to 77 K,[16] the extracted dephasing times increase only moderately (to 320 fs) upon cooling to 70 K. Extending the experiment to lower temperatures reveealed an unexpected marked increase in the 2PE decay rate (see Figures 11.5a and b). Since lowering temperature necessarily decreases the phonon population, the observed increase in dephasing rate for T $\lesssim$ 80K plotted in Figure 11.5b is not consistent with line-broadening associated with exciton-phonon interactions (i.e., Γ_{ex-ph}(T)).

For all temperatures examined, we find the population dynamics are sufficiently fast to significantly broaden the corresponding homogeneous linewidths. Using equation 11.1, the contributions from population relaxation (T_1) are removed to estimate the pure dephasing rate ($1/T_2^*$). The $1/T_2^*$ rate is plotted in Figure 11.5b (open circles), and has a distinctly different temperature dependence than the $1/T_2$ rate owing to an acceleration in the initial E_{11} population decay rate ($1/T_1$) for T $\lesssim$ 80 K. In particular, the resulting pure dephasing rate increases linearly for T $\lesssim$ 180 K. Such linear rate dependence on temperature is a strong indicator of dephasing induced by one-phonon interactions.[12]

To fit the pure dephasing rates obtained, the following line-broadening function is used to determine what exciton-phonon scattering processes contribute to optical dephasing of the E_{11} excitation for (6,5) SWNTs,

$$\Gamma_h(T) = \Gamma_0 + aT + \frac{b}{e^{(\hbar\omega_{LO}/k_bT)} - 1} \tag{11.8}$$

which is shown in Figure 11.5b as the fitted solid line.[12] The first term Γ_0, represents the finite homogeneous linewidth at T = 0 K, which is 2.45$\pm$0.05 meV (or $T_2^* \cong$ 535 fs). The second parameter is the linear temperature-dependent line-broadening rate a = 6.7$\pm$0.6 μev/K, and corresponds to one-phonon scattering processes commonly from acoustic phonons. For T $\lesssim$ 180 K, we find such one-phonon acoustic scattering processes are the dominant contribution inducing pure optical dephasing (shown by dotted linear fit in Figure 11.5b). Remarkably similar linear line-broadening rates (a) have also been reported in GaAs quantum wells using a similar 2PE analysis.[21, 20] The last term in equation 11.8, provides contributions from optical phonon scattering which scale with the Bose optical phonon occupation factor. The corresponding fit suggests an intrinsic optical phonon energy of $\hbar\omega = 1028 \pm 231$ cm^{-1} with $b = 250 \pm 180$ meV. However, the sparsity of points collected in this T > 180 K region previously investigated in detail by Ma *et al.*,[16] prevents accurate assignment of the optical modes involved. Nonetheless, within the error calculated, the previously implicated traverse optical (TO) mode at 860 cm^{-1},[16] or the longitudinal acoustic + TO mode present at 960 cm^{-1} are potential candidates.[56]

Reasonable correspondence is found between our time-domain on an ensemble of (6,5) SWNTs and recently reported single nanotube photoluminescence work on (9,8) tubes. Both measurements reported a nearly identical low temperature linewidth of $\sim$2.5 meV.[23] This

particular single-tube measurement also produced a linewidth which scaled linearly with temperature (below ∼160 K), although the reported slope was almost three times as steep as the values we extracted for (6,5) SWNTs.[23] A more meaningful comparison however would require information on the lifetimes associated with the (9,8) SWNTs investigated in this single-nanotube study.

The observation of a significant homogeneous linewidth (Γ_0 = 2.45 meV) as T → 0, suggests the presence of a large intrinsic environmental disorder that should be highly sample dependent. Calculations by Perebeinos *et al.* suggest that even a small amount of spectral diffusion from the surrounding environment can give rise to a significant homogeneous linewidth as T → 0.[10] To investigate the the origin of this low-temperature disorder, the role of the local environment on dephasing processes will be examined in section E.

11.3.4 Spectral diffusion contribution; a 3PEPS measurement

In order to investigate the timescales extracted from 2PE and transient absorption results, a room temperature pure dephasing time of 285 fs is determined for aqueous (6,5) SWNTs. In order to investigate this apparently weak exciton-phonon coupling in the E_{11} band, we next investigate the role of spectral diffusion processes for $t_{23} > 0$, using temperature-dependent 3PEPS spectroscopy. Using 3PEPS, the photon echo signal is simultaneously collected in the $\mathbf{k}_1 - \mathbf{k}_2 + \mathbf{k}_3$ and $-\mathbf{k}_1 + \mathbf{k}_2 + \mathbf{k}_3$ phase matching directions, allowing access to the time delay between the second and third pulses corresponding to the population time (i.e., t_{23}). Here we report a measurement of the temperature-dependent 3PEPS, full details on SWNT 3PEPS measurements at room temperature have been reported elsewhere.[15]

When the time delay t_{23}=0, the 3PEPS (τ^*) measurement provides an indirect measurement optical dephasing time. While there is no analytic relation between the peak shift and T_2, both quantities scale with the mean square of E_{11} state frequency fluctuations (Δ_m^2) that are modulated by the phonon bath.[33] After an established scaling ratio is used to correct for the 45 fs pulse duration employed, the numerically converted initial peak shift values agree remarkably well with the corresponding dephasing rates obtained directly from 2PE experiments collected under the same excitation fluence (see Figure 11.6a).[57, 17] Such high correspondence with peak-shift measurements provides independent support of the dephasing times obtained directly from 2PE measurements.

Examining the peak shift dependence as a function population times, the 3PEPS decay profile provides information about spectral diffusion processes in the E_{11} band. The 3PEPS decay profiles shown in Figure 11.6b were collected under a low excitation fluence of 4.3 μJ/cm^2 at various temperature increments. The room temperature 3PEPS decay profiles have been previously analyzed to obtain spectral lineshapes and estimation of exciton-phonon coupling strengths.[15] Since the low temperature band thermalization processes are not yet well understood in SWNTs, we instead analyze the temperature-dependent 3PEPS profiles qualitatively. Upon cooling, the peak shift decays at a markedly slower rate toward a constant long-time peak shift value of ∼22 fs. This long-time offset is largely temperature-independent, and suggests a fixed inhomogeneous linewidth contribution arising from static

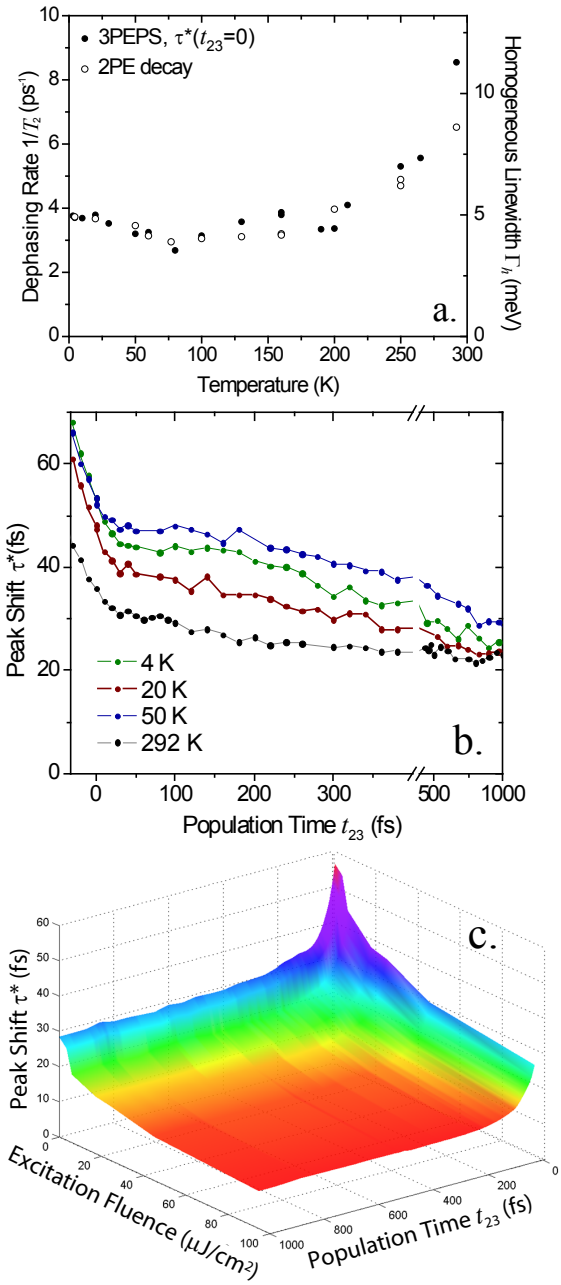

Figure 11.6. (a) The initial (t_{23}=0) peak shift provides an alternative measure of exciton dephasing. It yields complimentary results to 2PE measurements after proportionality is applied to account for pulse duration. (b) With decreasing temperature, the peak shift increases non-uniformly (shown for a 4.3 μJ/cm^2 excitation fluence in PVP polymer composites). For long population times, all 3PEPS curves decay to a similar asymptotic value which is indicative of inhomogeneous spectral broadening. (c) A plot of the photon echo peak shift decay at 292 K shown as function of excitation fluence. The observed intensity dependence at a given population time is qualitatively similar to what is observed from 2PE experiments.

environmental interactions. As the temperature is lowered, the decay rate of the peak shift profile slows considerably (Figure 11.6b). A slower 3PEPS decay rate at lower temperatures is physically consistent with a smaller thermal phonon population, resulting in a statistically longer time for spectral diffusion to effectively erase the system memory associated with the E_{11} band transition.[35]

In Figure 11.6c, the intensity dependence of the 3EPES profiles is plotted for room temperature. Their exists a strong correlation between the excitation fluence dependence of the initial peak shift values, and those of the 2PE decay rates extracted section in IIIc. When normalized to a specified t_{23} time the peak-shift profile measured at various excitation flueces can be approximately superimposed (data not shown). Similar to the 2PE echo results, we attribute the origin of the intensity-induced spectral diffusion contribution to exciton-exciton scattering processes. Recently Abramavicius *et al.* modeled this intensity dependence using a non-perturbative phase cycling approach that explicitly accounts for the contribution of exciton-exciton scattering and annihilation processes to the measured photon echo signal. Using this theoretical construct, it was shown that by inclusion of higher than third-order polarization terms, that the observed intensity dependent peak-shift and 2PE profiles can be simulated. The necessary inclusion of higher than third-order terms necessitates the involvement of coherent multiple-exciton states that induce optical dephasing primarily through annihilation pathways.[37] The requirement for multi-exciton states to model SWNT photon echo spectroscopy highlights the importance of analyzing photon echo spectroscopy in the regime of low excitation fluence, where such complicating contributions are greatly reduced.

11.3.5 Temperature-dependent dephasing and the local environment

Below 60 K, the existence of a ∼4 nm spectral blue-shift in the E_{11} absorption peak of SWNT-PVP polymer composite films (Figure 11.1b inset), suggests possible hydrostatic effects from the local environment may provide an alternative explanation for the acceleration in dephasing rates ($1/T_2$) plotted in Figure 11.6a. To investigate, select 2PE measurements were repeated with a central excitation wavelength tuned resonantly with the E_{11} spectral red edge at 1012 nm. For a given temperature and photon fluence, the dephasing times obtained were moderately shorter for excitation at the red edge, but the overall temperature-dependent trend observed (data not shown) was identical to the original resonant excitation case plotted in Figure 11.6a.

Selected for its comparatively small (∼2 nm) temperature-dependent E_{11} spectral shift, a gelatin-SWNT composite was used as a model system to investigate how surrounding polymer matrix effects the optical dephasing rates extracted. In Figure 11.7a, the corresponding room temperature dephasing rates are plotted for resonantly excited (6,5) SWNTs in aqueous solution, PVP polymer and gelatin composite environments. Nanotubes in all three local

environments produce long room temperature optical dephasing times (T_2 = 120 to 205 fs, see table I).

The temperature-dependent 2PE and 3PEPS measurements preciously presented were repeated on resonantly excited (6,5) SWNTs embedded in gelatin composite films. Comparing the 2PE decay profiles obtained for gelatin composites in Figures 11.7b to PVP polymer composite films shown in 11.5b, the optical dephasing rate is found to have a similar temperature dependence in the two host environments. The corresponding dephasing rates for gelatin composites are plotted in Figure 11.7c alongside the initial peak shift values. All data presented has been extrapolated to the zero-intensity limit. As with PVP composites, the initial peak shift values measured in gelatin composites show a parallel temperature dependence to the dephasing rates obtained directly from the 2PE decay profile.

The pure dephasing time for gelatin-SWNT composites was determined for select temperatures only (see table I below). Compared to SWNT aqueous suspensions, moderately faster pure dephasing rates are obtained after incorporating aqueous (6,5) SWNTs into the different polymer environments such as PVP and gelatin. This environmental dependence suggests bath fluctuations from the surrounding polymer are moderately coupled to the E_{11} exciton transition, however under ambient conditions exciton-phonon scattering intrinsic to the SWNT remains the dominant contribution to optical dephasing. As T $\rightarrow$ 0, the predicted pure dephasing time for the gelatin composite is $\sim$30% smaller than the PVP case, suggesting that changes in environmental static disorder and spectral diffusion also contribute substantially to the homogeneous broadening. The timescales of E_{11} exciton dynamics for (6,5) carbon nanotubes are sumearized in Table 11.3.5:

	T(K)	T_1	T_2	$T_{2,m}$	τ^*	T_2^*
PVP	292	295	162	132	53	223
polymer	80	460	311	275	–	470
	4.4	289	269	242	–	508
Gelatin	292	302	124	121	48	155
	110	683	228	170	68	274
	4.4	146	158	130	55	344
Aqueous	292	372	205	184	52	283

Table 11.1. Extracted values (in fs) that characterize the various timescales of E_{11} exciton dynamics for (6,5) SWNTs. With the exception of the dephasing time measured at lowest excitation intensity (denoted $T_{2,m}$), all decay times and peak shifts (τ^*) have been extrapolated to the zero intensity limit.

For gelatin-SWNT composites, an oscillatory feature consistent with vibrational beating was also apparent in the 2PE decay during the pulse overlap region. Using singular value decomposition a dominant beat frequency of 1770 cm^{-1} is extracted which is similar to the 1610 cm^{-1} ground state tangential Raman mode(G-band) for the (6,5) SWNT.[58] Such oscillatory behavior has been previously observed in transient absorption measurements using pulse widths shorter than the G-band vibrational period ($\sim$21 fs).[59] Interestingly, for the 2PE measurements this oscillatory component diminishes almost entirely in amplitude for

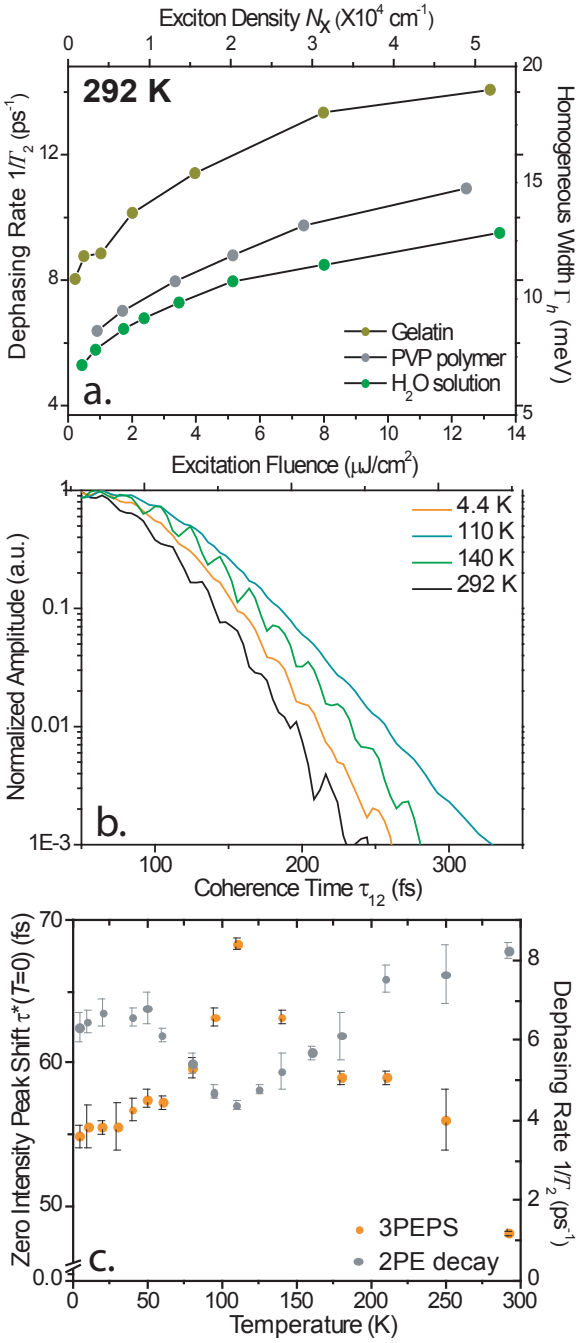

Figure 11.7. (a) Extracted room temperature optical dephasing rates for (6,5) SWNTs in different local environments. (b) Temperature-dependent 2PE collected at 6.0 μJ/cm^2 in a gelatin matrix. Below 100 K, T_2 decreases markedly. A weak oscillatory frequency closely matching the G-band period is apparent for T ~130 K. (c) Corresponding peak shift measurements were collected concurrently with 2PE decays for (6,5) SWNTs in gelatin. The peaks shifts were extrapolated to the zero intensity limit, yielding complimentary results.

temperatures corresponding to the longest dephasing times. One potential explanation is at low temperature the exciton wavepacket may be sufficiently delocalized to effectively "average over" the coupled G-band tangential mode. This phenomenon of motional narrowing that has been extensively described in other quasi 1-D systems such as molecular aggregates.[18, 60] If present in SWNTs, motional narrowing may help explain why long pure dephasing times are realized under ambient conditions.

11.3.6 Motional Narrowing and Exciton-Phonon Coupling Strength

Considering the well-defined nanotube vibrational modes, and large surface area exposure to the surrounding environment, the observation of weak exciton-phonon coupling at room temperature is perhaps surprising. We explore the role of motional narrowing by fitting the non-exponential behavior in the 2PE decay profile across a range of temperatures. Using the model discussed below, the shape of 2PE decay profiles suggests the corresponding E_{11} homogeneous linewidths are motionally narrowed for all temperatures measured.

The non-exponential component of the 2PE decay is extracted using a model function derived out of the stochastic Kubo line-shape theory for a system coupled to a fluctuating reservoir of phonons, and full details can be found elsewhere.[19, 32, 61] In short, an ensemble of E_{11} optical transitions is described by a frequency correlation function ($M(t)$) that we assume decays at an exponential rate, $M(t) = e^{-t/\tau_m}$, as the result of exciton coupling to the phonon bath.[32] Here, τ_m is the frequency modulation time that provides the timescale of the phonon frequency perturbations which induce electronic dephasing. The expected profile of a given 2PE curve ($S_E(\tau)$) can then be obtained analytically from $M(t)$,[32]

$$S_E(\tau) = \exp\left\{-4\left(\Delta_m\tau_m\right)^2\left[2\exp\left(\tfrac{-\tau}{\tau_m}\right) - \tfrac{1}{2}\exp\left(\tfrac{-2\tau}{\tau_m}\right) + \tfrac{\tau}{\tau_m} - \tfrac{3}{2}\right]\right\}. \tag{11.9}$$

$\Delta_m\tau_m$ is a dimensionless product of τ_m and the amplitude of the frequency fluctuation (Δ_m). $1/\Delta_m$ represents the minimum time required by the uncertainty principle for an exciton to couple to a phonon mode.[62] If $\tau_m > 1/\Delta_m$, the exciton wavepacket is propagating too fast to fully experience the applied fluctuation.[32, 62] Hence when $\Delta_m\tau_m \ll 1$, the exciton-phonon coupling process is said to be strongly motionally narrowed. The presence of motional narrowing weakens the effective exciton-phonon coupling strength, resulting in narrower homogeneous linewidth with a characteristic Lorentzian spectral shape.[18, 62]

Across all temperatures investigated, the 2PE decay profile suggests our corresponding homogeneous linewidth is motionally narrowed with an average $\Delta_m\tau_m = 0.28 \pm 0.04$ (see Figure 11.8). Thus, E_{11} excitons in (6,5) SWNTs may not couple effectively to many phonon modes, because nuclear fluctuations from the phonon bath are averaged over from the spatial extent of the exciton along the tube.[18] Certain modes (e.g. the TO optical mode), may invariably couple stronger than others depending upon the geometry and strength the applied nuclear fluctuation. When modes involved in motional narrowing are no longer populated

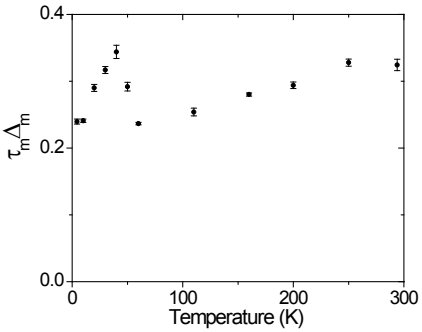

Figure 11.8. Modeling the non-exponential component of the decay for the 2-pulse echo signal (S_{PE}) for (6,5) SWNTs in PVP polymer suggests we are in a motionally narrowed regime for all temperatures measured.

at lower temperature, no net effect on the dephasing time is expected. This observation is in accord with the weak overall temperature dependence associated with the pure optical dephasing rate shown in Figure 11.5b.

In site basis, motional narrowing can be modeled as a form of ballistic exciton transport along the nanotube axis (during T_2^*). Ballistic transport implies the exciton is moving faster than it can be thermalized by exciton phonon-coupling. For metallic SWNTs, ballistic transport is a well-established physical property.[63] To check if such a transport process is reasonable for semiconducting SWNTs, we can approximate the kinetic energy of ballistic excitons by $E_{ball} = \frac{1}{2} m_{ex}^* \left(\frac{d}{T_2^*}\right)^2$, where m_{ex}^* is the exciton effective mass and d is the exciton delocalization length.[64] In this classical approximation we find $E_{ball} \approx 3.5 d^2 \mu\text{eV/nm}^2$, which exceeds the room temperature thermalization energy (given by $E_k = \frac{1}{2} k_b T$) for initial exciton delocalization lengths on the order 50 nm. With literature values for d ranging from 10 to 100s of nm,[14, 10] this simple classical model suggests the exciton kinetic energy (E_{ball}) may exceed the thermalization energy even at room temperature. Since this model suggests $E_{ball} > E_k$ for temperatures ranging from 4.4 to 292 K, it is reasonable that E_{11} excitons may experience ballistic transport during the period T_2^*. The presence of ballistic transport further implies that exciton band thermalization may not occur appreciably until after the corresponding T_2^* time has elapsed.[65]

These *ad hoc* calculations for ballistic transport in (6,5) SWNTs, lend support to our 2PE results which suggest a motionally narrowed exciton dephasing process at all temperature measured. As previously reported for quasi 1D molecular aggregates,[18] motional narrowing in SWNTs effectively averages over large dynamic disorder, suggests the presence of considerable exciton delocalization upon optical excitation. This averaging effect reduces the effective exciton-phonon coupling strength, and provides a possible explanation for the realization of long 285 fs E_{11} pure optical dephasing times at room temperature.

11.4 Conclusions

We find that motional narrowing is a significant process that modulates the phonon bath fluctuations coupled to the E_{11} exciton state for (6,5) SWNTs. This process effectively weakens the exciton-phonon interaction and suggests a physical explanation for the unusually long 285 fs T_2^* times realized at room temperature. Below ∼80 K in PVP polymer, and ∼100 K in gelatin-SWNT composites, a marked increase in dephasing rate was attributed to a corresponding acceleration in the E_{11} pump-probe decay rate. Applying a three state model previously developed for SWNT PL kinetics[43], this acceleration in population decay was attributed to exciton thermalization with a low-lying state, found to be ∼9 meV below the E_{11} state. By combining the resulting pump probe decay components and extracted 2PE decay times in the low excitation intensity limit, the pure dephasing times (T_2^*) are determined. Cooling from ambient conditions to 4.4 K, the overall pure dephasing rate decreases just under three fold, and has a linear rate below ∼180 K consistent with optical dephasing induced by acoustic phonon processes. Such a moderate T_2^* temperature dependence may be expected for ensemble measurements of (6,5) SWNTs because of motional narrowing effects and the presence of a large, environmentally induced homogeneous linewidth as $T \to 0$. Collectively, this study highlights the important contributions of coherent excitons to the overall E_{11} spectral dynamics of (6,5) SWNTs, and suggests an important interplay between exciton-phonon coupling and the exciton delocalization length motivating further investigation.

11.5 References

[1] M.S. Dresselhaus, G. Dresselhaus, and A. Jorio. Unusual properties and structure of carbon nanotubes. *Annu. Rev. Mater. Res.*, 34:247–278, 2004.

[2] Y.-Z. Ma, T. Hertel, Z.V. Vardeny, G.R. Fleming, and L. Valkunas. Ultrafast spectroscopy of carbon nanotubes. volume 111, pages 321–352. Springer-Verlag Berlin, Heidelberg, 2008.

[3] Sang-Yong Ju, William P. Kopcha, and Fotios Papadimitrakopoulos. Brightly fluorescent single-walled carbon nanotubes via an oxygen-excluding surfactant organization. *Science*, 323(5919):1319–1323, 2009.

[4] N. M. Gabor, Z. Zhong, K. Bosnick, J. Park, and P. L. McEuen. Extremely efficient multiple electron-hole pair generation in carbon nanotube photodiodes. *Science*, 325(5946):1367–1371, 2009.

[5] Feng Wang, Gordana Dukovic, Louis E. Brus, and Tony F. Heinz. The optical resonances in carbon nanotubes arise from excitons. *Science*, 308(5723):838–841, May 2005.

[6] J. Maultzsch, R. Pomraenke, S. Reich, E. Chang, D. Prezzi, A. Ruini, E. Molinari, M.S. Strano, C. Thomsen, and C. Lienau. Exciton binding energies in carbon nanotubes from two-photon photoluminescence. *Phys. Rev. B*, 72:241402(R)–241402(R), 2005.

[7] Y.-Z. Ma, L. Valkunas, S.M. Bachilo, and G.R. Fleming. Exciton binding energy in semiconducting single-walled carbon nanotubes. *J. Phys. Chem. B*, 109(33):15671–15674, 2005.

[8] M.S. Dresselhaus, G. Dresselhaus, R. Saito, and A. Jorio. Exciton photophysics of carbon nanotubes. *Annu. Rev. Phys. Chem.*, 58:719–747, 2007.

[9] C.D. Spataru, S. Ismail-Beigi, L.X. Benedict, and S.G. Louie. Excitonic effects and optical spectra of single-walled carbon nanotubes. *Phys. Rev. Lett.*, 92(7):077402–077402, 2004.

[10] V. Perebeinos, J. Tersoff, and P. Avouris. Radiative lifetime of excitons in carbon nanotubes. *Nano Lett.*, 5(12):2495–2499, 2005.

[11] J. Shaver and J. Kono. Temperature-dependent magneto-photoluminescence spectroscopy of carbon nanotubes: evidence for dark excitons. *Laser & Photonics Review*, 1(3):260–274, 2007.

[12] J. Shah. *Ultrafast spectroscopy of semiconductors and semiconductor nanostructures.* Berlin; New York: Springer Verlag, 1999.

[13] T. Joo, Y. Jia, J.-Y. Yu., M.J. Lang, and G.R. Fleming. Third-order nonlinear time domain probes of solvation dynamics. *J. Chem. Phys.*, 104:6089–6108, 1996.

[14] Yuhei Miyauchi, Hideki Hirori, Kazunari Matsuda, and Yoshihiko Kanemitsu. Radiative lifetimes and coherence lengths of one-dimensional excitons in single-walled carbon nanotubes. *Phys. Rev. B*, 80(8):081410–4, 2009.

[15] Matthew W Graham, Ying-Zhong Ma, and Graham R Fleming. Femtosecond photon echo spectroscopy of semiconducting single-walled carbon nanotubes. *Nano Lett.*, 8(11):3936–3941, 2008.

[16] Ying-Zhong Ma, Matthew W. Graham, Alexander A. Green, and Graham R. Hersam, Mark C.and Fleming. Ultrafast exciton dephasing in semiconducting single-walled carbon nanotubes. *Phys. Rev. Lett.*, 101(21):217402–4, 2008.

[17] Masao Ichida, Yumie Kiyohara, Shingo Saito, Yasumitsu Miyata, Hiromichi Kataura, and Hiroaki Ando. Phase-relaxation processes of excitons in semiconducting single-walled carbon nanotubes. *physica status solidi (b)*, 245(12):2712–2715, 2008.

[18] H. Fidder, J. Terpstra, and D.A. Wiersma. Dynamics of frenkel excitons in disordered molecular aggregates. *J. Chem. Phys.*, 94:6895–6907, 1991.

[19] S. Mukamel. *Principles of Nonlinear Optical Spectroscopy.* Oxford University Press, New York, 1995.

[20] D.-S. Kim, J. Shah, J.E. Cunningham, T.C. Damen, W. Schfer, M. Hartmann, and S. Schmitt-Rink. Giant excitonic resonance in time-resolved four-wave mixing in quantum wells. *Phys. Rev. Lett.*, 68(7):1006–1009, 1992.

[21] A. Honold, L. Schultheis, J. Kuhl, and C.W. Tu. Collision broadening of two-dimensional excitons in a gaas single quantum well. *Phys. Rev. B*, 40(9):6442–6445, 1989.

[22] A. Hartschuh, H.N. Pedrosa, L. Novotny, and T.D. Krauss. Simultaneous fluorescence and raman scattering from single carbon nanotubes. *Science*, 301:1354–1354, 2003.

[23] Kohei Yoshikawa, Ryusuke Matsunaga, Kazunari Matsuda, and Yoshihiko Kanemitsu. Mechanism of exciton dephasing in a single carbon nanotube studied by photoluminescence spectroscopy. *Applied Physics Letters*, 94(9):093109, 2009.

[24] J. Lefebvre, D.G. Austing, J. Bond, and P. Finnie. Photoluminescence imaging of suspended single-walled carbon nanotubes. *Nano Lett.*, 6(8):1603–1608, 2006.

[25] Matthew W Graham, Ying-Zhong Ma, and Graham R Fleming. Femtosecond photon echo spectroscopy of semiconducting single-walled carbon nanotubes. *Proc of SPIE*, 7600:76001F1–13, 2010.

[26] M.S. Arnold, A.A. Green, J.F. Hulvat, S.I. Stupp, and M.C. Hersam. Sorting carbon nanotubes by electronic structure using density differentiation. *Nature Nanotech.*, 1:60–65, 2006.

[27] O.N. Torrens, D.E. Milkie, M. Zheng, and J.M. Kikkawa. Photoluminescence from intertube carrier migration in single-walled carbon nanotube bundles. *Nano Lett.*, 6(12):2864–2867, 2006.

[28] P.H. Tan, A.G. Rozhin, T. Hasan, P. Hu, V. Scardaci, W.I. Milne, and A.C. Ferrari. Photoluminescence spectroscopy of carbon nanotube bundles: evidence for exciton energy transfer. *Phys. Rev. Lett.*, 99:137402–137402, 2007.

[29] R.B. Capaz, C.D. Spataru, P. Tangney, M.L. Cohen, and S.G. Louie. Hydrostatic pressure effects on the structural and electronic properties of carbon nanotubes. *Phys. Stat. Sol. (b)*, 241(14):33523359–33523359, 2004.

[30] R.B. Capaz, C.D. Spataru, S. Ismail-Beigi, and S.G. Louie. Diameter and chirality dependence of exciton properties in carbon nanotubes. *Phys. Rev. B*, 74:121401(R)–121401(R), 2006.

[31] S.B. Cronin, Y. Yin, A. Walsh, R.B. Capaz, A. Stolyarov, P. Tangney, M.L. Cohen, S.G. Louie, A.K. Swan, M.S. Unlu, B.B. Goldberg, and M. Tinkham. Temperature dependence of the optical transition energies of carbon nanotubes: the role of electron-phonon coupling and thermal expansion. *Phys. Rev. Lett.*, 96:127403–127403, 2006.

[32] Mark A. Berg, K. D. Rector, and M. D. Fayer. Two-pulse echo experiments in the spectral diffusion regime. *J. Chem. Phys.*, 113(8):3233–3242, 2000.

[33] T. Joo and A.C. Albrecht. Electronic dephasing studies of molecules in solution at room temperature by femtosecond degenerate four wave mixing. *Chem. Phys.*, 176(1):233–247, 1993.

[34] C. Manzoni, A. Gambetta, E. Menna, M. Meneghetti, G. Lanzani, and G. Cerullo. Intersubband exciton relaxation dynamics in single-walled carbon nanotubes. *Phys. Rev. Lett.*, 94(20):207401–207401, 2005.

[35] Minhaeng Cho, Jae-Young Yu, Taiha Joo, Yutaka Nagasawa, Sean A. Passino, and Graham R. Fleming. The integrated photon echo and solvation dynamics. *J. Phys. Chem.*, 100(29):11944–11953, 1996.

[36] S. Berciaud, L. Cognet, P. Poulin, R.B. Weisman, and B. Lounis. Absorption sectroscopy of idividual sngle-wlled crbon nanotubes. *Nano Lett.*, 7(5):1203 – 1207, 2007.

[37] Darius Abramavicius, Ying-Zhong Ma, Matthew W. Graham, Leonas Valkunas, and Graham R. Fleming. Dephasing in semiconducting single-walled carbon nanotubes induced by exciton-exciton annihilation. *Phys. Rev. B*, 79(19):195445–6, 2009.

[38] Kazunari Matsuda, Tadashi Inoue, Yoichi Murakami, Shigeo Maruyama, and Yoshihiko Kanemitsu. Exciton dephasing and multiexciton recombinations in a single carbon nanotube. *Phys. Rev. B*, 77(3):033406–4, January 2008.

[39] H.P. Wagner, W. Langbein, J.M. Hvam, G. Bacher, T. Kmmell, and A. Forchel. Exciton dephasing in znse quantum wires. *Phys. Rev. B*, 57(3):1797–1800, 1998.

[40] Mayrose R. Salvador, P. Sreekumari Nair, Minhaeng Cho, and Gregory D. Scholes. Interaction between excitons determines the non-linear response of nanocrystals. *Chemical Physics*, 350(1-3):56–68, June 2008.

[41] H. van Amerongen, L. Valkunas, and R. van Grondelle. *Photosynthetic Excitons*. World Scientific, Singapore, New Jersey, London, Hongkong, 2000.

[42] W.K. Metzger, T.J. McDonald, C. Engtrakul, J.L. Blackburn, G.D. Scholes, G. Rumbles, and M.J. Heben. Temperature-dependent excitonic decay and multiple states in single-wall carbon nanotubes. *J. Phys. Chem. C*, 111(9):3601–3606, 2007.

[43] Gregory D. Scholes, Sergei Tretiak, Timothy J. McDonald, Wyatt K. Metzger, Chaiwat Engtrakul, Garry Rumbles, and Michael J. Heben. Low-lying exciton states determine the photophysics of semiconducting single wall carbon nanotubes. *J. of Phys. Chem. C*, 111(30):11139–11149, 2007.

[44] L. Valkunas, Y.-Z. Ma, and G.R. Fleming. Exciton-exciton annihilation in single-walled carbon nanotubes. *Phys. Rev. B*, 73:115432–115432, 2006.

[45] Catalin D. Spataru, Sohrab Ismail-Beigi, Lorin X. Benedict, and Steven G. Louie. Excitonic effects and optical spectra of single-walled carbon nanotubes. *Phys. Rev. Lett.*, 92(7):077402–077402, 2004.

[46] C.D. Spataru, S. Ismail-Beigi, R.B. Capaz, and S.G. Louie. Theory and ab initio calculation of radiative lifetime of excitons in semiconducting carbon nanotubes. *Phys. Rev. Lett.*, 95:247402–247402, 2005.

[47] S. Berger, C. Voisin, G. Cassabois, C. Delalande, P. Roussignol, and X. Marie. Temperature dependence of exciton recombination in semiconducting single-wall carbon nanotubes. *Nano Letters*, 7(2):398–402, 2007.

[48] M.F. Lin and K.W.-K. Shung. Plasmons and optical properties of carbon nanotubes. *Phys. Rev. B*, 50(23):17744–17747, 1994.

[49] S.H. Lin and R. Bersohn. Effect of partial deuteration and temperature on triplet-state lifetimes. *J. Chem. Phys.*, 48(23):2732–2738, 1968.

[50] Ryusuke Matsunaga, Yuhei Miyauchi, Kazunari Matsuda, and Yoshihiko Kanemitsu. Symmetry-induced nonequilibrium distributions of bright and dark exciton states in single carbon nanotubes. *Physical Review B*, 80(11):115436, 2009.

[51] Hayk Harutyunyan, Tobias Gokus, Alexander A. Green, Mark C. Hersam, Maria Allegrini, and Achim Hartschuh. Defect-induced photoluminescence from dark excitonic states in individual single-walled carbon nanotubes. *Nano Lett.*, 9(5):2010–2014, 2009.

[52] Kazunari Matsuda, Tadashi Inoue, Yoichi Murakami, Shigeo Maruyama, and Yoshihiko Kanemitsu. Exciton fine structure in a single carbon nanotube revealed through spectral diffusion. *Phys. Rev. B*, 77(19):193405–4, 2008.

[53] Y.-Z. Ma, L. Valkunas, S.M. Bachilo, and G.R. Fleming. Temperature effects on femtosecond transient absorption kinetics of semiconducting single-walled carbon nanotubes. *Phys. Chem. Chem. Phys.*, 8:5689–5693, 2006.

[54] A. Hagen, M. Steiner, M.B. Raschke, C. Lienau, T. Hertel, H. Qian, A.J. Meixner, and A. Hartschuh. Exponential decay lifetimes of excitons in individual single-walled carbon nanotubes. *Phys. Rev. Lett.*, 95:197401–197401, 2005.

[55] B.F. Habenicht, H. Kamisaka, K. Yamashita, and O.V. Prezhdo. Ab initio study of vibrational dephasing of electronic excitations in semiconducting carbon nanotubes. *Nano Lett.*, 7:3260–3265, 2007.

[56] R. Saito, C. Fantini, and J. Jiang. Excitonic states and resonance raman spectroscopy of single-wall carbon nanotubes. volume 111, pages 251–285. Springer-Verlag Berlin, Heidelberg, 2008.

[57] A. M. Weiner, S. De Silvestri, and E. P. Ippen. Three-pulse scattering for femtosecond dephasing studies: theory and experiment. *Journal of the Optical Society of America B*, 2(4):654–662, 1985.

[58] S.M. Bachilo, M.S. Strano, C. Kittrell, R.H. Hauge, R.E. Smalley, and R.B. Weisman. Structure-assigned optical spectra of single-walled carbone nanotubes. *Science*, 298:2361–2366, 2002.

[59] A. Gambetta, C. Manzoni, E. Menna, M. Meneghetti, G. Cerullo, G. Lanzani, S. Tretiak, A. Piryatinski, A. Saxena, R.L. Martin, and A.R. Bishop. Real-time observation of nonlinear coherent phonon dynamics in single-walled carbon nanotubes. *Nature Phys.*, 2(8):515 – 520, 2006.

[60] H. Pschierer and J. Friedrich. Pressure broadening and motional narrowing in excitonic states of J-Aggregates. *physica status solidi (b)*, 189(1):43–49, 1995.

[61] R. Kubo. *A Stochastic Theory of Line-shape and Relaxation*. Edinburgh, 1962.

[62] Yutaka Toyozawa. *Optical Processes in Solids*. Cambridge University Press, Cambridge, 2003.

[63] C. T. White and T. N. Todorov. Carbon nanotubes as long ballistic conductors. *Nature*, 393(6682):240–242, May 1998.

[64] Guillaume Cassabois and Robson Ferreira. Dephasing processes in a single semiconductor quantum dot. *Comptes Rendus Physique*, 9(8):830–839, 2008.

[65] Laurent Cognet, Dmitri A. Tsyboulski, John-David R. Rocha, Condell D. Doyle, James M. Tour, and R. Bruce Weisman. Stepwise quenching of exciton fluorescence in carbon nanotubes by single-molecule reactions. *Science*, 316(5830):1465–1468, 2007.

Chapter 12

Two-Dimensional Electronic Spectroscopy of Carbon Nanotubes

Application of 2D Fourier transform electronic spectroscopy to semiconducting SWNTs is demonstrated to decongest complex exciton dynamics. Analysis provides the E_{22} homogeneous linewidth, and elucidates the roles of vibrational and multi-exciton states in population relaxation.

12.1 Introduction

In contrast to the established electrical and mechanical properties the optical properties of semiconducting single-walled carbon nanotubes (SWNTs) are only just emerging with greatly enhanced fluorescence yields (up to 20%) and development of efficient nanotube photodiodes [1] The scope of optoelectronic applications for SWNTs depends critically on a detailed understanding of their highly congested absorption features consisting of excitonic (E_{11}, E_{22}, etc.), vibrational and partially dark transitions. While ultrafast techniques such as transient absorption and fluorescence up-conversion provide the general timescales of population relaxation substantial inhomogeneous broadening (four times the homogeneous linewidth), pronounced exciton-exciton scattering, and contribution of minor tubes types prevent unambiguous determination of the relaxation pathways associated with the most basic optical excitations [2-4]. Providing clarity amongst congestion, we demonstrate how 2D Fourier transform (2DFT) electronic spectroscopy gives an incisive time and frequency domain map of exciton dynamics in SWNTs. In contrast to other nanosystems studied using 2DFT spectroscopy (such as GaAs quantum wells), semiconducting SWNTs are char-

acterized by remarkably large exciton binding energies (0.4 to 1.0 eV) quasi one-dimensional confinement and long room temperature optical dephasing times ($T_2 \approx 200$ fs) [3,4].

Dominating SWNT optical absorption are two bright exciton states, the lower E_{11} and its counterpart in the next brillouin zone, the E_{22}. Associated with each bright exciton state is a manifold of continuum and low oscillator strength states which are believed to play a critical role in processes like non-radiative emission [4]. Using 2DFT spectroscopy, such states of low oscillator strength will be inherently brightened with heterodyne enhancement of cross-peaks that are linked to optically bright states of the same tube chirality. In this contribution, we demonstrate the utility of 2DFT electronic spectroscopy to uncover new photophysics in strongly confined excitonic systems such as semiconducting SWNTs.

12.2 Experimental Details

Until recently, carbon nanotube samples were highly inhomogeneous mixtures of many tube types, making advanced spectroscopic studies intractable. The sample used in this study is highly enriched in the (6,5) semiconducting tube type, through a density-gradient ultracentrifuguation process [5]. Such high sample purity allowed for (6,5) specific excitation of the E_{22} manifold of states using a 90 nm FWHM broadband pulse centered at 550 nm generated from a non-collinear optical parametric amplifier (NOPA) pumped by home-built 3.4 kHz Ti:sapphire/regenerative amplifier system. The 2DFT technique used is described in detail elsewhere [6]. Briefly, three 20 fs laser pulses were focused on the sample in a box geometry to generate the third order signal. In order to suppress laser light scattering, an aqueous solution enriched in (6,5) individualized tubes was used to fabricate a thin SWNT-polymer composite film using water soluble polyvinyl-pyrrolidone polymer. A heterodyne detection scheme on CCD camera was accomplished by passing a fourth pulse through the sample to serve as the local oscillator. This enabled us to spectrally resolve the SWNT four-wave mixing signal in both amplitude and phase while scanning the coherence time, τ (between pulses 1 and 2) at various population times, T (between pulses 2 and 3), from -25 to 500 fs. The coherence time was scanned from 0 to $\pm$300 fs, allowing the pulse ordering to select rephasing ($+\tau$) and non-rephasing ($-\tau$) signals

12.3 Results and Discussion

The collected absolute-value signal ($S(\Omega_\tau,\Omega_t,T)$) is plotted in figures 12.3a and b at T=0 and 50 fs as function of the absorption or coherence energy (Ω_τ) and emission or rephasing energy (Ω_t). For T=0, the salient diagonal features correspond to linear absorption for the E_{22} transition (2.17 eV) and a phonon-sideband peak (upshifted 220 meV or 1780 cm^{-1}) consistent with vibrational exchange with the G-band mode (tangential tube stretching). This assignment is supported by the vibrational beat period and weak cross-peaks linking

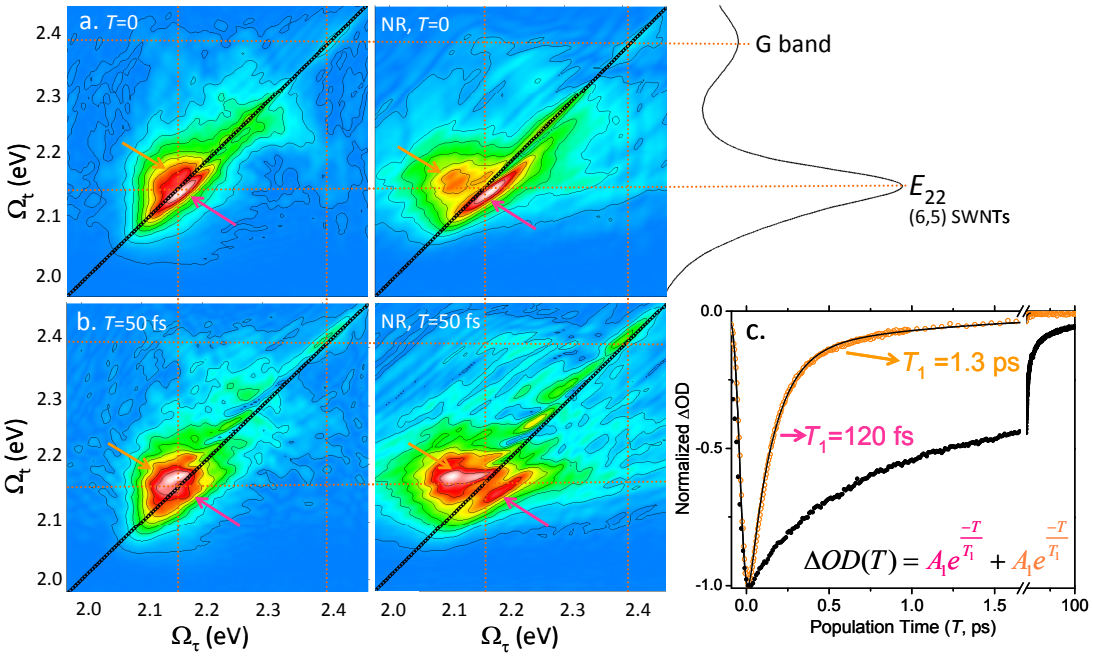

Figure 12.1. Preliminary 2D-electronic relaxation (left) and non-rephasing (NR, right) spectra shown for (**a**) T=0 and (**b**) T=50 fs. Dashed orange lines identify the linear absorption peak energies (far right) of the (6,5) E_{22} and phonon sideband. (**c**) E_{22} transient pump probe signal (open circles) decays biexpoentially (black line), each exponential component can be assigned to the arrowed spectral features shown in 1a and 1b. E_{22} pump, E_{11} probe relaxation kinetics (filled circles) has a slower non-exponential decay from exciton-exciton annihilation contributions [4].

the diagonal E_{22} and G-band peaks (recovered in an arcsinh scaling to amplify the noise-floor, not shown).

Since the E_{22} population relaxation is fast and non-radiative, the homogeneous linewidth cannot be estimated by common methods such as single-tube photo emission [4]. 2DFT spectroscopy enables direct extraction of the E_{22} anti-diagonal (homogeneous) linewidth that is fivefold smaller than the diagonal (homogeneous + inhomogeneous) linewidth. This (6,5) SWNT E_{22} linewidth estimate agrees with recently reported photon echo measurements providing the E_{11} absorption lineshape [2,3]. Such similarity in linewidth is expected because the E_{22} and E_{11} states should possess near-identical exciton band structures and associated environmental disorders.

Further decongestion of the (6,5) SWNT E_{22} lineshape is obtained by plotting the corresponding non-rephasing spectra (fig. 12.3a and b). We find that while the diagonal E_{22}peak decays rapidly, an unexpected feature shifted 50 meV off the diagonal persists for times longer than 500 fs (orange arrow). Subsequent 2DFT measurements also identify a similar feature associated with E_{22} excitation for the (7,6) tube using 650 nm excitation. To bet-

ter characterize this new feature, a one-color pump probe measurement (fig. 12.3c, open circles) spectrally tuned to the (6,5) E_{22} resonance was carried out. Fitting using a least-squares deconvolution algorithm (black line), we conclude the decay is biexponential with lifetimes of 120 fs (88%) and 1.3 ps (12%). The timescales and relative amplitudes assign these two exponential components to the arrowed spectral features (fig. 12.3a and b). The 120 fs lifetime corresponds to the expected exponential relaxation of the diagonal E_{22} peak (pink arrow) towards the longer lived E_{11} state (fig. 12.3c, filled circles) [7]. To explain the origin of the 1.3 ps decay and associated spectral feature (orange arrow), comparison of relative peak positions with 2DFT studies on GaAs quantum wells leads us to suspect involvement of multiple excitonic resonances [8]. As further support, we observe strong multiexciton contributions from exciton-exciton annihilation evidenced by an E_{22} pump probe amplitude dependence which increases only with the square root pump intensity. Biexciton contributions in particular, have been calculated with binding energies of $\sim$40 meV for (6,5) SWNTs, but experimental evidence has not yet proven their existence [9]. To investigate such potential peak assignments, future experiments will compare the beat frequency with known Raman modes and exploit the fact that biexciton formation can be suppressed by use of established polarization schemes [8].

12.4 Conclusions

We demonstrate successful application 2DFT spectroscopy to semiconducting SWNTs, and show how it simplifies complex exciton dynamics, such as explaining the origin of the biexponential E_{22} pump probe decay. 2DFT on SWNTs can further provide quantitative information such as the E_{22} homogeneous linewidths and vibrational coupling strengths; information not readily accessible by other spectroscopic means.

12.5 References

[1] N.M. Gabor, Z. Zhong, K. Bosnick, J. Park, P.L. McEuen, Science **325**, 1367 (2009).

[2] M.W. Graham, Y.-Z. Ma, G.R. Fleming, Nano Lett. **8**, 3936 (2008).

[3] Y.-Z. Ma, M.W. Graham and G.R. Fleming and A. Green and M.C. Hersam, Phys. Rev. Lett. **101**, 217402 (2008).

[4] Y.-Z. Ma, T. Hertel, Z. V. Vardeny, G.R. Fleming, L. Valkunas, *Carbon nanotubes*, (Springer series Topics in Applied Physics, 2008).

[5] M.S. Arnold, A.A. Green, J.F. Hulvat, S.I. Stupp, M.C. Hersam, Nature Nanotech. **1**, 60 (2006).

[6] T. Brixner, T. Mancal, I. V. Stiopkin and G. R. Fleming, J. Chem. Phys. **121**, 4221 (2004).

[7] C. Manzoni, A. Gambetta, E. Menna, M. Meneghetti, G. Lanzani, and G. Cerullo, Phys Rev Lett **94**, 207401 (2005).

[8] S.T. Cundiff, T. Zhang, A.D. Bristow, D. Karaiskaj, and X. Dai, Acc. Chem. Res. **42**, 1423 (2009).

[9] T.G. Pedersen, K. Pedersen, H.D. Cornean and P. Duclos, Nano Lett. **5**, 291 (2005).

Appendix A

Determination of Nonlinear Optical Susceptibility for (6,5) SWNTs

A.1 Introduction

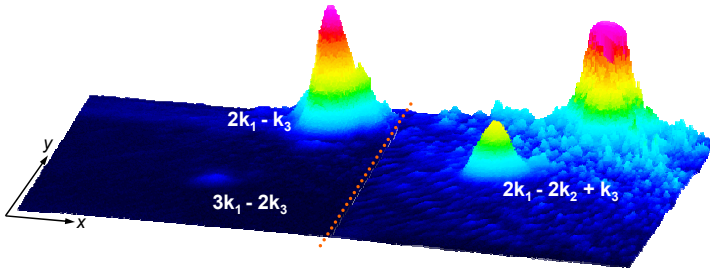

Figure A.1. Camera image of 2PE signals (in the $2\mathbf{k}_1 - \mathbf{k}_3$ direction), and signals emerging in the 5^{th} order directions of $3\mathbf{k}_1 - 2\mathbf{k}_3$ and $2\mathbf{k}_1 - 2\mathbf{k}_2 + \mathbf{k}_3$, from E_{11} resonant excitation of (6,5) SWNTs embedded in gelatin.

Until recently, SWNT samples were poly-disperse in many tube chiralities and were often highly bundled. As a consequence, the nonlinear properties (i.e. $\chi^{(3)}$) have not been well characterized for highly pure samples of individually separated SWNTs, such as the highly (6,5) enriched nanotubes used for the majority of work presented in this manuscript.[1] In the photograph shown in figure 1.1, resonantly excitation of (6,5) SWNTs produce intense, macroscopic scattered third order polarizations signals, suggestive of an inherently large nonlinearity. The remarkable nonlinear properties of SWNTs were best captured using a high resolution camera near the laser beam focal waist, where distinct signals emerging in the third and fifth-order phased matched direction are apparent (see figure A.1). To roughly

quantify the intrinsic nonlinearity, optical Kerr effect (OKE) measurements are preformed on resonance with the (6,5) E_{11} optical transition.

A.2 Hyperpolarizability

It can be shown that at sufficiently high intensities that both the refractive index (n) and absorption coefficient (α) can be expanded in a power series of the applied intensity.[2]

$$\begin{aligned} n(I) &= n_o + \gamma I + ... \\ \alpha(I) &= \alpha_o + \beta^{2\omega} I + ... \end{aligned} \tag{A.1}$$

The lowest order intensity-dependent terms are the hyperpolarizibility (γ) and the two-photon absorption coefficient ($\beta^{2\omega}$) respectively. By measuring the macroscopic observables $n(I)$ and $\alpha(I)$, we can relate them back to their corresponding linear and non-linear susceptibilities. To demonstrate this, the polarization expansion for first and third order processes can be truncated to give $P(\omega) = \chi^{(1)}E(\omega) + \chi^{(3)}(\omega)\left|E(\omega)\right|^2 E(\omega) \equiv \chi_{eff}E(\omega)$. By inserting χ_{eff} into the definition of the refractive index n we obtain the third-order correction given by,

$$\begin{aligned} & n^2 = 1 + 4\pi\chi_{eff} \\ & \Rightarrow \left(n_o + \gamma\left|E(\omega)\right|^2\right)^2 = 1 + 4\pi\chi^{(1)} + 12\pi\chi^{(3)}\left|E(\omega)\right|^2. \end{aligned} \tag{A.2}$$

When the terms up to second order in E are retained, the first and third order susceptibilities are proportional to the corresponding linear and nonlinear refractive indexes.

A.3 Optical Kerr Effect (OKE) Measure of Nonlinearity

Under intense E-fields many materials exhibit nonlinear phenomena such as high harmonic generation, four wave mixing and self focusing which are all hallmarks of a large intrinsic nonlinear susceptibility.[2] One common approach to quantify material nonlinearity is to perform a Z-scan. Here a material is slowly translated through the beam waist of a focused laser. As the intensity peaks near the beam waist, induced nonlinear effects from the sample will cause a phase shift in the emerging beam, leading to a small shift in the refractive index. The resulting change in beam direction is measured through the angular shift in beam intensity. Finally the corresponding $\chi^{(2)}(\omega = \omega - \omega)$ or $\chi^{(3)}(\omega = \omega + \omega - \omega)$ tensorial components can be calculated from plots of the signal response vs. sample translation position.[3, 2]

Here, the SWNT $\chi^{(3)}$ value is estimated using a four wave-mixing optical kerr experiment by comparison against a reference signal from CS_2 where the $\chi^{(3)}$ value has been well characterized. A schematic of the OKE experimental setup used is shown in figure A.2. Full experimental details are available in the literature.[4, 3]

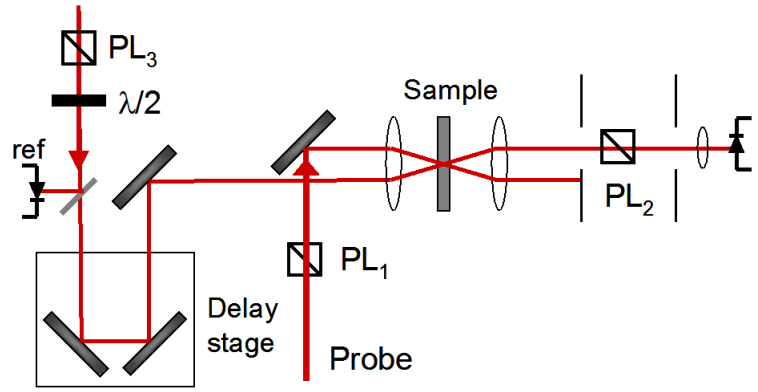

Figure A.2. Experimental setup for the OKE measurement of nonlinear susceptibility for (6,5) SWNTs.

The strength of nonlinear interaction cannot be inferred directly from the detected pump probe signal because the signal contains both both a homodyne and heterodyne contribution from interference with the local oscillator field (E_{LO}). To obtain the desired hetrodyne signal component (E_S), a series of polarizers (PL) and waveplates ($\lambda/2$) are used to selectively isolate the heterodyne cross terms of the total signal (I_{tot}) given below,

$$I_{tot} = (E_S + E_{LO})(E_S + E_{LO})^* = C(I_{LO} + I_S + I_b + Re[E_S^* E_{LO} + E_S E_{LO}^*]) \qquad \text{(A.3)}$$

where I_s and E_S are proportional to the selected $\chi^{(3)}$ element. To establish this proportionality under the given experiment conditions, a reference sample (commonly CS_2) of known nonlinearity $\chi^{(3)}_{ref}$ is employed. By additionally measuring the first-order order observables (n_{SWNT} and α) and $\chi^{(3)}_{ref}$ for CS_2, the third order susceptibility of carbon nanotubes ($\chi^{(3)}_{SWNT}$) was estimated using the relation,

$$\chi^{(3)}_{SWNT} = \chi^{(3)}_{ref} \sqrt{\frac{I_{SWNT}}{I_{CS_2}}} \left(\frac{n_{SWNT}}{n_{CS_2}}\right)^2 \left(\frac{l_{CS_2}}{l_S}\right) \frac{\alpha l}{(1 - e^{\alpha l}) e^{-\alpha l/2}}$$

The magnitude of the nonlinear susceptibility $\chi^{(3)}$ was calculated using the linear refraction index ($n_{SWNT} \cong n_{H_2O} = 1.33$ and $n_{CS_2} = 1.66$), the measured linear SWNT E_{11} extinction coefficient ($\alpha = 5.60$ cm^{-1}) and a literature CS_2 value for $\chi^{(3)}_{CS_2}$ of 5.87×10^{-13} esu at 1050 nm. Combining these established values with the experimental measurements for I_{CS_2} and I_{SWNT} shown in figure A.3, we report a $\chi^{(3)}$ value of 1.30×10^{-11} esu for (6,5) SWNTs at ~990 nm. Since SWNTs differ in composition between various samples, a more useful

measure of nonlinearity is the hyperpolarizability (γ) per carbon nanotube which is given by,

$$\gamma_{SWNT} = \frac{\chi^{(3)}}{NL} \tag{A.4}$$

where N is the number density of carbon atoms in our sample and L is the local field correction factor. The resulting hyperpolarizability is estimated to be 2.4×10^{-26} esu per (6,5) carbon nanotube. This value is very similar to other nanostructures such as semiconducting CdSe quantum dots where values of 1.6×10^{-26} esu have been reported.[5]

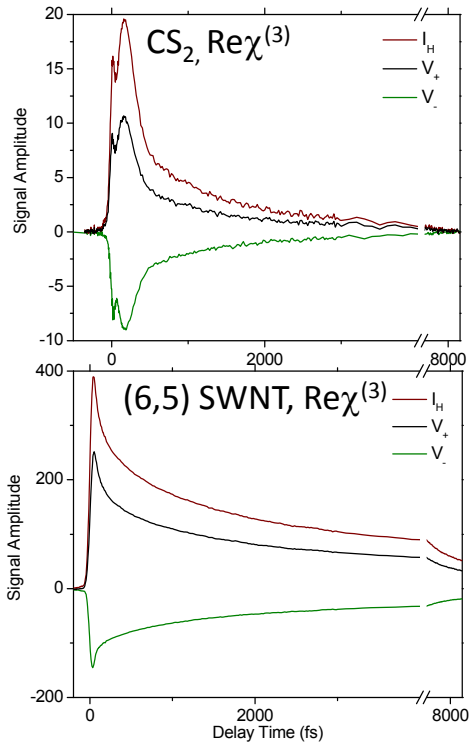

Figure A.3. OKE measurements on CS_2 (top) and resonantly excited (6,5) SWNTs (bottom). Each shows the time-dependent heterodyne leak for positive (V_+) and negative (V_-) phase, and the resulting pure-heterodyne signal (I_{SWNT}) used to estimate $\chi^{(3)}_{SWNT}$.

A.4 References

[1] M.S. Arnold, A.A. Green, J.F. Hulvat, S.I. Stupp, and M.C. Hersam. Sorting carbon nanotubes by electronic structure using density differentiation. *Nature Nanotech.*, 1:60–65, 2006.

[2] R. Boyd. *Nonlinear Optics 2nd Ed.* Academic Press, San Diego, 2003.

[3] Wenhui Yi, Wei Feng, Chunyu Zhang, Yingbing Long, Zhiguo Zhang, Baoming Li, and Hongcai Wu. The third-order optical nonlinearities of carbon nanotube modified conjugated polymer in the femtosecond and nanosecond regimes. *Journal of Applied Physics*, 100(9):094301, 2006.

[4] W. Lotshaw, D. McMorrow, N. Thantu, J. Melinger, and R. Kitchenham. *Intermolecular Vibrational Coherence in Molecular Liquids*. John Wiley and Sons, New York, 1996.

[5] JaeTae Seo, SeongMin Ma, Qiguang Yang, Linwood Creekmore, Russell Battle, Herbert Brown, Ashley Jackson, Tifney Skyles, Bagher Tabibi, William Yu, SungSoo Jung, and Min Namkung. Large resonant third-order optical nonlinearity of cdse nanocrystal quantum dots. *Journal of Physics: Conference Series*, 38(1):91, 2006.

Appendix B

Nanotube Polymer Composites; fabrication and optical properties

B.1 Introduction

In order to be individually separated, SWNTs in solutions must be stabilized by aqueous surfactants. Unfortunately both surfactant and water absorb highly in these regions of interest. As a consequence, the ability to obtain SWNT samples that have sufficient transparency for spectroscopic study in the mid-IR and terahertz region is challenging, requiring new synthetic preparations. Careful analysis suggest only a SWNT-polyethylene polymer composite the broad spectral window required for such detailed measurements.

B.2 Phase transfer procedure for SWNT-polyethylene polymer films

Special acknowledgment and thanks to Dr. Sergei Bachilo of Rice University for providing the technical guidelines needed for the method developed (below) for the fabrication CoMoCAT synthesized polyethylene composite films.

The starting sample in this procedure is CoMoCAT synthesized SWNTs from SouthWest Nanotechnologies that have been individually dispersed in sodium dodecylbenzene sulfonate (NaDDBS) surfactants. This suspension contains over one critical micelle concentration

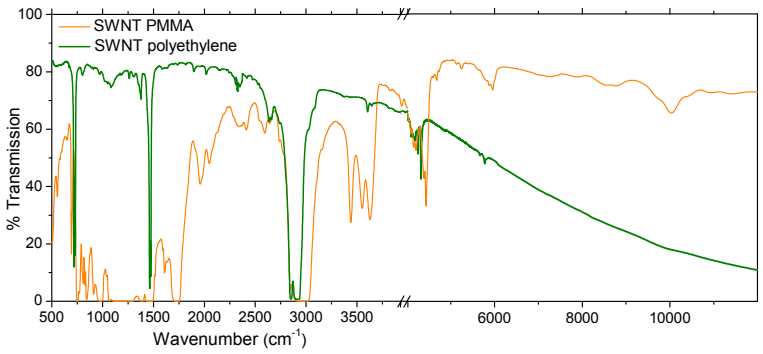

Figure B.1. Aqueous and polymer based (e.g. polymethylmethacrylate, PMMA) composites of individually separated SWNTs all absorb strongly in the mid-IR regions. The SWNT-polyethylene composites fabricated by the method outlined below provides a sufficiently large background in the mid-IR region to preform spectroscopic experiments (see chapters 5 and 6).

for long term stability. Excess surfactants in solution make achieve good phase separation difficult. Excess surfactants in CoMoCAT NaDDBS suspensions are removed, by adding small amount of decalin, followed briefly sonication (with a cell disruptor or cup-horn arrangement). Centrifugation brings the foamy excess surfactant to the surface. Discard and repeat.

Dissolve polyethylene (PE) powder (Sigma Aldrich, spectra grade) in decalin at 70^0C. Add 20% by volume CoMoCat suspension and immediately sonicate (using a Misonix cell disrupter, 8W max) until all aqueous components have evaporated and the suspension is clear. Additional decalin may need to added. A vacuum line was operated continuously over the sample (to prevent H_2O vapor from refluxing) and it was thermally insulated to prevent the PE from cooling and precipitating.

Once all aqueous component has been removed the colloidal suspension instantly becomes a transparent gray color, signaling the end of the phase transfer process. The clear solution is transferred to vacuum oven at 80^0C, where the solution was cast into various molds and left to dry at elevated temperature overnight.

The procedure developed works on a wides variety of organic solvents (decalins, xylenes and toluene) and can be adapted to make SWNT-polymer composites in a wide variety of media (including polyethylene, polypropylene, polymethylmethacrylate (PMMA) and polystyrene). Original demonstration of a similar technique was carried out by Dr. Sergei Bachilo (Rice University) who fabricated HiPCO PMMA films.

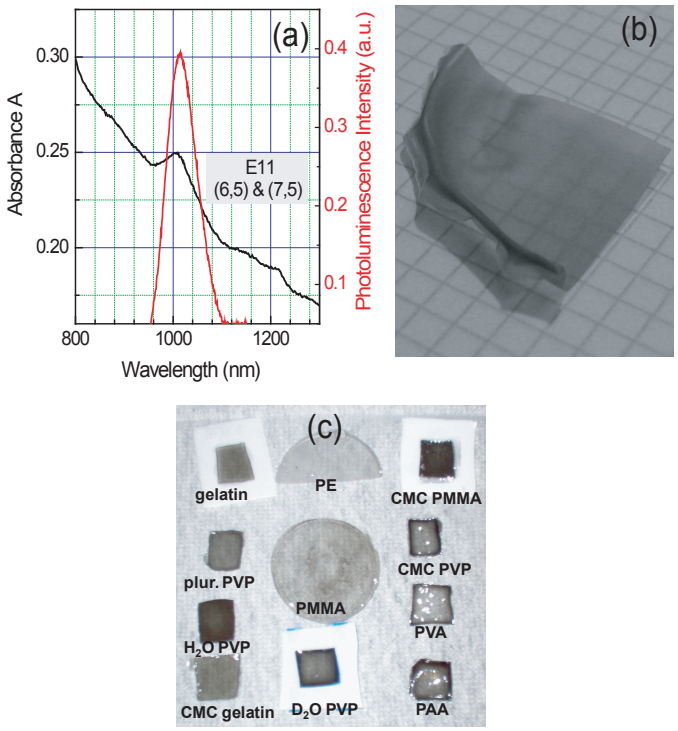

Figure B.2. (a) Linear absorption and fluorescence spectrum of individually separated SWNTs in a polyethylene. (b) Photograph of the SWNT-polyethylene composite films fabricated. (c) Photograph of various SWNT-polymer composites fabricated.

B.3 Characterization in visible and mid-IR regions

To characterize the resulting SWNT-polyethylene composites absorption, fluorescence and pump-probe spectroscopy are used. In figure B.1 a broad spectral window in the mid-infrared region is confirmed. In figure B.2a, relatively strong E_{11} fluorescence upon E_{22} optical excitation, confirm the majority of the (6,5) and (7,5) types tubes remain individually separated after being incorporated in polyethylene.

Various other CoMoCAT SWNT-polymer composites were fabricated including; PMAA, PAA = poly acrylic-acid, CMC = carbocymethylcellulose, PVP = polyvinylpyrrolidone, PE = polyethylene, PVA = poly vinly alcohol polymers (see figure B.2c). The overall E_{11} spectral shifts induced by different local environments are summarized below in table B.1.

Polymer	***Surfactant***	***Original Solvent***	***Fluor (6,5)***	***Fluor (7,5)***	***Abs Max (6,5)***
Solution	NaDDBS	H_2O	985	1030	1000*
	NaDDBS (2 C.M.C.)	D_2O	983	1028	980
	carboxymethylcellulose	H_2O	997	1042	993
	Pluronic	H_2O	1003		1006*
PVP	NaDDBS	H_2O	1009	1060	1010*
	NaDDBS (2 C.M.C.)	D_2O	1021	1032	1019
	carboxymethylcellulose	H_2O	1003	1054	995.5
PVA	NaDDBS	H_2O	1020		1018
PAA	NaDDBS	H_2O	1004		1003
Gelatin	NaDDBS	H_2O	1004		1015*
PMMA	NaDDBS	Xylenes/H_2O	1004	1032	997
	carboxymethylcellulose	Xylenes/H_2O	1000	1042	996
Polyethylene	NaDDBS	Decalin/H_2O	1013	1045	1015*
Polypropylene	NaDDBS	Decalin/H_2O	1015		1004

Table B.1. Linear absorption and fluorescence peak energies (in nm) for the E_{11} transition, in different surfactant micelles and/or surrounding polymer media. All samples contain approximately one critical micelle surfactant concentration (C.M.C.) unless otherwise noted. **Contributions from (6,5) and (7,5) SWNT peaks could not be doconvoluted.*